# INJECTION MOULDING POLYMER MICRONEEDLES USING LASER ABLATED MOULDS

Tim EVENS

Supervisor:
Prof. dr. ir. A. Van Bael

Co-supervisors:
Prof. dr. ir. S. Castagne
Prof. dr. ir. D. Seveno

Members of the Examination Committee:
Prof. dr. ir. M. Wevers, assessor
Dr. J. A. Ramos, assessor
Prof. dr. ir. F. Desplentere
Prof. dr. ing. C. Hopmann

Dissertation presented in partial fulfilment of the requirements for the degree of Doctor of Engineering Technology (PhD)

March 2023

© 2023 KU LEUVEN, Faculty of Engineering Technology
Uitgegeven in eigen beheer, TIM EVENS, OUDSBERGEN

Alle rechten voorbehouden. Niets uit deze uitgave mag worden vermenigvuldigd en/of openbaar gemaakt worden door middel van druk, fotokopie, microfilm, elektronisch of op welke andere wijze ook zonder voorafgaandelijke schriftelijke toestemming van de uitgever.

All rights reserved. No part of the publication may be reproduced in any form by print, photoprint, microfilm, electronic or any other means without written permission from the publisher.

# Voorwoord

*"It always seems impossible until it's done." Nelson Mandela*

Op 22 september 2018, tijdens mijn terugreis in de trein van het PMI-congres in Guimarães Portugal, ontving ik van mijn promotor een e-mail met daarin de vraag of het mogelijk zou zijn om micronaalden te produceren met behulp van spuitgieten. Deze naaldjes met een lengte van enkele honderden micrometers, opgesteld in een array, zouden in staat moeten zijn om de menselijke huid te doorprikken en medische substanties toe te dienen. Een uitdaging die door nagenoeg iedereen, inclusief mezelf, als onmogelijk werd geacht. En toch, door gedurende 4 jaar met vastberadenheid, passie, en doorzettingsvermogen aan dit onderwerp te hebben gewerkt, kan ik u met trots het eindresultaat voorstellen. Natuurlijk heb ik deze resultaten niet alleen bereikt. In dit woord vooraf wil ik dan ook van de gelegenheid gebruik maken om de mensen te bedanken die dit mee mogelijk hebben gemaakt.

In eerste instantie wil ik mijn promotor Prof. dr. ir. Albert Van Bael en mijn copromotoren Prof. dr. ir. Sylvie Castagne en Prof. dr. ir. David Seveno bedanken voor de kans die ze mij hebben gegeven om dit doctoraat uit te voeren. Jullie input, advies, begeleiding en interessante gesprekken hebben mij als onderzoeker naar een hoger niveau getild. Bovendien bedank ik graag de leden van mijn begeleidingscommissie: Prof. dr. ir. Martine Wevers en Dr. Jose A. Ramos voor hun kritische blik op mijn werk. Verder gaat mijn dank uit naar Prof. dr. ir. Frederik Desplentere en Prof. dr. ing. Christian Hopmann voor het zetelen in mijn examencommissie en het evalueren van mijn proefschrift.

Daarnaast wil ik ook alle collega's van 'Polymer Processing & Engineering' bedanken voor de fijne tijd die we samen hebben doorgebracht, zowel tijdens als na het werk. Jullie zorgden ervoor dat ik 's morgens steeds gemotiveerd aan de dag begon en 's avonds met een goed gevoel naar huis kon. Twee van deze collega's zou ik graag in het bijzonder bedanken. Gert-Jan, samen maakte we een heuse transformatie door van begeleider en student naar collega's, tot onafscheidelijk duo. Jouw passie voor onderzoek en kunststof-verwerking was voor mij een inspiratie om te starten aan dit avontuur. Nog steeds kan ik op u rekenen voor uw advies en brainstorm sessies, zelfs tijdens onze wekelijkse padel-sessies. Kristof, de congressen, evenementen en beurzen die wij samen bezochten waren onvergetelijk. Al vraag ik mij soms af of dit volledig onze verdienste is, of dat de steeds aanwezige Erdinger's hier ook voor iets tussen zitten. Desondanks, weet ik dat ik bij u steeds terecht kan voor ondersteuning, de nodige afleiding en uw oprechte mening.

Dit onderzoek zou uiteraard niet mogelijk geweest zijn zonder financiële steun. Graag bedank ik Johan Baeten en Kris Henrioulle van KU Leuven campus Diepenbeek voor het vertrouwen en de ruimte die ik van hen kreeg om dit werk te kunnen combineren met mijn onderwijsopdrachten. Daarnaast wil ik Olivier Malek van Sirris bedanken voor het ter beschikking stellen van hun laserapparatuur en de uitgebreide ondersteuning op gebied van microfabricage.

Ook mijn kameraden 'De Boys' en mede padel liefhebbers wil ik bedanken om ervoor te zorgen dat het werk toch af en toe naar de achtergrond verdween.

Uiteindelijk zijn we dan aangekomen bij de belangrijkste personen uit mijn leven, mijn familie. Mama en papa, bedankt om mij te steunen en mij de kans te hebben gegeven om

uit te groeien tot de persoon die ik vandaag ben. Woorden schieten tekort om uit te drukken hoe dankbaar ik jullie ben voor alles. Ben, jou technisch inzicht tijdens het ontwerpen van LEGO-constructies, het bouwen van modelvliegtuigjes en stoken van vuurtjes, bracht mij reeds op jonge leeftijd in contact met allerhande techniek. Het was dan ook vanzelfsprekend dat ik in jouw voetsporen wou treden tijdens het maken van mijn studiekeuzes.

Tenslotte blijft er nog één iemand over die mij op alle vlakken in het leven bijstaat. Zij helpt mij om kleine bekommernissen te relativeren, laat mij dagelijks lachen door onze unieke humor, zorgt ervoor dat ik mij steeds thuis kan voelen en nog zo veel meer. Lien, mijn mupke, bedankt voor de onvoorwaardelijke steun, waaruit ik de nodige dosis energie en motivatie kan putten!

Voorlopig gaat mijn avontuur aan de KU Leuven nog eventjes verder, dus de meerderheid van bovenstaande personen verdwijnen niet uit het zicht en dus zeker ook niet uit het hart.

Tim Evens

# Abstract

Microneedles are needle-like microscopic structures used to pierce the skin in order to either deliver medical substances, or to extract fluids from a body for sampling purposes. These needles are usually arranged in an array with individual needle lengths ranging from 25 to 2000 µm. Micro-sized needles offer various advantages compared to traditional hypodermic needles, such as a pain free delivery of medical substances. However, manufacturing microneedles represents a real challenge and a mass production process with high volume outputs at low cost is currently lacking.

A promising manufacturing process which fits these criteria is polymer injection moulding. By applying the negative geometry of the microneedles on a mould cavity, millions of polymer microneedle systems can be produced at a low cost. However, within the current state of the art, methods for applying the negative of the microneedles on the injection mould are limited to expensive and time consuming precision techniques. Besides, manufacturing microneedle cavities with a sharp tip has proven to be very difficult with these techniques, while small tip-radii are essential for microneedles to effectively penetrate the skin.

In this thesis, a production methodology for the fabrication of high volume, low cost polymer microneedles was developed. This methodology consists of a laser ablation process to produce cone-shaped microneedle cavities, which are afterwards replicated using injection moulding. First, insights are established in the influence of the laser scanning parameters on the geometry of the ablated microneedle cavities, being the cavity depth, the cavity base diameter and the shape of the needle flank. Next, the effect of various parameters on the replication fidelity and uniformity is investigated, being (i) the geometry of the microcavity, (ii) the location of the microneedles on the macroscopic product, (iii) the polymer characteristics, (iv) the mould material, and (v) the injection moulding technique (conventional injection moulding and injection compression moulding) with corresponding processing parameters. Furthermore, it is demonstrated that numerical flow simulations can be used to accurately predict the replication fidelity, in order to prevent extensive experimental injection moulding experiments.

A valorisation plan is then proposed which includes an identification of the target group that can benefit from the obtained research results, and an estimation on the market size is provided. The position of the developed methodology in the market is presented together with an economical evaluation. From an industrial point of view, the developed methodology is proven to be a suitable mass manufacturing technique to produce high volume, low cost polymer microneedles. Additionally, a key advantage of the methodology is its flexibility, which allows the development of microneedles with different shapes and dimensions in various thermoplastics.

# Samenvatting

Micronaalden zijn naaldachtige microscopische structuren die worden gebruikt om de huid te doorprikken, hetzij om medische stoffen toe te dienen, hetzij om vloeistoffen uit een lichaam te extraheren voor bemonsteringsdoeleinden. Deze naalden worden doorgaans geplaatst in een array, waarbij de individuele naaldlengtes variëren van 25 tot 2000 μm. Microscopische naalden bieden diverse voordelen in vergelijking met traditionele hypodermische naalden, zoals een pijnloze toediening van medische stoffen. De fabricage van micronaalden is echter een ware uitdaging en een massaproductieproces met hoge productievolumes en lage kosten ontbreekt momenteel.

Een veelbelovend productieproces dat aan deze criteria voldoet is kunststof spuitgieten. Door de negatieve geometrie van de micronaalden op een matrijsholte aan te brengen, kunnen miljoenen kunststof naaldjes tegen lage kosten worden geproduceerd. Binnen de huidige stand van de techniek zijn de methoden voor het aanbrengen van het negatief van de micronaalden op de spuitgietmatrijs momenteel echter beperkt tot dure en tijdrovende precisietechnieken. Bovendien is het met deze technieken zeer moeilijk om microholtes met een scherpe tip te maken, terwijl een kleine tipradius essentieel is om de huid effectief te kunnen doordringen.

In deze thesis is een productiemethode ontwikkeld voor het vervaardigen van kunststof micronaalden in grote volumes, tegen een lage kost. Deze methodologie bestaat uit een laserablatieproces om kegelvormige microholtes te produceren die vervolgens met behulp van spuitgieten worden gerepliceerd. Eerst wordt inzicht verkregen in de invloed van de laserparameters op de geometrie van de microholtes, meer bepaald de holte-diepte, de holte-diameter en de vorm van de naaldflank. Vervolgens wordt het effect van verschillende parameters op de replicatie tijdens het spuitgieten onderzocht, zijnde (i) de geometrie van de microholte, (ii) de plaats van de micronaalden op het macroscopische product, (iii) de polymeereigenschappen, (iv) het matrijsmateriaal, en (v) de spuitgiet-techniek met overeenkomstige verwerkings-parameters. Daarnaast wordt aangetoond dat numerieke vloeisimulaties gebruikt kunnen worden om de replicatie nauwkeurig te voorspellen, zodat uitgebreide experimentele spuitgietproeven kunnen worden vermeden.

Vervolgens wordt een valorisatieplan voorgesteld met de doelgroep die voordeel kan hebben bij de verkregen onderzoeksresultaten en een raming van de marktomvang. De positie van de ontwikkelde methode op de markt wordt bovendien gepresenteerd, samen met een economische evaluatie. Vanuit industrieel oogpunt is gebleken dat de ontwikkelde methode een geschikte massaproductietechniek is voor het produceren van goedkope kunststof micronaalden in grote volumes. Een belangrijk voordeel van de methode is bovendien de flexibiliteit, die de ontwikkeling van micronaalden met verschillende vormen en afmetingen in verscheidene thermoplasten mogelijk maakt.

# Contents

**Voorwoord** ..... **V**

**Abstract** ..... **VII**

**Samenvatting** ..... **IX**

**Contents** ..... **XI**

**List of Symbols** ..... **XV**

**List of Figures** ..... **XIX**

**List of Tables** ..... **XXV**

**Chapter 1 Introduction** ..... **1**

1.1 Motivation and problem statement ..... 1
1.2 Objectives ..... 2
1.3 Thesis outline ..... 2

**Chapter 2 State of the art** ..... **5**

2.1 Introduction ..... 5
2.2 Microneedles ..... 5
2.2.1 Characteristics ..... 5
2.2.2 Skin structure ..... 6
2.2.3 Types of microneedles ..... 7
2.2.4 Material types and properties ..... 8
2.2.5 Methods of fabricating microneedles ..... 10
2.2.6 Microneedle design ..... 12
2.2.7 Mechanical characterisation of microneedles ..... 13
2.2.8 Applications of microneedles ..... 13
2.3 Mould surface patterning technologies ..... 15
2.3.1 Mechanical machining ..... 15
2.3.2 Electrochemical etching ..... 16
2.3.3 Thermoelectric engraving ..... 17
2.3.4 Additive manufacturing ..... 19
2.4 Polymer replication techniques ..... 21
2.4.1 Injection moulding ..... 22
2.4.2 Imprinting ..... 25
2.5 Conclusion ..... 26

**Chapter 3 A novel method for producing solid polymer microneedles using laser ablated moulds in an injection moulding process** ..... **29**

3.1 Abstract ..... 29
3.2 Introduction ..... 29
3.3 Materials and Methods ..... 30

3.3.1 Materials ..... 30
3.3.2 Representation of the process chain ..... 30
3.3.3 Laser machining ..... 30
3.3.4 Replication of microneedles through injection moulding ..... 31
3.3.5 Topography characterization ..... 31
3.4 Results and Discussion ..... 32
3.5 Conclusions ..... 34

**Chapter 4 Controlling the geometry of laser ablated microneedle cavities in different mould materials and assessing the replication fidelity within polymer injection moulding ..... 35**

4.1 Abstract ..... 35
4.2 Introduction ..... 36
4.3 Materials and Methods ..... 37
4.3.1 Thermoplastic and mould materials ..... 37
4.3.2 Laser machining experiments ..... 38
4.3.3 Replication through injection moulding ..... 39
4.3.4 Topography characterization ..... 40
4.3.5 Contact angle measurements of polymer melts ..... 41
4.4 Results and Discussion ..... 41
4.4.1 Diameter of the microcavities ..... 41
4.4.2 Formation of the cone-shaped microcavities ..... 42
4.4.3 Depth of the microcavities ..... 45
4.4.4 Replication through polymer injection moulding ..... 46
4.4.5 Difference in replication between the mould materials ..... 49
4.4.6 Difference in replication between the thermoplastic ..... 50
4.4.7 Surface topography of the replicated microneedles ..... 52
4.5 Conclusion ..... 53

**Chapter 5 Controlling the flank geometry of injection moulded polymer microneedles made with laser ablated moulds by adapting laser scanning parameters ..... 55**

5.1 Abstract ..... 55
5.2 Introduction ..... 55
5.3 Materials and methods ..... 56
5.3.1 Materials ..... 56
5.3.2 Laser machining experiments ..... 56
5.3.3 Replication through injection moulding ..... 58
5.3.4 Topography characterization ..... 59
5.4 Results ..... 59
5.4.1 Laser ablation ..... 59
5.4.2 Injection moulding ..... 60
5.5 Conclusion ..... 61

**Chapter 6 Predicting the replication fidelity of injection moulded solid polymer microneedles ..... 63**

6.1 Abstract ..... 63
6.2 Introduction ..... 63

6.3 Materials and Methods ..... 66
6.3.1 Thermoplastic polymers ..... 66
6.3.2 Mould insert ..... 66
6.3.3 Injection moulding product ..... 67
6.3.4 Injection moulding experiments ..... 67
6.4 Injection moulding simulation settings ..... 68
6.4.1 Macroscopic flow ..... 69
6.4.2 Simulation parameters in Moldex3D ..... 69
6.4.3 Mesh convergence study using multi-scale meshing ..... 70
6.4.4 Heat transfer coefficient ..... 71
6.4.5 Replication fidelity in function of the location of the microfeatures ..... 72
6.4.6 Replication fidelity in function of the injection moulding parameters ..... 72
6.4.7 Replication fidelity in function of the mould material ..... 73
6.5 Results and Discussion ..... 74
6.5.1 Macroscopic flow ..... 74
6.5.2 Mesh convergence study ..... 75
6.5.3 Effect of the heat transfer coefficient ..... 76
6.5.4 Replication fidelity in function of the location of the microfeatures ..... 78
6.5.5 Replication fidelity in function of the injection moulding parameters ..... 80
6.5.6 Replication fidelity in function of the mould material ..... 81
6.6 Conclusion ..... 85

**Chapter 7 Comparing the replication fidelity of solid microneedles using injection compression moulding and conventional injection moulding ..... 87**

7.1 Abstract ..... 87
7.2 Introduction ..... 87
7.3 Materials and Methods ..... 89
7.3.1 Thermoplastic and mould material ..... 89
7.3.2 Mould product cavity and laser machining experiments ..... 90
7.3.3 Experimental injection moulding set-up ..... 90
7.3.4 Two-level full factorial design ..... 91
7.3.5 Topography characterisation ..... 92
7.3.6 Injection moulding simulations ..... 92
7.4 Results and Discussion ..... 94
7.4.1 Geometry of the ablated microneedle cavities ..... 94
7.4.2 DoE to define IM parameters for a high replication fidelity ..... 95
7.4.3 IM using parameters for an optimal replication fidelity ..... 101
7.4.4 Injection compression moulding ..... 104
7.4.5 Comparison between IM and ICM ..... 105
7.5 Conclusion ..... 108

**Chapter 8 Producing hollow polymer microneedles using ablated moulds in an injection moulding process ..... 111**

8.1 Abstract ..... 111
8.2 Introduction ..... 111
8.3 Materials and Methods ..... 114
8.3.1 Materials ..... 114
8.3.2 Representation of the process chain ..... 114
8.3.3 Laser machining ..... 115

8.3.4 Polymer injection moulding ..... 116
8.3.5 Micro drilling ..... 117
8.3.6 Topography characterization ..... 117
8.3.7 Preparation of a skin-mimicking substrate ..... 117
8.3.8 Validation of single-needle injections ..... 118
8.4 Results and Discussion ..... 119
8.4.1 Laser ablation ..... 119
8.4.2 Replication through injection moulding ..... 121
8.4.3 Validation on skin-mimicking substrate ..... 124
8.5 Conclusion ..... 125

**Chapter 9 Valorisation plan ..... 127**

9.1 Introduction ..... 127
9.2 Existing patents ..... 127
9.3 Target group and positioning ..... 128
9.4 Position in the market ..... 129
9.5 Economical evaluation ..... 131
9.5.1 Derivation of the product cost ..... 131
9.5.2 Input data ..... 132
9.5.3 Results of the economic evaluation ..... 134
9.6 Intellectual property rights ..... 135
9.7 Future perspectives ..... 136
9.7.1 Current status ..... 136
9.7.2 Gaps towards valorisation ..... 136

**Chapter 10 Conclusions and outlook ..... 139**

10.1 Introduction ..... 139
10.2 Conclusions ..... 139
10.2.1 Developed methodology ..... 139
10.2.2 Laser ablation ..... 140
10.2.3 Injection moulding ..... 140
10.2.4 Numerical flow simulations ..... 141
10.2.5 Valorisation ..... 142
10.3 Outlook ..... 142

**Bibliography ..... 145**

**List of Publications ..... 169**

**Curriculum Vitae ..... 171**

# List of Symbols

**Arabic symbols**

| *Symbol* | *Description* | *Unit* |
|---|---|---|
| a | Man/machine ratio | - |
| b | Thickness of polymer part | m |
| $C_a$ | Cost for laser machining microneedles | € |
| $C_c$ | Cost of the mould cavity | € |
| $C_H$ | Mould housing cost | € |
| $C_{IM}$ | Purchase cost injection moulding equipment | € |
| $C_l$ | Hourly labour cost | € |
| $C_m$ | Hourly machine cost | € |
| $C_t$ | Cost of the polymer material | €/kg |
| D | Depreciation years | - |
| H | Height of the mould cavity | m |
| H | Total production time per year | hours |
| m | Mass of the polymer product | kg |
| N | Number of cavities | - |
| P | Pressure | Pa |
| q | Heat flux | $W/m^2$ |
| $r_v$ | The ratio of the specific volumes | - |
| S | Distance between pressure and temperature sensor | m |
| s | Shrinkage | - |
| t | Time | s |
| $T_c$ | Temperature of a cold interface | °C |
| $t_c$ | Cycle time | s |
| $T_h$ | Temperature of a hot interface | °C |
| $T_i$ | Injection temperature | °C |
| $T_m$ | Mould temperature | °C |
| $T_{nf}$ | No-flow temperature | °C |
| v | Specific volume | $m^3/kg$ |
| $v_0$ | Reference specific volume | $m^3/kg$ |
| Z | Series size | - |

**Greek symbols**

| *Symbol* | *Description* | *Unit* |
|---|---|---|
| $\alpha$ | Thermal diffusivity | $m^2/s$ |
| $\beta$ | Compressibility | 1/MPa |
| $\eta$ | Viscosity | Pa s |

**Abbreviations**

| *Symbol* | *Description* |
|---|---|
| µ-CT | Micro-computed tomography |
| ABS | Acrylonitrile butadiene styrene |
| CNC | Computer numerical control |
| COP | Cyclic olefin copolymer |
| DED | Directed energy deposition |
| DoE | Design of experiments |
| ECMM | Electro-chemical micromachining |
| EDM | Electrical discharge machining |
| FDA | Food and drug administration |
| HTC | Heat transfer coefficient |
| ICM | Injection compression moulding |
| IM | Injection moulding |
| LIGA | Lithographie, Galvanoformung, Abformung |
| LIPSS | Laser induced periodic surface structures |
| MVR | Melt volume rate |
| OEM | Original equipment manufacturer |
| PC | Polycarbonate |
| PDMS | Polydimethylsiloxane |
| PEEK | Polyether ether ketone |
| PLA | Polylactic acid |
| PMMA | Polymethyl methacrylate |
| PP | Polypropylene |
| PS | Polystyrene |
| PSA | Pressure-sensitive adhesive |
| PVA | Polyvinyl alcohol |
| PVC | Polyvinyl chloride |
| PVD | Physical vapor deposition |
| pvT | Pressure-specific volume-temperature |
| RAM | Random access memory |
| SLA | Stereolithography |

| *Symbol* | *Description* |
|---|---|
| SLM | Selective laser melting |
| TCC | Thermal contact conductance |
| UV | Ultraviolet |
| WLF | Williams-Landel-Ferry |

# List of Figures

Figure 1: Number of articles about microneedles being published per year. ..... 6

Figure 2: Illustration of the skin, showing the different skin layers (stratum corneum, epidermis, dermis, and hypodermis), together with a hypodermic needle and a microneedle array. Inspired by [18]. ..... 7

Figure 3: A schematic representation of the five different types of microneedles, being (a) solid microneedles, (b) coated microneedles, (c) dissolvable microneedles, (d) hydrogel-forming microneedles, and (e) hollow microneedles. Inspired by [7]. ..... 8

Figure 4: Illustration of the sequential process of transferring a pattern on a silicon substrate. (a) Deposition of a photoresist layer using spin-coating. (b) Creating a patterned shape using selective radiation using a mask. (c) Selective etching of the oxide layer. (d) Removal of the photoresist material. Inspired by [10]. ..... 11

Figure 5: Illustration of the micro EDM methods: (a) sinking EDM, (b) wire EDM, (c) EDM drilling, and (d) EDM milling. Inspired by [134]. ..... 16

Figure 6: Illustration of the ECMM methods: (a) through-mask ECMM, (b) conventional ECMM, and (c) jet ECMM. Inspired by [149]. ..... 17

Figure 7: Illustration of the chemical etching process. Inspired by [138]. ..... 17

Figure 8: Illustration of the ultrashort pulsed laser machining using a femtosecond laser source. Inspired by [163]. ..... 18

Figure 9: Illustration of (a) selective laser melting and (b) direct energy deposition. Inspired by [170]. ..... 20

Figure 10: Illustration of the LIGA principle, consisting out of several process steps. Inspired by [179]. ..... 21

Figure 11: Capabilities of polymer replication techniques according to the state of the art. Inspired by [180], [181]. ..... 21

Figure 12: Schematic representation of the conventional injection moulding process. ..... 22

Figure 13: (a) Illustration cavity wall temperature as a function of time for a conventional injection moulding process, with $T_g$ the cavity wall temperature before injection, $T_e$ the ejection temperature, and $t_z$ the cycle time. (b) Illustration of the cavity wall temperature as a function of time for rapid heat cycle moulding process, with $t_H$ the heating time and $t_C$ the cooling time. ..... 23

Figure 14: Illustration of the injection compression moulding process sequence. (a) Injecting the polymer melt into a slightly opened mould. (b) Compressing the polymer melt through the mould closing action. ..... 24

Figure 15: Entrapment of air inside micro feature cavities during the filling phase. ..... 24

Figure 16: Schematic representation of the thermal imprinting process. Inspired by [198]. ..... 25

Figure 17: Schematic representation of the UV imprinting process. Inspired by [198]. ..... 26

Figure 18: Schematic representation of the roll-to-roll imprinting process. Inspired by [203]. ..... 26

Figure 19: Illustration of the process chain to produce solid polymer microneedles. ..... 30

Figure 20: Illustration of the cross-hatching laser strategy. ..... 31

Figure 21: Reconstructed μCT XY datasets for the four different laser parameter settings: (a) 150 layers; (b) 300 layers; (c) 450 layers and (d) 600 layers. ..... 33

Figure 22: Microscopic images of the polymer microneedles, achieved by replicating the laser ablated micro holes with four different laser settings: (a) 150 layers; (b) 300 layers; (c) 450 layers and (d) 600 layers. ..... 34

Figure 23: A schematic representation of the different types of microneedles. (a) Solid microneedles (b) Coated microneedles. Inspired by [7]. ..... 37

Figure 24: Illustration of the design of laser experiments, in which the number of layers and the base diameter was varied. ..... 39

Figure 25: Illustration of the flat plate with all dimensions in mm, the thickness is 1.5 mm. ..... 39

Figure 26: Microcavity diameter at the surface of the mould insert in function of varying number of layers for different programmed diameters for following materials: (a) tool steel, (b) copper alloy, and (c) aluminium alloy. The error bars represent the 95 % confidence interval. ..... 42

Figure 27: Cross sectional views obtained from the μ-CT measurements of the micro-holes created with the design of laser experiments for following materials: (a) tool steel, (b) copper alloy, and (c) aluminium alloy. A scale bar is included for each of the materials. ..... 44

Figure 28: Hole depth in function of the programmed hole diameter for varying number of layers for following materials: (a) tool steel, (b) copper alloy, and (c) aluminium alloy. The error bars represent the 95 % confidence interval. ..... 46

Figure 29: (a) Microscopic image of a polypropylene plate replicated with an aluminium mould insert. (b) Representation of a polypropylene microneedle fitted in the corresponding aluminium microneedle cavity created with a diameter of 400 μm and 300 layers. ..... 46

Figure 30: pvT plots of PC and PP, based on the Autodesk Moldflow® 2019 material database. ..... 48

Figure 31: Replication of the PP and PC microneedles in height, relative to the aspect ratio of the holes in (a) tool steel, (b) copper alloy and (c) aluminium alloy. The vertical error bars represent the combined 95 % confidence interval of the hole depth and the replicated microneedle; the horizontal error bars represent the combined 95 % confidence interval of the hole depth and the hole diameter. ..... 49

Figure 32: Contact angle of (a) PP and (b) PC, during the spreading on the different mould materials. The error bars represent the 95 % confidence interval. ..... 50

Figure 33: Comparison between Cross-WLF model viscosities and online apparent viscosity measurements for PP and PC. ..... 52

Figure 34: Representation of a replicated PC microneedle (a) with micro grooves along the length of the needle, created with a linear cross-hatching laser strategy; (b) without micro-grooves, created with a circular-hatching strategy. ..... 53

Figure 35: Three different laser scanning designs, each having a different programmed diameter throughout the laser ablation process. ..... 58

Figure 36: Reconstructed μ-CT XY datasets of the ablated microcavities for: (a) design 1; (b) design 2, and (c) design 3. ..... 60

Figure 37: Microscopic images of the polymer microneedles corresponding to: (a) design 1, (b) design 2, and (c) design 3. ..... 61

Figure 38: Illustration of the flat plate with all dimensions in mm, the thickness is 1.5 mm. ..... 67

Figure 39: Default and adapted simulation parameters in Moldex3D. ..... 70

Figure 40: Illustration of (a) a uniform mesh corresponding to the 430,000 elements, and (b) multi-scale meshing corresponding to the 4,900,000 elements. ..... 71

Figure 41: Illustration of the macroscopic part with two identical microneedle cavities, positioned at different distances from the injection location. All represented dimensions are in mm and the part thickness is 1.5 mm. ..... 72

Figure 42: Comparison between the simulated and experimental mould cavity (a) pressure and (b) temperature in function of time for polypropylene. The experimental curve shows the average obtained pressure and temperature profile (n = 3) and the shaded area corresponds to the 95 % confidence interval. ..... 74

Figure 43: Comparison between the simulated and experimental mould cavity (a) pressure and (b) temperature in function of time for polycarbonate. The experimental curve shows the average obtained pressure and temperature profile (n = 3) and the shaded area corresponds to the 95 % confidence interval. ..... 75

Figure 44: The average absolute deviation between the simulated and experimental replication fidelity of the microneedles in function of the number of mesh elements for (a) polypropylene and (b) polycarbonate. ..... 76

Figure 45: The average absolute deviation between the simulated and experimental replication fidelity of the microneedles in function of the varied HTC for (a) polypropylene and (b) polycarbonate. The red dotted lines correspond to the average absolute deviation when using the automatically determined HTC in Moldex3D. ..... 77

Figure 46: The experimental and simulated replication in height of the 16 different microneedle arrays, in function of the aspect ratio of the micro hole for (a) polypropylene with a HTC of 10,000 $W/m^2 \cdot K$ and (b) polycarbonate with a HTC of 30,000 $W/m^2 \cdot K$. The vertical error bars represent the combined 95 % confidence interval of the hole depth and the replicated microneedle; the horizontal error bars represent the combined 95 % confidence interval of the hole depth and the hole diameter. ..... 78

Figure 47: Difference in replication in height between the microneedles close to the gate and far from the gate for polypropylene and polycarbonate. The error bars represent the 95 % confidence interval. ..... 78

Figure 48: (a) Illustration of the XY cross-section of the PP part; cross-sections with time dependent filling and temperature progress of the microneedles close and far from the gate for (b) PP and (c) PC; cross-sections with time dependent filling and pressure progress of the microneedles close and far from the gate for (d) PP and (e) PC. ..... 80

Figure 49: The experimental and simulated replication in height of the 16 different microneedle arrays created with the adapted injection moulding parameters, in function of the aspect ratio of the micro hole, for (a) polypropylene with a HTC of 10,000 $W/m^2 \cdot K$ and (b) polycarbonate with a HTC of 30,000 $W/m^2 \cdot K$. The vertical error bars represent the combined 95 % confidence interval of the hole depth and the replicated microneedle; the horizontal error bars represent the combined 95 % confidence interval of the hole depth and the hole diameter. .81

Figure 50: The average absolute deviation between the simulated and experimental replication fidelity of the microneedles created with the aluminium alloy, in function of the varied HTC for (a) polypropylene and (b) polycarbonate. The red dotted lines correspond to the average absolute deviation when using the automatically determined HTC in Moldex3D. ..... 82

Figure 51: The average absolute deviation between the simulated and experimental replication fidelity of the microneedles created with the copper alloy, in function of the varied HTC for (a) polypropylene and (b) polycarbonate. The red dotted lines correspond to the average absolute deviation when using the automatically determined HTC in Moldex3D. ..... 83

Figure 52: The experimental and simulated replication in height of the 16 different microneedle arrays created in the aluminium alloy, in function of the aspect ratio of the micro hole for (a)

polypropylene with a HTC of 25,000 W/m²·K and (b) polycarbonate with a HTC of 55,000 W/m²·K. The vertical error bars represent the combined 95 % confidence interval of the hole depth and the replicated microneedle; the horizontal error bars represent the combined 95 % confidence interval of the hole depth and the hole diameter. ..... 84

Figure 53: The experimental and simulated replication in height of the 16 different microneedle arrays created in the copper alloy, in function of the aspect ratio of the micro hole for (a) polypropylene with a HTC of 10,000 W/m²·K and (b) polycarbonate with a HTC of 35,000 W/m²·K. The vertical error bars represent the combined 95 % confidence interval of the hole depth and the replicated microneedle; the horizontal error bars represent the combined 95 % confidence interval of the hole depth and the hole diameter. ..... 84

Figure 54: Illustration of the flat plate mould product cavity, including the two different arrays of microneedle cavities located on 15 locations. The polymer is injected through a hot runner, located in the centre of the mould product cavity ..... 90

Figure 55: Representation of the XY datasets of the reconstructed μCT analysis for 3 large and 3 small microneedle cavities. The average cavity depth and cavity base diameter along with the standard deviation, for the complete array of 9 microneedles is also displayed for both types of microneedles. ..... 94

Figure 56: Illustration of a cross section of a microneedle cavity for (a) an empty large microneedle cavity, and (b) a large microneedle cavity from array 8 with an entrapped broken microneedle. ..... 95

Figure 57: Average replication in height plotted against the 16 DoE runs with a repetition of 3 for (a) the large microneedle arrays and (b) the small microneedle arrays. The error bars represent the 95 % confidence interval. ..... 96

Figure 58: Illustration of one replicated large and small microneedle from array number 2 for (a) DoE run 13 (b) DoE run 11, (c) DoE run 3, and (d) DoE run 12. The average length of the needles are reported together with the standard deviation ($n$ = 9) ..... 97

Figure 59: Illustration of the DoE results, with the barrel temperature ($T_{barrel}$), volumetric injection rate ($v_{inj}$), holding pressure ($P_{hold}$), and mould coolant temperature ($T_{mould}$) as the varied parameters. (a) and (b) show the Pareto charts for the large and small microneedles, respectively. The red dashed lines represents the significance limit at a confidence level of at 95%. (c) and (d) show the main effect plot for the replication in height for the large and small microneedles. (e) and (f) show the two-factor interactions for the replication in height for the large and small microneedles respectively. ..... 98

Figure 60: Illustration of the Cross-WLF model viscosity and online apparent viscosity for PC, measured at an injection rate of 50 cm³/s and 150 cm³/s in combination with a barrel temperature of 315 °C. ..... 99

Figure 61: Illustration of a small microneedle which is (a) undeformed during the demoulding process, (b) deformed during the demoulding process. ..... 102

Figure 62: The experimental and simulated replication in height in function of the microneedle arrays, created with the optimal IM parameters for (a) the large microneedle arrays and (b) the small microneedle arrays. The error bars represent the 95 % confidence interval. ..... 103

Figure 63: The average replication in height of the microneedle arrays as a function of the distance between the corresponding array and the gate location for (a) the large and small microneedle arrays together with a trendline and the linear correlation coefficient (R); (b) the experimental and simulated replication in height in function of the distance from the gate. The error bars represent the 95 % confidence interval. ..... 104

Figure 64: Illustration of the replication in height in function of the compression stroke obtained through ICM, for the large and small microneedles. The error bars represent the 95 % confidence interval. ..... 105

Figure 65: Illustration of the injected melt volume inside the mould cavity, before the mould compression phase, for the different compression strokes. The pink volume represents the compression gap. A compression stroke of 0 mm corresponds to conventional injection moulding. ..... 105

Figure 66: The average replication in height of the microneedle arrays as a function of the distance between the corresponding array and the gate location for injection moulding and injection compression moulding using the process parameters for an optimal replication fidelity..... 106

Figure 67: Illustration of a single (a) large and (b) small microneedle from array 1, created with ICM having a mould stroke of 4 mm. ..... 107

Figure 68: Illustration of the simulated melt front time, temperature, and pressure of the macroscopic part and a small microneedle from array 1 for injection moulding (IM) and injection compression moulding (ICM) with a stroke of 4 mm, at (a) a filling time of 0.1 seconds and; (b) a filling time of 0.2 seconds. ..... 108

Figure 69: A schematic representation of the different types of microneedles. (a) solid microneedles, (b) coated microneedles, (c) dissolving microneedles, and (d) hollow microneedles for drug and vaccine delivery. Inspired by [7]. ..... 113

Figure 70: Illustration of the process chain to produce hollow polymer microneedles. ..... 115

Figure 71: Illustration of the laser strategy with internal scan-free area. ..... 116

Figure 72: Exploded view of the chip containing a single, straight microfluidic channel. A single microneedle was tightly incorporated into the chip by a PSA connecting piece. At the other end of the channel, a hole serves for connecting a fluidic pump. ..... 118

Figure 73: Setup for controlling the injection into agarose. From left to right the pressure controller, a pressurized reservoir containing the to be injected liquid, the flow sensor with feedback to the pressure controller, the microfluidic chip with integrated microneedle and the agarose slab. ..... 119

Figure 74: Cross sectional views obtained from the μ-CT measurements of the micro-hole arrays, with the scan-free area: (a) close to the edge of the needle and (b) close to the center of the needle. The distance below each image indicates the position of the cross section. For XY, 0 μm corresponds to the mold surface, while for XZ and YZ 0 μm corresponds to the edge of the microneedle. ..... 120

Figure 75: Microscopic image of the replicated polymer microneedle arrays created with a scan-free internal area (a) close to the edge of the needle, and (b) close to the centre of the needle. ..... 121

Figure 76: Microscopic image of the front and side view of the replicated polymer microneedles created with: (a) 'low' injection moulding parameters, (b) 'middle' injection moulding parameters and (c) 'high' injection moulding parameters. The average value of the dimensions of the needles are reported together with the standard deviation (n = 10). ..... 122

Figure 77: (a) Needle length, (b) ridge height and (c) tip wall thickness of the replicated microneedles from array 2 in function of the three different sets of injection molding parameters, being 'low', 'middle' and 'high'. The percentages in (a) represent the replication in height. ..... 122

Figure 78: Injection profiles accompanied with the pressure obtained during injection through a single microneedle into skin-mimicking agarose at 0.5 μL/min. The black curve shows the average obtained pressure profile (n = 3) and the grey shaded area shows one standard deviation. ..... 124

Figure 79: Illustration of the flat plate used in the economic evaluation. All represented dimensions are in mm and the part thickness is 1.5 mm. ..... 131

Figure 80: Product cost in function of the series size for injection moulding. ..... 134

Figure 81: Composition of the product cost for a series size of (a) 50,000 products and (b) 300,000 products..... 134
Figure 82: Product cost in function of the number of mould cavities for a series size of 300,000 products..... 135

# List of Tables

Table 1: Main properties of the thermoplastics based on material datasheets and Autodesk Moldflow® 2019 material database. ....37

Table 2: Main properties of the different mould materials based on material datasheets and GRANTA EduPack. ....38

Table 3: Injection moulding process parameters for the two thermoplastic materials. ....40

Table 4: Electron-phonon coupling constants for stainless steel 316L, aluminium and copper. ...44

Table 5: Process parameters for injection moulding ....58

Table 6: Main properties of the thermoplastics based on material datasheets and the Moldex3D 2020 material database. ....66

Table 7: Thermal properties of the different mould materials based on material datasheets. ....67

Table 8: Injection moulding process parameters for the two thermoplastic materials. ....68

Table 9: Adapted injection moulding process parameters for the two thermoplastic materials. ....73

Table 10: Heat transfer coefficients, corresponding to a minimal average absolute deviation between the simulated and experimentally determined replication fidelity, for the PP and PC in combination with the tool steel, the aluminium alloy and the copper alloy mould insert. ..83

Table 11: Different settings for the process parameters used within the design of experiments...91

Table 12: IM simulation parameters. ....93

Table 13: IM parameters for an optimal replication fidelity .... 102

Table 14: Three sets of injection moulding parameters: 'low', 'middle' and 'high'. .... 116

Table 15: List of existing patents related to microneedle manufacturing. .... 127

Table 16: Input data associated with the material cost. .... 133

Table 17: Input data associated with the mould cost. .... 133

Table 18: Input data associated with the production cost. .... 133

# Chapter 1 Introduction

## 1.1 Motivation and problem statement

Traditional needles, known as hypodermic needles, are used in clinical practice to sample blood or to deliver vaccines or drugs across the skin into the blood stream. Although such needles are very frequently used, they are known to induce discomfort to the patient, like pain or bruising and carry the risk of infections. Besides, the use of these systems requires trained medical staff. A possible alternative to hypodermic needles are microneedles, which are needle-like microscopic features that can be used to deliver medical substances or to extract fluids from a body for sampling purposes. These needles can have various shapes and are usually arranged in an array with individual needle lengths ranging from 25 to 2000 μm. Using these systems offers various advantages such as (i) pain free delivery of medical substances, (ii) self-administration, (iii) lower storage, distribution and disposal cost due to the small volume, and (iv) direct administration of vaccines to key immune cells.

The first concept using microneedles for vaccine delivery was conceived by Alza corporation, as described in a 1976 patent [1]. Making these devices was not possible until the 1990s, when the production technology needed to fabricate micrometre sized structures became available. Since then, many researches both from academia and industry have demonstrated the applicability of microneedle devices, from the development phase up to clinical experiments. The investigated methods for manufacturing these microscale devices cover a wide range of techniques, such as chemical etching, polymer replication techniques, additive manufacturing, surface micromachining, and lithography.

According to World Health Organization guidelines, cost-effective, portable, disposable medical devices are needed in order to enhance the health-related quality of life worldwide [2]. Yet, for most of the current manufacturing methods the low cost and high volumes still pose a great challenge. Polymer injection moulding has a huge potential, as this manufacturing process has already proven to be very suitable to manufacture polymer medical devices, due to its high accuracy, potential for full-automation, short cycle times, and low cost. Moreover, polymers can offer excellent biocompatibility, biodegradability, and good mechanical properties at a low cost. However, within the current state of the art, methods for applying the negative of the microneedles on the injection mould are limited to expensive and time consuming precision techniques such as micro-electrical discharge machining, milling, drilling, or indirect mould making. Besides, manufacturing microneedle cavities with a sharp tip has proven to be very difficult with these techniques, while small tip-radii are essential to effectively penetrate the skin. Thus, there is a need for a novel mass production process which can manufacture polymer microneedles in large volumes at a low cost.

## 1.2 Objectives

**The main objective of this PhD is to develop a production methodology for the fabrication of high volume, low cost microneedle devices using laser ablated moulds and polymer injection moulding.**

To accomplish this objective, the study is divided into technological and scientific objectives.

**The scientific objectives:**

(1) Gain insight in the influence of the laser scanning parameters on the geometry of the ablated microneedle cavities, being the cavity depth, cavity base diameter and shape of the needle flank.
(2) Establish insights in the replication behaviour of polymers during the injection moulding of microneedles, taking into account (i) the geometry of the micro-cavity, (ii) the location of the microneedles on the macroscopic product, (iii) the polymer characteristics, (iv) the mould material, and (v) the injection moulding technique and corresponding process parameters.

**The technological objectives**:

(1) Develop a laser machining strategy to create microneedle cavities with small tip radii in conventional mould materials.
(2) Set up guidelines for injection moulding microneedle arrays with a high replication fidelity together with a low variability between the individual needles.
(3) Assess the capabilities of finite element flow simulations to predict the injection moulding replication fidelity of polymer microneedles.
(4) Evaluate the functionality of the manufactured microneedles in terms of administering a fluid to a skin mimicking substrate.

## 1.3 Thesis outline

The thesis is structed as follows:

**Chapter 1** describes the motivation and problem statement together with the objectives and general outline of the thesis.

**Chapter 2** provides the state of the art concerning microneedles, existing surface patterning technologies, and available replication techniques.

**Chapter 3** presents the developed method to produce solid polymer microneedles using laser ablated moulds in an injection moulding process.

**Chapter 4** elaborates on the influence of two laser scanning parameters, being the programmed base diameter and the number of layers, on the geometry of microneedle cavities in three mould materials. Furthermore, the replication

fidelity of the laser induced cavities in these materials were evaluated using polymer injection moulding.

**Chapter 5** explains how the flank geometry of the ablated microneedle cavities can be adapted by changing laser scanning parameters.

**Chapter 6** explains the capabilities of finite element flow simulations to predict the injection moulding replication fidelity of polymer microneedles and compares the results to injection moulding experiments.

**Chapter 7** describes the effect of injection moulding parameters on the replication fidelity and compares the replication fidelity of solid microneedles using injection compression moulding and conventional injection moulding.

**Chapter 8** presents the developed method to produce hollow polymer microneedles and evaluates the functionality of the manufactured hollow microneedles by injecting a controlled flow of water into a skin mimicking substrate.

**Chapter 9** provides a valorisation plan concerning the injection moulding of solid and hollow polymer microneedles using the developed methods.

**Chapter 10** gives the conclusions for the thesis and provides an overview of possible further research on this topic.

# Chapter 2 State of the art

## 2.1 Introduction

This chapter provides a state of the art concerning the injection moulding of polymer microneedles. First, microneedles are addressed and relevant literature is discussed (section 2.2). This entails a description on the microneedle characteristics and the skin structure, the different types of microneedles currently available in literature, materials used in this application, possible methods for fabricating microneedles, typical microneedle designs, mechanical characterisation of the microneedles, and possible applications where microneedles can be used. Second, an overview is given of available manufacturing technologies for patterning a mould surface (section 2.3). These techniques are classified into mechanical machining, electrochemical etching, thermoelectric engraving, and additive manufacturing. Finally, polymer replication techniques which can be used to transfer a desired surface pattern from a mould to a polymer product are described (section 2.4).

## 2.2 Microneedles

### 2.2.1 Characteristics

Microneedles are needle-like microscopic structures used to pierce the skin in order to either deliver medical substances, or to extract fluids from a body for sampling purposes. Over the years, various types of microneedles have been developed, most often arranged in an array, having various shapes and lengths ranging from 25 to 2000 μm [1], [3], [4]. Typically, microneedles are long enough to penetrate the skin's protective barrier, the stratum corneum, but are short and narrow enough to avoid stimulation of the nerves, making them painless [5]–[8]. In 1976, a first concept to surpass the stratum corneum using microneedles was described by Alza corporation [9]. This concept was first tested almost 30 years later, when the technology needed to fabricate micrometre sized structures became available [10]. Since then, there has been great interest in this technology and significant developments in the manufacture of microneedles and their use. This can be observed by the rising number of articles about microneedles being published per year, as illustrated in Figure 1. This graph was generated by recording the number of articles found in the KU Leuven scientific database, with the term "microneedles" in the title for each year.

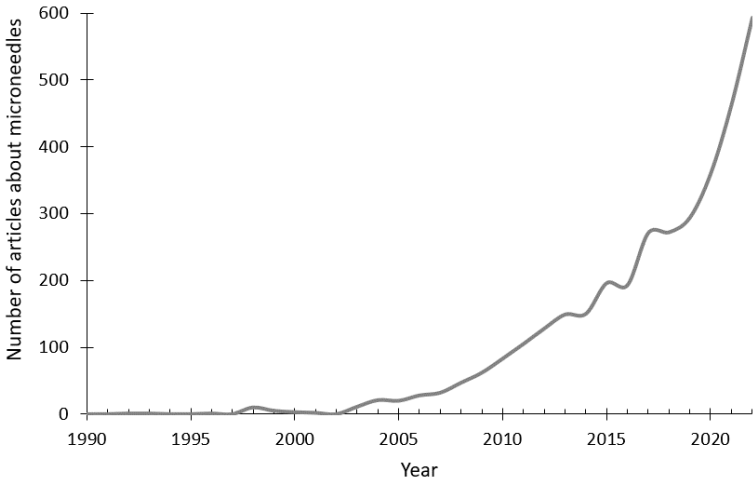


Figure 1: Number of articles about microneedles being published per year.

Microneedles offer multiple advantages for the delivery of medicines or sampling of fluids, compared to conventional hypodermic needles. First of all, as already mentioned, it is possible to use the needles in a pain-free way avoiding needle phobia, which affects at least 10 % of the population [11]. An additional advantage is the presence of an abundance of specialized antigen cells in the skin, which can be directly targeted using microneedles. As a result, superior immunogenicity can be achieved using a lower vaccine dose [12]. Moreover, due to their small volume, costs related to distribution are lower, compared to traditional hypodermic needles.

### 2.2.2 Skin structure

The skin is the largest and one of the most complex organs of the human body. It forms a surface of approximately 1.5 $m^2$, compromising 16% of the total body mass of an average person [1]. It performs a wide variety of functions, such as protecting the body from microbes and infections, regulating the body temperature, and permitting the sensation of cold, heat, touch, and pressure [13]. The skin thickness of a person varies depending of the region within the body, gender, age and race [14].

Skin is composed out of multiple distinctive layers. The outermost layer is called the epidermis, beneath lies the larger dermis, and the deepest layer is the hypodermis (also known as subcutis), as shown in Figure 2. The thickness of the epidermis is between 50 to 150 μm. The outer most layer of the epidermis is called the stratum corneum, which is 8 to 20 μm in thickness and acts as a barrier to almost all macromolecules and hydrophilic drugs [15]–[17]. The second layer, being the dermis, is 1 to 2 mm in thickness and has a rich blood supply, containing microscopic blood vessels. If a drug reaches this dermis, it will be rapidly absorbed in the blood circulation. The key advantage of microneedles is the ability to specifically reach this dermis, by surpassing the stratum corneum barrier. The deepest layer is the hypodermis, being a few millimetres in thickness and is the location where fat is stored.

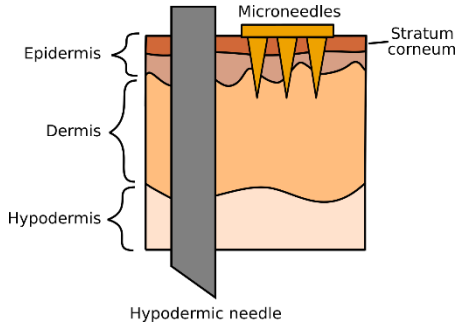


Figure 2: Illustration of the skin, showing the different skin layers (stratum corneum, epidermis, dermis, and hypodermis), together with a hypodermic needle and a microneedle array. Inspired by [18].

### 2.2.3 Types of microneedles

Five different types of microneedles are currently described in literature, being solid, coated, dissolvable, hydrogel-forming and hollow microneedles, as illustrated in Figure 3.

#### 2.2.3.1 Solid microneedles

Solid microneedles are used in the "poke with patch" methodology [19]. First, the microneedles are used to pierce the skin, creating transient aqueous micropores. Subsequently, a drug formulation (solution, cream or gel) is applied, which can passively diffuse through the micropores (Figure 3 a). The lifetime of these micropores varies between 44 and 61 hours, depending on the person's race. This was recently investigated by applying stainless steel microneedles to the upper arm, after which impedance and transepidermal water loss were measured to determine the micropore lifetime [20]. The main drawback of this methodology is the requirement for a two-step application process, which may lead to practicality issues for patients [7].

#### 2.2.3.2 Coated microneedles

Coated microneedles are created by coating solid microneedles with a drug formulation, and are referred to as "coat and poke". When inserted in the skin, the coating will be dissolved, and the medicine will be deposited in the skin (Figure 3 b). Various techniques have been developed in literature to apply the coating to the needle shafts, such as gas-jet drying and dip-coating [21], [22]. The main drawback of this methodology is the restricted amount of drug formulation that can be coated onto the small surface area of the microneedles.

#### 2.2.3.3 Dissolvable microneedles

Dissolvable needles consist of a soluble material, such as a biodegradable polymer or sugar, in which the drug formulation is encapsulated. The "poke and release" methodology is used for these microneedles, where the microneedles are inserted into the skin and dissolve, to release the medical formulation (Figure 3 c). Controlled drug delivery is achievable by adjusting the polymer composition, thereby altering the

dissolution rate. Various materials have been used to produce these types of microneedles, such as polylactic acid, polyvinyl alcohol, dextran, carboxymethyl cellulose, and sugars [23].

#### 2.2.3.4 Hydrogel-forming microneedles

Hydrogel-forming microneedles are a relatively new type of microneedle, which are made from hydro-gel forming matrices [24]. These needles are also categorised in the "poke and release" methodology. The needles made from a crosslinked polymer, such as polyvinyl alcohol, and are connected to a drug loaded reservoir. Once the needles are pierced into the skin, they take up interstitial fluid, thereby forming a pathway between the dermal microcirculation and the drug reservoir (Figure 3 d). After the medical formulation is diffused into the skin, the swollen microneedles can be removed. The main drawback of this methodology is once again the restricted amount of drug formulation that can be encapsulated inside the hydrogel-forming microneedles [7].

#### 2.2.3.5 Hollow microneedles

Hollow microneedles have a lumen, or internal bore, which enables the transportation of fluids (Figure 3 e). This allows for the delivery of a fluidic drug formulation or enables the extraction of fluids from a body for sampling purposes. A huge advantage compared to the other types of microneedles is the capability of delivering larger amounts of drug formulations. Undoubtedly, the most challenging problem for hollow microneedles is their complex production process. In fact, a mass production process to manufacture hollow microneedles at a low cost does currently not exist.

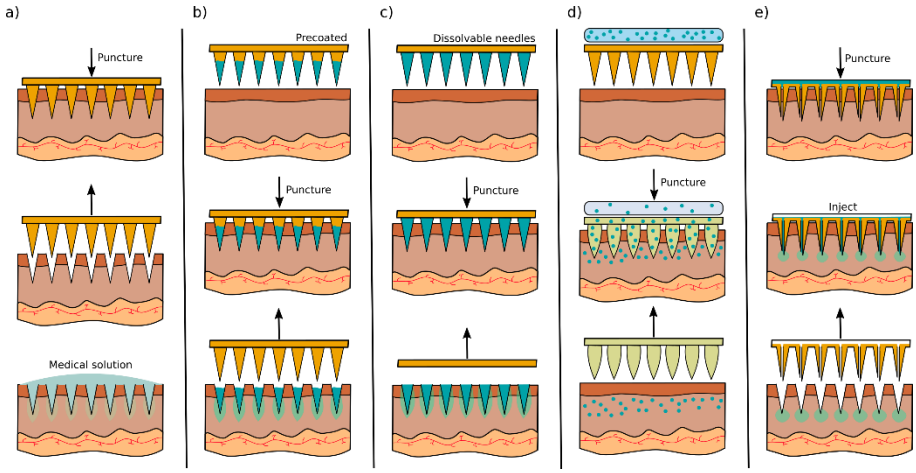


Figure 3: A schematic representation of the five different types of microneedles, being (a) solid microneedles, (b) coated microneedles, (c) dissolvable microneedles, (d) hydrogel-forming microneedles, and (e) hollow microneedles. Inspired by [7].

### 2.2.4 Material types and properties

Several materials have been used in literature for manufacturing microneedles. The material selection depends on the intended manufacturing technique, mechanical

properties and biocompatibility. The most common materials are silicon, metals, ceramics, sugars and polymers.

#### 2.2.4.1 Silicon

Silicon is among the most commonly used material for microneedles and it was the material for manufacturing the first microneedles in the 1990s. At that time, high precision microelectronic industrial tools became available, required to manufacture silicon microneedles [25], [26]. Shaping silicon requires complex multistep processes, which allow the manufacture of a variety of desirable 3D-shapes with dimensions ranging from micro- to nanometres. The shaping process consists out of 3 techniques; (i) deposition of a photosensitive layer, (ii) patterning a desired shape, and (iii) selective etching. This microfabrication technique will be further discussed in section 2.2.5.1. A variety of microneedles with different shapes and geometries have been manufactured in silicon. The three main types of microneedles that have been manufactured in this material are solid microneedles [27]–[33], hollow microneedles [34]–[40], and coated microneedles [41]. The main downside of silicon microneedles is the complex multi-step fabrication processes, which result in a high manufacturing cost and long fabrication times. Moreover, there have been concerns with the biocompatibility of silicon, and as silicon is a very brittle material, pieces of the microneedle may break during the insertion and remain in the skin [42].

#### 2.2.4.2 Metals

Metals have been extensively used in medical applications for decades. A few examples are stainless steel used for hypodermic needles or titanium used in implants. As these materials are already clinically approved in similar applications, using these materials could be a good option for regulatory reasons. Moreover, metals exhibit excellent mechanical properties such as a high Young's modulus, yield strength and fracture toughness, as well as a good biocompatibility [43]. Various fabrication techniques have been used to create microneedles from stainless steel, such as micro-electrical discharge machining, milling, drilling, and laser cutting. Consequently, solid microneedles [44]–[51], hollow microneedles [44], [45] and coated microneedles [22], [52]–[54] were manufactured in stainless steel. Some researchers also used titanium as an alternative to stainless steel to produce microneedles [55]–[57].

#### 2.2.4.3 Ceramics

Ceramics have also been reported to be used in the production of microneedles. Alumina is an example of this, which can be micro-moulded and sintered to create microneedles [58], [59]. Polymer-ceramic hybrid materials called Ormocer® can also be used to fabricate microneedles by two photon polymerization using a femtosecond laser [60], [61]. The properties of this organic-ceramic material can be adjusted by varying the composition and the synthesis parameters [62]. Manufacturing hollow silica glass microneedles has also been demonstrated in literature [63]–[65]. This material is physiologically inert and its transparency allows for easy visualisation of the fluid flow.

#### 2.2.4.4 Polymers

Polymers are also an excellent candidate material for microneedles, as they can be very cost-effective for mass production of disposable microneedles systems. Moreover, a wide range of properties are possible like good mechanical properties (high toughness, strength and Young's modulus), high chemical stability, good optical properties, good biocompatibility and possible biodegradability. In literature, polymers have been used to create all of the available microneedles types being, solid, coated, dissolvable, hydrogel-forming, and hollow. As such, a wide variety of polymers has been used to fabricate microneedles. Solid microneedles have been produced in acrylonitrile butadiene styrene (ABS) [66], polycarbonate (PC) [67]–[71], polyether ether ketone (PEEK) [72], polymethyl methacrylate (PMMA) [71], [73], and polypropylene (PP) [74]–[76]. Coated microneedles have been fabricated in PMMA [77], polylactic acid (PLA) [78], and polystyrene (PS) [79]. Dissolving microneedles have been mainly produced in polysaccharides [9], [80], [81], polyvinyl alcohol (PVA) [82] and polyvinylpyrrolidone [82], [83]. Lastly, hydrogel-forming microneedles were successfully produced in polyanhydride type polymers, PVA, and mixtures of polysaccharides [1], [80], [84]–[86].

### 2.2.5 Methods of fabricating microneedles

Several methods of fabricating microneedles have been proposed in literature, depending on the material and the design of the microneedle. Following section briefly describes possible microneedle fabrication methods for silicon, metals, ceramics and polymers.

#### 2.2.5.1 Fabrication of silicon microneedles

The fabrication for silicon microneedles, as illustrated in Figure 4, relies on three sequential operations, (i) deposition of a photosensitive layer a silicon substrate, (ii) patterning the desired shape using lithography, (iii) selective etching, and (iv) removal of the excess photoresist [87]. First, an organic polymer (the so-called photoresist material) is spin coated onto a silicon surface. Next, the surface is selectively exposed to a radiation source, often ultraviolet (UV) light, to create a surface pattern. The selective exposure is achieved through a mask, which only allows light to pass through a desired pattern. Either a positive or a negative resit can be used in this step. In the positive resist, the chains of the photo-resistant material break up after exposure, while in the negative resist the chemical bonds of the photo-resist are strengthened. By etching on top the thin layers, the pattern is applied on the silicon substrate. Two types of etching can be used, being wet- and dry-etching [88]. As a last step, the photoresist material is removed from the patterned silicon substrate using an oxygen-plasma treatment.

The first solid silicon microneedles were created using the above described technique using reactive ion etching [89]. Since then, several researchers have used both wet- and dry-etching in the fabrication of microneedles [31], [36], [39]. As a downside, these multi-step processes require a long fabrication time and are relatively expensive [87].

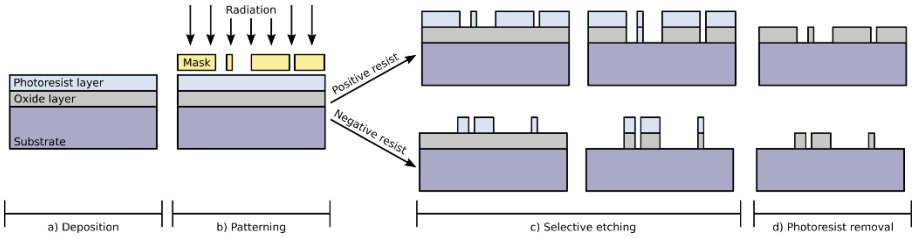


Figure 4: Illustration of the sequential process of transferring a pattern on a silicon substrate. (a) Deposition of a photoresist layer using spin-coating. (b) Creating a patterned shape using selective radiation using a mask. (c) Selective etching of the oxide layer. (d) Removal of the photoresist material. Inspired by [10].

#### 2.2.5.2 Fabrication of metal microneedles

A number of fabrication methods have been presented for the fabrication of metal microneedles, including laser cutting, micro milling and electroplating. The easiest way of creating an array of hollow stainless steel microneedles is by assembling conventional hypodermic needles. At this moment, the smallest commercially available hypodermic needles are 36 G (gauge, referring to the size of the lumen) needles with an outer diameter of around 110 μm, which are used for insulin delivery [90]. As an example, 30 G hypodermic needles were assembled on a polyether ether ketone substrate in a 4 x 4 array. The needles were manually adjusted to a length of 300, 550, 700 and 900 μm. Solid metal microneedles have also been created by assembling stainless steel wires of 200 μm diameter and 300 μm height into a 4 × 4 arrays. To obtain a sharp tip, the wires were tangentially cut [45].

Another method to produce solid stainless steel microneedles was demonstrated by laser cutting small triangles from a sheet and bending them 90° [91]. An array of 7 x 15 needles with a base width of 200 μm and a length of 1000 μm were created from a 75 μm thick stainless steel sheet. Similar to this technique, titanium microneedles with a hight of 200 μm, a base width of 170 μm, and a thickness of 35 μm were created by chemical etching and bending [57].

Very recently, circular- and square-shaped microneedles with a width of 200 μm and a length of 2 mm were fabricated from a titanium alloy using micro milling [92].

#### 2.2.5.3 Fabrication of ceramic microneedles

Ceramic microneedles are usually produced by micro moulding techniques, in which a ceramic slurry is cast inside a mould, followed by a sintering process. An example of this was demonstrated by casting alumina into a polydimethylsiloxane (PDMS) mould with microneedle cavities having varies geometries. Afterwards the ceramic was cured to obtain the various microneedles [59]. This process was also used to produce two types of pyramid shaped microneedles in calcium sulphate dihydrate, having lengths of 100 and 200 μm and a base width of 160 and 285 μm [93]. Another study created microneedle arrays from organically modified ceramic using micro moulding and two-photon polymerization. The ceramic material was casted into an elastomer mould under vacuum and was photo-polymerized inside the mould, to obtain the microneedles [94].

#### 2.2.5.4 Fabrication of polymer microneedles

In recent years, a large variety of fabrication methods has been presented to produce polymer microneedles. Almost all of these studies used a type of micro moulding or micro replication technique to produce the microneedles, such as injection moulding, hot embossing, casting, or soft lithography. These replication processes will be described in more detail in section 2.4. Yet, some studies presented other fabrication techniques compared to the micro replication, namely additive manufacturing [95], [96] and drawing lithography [97]. In drawing lithography, a 3D polymeric structure is extended from a 2D viscous polymer material. SU-8 photoresist epoxy is first spin coated onto a plate. Next, patterned pillars called drawing pillars are brought in contact with the coated polymer. The pillars are moved upwards, creating tensile stress in the polymer, which result in an elongation of the initially 2D polymer. Afterwards, the polymer is cured and the polymer is separated from the drawing pillars. This unique manufacturing technique can be used to create very high aspect ratio microneedles. Two types of additive manufacturing techniques are distinguished, being photon-polymerization and a single-step stereolithography (SLA) based method. The photon-polymerization method uses a femtosecond laser to polymerize photosensitive resin. With this technique it is possible to achieve a very high print resolution down to 100 nm [61]. Two types of cone shaped microneedles having a base radius of 100 and 187.5 μm with a length of 300 and 250 μm were created using photon-polymerization [96]. In comparison with the photon-polymerization strategy, the SLA printing methods are able to print sub-millimetre components with a print resolution of 100 μm in larger build volumes at a higher throughput [95]. Using this printing technique, hollow microneedles with a base width of 800 μm, a lumen of 600 μm and a length below 1 mm were successfully fabricated [95].

### 2.2.6 Microneedle design

A wide variety of microneedle designs are found in literature, ranging from cylindrical, rectangular, pyramidal, conical, octagonal, and quadrangular, with different geometries and dimensions. Typically, the length of the microneedle varies from 25 to 2500 μm, with a base diameter between 50 to 500 μm and a tip radius below 50 μm. When investigating microneedle arrays, the number of needles and the density are also parameters which can be varied. Yet for all designs, it is important that the microneedles are able to pierce the skin without breaking. Due to the elastic nature of the skin, microneedles can be prevented from penetrating as the skin can bend or fold around the microneedles. This is particularly the case for microneedles with a large tip radius and for short microneedles [45], [98]. Thus, for a successful skin penetration, the shape of the microneedle tip is important. Microneedles with a small tip radius have a higher potential of penetrating the skin, yet they might become too fragile, leading to needle bending or breaking. Contrary, needles with a large tip radii have a higher mechanical strength, but also require higher insertion forces [99], [100].

For hollow microneedles, the tip is also an important design parameter. Hollow needles with a centred lumen can compact the skin and thus have a higher risk of skin clogging in the lumen [101], [102]. To overcome this problem, it is advised to have a sharp tip radius together with an off-centred lumen [3].

### 2.2.7 Mechanical characterisation of microneedles

Microneedle systems will be exposed to a variety of mechanical loads, both during insertion and removal, which can cause possible failures such as buckling, bending, compression or fracture [1]. It is therefore crucial to characterise the mechanical strength of the microneedles to ensure that they are safe to use. Two types of mechanical tests can be found in literature, being axial compression tests and lateral shear tests.

#### 2.2.7.1 Axial compression tests

Multiple studies can be found in literature which conduct axial compression tests to determine the mechanical strength of microneedles. Most of them used polymer microneedles [80], [99], [103]–[110], and one study used silicon microneedles [111]. In general, the axial test involves applying a compression force to the microneedles, which is perpendicular to a solid metal base-plate, while the force and displacement are recorded. The tests are usually performed at a compression speed between 0.01 mm/s and 1.1 mm/s, with most researchers in literature using 0.5 mm/s. Three test approaches have been reported in literature for evaluating the mechanical strength of microneedles. In the first approach, the microneedles are compressed until a set maximum force is reached [108]–[113]. Afterwards, the force displacement data is evaluated to determine the failure force. Usually, a sudden decrease in force can be identified at the moment of failure [112]. In the second approach, a compression force is set to the required force to penetrate the microneedles into the skin, along with a possible safety factor [103]. If no deformation is detected after the applied compression force, it is assumed they will penetrate without failure. In the third approach, several consecutive compression tests are performed with increasing forces. After each compression, the needle is visually inspected for possible damage [103]–[105]. However, it should be noted that the applied force during this test approach, does not accurately represent the real insertion forces when penetrating microneedles into skin. In the test approach, the microneedles are pressed against a solid surface, leading to a stress concentration at the tip, whereas in real skin penetration, the forces are distributed over a larger surface as the skin wraps around the microneedles.

#### 2.2.7.2 Lateral shear tests

A few researchers have investigated the lateral strength of microneedles with shear tests. This shear stress could be experienced when microneedles are inserted at an angle or due to lateral movements when microneedles are inserted in skin [7]. A mechanical test setup applies a lateral force on a defined location of the microneedle until microneedle failure is detected. To the best of our knowledge, shear tests have only been conducted three times in literature. Lateral failure forces of 40 mN to 460 mN per needle are reported [80], [103], [112]. The failure force is again detected by a drop in the force in the curve.

### 2.2.8 Applications of microneedles

Microneedles have several applications in the medical field, being drug delivery, vaccine delivery, cosmetic applications, and patient monitoring and diagnosis.

#### 2.2.8.1 Drug delivery

Drug delivery using microneedles has been demonstrated in a wide variety of studies over the last 25 years. The first study which used microneedles for drug delivery was in 1998, where solid silicon microneedles were applied using the "poke with patch" approach [89]. Since then, multiple researchers have employed solid microneedles, for the delivery of different molecules, such as insulin, paracetamol and ketoprofen [98], [114]. Coated and dissolving microneedles have also been used in transdermal (in the dermal skin layer) drug delivery for a wide range of drugs including desmopressin (synthetic hormone) [57], caffeine [115] and ibuprofen [104]. Hollow microneedles have primarily been used in drug delivery for the administration of insulin [65], [116]. Hydrogel forming microneedles on the other hand, have been usefully used to deliver proteins [85].

#### 2.2.8.2 Vaccine delivery

Vaccine delivery with microneedles offers a huge application, as a large network of immunologically active cells responsible for initiating the immune response are found in the skin [117]. Most studies in literature dealing with vaccine delivery through microneedles, investigated the delivery of influenza vaccines through coated [118]–[120], hollow [121], and dissolving microneedles [122], [123]. Good immunisation results have been shown with these vaccines, which are in some cases even with a lower vaccine dosage superior compared to the traditional intramuscular injection [12], [119], [120]. Moreover, microneedles were also used to deliver vaccines for the Edmonston-Zagreb measles [124] and Anthrax [125]. Very recently, researchers have also used microneedles to deliver the SARS-CoV-2 vaccine for the COVID-19-virus, which induced a statistically significant increases in immune response [126].

#### 2.2.8.3 Cosmetic applications

Microneedles can also be used in cosmetic applications to treat skin blemishes (any type of mark, spot, discoloration, or flaw that appears on the skin) or to administer active cosmetic ingredients. Well-known examples of this are the Dermaroller, Dermapen and Derma-stamp, which are medical hand-held devices which are equipped with solid steel microneedles (needle length of 1500-2000 μm) [127], [128]. The microneedles can directly be applied to the skin to create microscopic pores, through which collagen, serum, or acne medication can diffuse to the skin [129].

#### 2.2.8.4 Patient monitoring and diagnostics

As already mentioned, the use of hypodermic needles has some drawbacks such as needle-phobia and the need of medical staff [42]. Microneedles have the potential to overcome these drawbacks, as they can be used to extract interstitial fluid and capillary blood. The easiest way of extracting interstitial fluid is by using solid microneedles to create micro pores, after which vacuum can be used to extract the fluid. An example of this is a developed device with an array of solid microneedles, combined with stored vacuum [130]. A more complex approach to achieve patient monitoring and diagnostics are hollow microneedles. Hollow glass microneedles have been used to monitor glucose in interstitial fluid. Results with human volunteers showed that the concentration of glucose in the interstitial fluid had a good correlation to the glucose concentration in

blood [131]. Moreover, longer hollow metal microneedles with a length of 1800 μm have also been used to extract 20 μl of blood from the tail of a mouse [132]. The metallic microneedles were created by depositing nickel in an epoxy mould, using electroplating.

## 2.3 Mould surface patterning technologies

Moulds used for creating polymer products with micro surface features are usually compiled out of multiple inserts, which are fitted in the main mould body [133]. The negative shape of the product cavity and micro surface features are manufactured in the mould insert. The use of inserts reduces the overall cost of the mould manufacture, as it allows iterative steps that are often required during the manufacturing and designing process. Moreover, micro patterning technologies often have restricted mounted dimensions for a workpiece. Furthermore, the insert can be manufactured in a different material than the mould body, such as aluminium alloy, copper alloy, or hardened steel [134]. This section gives an overview of the most suitable manufacturing technologies for patterning a mould surface. These technologies have been classified by Masato et al. [135] into four groups: mechanical machining, electrochemical etching, thermoelectric engraving, and additive manufacturing.

### 2.3.1 Mechanical machining

#### 2.3.1.1 Micro-milling

Micro-milling is a three-dimensional mechanical machining process which is widely applied for patterning mould surfaces and manufacturing micro product cavities [136]. In this process, chips are removed from the workpiece using a milling tool that rotates at a very high speed as it moves along a defined path [137]. Advanced computer numerical control (CNC) allows the simultaneous movement of several axes, enabling the creation of complicated tool paths at a high precision [138]. Micro-milling is often considered as a downscaled conventional milling process, yet micro-milling tools are significantly more expensive (i.e. up to 10 times higher), and it presents several challenges compared to the traditional process [135]. As the tool diameter is reduced, vibrations are amplified which can result in burr formation. This is usually unacceptable, as deburring of such small features is often not feasible [139]. Moreover, the high spindle speeds and the possible formation of chip clogging may easily lead to tool failure. Micro-milling often requires long machining times, depending on the desired surface pattern and workpiece material [137].

#### 2.3.1.2 Abrasive jet machining

Abrasive jet machining, also known as abrasive micro-blasting, uses abrasive particles to remove material from a workpiece. The particles together with water or air are blasted at the workpiece surface, hereby chipping and eroding microparticles to create a surface texture [140]. The abrasive mixture also cools the workpiece down and removes debris from the working area. Using abrasive jet machining to create surface features can be done by masking the workpiece with a material which needs to withstand the erosion. The shape and sizes of the mask itself define the eventual surface features on the workpiece [141]. Micro jet machining has been used to create squared microcavities of widths between 50 to 200 μm with depths up to 10 μm [142].

### 2.3.2 Electrochemical etching

#### 2.3.2.1 Micro electro discharge machining

Electrical discharge machining (EDM) is a machining process for electrically conductive materials, which uses precisely controlled sparks that occur between a tool electrode and a workpiece in the presence of a dielectric fluid [143]. The tool and workpiece are both electrodes, as they are part of an electrical circuit. Sparking takes place between these two electrodes due to a discharge pulse, which removes a small amount of material from both sides. Multiple discharge pulses (up to 500 000 per second) are used to generate a micro surface feature on the workpiece. The dielectric fluid flushes the debris away and cools the electrodes [144]. Micro EDM can be considered as a downscaled conventional EDM process, which generates features with dimensions below 500 μm. The process requires the use of lower energy pulses, high accuracy tools, and precise machine tool systems. The micro EDM methods found in literature, being micro EDM sinking, wire micro EDM, micro EDM drilling, and micro EDM milling are illustrated in Figure 5 [134].

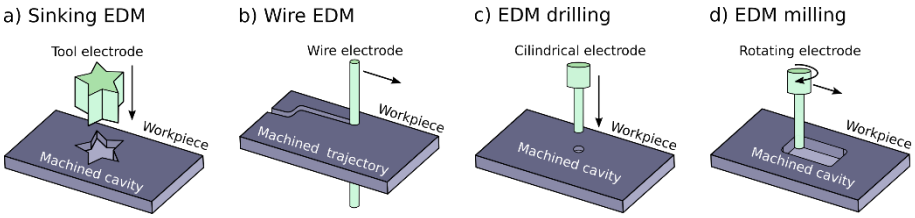


Figure 5: Illustration of the micro EDM methods: (a) sinking EDM, (b) wire EDM, (c) EDM drilling, and (d) EDM milling. Inspired by [134].

In micro EDM sinking (Figure 5 a), a shaped tool electrode can be used for manufacturing three-dimensional shapes. The tool electrode geometry is the negative of the cavity and must be produced by another micro manufacturing technology, such as micro milling [145]. Micro wire EDM (Figure 5 b) is similar to conventional wire EDM, where a wire electrode is fed from a spool to cut the workpiece by displacement along a defined contour [146]. Micro EDM drilling (Figure 5 c) is a special form of micro EDM sinking, in which a micro-sized cylindrical tool electrode is used along its length. Using this method, circular cavities with very high aspect ratios can be generated [134]. Similar to micro EDM drilling, micro EDM milling (Figure 5 d) also uses an cylindrical electrode down to a diameter of 10 μm. The electrode is driven along a tool path while rotating, similar to three axis milling. Material from the workpiece is removed in layers ranging from a 1 μm to 100 nm [147].

#### 2.3.2.2 Electro-chemical micromachining

Electro-chemical micromachining (ECMM) follows a similar machining process as chemical etching, yet the chemical bath is instead replaced by an electrolytic cell. An electric current is applied between the tool (cathode) and the workpiece (anode), inducing electrolysis [148]. Applying micro surface features on a workpiece can be done using three methods, being through-mask ECMM, conventional ECMM, and jet ECMM as illustrated in Figure 6 [149].

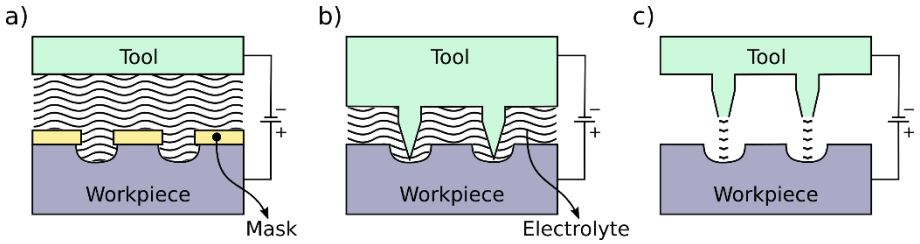


Figure 6: Illustration of the ECMM methods: (a) through-mask ECMM, (b) conventional ECMM, and (c) jet ECMM. Inspired by [149].

In through-mask ECMM (Figure 6 a), a workpiece is masked with a non-conductive material. Only the un-masked areas will be exposed to the electrolyte, thus resulting a selective material removal [150]. In conventional ECMM (Figure 6 b), the surface is etched using a pre-patterned cathode. This process avoids the masking step, making set-up easier and faster. However, this process requires the manufacturing of a pre-patterned cathode [151]. In jet ECMM (Figure 6 c) a negatively charged electrolyte jet of a few micrometres is used as a tool to generate micro surface features. Researchers have demonstrated that micro dimples, micro channels and micro grooves can be created on a surface, using this technique [152].

#### 2.3.2.3 Chemical etching

Chemical etching, also known as wet etching, uses an etching solution to remove material from a workpiece and is illustrated in Figure 7. For selective etching of the surface, a mask should be applied to cover specific areas of the surface (Figure 7 a) [153]. Different masking techniques are available depending on the workpiece's dimension, the texture dimension and the etching solution. An example of this is inkjet printing, which proved to be a fast and highly feasible technique for texturing steel surfaces [154]. The un-masked areas will be exposed to the etching solution, which results in a selective material removal of the surface (Figure 7 b). Afterwards, the masking layer is removed and the workpiece is rinsed to remove any residual chemicals on the surface (Figure 7 c) [155].

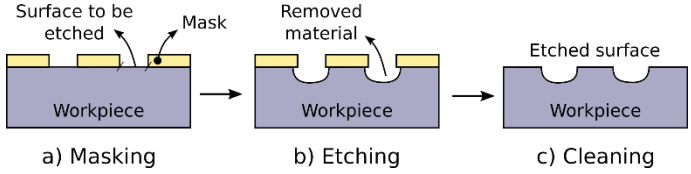


Figure 7: Illustration of the chemical etching process. Inspired by [135].

### 2.3.3 Thermoelectric engraving

#### 2.3.3.1 Ultrashort pulsed laser ablation

Ultrashort pulsed laser ablation also known as ultrafast laser ablation, is a recently developed advanced processing technique, which can be used to create a wide variety of surface features. Ultrashort pulsed lasers are characterized by a pulse duration in the range of pico- and femtoseconds [156]. The pulse repetition rate (frequency), on the other

hand, is in the range of several hundred thousands of pulses per second. A huge advantage of the ultrashort laser pulses, is the possibility to reduce the heat affected zone, resulting in high accuracy machining without crack formations or the formation of recast (redeposition of ablated material on the surface) [157]. Laser ablation is defined as the removal of the material from workpiece by direct absorption of laser energy. This is achieved, when the energy of the laser pulses surpasses the ablation threshold of the material. The ablation threshold is a material specific parameter, which is defined as the critical fluence (pulse energy per area) required to achieve ablation [158].

Two types of ultrashort pulsed laser machining strategies can be used to create surface patterns, being direct laser writing and percussion drilling. With direct laser writing, cavities, trenches or other complex 3D-features can be created by scanning the pulsed laser over a surface, with a defined machining path. Depending on the laser spot size, features can be created in the order of micrometres. The periodic distance between the pulses can be altered, by changing the pulse repetition rate and the scanning speed. In percussion drilling, the pulsed laser beam is focused on a fixed position of the surface. Using this strategy, it is possible to create high aspect ratio microcavities [159].

Ultrashort pulsed lasers can also be used to create textures being smaller than the laser spot size (in the range of nanometres), called laser induced periodic surface structures (LIPSS) [160]. In the field of micro fabrication, these LIPSS are usually undesired as they can diminish the surface finish. However, in the field of surface texturing, these LIPSS can offer some unique opportunities. Three categories of LIPSS morphologies can be distinguished, being low spatial frequency LIPSS, high spatial frequency LIPSS, and late-stage LIPSS. Low spatial frequency LIPSS are usually wavy ripples or regular gratings with sizes in the same order as the wavelength of the used laser. High spatial frequency LIPSS also have a ripple-shape, yet these structures are much smaller than the laser wavelength. The last type of structures are late-stage LIPSS, which have more defined shapes such as a nanoforest, nanobubbles or triangular LIPSS [161], [162].

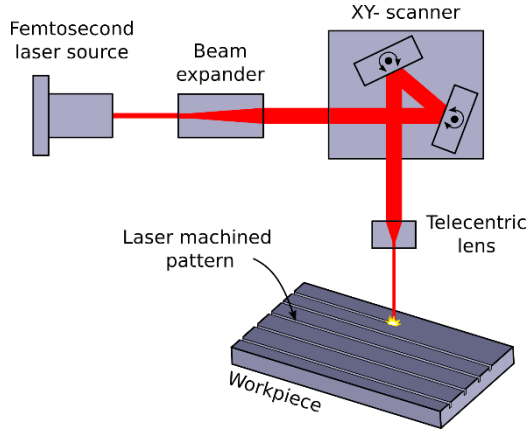


Figure 8: Illustration of the ultrashort pulsed laser machining using a femtosecond laser source. Inspired by [163].

The throughput and productivity of machining micro surface features using ultrashort pulsed laser ablation is a big challenge [164]. A possible easy, yet limited solution to overcome this challenge is ultrafast scanning ablation, where the scanning speed is greatly increased. The second, very recent approach to increase productivity is

the use of multiple beams to achieve parallel processing. This system consists of a beam splitting device which splits the very high powered input beam in a bundle of individual beams. Although parallel processing holds a huge potential in the field of micro manufacturing, it is still a very complex process and all the parameters must be re-optimized for industrial laser processing [165].

#### 2.3.3.2 Electron-beam and ion-beam machining

Electron-beam and ion-beam machining are comparable processes, which can be used to fabricate micro- and nano surface patterns on metal surfaces. Electron-beam machining uses high-velocity electrons to irradiate the sample [166], while ion-beam machining uses ions as the beam medium [167]. Both processes require advanced and expensive equipment, including a high-vacuum environment and the material removal rate is very low, down to 0.1 $mm^3$/min. However, the processes can be used to accurately machine three-dimensional structures in the order of a few nanometres.

### 2.3.4 Additive manufacturing

#### 2.3.4.1 Selective laser melting and directed energy deposition

The two additive manufacturing technologies for producing metal surface patterns are selective laser melting (SLM) [168], [169] and directed energy deposition (DED) [170]. Both processes use a laser beam to locally melt metal powder onto a substrate, hereby building products layer by layer, as shown in Figure 9. The difference between both processes is the powder depositing mechanism. In SLM, a layer of powder is spread on top of the base plate and is subsequently melted by a laser beam projected from above. The laser scans the powder bed according to the desired shape. After each layer has been scanned, the powder bed is moved down over a distance of one layer thickness and the laser then melts a new cross-section. The process is repeated to form the desired part [171]. In DED, powder is sprayed on a surface through a nozzle. The nozzle moves along a machining path, depositing the power in specific locations [170]. The most commonly used material in these additive manufacturing techniques is stainless steel (AISI 316 L). Micro surface patterns created using powder melting typically show low surface quality due to defects such as pores and voids. Micro surface patterns with unique geometries can be achieved using SLM, yet finer powder particles have to be used [172]. Moreover, the created patterns usually exhibit a lower surface quality due to defects such as pores and voids [173]. DED can also be used to create micro surface patterns on complex geometries, by directly depositing and sintering the particles, yet a process parameter optimization should be conducted to improve the texture accuracy and uniformity [174]. Both types of powder-based additive manufacturing processes are expensive setup and high material costs. Moreover, to prevent powder oxidation, it is necessary to establish a protective atmosphere within the CNC machine [135].

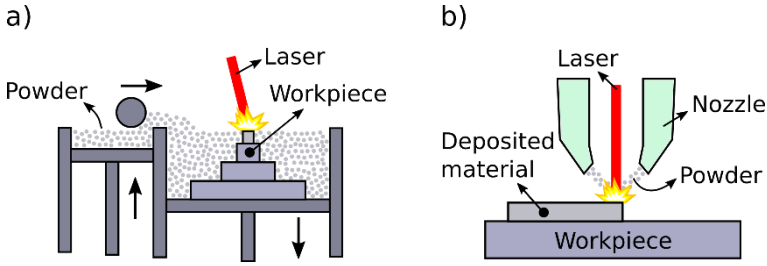


Figure 9: Illustration of (a) selective laser melting and (b) direct energy deposition. Inspired by [170].

#### 2.3.4.2 Lithography

Lithography-based processes were initially developed for the electronics industry, yet this technique was recently also used to create three-dimensional micro surface patterns [175]. The process uses a mask to create a texture on a photo-sensitive material by selective irradiation, as previously explained in section 2.2.5.1.

The resolution of the lithography process mainly depends on the irradiation source and can vary between 1 to 100 nm. For optical lithography, the resolution is restricted by the diffraction-limit (about half the wavelength) of the light. Therefore, light sources with a short wavelength are usually employed such as deep or extreme ultraviolet, having wavelengths of a few tens of nanometres. Besides optical lithography, electron-beam lithography and ion-beam lithography were developed to overcome the resolution limitations. Using these techniques, nano surface patterns of a few nanometres can directly be machined without the need of a mask. However, these are very expensive processes having a low throughput [176]. In general, creating a micro surface pattern using lithography techniques is an expensive process due to the multiple steps involved, specialized equipment, and costly consumables such as the required masks. Despite these challenges, lithography has become widely adopted thanks to its scalability and high throughput. Photolithography manufacturing facilities require significant investments, with costs around USD 30 million [135].

#### 2.3.4.3 LIGA

LIGA is the German derived acronym for Lithographie, Galvanoformung, Abformung (translated as Lithography, Electroplating, and Moulding) which is a process that can be used to manufacture substrates with micro surface patterns. The process consists out of several steps, as illustrated in Figure 10. First, lithography is used to manufacture a substrate with a micro surface pattern, called the master. Next, the micro surface pattern is electroplated to get a metal mould insert. At last, the mould insert is used in hot embossing or injection moulding, to obtain the structured thermoplastic part. High aspect ratio surface patterns up to 100:1 can be created using this technology. The achievable dimensions are mainly linked to the resolution of the used lithography process [177]. The side walls of the micro features are typically straight without draft angles, which can lead to ejection problems during demoulding. However, draft angles can be included using multiple x-ray exposures of the photoresists [178].

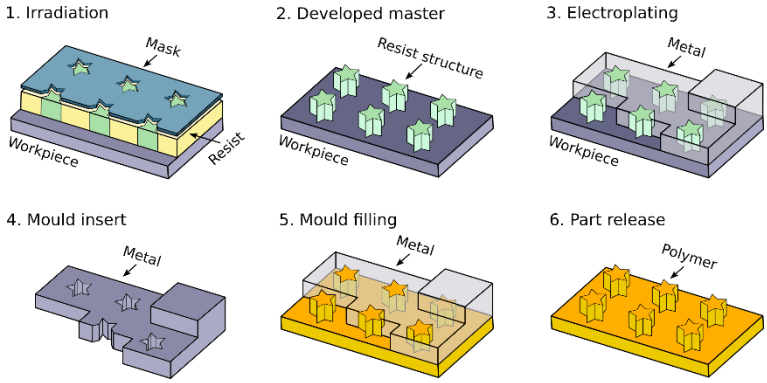


Figure 10: Illustration of the LIGA principle, consisting out of several process steps. Inspired by [179].

## 2.4 Polymer replication techniques

Polymer replication techniques which transfer a desired surface pattern from a mould to a polymer product can be divided in two main categories, being injection moulding (including rapid heat cycle moulding, injection compression moulding, and vacuum assisted injection moulding) and imprinting (including thermal imprinting, UV imprinting, roll-to-roll imprinting, and nano imprint lithography). Figure 11 gives an illustration of the capabilities of these replication techniques according to the state of the art. This section gives an overview of the two replication technologies together with possible process adaptations and extensions which facilitate the replication fidelity.

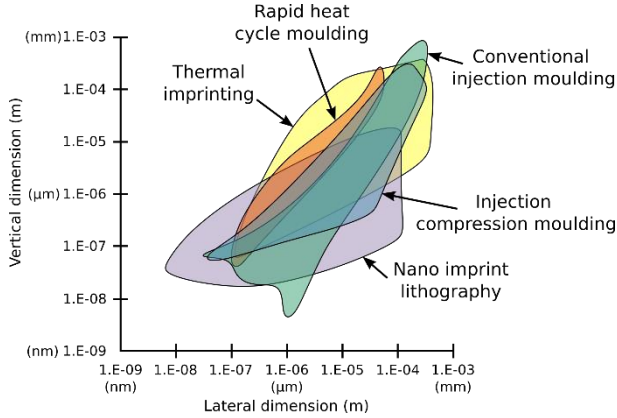


Figure 11: Capabilities of polymer replication techniques according to the state of the art. Inspired by [180], [181].

### 2.4.1 Injection moulding

#### 2.4.1.1 Conventional injection moulding

Injection moulding is the most common process used to produce polymer parts. More than one third of all thermoplastic products are produced using this mass production process. A schematic representation of the injection moulding process is illustrated in Figure 12. Injection moulding is a cyclic process, which can be divided into three stages. In the first stage, polymer material, generally in the shape of granulates or powder, is fed to the barrel through the hopper. The polymer inside the barrel melts due to both the electric heating elements outside the barrel and internal shearing of the polymer during the rotational movement of the screw. This rotational movement pushes the molten polymer forwards, creating an accumulation of melt material in front of the screw. The screw stops rotating when sufficient material is molten. In the second stage the screw moves forward thereby forcing the accumulated molten polymer into the mould. To compensate for material shrinkage, the screw keeps forcing more polymer into the mould using a set pressure, called the holding pressure. Once the polymer is solidified within the colder mould, the mould opens and the product is ejected [182], [183].

The main process parameters that need to be specified are the amount of injected material, the barrel temperature, the mould temperature, the speed at which the material is injected, the holding pressure and the required cooling time. All of these parameters will, to some extent, have an influence on the final part. Injection moulding defects such as flash, incomplete filling, burn marks, sink marks, etc. can occur if one or more parameters are set incorrectly.

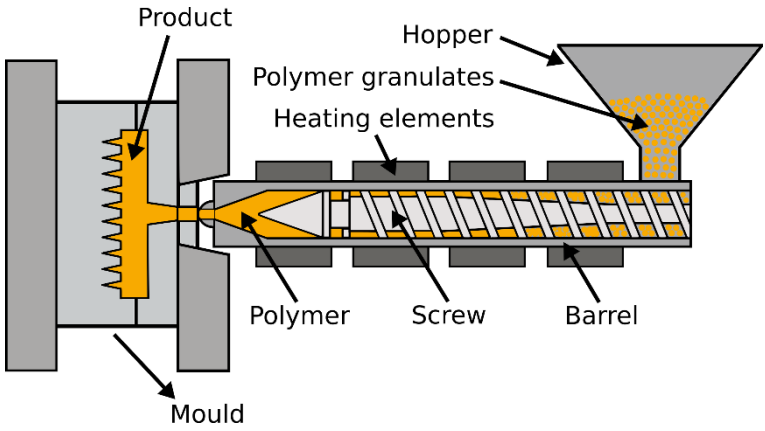


Figure 12: Schematic representation of the conventional injection moulding process.

#### 2.4.1.2 Rapid heat cycle moulding

Rapid heat cycle moulding or variothermal injection moulding is an adaptation of the conventional mould heating strategy, which is often used to improve the replication fidelity of small micro surface features [184]. In conventional injection moulding (Figure 13 a), the mould surface is continuously cooled to ensure a nearly constant temperature below the glass transition or the melting temperature for amorphous or semi-crystalline

polymers, respectively. Hence, a layer of frozen polymer material (skin layer) will be formed as soon as the polymer flows into the mould. The core of the melt flow, however, remains in a fluid state, leading to the well-known fountain flow effect. The rapid solidification of the skin layer hinders the filling of the micro features, which could lead to incomplete filling. In rapid heat cycle moulding (Figure 13 b), the cavity wall temperature is no longer a constant, but it is varied between a high value (above the glass transition or melt temperature) during the filling stage and a lower value during the cooling stage. This way the formation of a frozen layer can be delayed, leading to a better and more uniform filling of micro features. However, compared to the conventional injection moulding process, this process is more complex and expensive, due to more expensive moulds and side equipment. Besides, the cycle time remains a point of attention as it is increased in most cases [185].

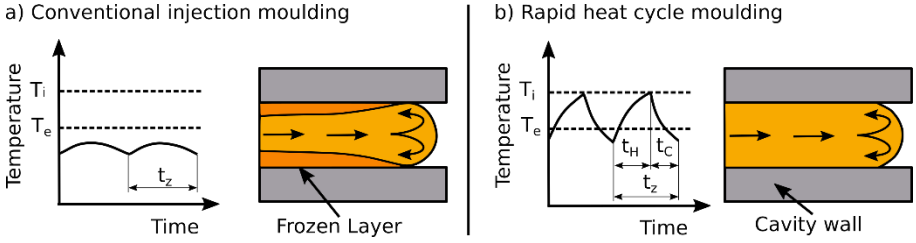


Figure 13: (a) Illustration cavity wall temperature as a function of time for a conventional injection moulding process, with $T_g$ the cavity wall temperature before injection, $T_e$ the ejection temperature, and $t_z$ the cycle time. (b) Illustration of the cavity wall temperature as a function of time for rapid heat cycle moulding process, with $t_H$ the heating time and $t_C$ the cooling time.

### 2.4.1.3 Injection compression moulding

Injection compression moulding is an extension of conventional injection moulding, which incorporates an additional compression of the injected polymer through the mould closing action [186]. First, the melt is injected into a slightly opened cavity, with the two mould halves initially being separated from each other as illustrated in Figure 14 (a). After the injection phase (i.e. when 90–98% of the total product volume is filled), the mould cavity thickness is reduced by a mould closing movement, which forces the melt to fill and pack out the entire cavity, as illustrated in Figure 14 (b). The additional gap necessary to perform the compressing action is defined as the compression stroke. The major advantage of this technique is the more uniform pressure distribution across the mould cavity, leading to more homogenous properties across the product and less warpage and internal stress compared to conventional injection moulding. For this reason, injection compression moulding has been extensively favoured to conventional injection moulding in the production of optical components, as it is proven to reduce birefringence (double refraction) and enhance optical properties [187]. The more uniform pressure distribution can also lead to a higher and more uniform replication fidelity of microfeatures [188]. However, the injection moulding machine should be equipped with an additional control module, which facilitates the compression stage. Moreover, either the screw must be equipped with a nozzle shut-off mechanism or the mould should have a hot runner with a valve gate. Both systems prevent the polymer melt in the mould cavity from flowing back into the injection barrel during the compression phase.

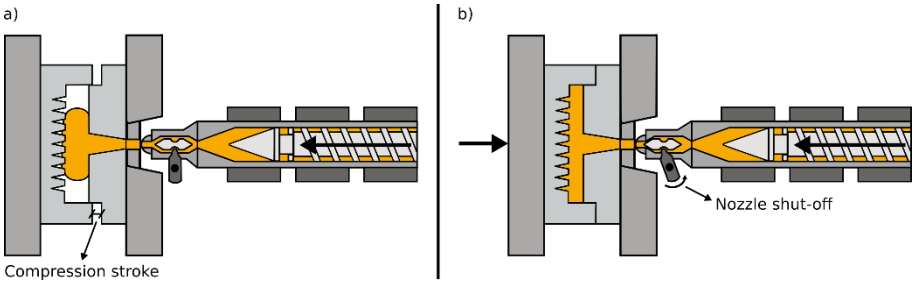


Figure 14: Illustration of the injection compression moulding process sequence. (a) Injecting the polymer melt into a slightly opened mould. (b) Compressing the polymer melt through the mould closing action.

#### 2.4.1.4 Vacuum-assisted injection moulding

Moulds with micro or nano surface features represent 'blind-holes' in which air tends to accumulate and be compressed during the filling stage, as illustrated in Figure 15 [187]. The entrapped and compressed air pockets can increase the melt flow resistance, which hinder the complete replication of the micro surface features [134]. Vacuum-assisted injection moulding has been introduced to evacuate the air from the microcavities, with the intent of improving the replication fidelity of the micro surface features. As the air in the microcavities is evacuated, it is possible to reduce the counteracting pressure generated by the entrapped air.

The effect of vacuum-assisted injection moulding on the replication fidelity of micro surface features has been investigated by multiple researchers as a possible technological improvement for the replication fidelity. However, the results found in literature are conflicting as both positive and negative effects on the replication fidelity are reported. In fact, the evacuation of air has been reported to improve the replication fidelity by a few percent for feature aspect ratios between 0.5 and 1 [189]–[192]. However, it has also been reported that vacuum-assisted injection moulding results in a decrease of the mould temperature before the beginning of the injection phase, therefore having an insignificant or negative effect on the replication fidelity [187], [193].

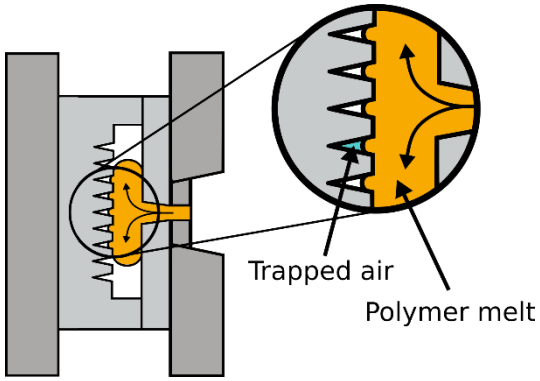


Figure 15: Entrapment of air inside micro feature cavities during the filling phase.

### 2.4.2 Imprinting

#### 2.4.2.1 Thermal imprinting

Thermal imprinting, often referred to as hot embossing, is a process used to produce polymer parts with micro or nano surface features [194]. In thermal imprinting, the surface pattern of a mould or stamp is transferred to a polymer substrate through mechanical compression, as illustrated in Figure 16. The polymer substrate and mould are heated above the glass transition temperature for amorphous polymers or a temperature close to the melting temperature for semi-crystalline polymers. This ensures that the polymer substrate is sufficiently softened, so it can be deformed. The mould or stamp is compressed into the polymer substrate at a specified pressure (in the order of 10 MPa) . Once the micro features are transferred to the polymer, the mould is cooled to ensure the solidification of the polymer. Afterwards, the replicated polymer substrate is removed from the mould during the demoulding phase.
A wide variety of micro surface features have been replicated in literature using this technique. An example of this are hierarchical hydrophobic micro and nano features, which were successfully replicated in polystyrene [195]. Besides, some researchers have also used thermal imprinting to produce microneedles. Solid polycarbonate microneedle arrays were replicated using a PDMS mould. The length of the fabricated needles ranges from 500 to 1500 μm, with a distance between the needles of 500 to 2000 μm [67]. Moreover, solid polymeric microneedles with a height of 880 μm were produced in a biocompatible polymer [196]. Furthermore, PMMA microneedle arrays where also created using LIGA together with hot embossing for the replication of microneedles with a length between 750 to 1000 μm [197].

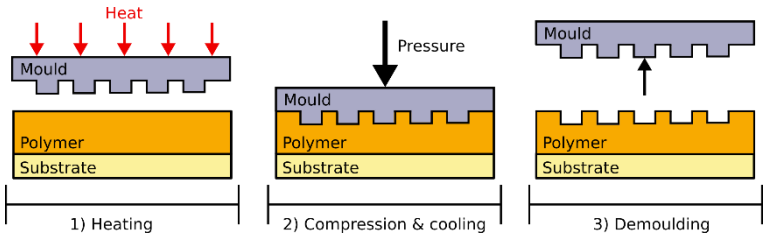


Figure 16: Schematic representation of the thermal imprinting process. Inspired by [198].

#### 2.4.2.2 UV imprinting

UV imprinting follows a similar process as thermal imprinting, yet in this process a patterned transparent mould is used together with a UV-curing polymer, as illustrated in Figure 17. The patterned mould, usually quartz or sapphire is compressed in the liquid polymer. In contrast to thermal imprinting, a lower pressure can be used because the polymeric material is a viscous liquid, which can easily be deformed. Next, UV light is exposed to the polymer, which cures the material by creating crosslinks [198]. The throughput time is significantly reduced compared to thermal imprinting, as in this process it is not necessary to increase and decrease the temperature of the polymer and the mould. However, the processing parameters such as curing time, intensity, and wavelength of the UV should carefully be selected to avoid the formation of possible microscopic air bubbles [199].

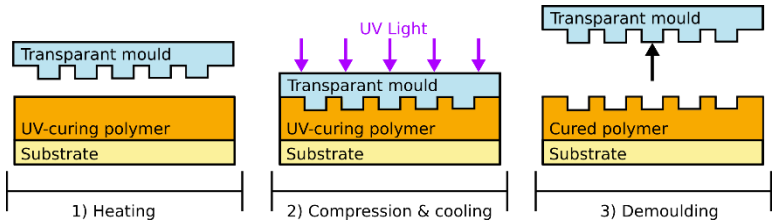


Figure 17: Schematic representation of the UV imprinting process. Inspired by [198].

#### 2.4.2.3 Roll-to-roll imprinting

The major disadvantage of conventional UV- and thermal imprinting is the discontinuous process which is difficult to upscale towards mass production. To overcome this drawback, a continuous imprinting process was developed called roll-to-roll imprinting [200]. In this process, a patterned roller is used to imprint micro or nano surface features onto a polymer substrate, which is supported on a roller as illustrated in Figure 18. Both the thermal and UV imprinting principle can be used in this technology. In the thermal imprinting, the patterned roller mould and polymer film are heated to be able to imprint the pattern, while in UV imprinting a photo-curable resin is used in combination with UV light. Extremely high imprinting rates up to 20 m/min can be achieved with this technique, which make it a suitable mass production process [198]. However, this technology also presents some drawbacks, as replicating micro or nano surface features with a high aspect ratio is very challenging [201], and fabricating the patterned roller moulds is difficult and expensive [202].

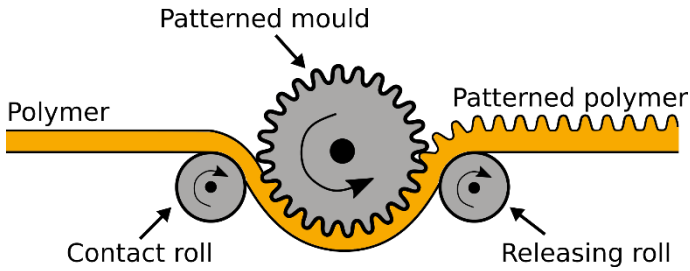


Figure 18: Schematic representation of the roll-to-roll imprinting process. Inspired by [203].

## 2.5 Conclusion

It can be concluded that different types of microneedles are described in literature, which can be manufactured using several materials and fabrication methods. However, a mass production process which can manufacture microneedles in large volumes at a low cost is currently lacking. When looking into injection moulding as a possible technique to produce polymer microneedles, it can be concluded that various manufacturing technologies are available for patterning a mould surface. In this thesis, it will be investigated if ultrashort pulsed laser ablation can be used to produce microneedle cavities in common mould materials. Furthermore, an overview is given on polymer replication technologies which can be used to replicate surface patterns from a mould to

a polymer product. Moreover, possible process adaptations and extensions which facilitate the replication fidelity are discussed. Techniques which will be investigated within this thesis are conventional injection moulding and injection compression moulding.

# Chapter 3 A novel method for producing solid polymer microneedles using laser ablated moulds in an injection moulding process

Evens T., Malek O., Castagne S., Seveno D. and Van Bael A. A novel method for producing solid polymer microneedles using laser ablated moulds in an injection moulding process. Manufacturing Letters, 24: 29-32, 2020. Some parts of the original publication are left out or modified to avoid redundancy.

## 3.1 Abstract

Microneedle arrays are minimally invasive devices which offer a pain free, straightforward and efficient method for transdermal drug delivery. Manufacturing these micro-systems represents a real challenge and a mass production process with high volume outputs at low cost is lacking. In this study, we present a novel method to produce polymer microneedles using laser ablated moulds in an injection moulding process. We successfully created cone-shaped micro holes with low tip radii in a tool steel mould, using a femtosecond laser with a cross-hatching strategy. Finally, the attained mould was used in an injection moulding process to replicate polypropylene microneedles.

## 3.2 Introduction

Microneedles are microscale invasive devices, usually arranged in an array, designed to by-pass the human stratum corneum skin barrier [5], [88], [204]. The length of the needles can range from 50 μm – 2000 μm and when penetrated in the skin, microscopic aqueous pores are created, through which drugs can diffuse to the dermal microcirculation [4]. The advantages of these devices have already extensively been studied in medical research [1], [9], [12], [24]. At this stage, a production process to manufacture these microneedles in large volumes at a low cost is required [5], [42]. A promising manufacturing process which fits these criteria is polymer injection moulding. By applying the negative geometry of the microneedles on a mould cavity, millions of polymer microneedle systems can be produced at a low cost [134]. However, within the current state of the art, methods for applying the negative of the microneedles on the injection mould are limited to expensive and time consuming precision techniques such as micro-electrical discharge machining [69], [72], [73], [205], milling [206], drilling [74], forging [207] or indirect mould making [208]. Besides, manufacturing microneedle

cavities with a sharp tip has proven to be very difficult with these techniques, while small tip-radii are essential for microneedles to effectively penetrate the skin [42], [72].

In this study, a novel manufacturing process to produce sharp-tipped solid polymer microneedle arrays using laser ablated moulds in an injection moulding process is presented.

## 3.3 Materials and Methods

### 3.3.1 Materials

The thermoplastic material is a high melt flow polypropylene (PP) grade 515A from SABIC, with a melt flow rate of 24 g/10 min (230° C/2,16 kg). A low-corrosion tool steel (grade 1.2083 - AISI 420), was selected for the mould insert material.

### 3.3.2 Representation of the process chain

A micromachining system with a laser source is employed to laser ablate a mould insert with dimensions 70 mm x 60 mm x 4.4 mm (Figure 19 a). The insert is then placed in the mould (Figure 19 b). Afterwards, the mould is used in an injection moulding process (Figure 19 c) to replicate polymer microneedles (Figure 19 d).

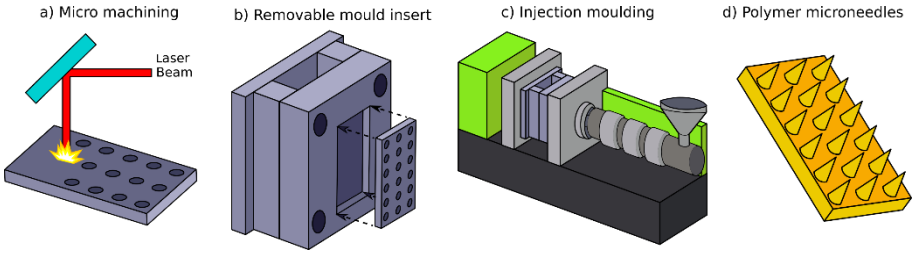


Figure 19: Illustration of the process chain to produce solid polymer microneedles.

### 3.3.3 Laser machining

A micromachining system (Lasea LS5) with a femtosecond laser (Satsuma HP, Amplitude Systemes) is employed to ablate the mould insert. The laser source emits a beam with a wavelength of 1030 nm, a pulse repetition rate of 500 kHz and a pulse length of 250 fs. The maximum average power of the laser is 7.85 W, giving a deliverable pulse energy of 15.7 µJ. Within the focal plane, the laser beam is steered at a scanning speed of 100 mm/s with a spot size of 15.0 µm and a pulse fluence of 2.22 J/cm$^2$.

A cross-hatching strategy was implemented as illustrated in Figure 20. The laser spot is scanned in parallel lines within a circular shape, in perpendicular directions. The distance between two consecutive lines is defined as the hatch pitch. Once the laser has scanned one circular grid, the focal point is lowered (with a vertical distance defined as the layer pitch) and the laser scans the same grid. This process is repeated multiple times and defines the number of layers. The selected laser parameters in this work are based on a previous exploratory research [209]. A hatch pitch of 15 µm, a layer pitch of 2 µm, a base diameter of 300 µm and a number of layers varying between 150, 300, 450 and 600 were selected. The number of layers is varied: 150, 300, 450 and 600 layers. For each

set of parameters, holes were created in an array of 3 x 3 with a distance of 1 mm between the centre points.

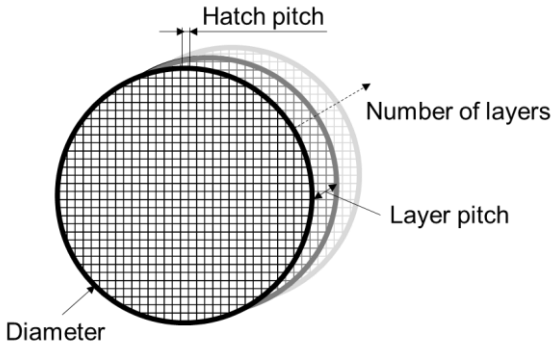


Figure 20: Illustration of the cross-hatching laser strategy.

### 3.3.4 Replication of microneedles through injection moulding

Injection moulding was done on an Engel ES 200/35 HL hydraulic injection moulding machine. The mould temperature is controlled by a Wittmann Tempro-controller. The injection moulded specimen is a 50 mm x 60 mm x 1.5 mm flat plate. Injection moulding parameters were defined to achieve a high replication fidelity. The injection temperature was set to 240°C. The mould temperature was set to 80°C, the maximum recommended ejection temperature of polypropylene [182]. The volumetric injection rate was set to a high value of 128 $cm^3/s$ to reduce the viscosity during injection. The holding pressure was set to 47.5 MPa, as it prevented flash while also ensuring that there were no demoulding problems due to internal stress within the part.

### 3.3.5 Topography characterization

Micro-computed tomography (μ-CT) was used to characterize the geometry of the ablated needle cavities. The μ-CT system (Phoenix Nanotom) is equipped with a nanofocus X-ray tube. A diamond-tungsten target was chosen for the high X-ray absorbing steel samples. The mould insert was cut down in cubic samples with an edge length of 3 mm. For each scan, 2400 X-ray 2D projection images were obtained. Acquisition parameters were fixed for all samples as follows: voltage = 100 kV, current = 158 μA, and voxel size = 3.75 μm. A 0.1 mm copper and 0.1 mm aluminium filter were used during scanning, as they reduced beam hardening artifacts and improved the quality of the scans. Reconstruction of the acquired 2D projections into 3D volumes was performed using GE Phoenix datos|x REC software. Reconstructed XY datasets were exported for further analysis and visualization within Fiji ImageJ.

The geometries of the replicated thermoplastic microneedles were assessed using a digital microscope (Keyence VH-S30) with a maximum magnification of 200X.

## 3.4 Results and Discussion

The analysis of the reconstructed μCT XY datasets of the laser ablated tool steel with different layers (Figure 21) clearly shows cone-shaped micro holes with very sharp tip radii. It can be observed that the hole depth is increased when a higher number of layers is used, due to the increase in accumulated fluence. The dimension of the acquired tip radii is close to the voxel size of the CT measurement of 3.75 μm. This dimension is much lower than micro holes with tip radii of 32 μm up to 80 μm, obtained respectively in [205] and [69]. The obtained cone-shape is expected to be a result of the plasma shielding effect [210]. During the ablation process, vapour material is partially ejected from the microcavity, but a part of it remains near the surface, held by surface tension forces, and forms a recast layer after each pulse [211]. Additionally, the vaporised material forms plasma during the duration of each pulse. This plasma absorbs and defocuses the laser beam, creating a protective shield called "plasma shielding effect". The deeper the ablated micro hole, the more difficult the vaporised material can escape the hole, resulting in an expanding plasma which in turn increases the protective shield [212]. Therefore, using the proposed laser strategy, it is possible to create cone-shaped micro holes with variable hole depths.

The laser ablated mould insert was used in an injection moulding process to replicate the micro holes. The replicated polymer microneedles (Figure 22) show a similar cone-shape as the corresponding micro holes. However, by comparing the depth of the micro holes to the length of the polymer microneedles, we observed that the micro holes were not completely replicated in the injection moulding process. As a result of the incomplete filling, the tip radii of the microneedles (< 20 μm) are larger than the very small tip radii of the micro holes. To give an estimation of volumetric filling, 2D profiles of both the micro holes and microneedles were imported in a CAD programme. By assuming that the profiles are axisymmetric, corresponding volumes could be compared. The percentages of volumetric filling for the micro holes created with laser parameters for 150, 300, 450 and 600 layers are respectively 97 %, 94 %, 88 % and 85 %. Besides, a higher percentage of volumetric filling corresponds to a smaller tip radius. This radius is, as already indicated, the most important feature of the microneedle. The smaller the tip radius, the lower the force required to penetrate the human skin. Thus, improving the replication process to further decrease the tip radius of the polymer microneedles is beneficial. Implementing a variothermal heating strategy is a possible way to achieve this [184]. The temperature of the mould is then no longer kept constant, but is varied between a high value during the filling stage and a lower value during the cooling stage. Therefore, the formation of a frozen layer can be delayed, which in turn leads to a better and more uniform filling of micro features [134].

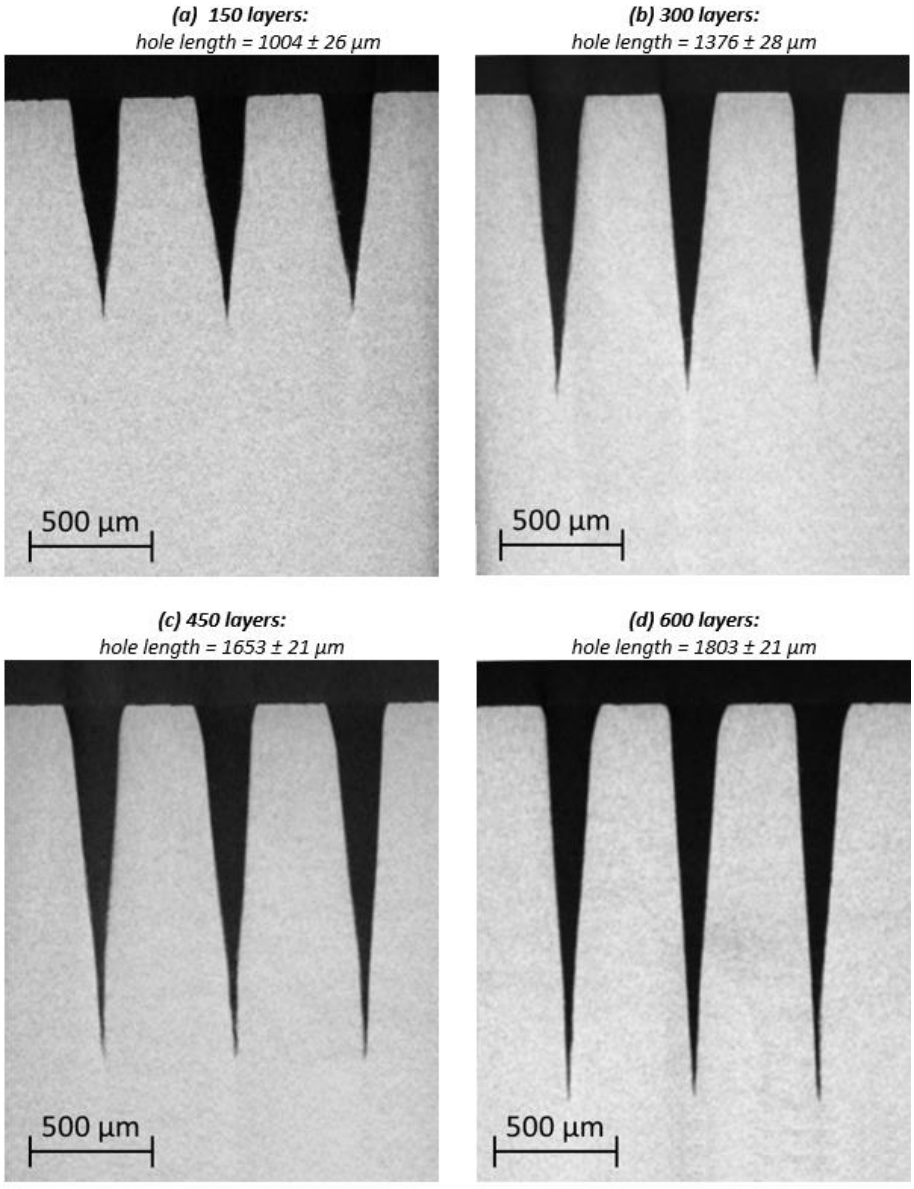


Figure 21: Reconstructed µCT XY datasets for the four different laser parameter settings: (a) 150 layers; (b) 300 layers; (c) 450 layers and (d) 600 layers.

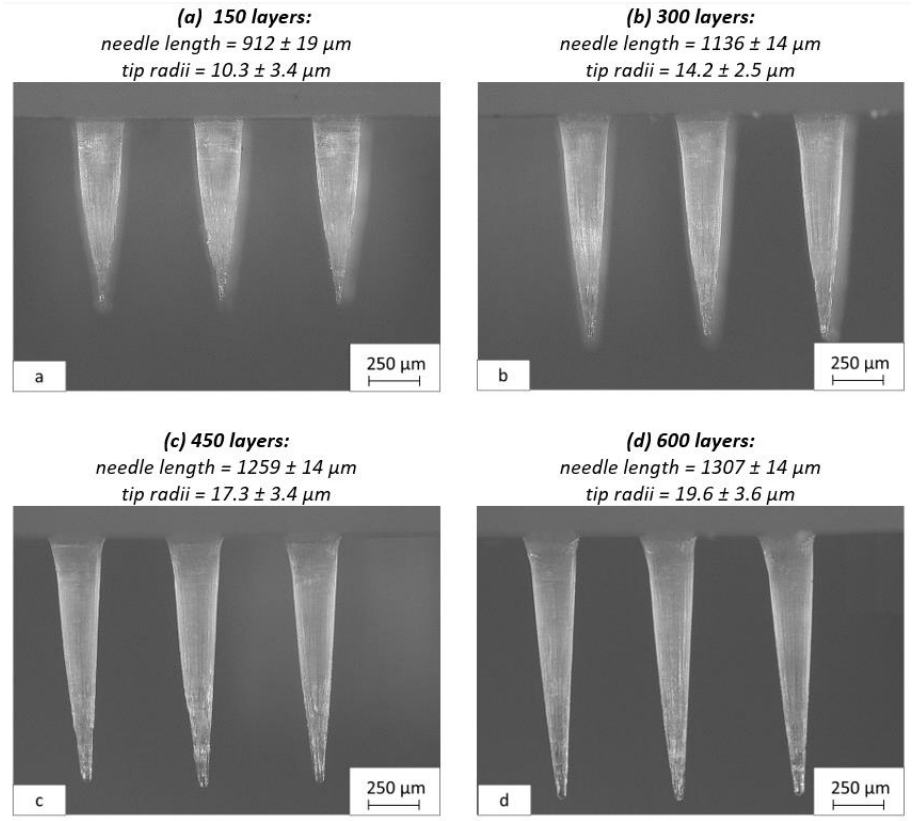


Figure 22: Microscopic images of the polymer microneedles, achieved by replicating the laser ablated micro holes with four different laser settings: (a) 150 layers; (b) 300 layers; (c) 450 layers and (d) 600 layers.

## 3.5 Conclusions

In this study, a method to produce solid polymer microneedles using laser ablated moulds in an injection moulding process was successfully demonstrated. Cone-shaped micro holes with very small tip radii were ablated in a tool steel insert. By changing laser process parameters, the height of the micro holes could be varied. After replicating the micro-holes, thermoplastic solid microneedles were achieved with tip radii < 20 µm. The replication fidelity was volumetrically assessed and the deeper the micro holes, the lower the replication (ranging from 97% - 85%).

The major advantages of the proposed laser ablation technique to create cone-shaped micro holes are the very sharp tip radii, the fast and flexible manufacturing and the low cost. Thus, the investigated process chain is proven to be a suitable mass manufacturing method to produce solid polymer microneedles with small tip-radii.

# Chapter 4 Controlling the geometry of laser ablated microneedle cavities in different mould materials and assessing the replication fidelity within polymer injection moulding

Evens T., Malek O., Castagne S., Seveno D. and Van Bael A. Controlling the geometry of laser ablated microneedle cavities in different mould materials and assessing the replication fidelity within polymer injection moulding. Journal Of Manufacturing Processes, 62: 535-545, 2021. Some parts of the original publication are left out or modified to avoid redundancy.

## 4.1 Abstract

Microneedle arrays are minimally invasive devices which enable self-administration of drugs in a straightforward and efficient way. Recently, a low-cost mass production method to produce solid polymer microneedles using laser ablated moulds in an injection moulding process has been developed. In this context, it is key to understand how the geometry of the microneedle cavities can be changed and what parameters affect the replication fidelity during injection moulding. In this study, two laser scanning parameters, being the programmed base diameter and the number of layers were varied in four levels and their effects on the geometry of the microneedle cavities were evaluated in tool steel, copper alloy, and aluminium alloy inserts. Afterwards, the microneedle cavities were replicated in polypropylene and polycarbonate using injection moulding. The study showed how the depth and base diameter of the microneedle cavity can be changed by varying laser scanning parameters. Moreover, the moulds in the three materials exhibited different microneedle cavity shapes and dimensions, due to differences in material properties. As to the injection moulding process, strong linear relationships were found between the aspect ratio of the microneedle cavities and the replicated thermoplastic microneedles, where a higher aspect ratio resulted in a lower replication. The replication fidelity for the polypropylene microneedles was in all cases higher compared to the polycarbonate needles. Between the three mould materials, a comparable replication fidelity was found for tool steel and copper alloy and a lower replication for the aluminium alloy, due to differences in thermal and wetting properties.

## 4.2 Introduction

Traditional needles, known as hypodermic needles, are used in clinical practice to sample blood or to deliver vaccines or medication across the skin into the blood stream [204]. Although such needles are very frequently used, they are known to induce discomfort to the patient, like pain or bruising and carry the risk of infections. Besides, the use of these systems requires trained medical staff. A possible alternative to the hypodermic needles are microneedles. These are microscale invasive devices, usually arranged in an array and designed to by-pass the human stratum corneum skin barrier [5], [88]. The length of the needles ranges from 25 μm – 2000 μm and when penetrated in the skin, they can deliver vaccines, antibodies or other drugs to the human body through the transdermal route [3]. These systems offer various advantages such as (i) a pain free drug delivery, (ii) self-administration, (iii) lower storage, distribution and disposal cost due to the small volume, and (iv) direct administration of vaccines to key immune cells [1], [9], [12].

The first concept using microneedles for vaccine delivery was conceived by Alza corporation, as described in a 1976 patent [1]. Making these devices was not possible until the 1990s, when the technology needed to fabricate micrometre sized structures became available. Since then, many researches both from academia and industry have demonstrated the applicability of microneedle devices, from the development phase up to clinical experiments. The investigated methods for manufacturing these microscale devices covers a wide range of techniques such as, chemical etching [213], polymer replication techniques [73], [196], [214], additive manufacturing [95], surface micromachining [37], and photolithography [215]. According to World Health Organization guidelines, cost-effective, portable, disposable medical devices are needed in order to enhance the health-related quality of life worldwide [2]. Yet, for most of the current manufacturing methods the low cost and high volumes still pose a great challenge [7]. Polymer injection moulding has a huge potential, as this manufacturing process has already proven to be very suitable to manufacture polymer medical devices, due to its high accuracy, potential for full-automation, short cycle times, and low cost. Moreover, polymers can offer excellent biocompatibility, biodegradability, low toxicity, and good mechanical properties at a low material cost [133].

In a recent work [216], we demonstrated a novel methodology to mass produce solid polymer microneedles using laser ablated moulds in an injection moulding process. We were able to create solid cone-shaped microneedles with low tip radii < 20 μm. These needles can be used for drug delivery using two techniques. With the first technique, called 'poke with patch' approach (Figure 23 a), the solid microneedles are used to pierce the skin, creating transient aqueous micro-pores through which a medical solution can passively diffuse. In the second approach, the solid needles are coated with a drug formulation (Figure 23 b). After insertion, the coated drug formulation will be dissolved and deposited in the skin.

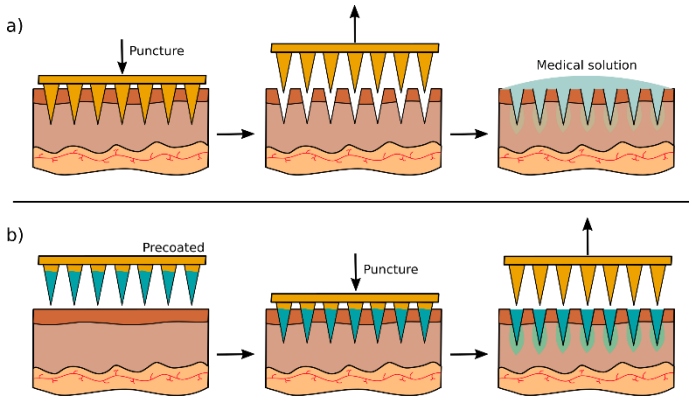


Figure 23: A schematic representation of the different types of microneedles. (a) Solid microneedles (b) Coated microneedles. Inspired by [7].

The size of the needles depends on the specific medical application, while the design should allow for the needles to penetrate into the skin or any other biological tissue without breaking or bending. It is therefore important to know how to fine-tune the parameters in the manufacturing process to optimize the geometry of the microneedles. The manufacturing method combines laser ablation and injection moulding and these two processes will both affect the geometry of the needle.

In this study, we investigate the influence of two laser scanning parameters, being the programmed base diameter and the number of layers, on the geometry of microneedle cavities within a femtosecond laser ablation process. This evaluation is done for the three most common mould materials used in injection moulding, being tool steel, copper alloy, and aluminium alloy [217]. In addition, the replication fidelity of the laser induced cavities is evaluated using polymer injection moulding.

## 4.3 Materials and Methods

### 4.3.1 Thermoplastic and mould materials

Two thermoplastic materials were used in this study: polypropylene (PP, 578N, manufactured by SABIC) and polycarbonate (PC, Lexan™ HPX8REU, manufactured by SABIC). The polypropylene material is a general purpose semi-crystalline homopolymer, which is easy to process and has a low cost. The polycarbonate material is a biocompatible amorphous grade, suitable for medical devices and pharmaceutical applications. Both materials have a high flowability as indicated by their very high melt volume rate (MVR) and are thus appropriate for filling small micro features. Table 1 reports the main characteristics for both thermoplastics.

Table 1: Main properties of the thermoplastics based on material datasheets and Autodesk Moldflow® 2019 material database.

| | PP | PC |
|---|---|---|
| **Density [kg/m³]** | 928.9 | 1188.9 |
| **Melt flow rate [g/10 min]** | 24<br>[230 °C/2.16 kg] | 35<br>[300 °C/1.2 kg] |

| | | |
|---|---|---|
| **Tensile Modulus [MPa]** | 2100 | 2360 |
| **Thermal conductivity [W/m °C]** | 0.171 | 0.267 |
| **Specific heat [J/g °C]** | 2.94 | 1.86 |
| **No-flow temperature [°C]** | 109 | 147 |

Three materials were selected as mould inserts: a low corrosion tool steel "Stavax" (grade 1.2083 - AISI 420), a high-strength aluminium zinc alloy (grade 3.4365), and a copper nickel alloy (grade AMPCOLOY® 940). Tool steel is most often used because of its high wear resistance, leading to a long lifetime. The aluminium material is regularly used for low production series and prototype moulds, due to its low cost and good machinability. The copper alloy exhibits a very high thermal conductivity which improves the cooling and can in turn, decrease the injection moulding cycle time [218]. Besides, this material currently acts as an excellent alternative for Beryllium copper alloys, as it avoids health risks [219]. The main properties of these three materials are listed in Table 2.

Table 2: Main properties of the different mould materials based on material datasheets and GRANTA EduPack.

| | Tool steel | Copper alloy | Aluminium alloy |
|---|---|---|---|
| **Density [kg/m³]** | 7700 | 8710 | 2800 |
| **Thermal conductivity at 100°C [W/m °C]** | 23.5 | 226 | 145 |
| **Specific heat capacity at 100°C [J/g °C]** | 0.48 | 0.38 | 0.95 |
| **Thermal diffusivity [mm²/s]** | 6.51 | 68.36 | 60.40 |

### 4.3.2 Laser machining experiments

A micromachining system (Lasea LS5) with a femtosecond laser source (Satsuma HP, Amplitude Systemes) is employed to laser ablate the mould inserts with dimensions 70 mm x 60 mm x 4.4 mm. The laser source emits a beam with a pulse length of 250 fs, a wavelength of 1030 nm and a pulse repetition rate of 500 kHz. The laser has a power of 10W with a loss factor of 0.785, giving a deliverable pulse energy of 15.7 µJ. A galvanometer steers the laser beam within the focal plane, with a spot size diameter of 15.0 µm and a pulse fluence of 8.88 J/cm². The energy distribution of the beam is Gaussian shaped with a laser beam quality value of $M^2 < 1.2$. Small dust particles which are formed from ablating the metal surface are extracted by a vacuum collect unit. After the laser texturing operation, the inserts are ultra-sonicated in an ethanol bath for 15 min to remove debris from the micro-holes.

A cross-hatching strategy was used as presented in a previous study [216]. The laser spot scans a circular region and follows parallel lines in two perpendicular directions. The distance between two consecutive lines is defined as the hatch pitch. Once the laser has scanned one circular grid, the focal point is lowered (with a vertical distance defined as the layer pitch) and the laser scans again the same area. This process is repeated multiple times for a prescribed number of layers. A design of experiments was used, in which the number of layers and the base diameter was varied as illustrated in Figure 24. The base diameter was varied from 100 µm to 400 µm in steps of 100 µm and the number of layers was varied from 150 to 600 in steps of 150. The hatch pitch and layer pitch were fixed at 15 µm and 2 µm, respectively. For each set of parameters, microcavities were created in

an array of 3 x 3 with a distance between the centre points equal to two times its base diameter.

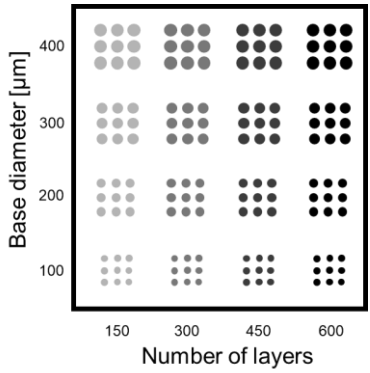


Figure 24: Illustration of the design of laser experiments, in which the number of layers and the base diameter was varied.

### 4.3.3 Replication through injection moulding

The injection moulded part selected for this study is a 50 mm x 60 mm x 1.5 mm flat plate, as shown in Figure 25. The polymer is injected through a hot runner which is located 3 mm from the edge of the product, indicated by a white dot. The array of micro needles is 12 mm x 12 mm in size, located 10 mm from the edge of the plate.

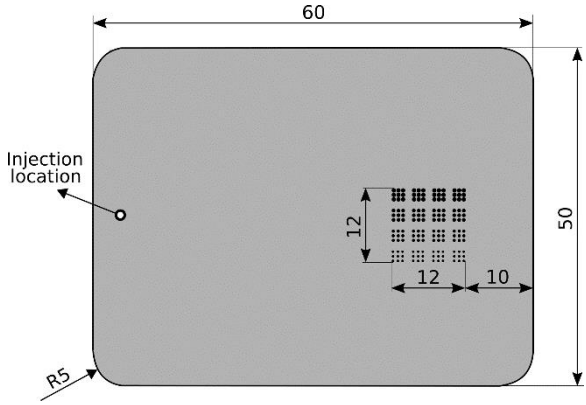


Figure 25: Illustration of the flat plate with all dimensions in mm, the thickness is 1.5 mm.

The injection moulding machine used for this study is an Engel ES 200/35 HL hydraulic injection moulding machine with a maximum clamping force of 350 kN and a 25 mm horizontal screw with an L/D ratio of 24.8. The temperature of the mould is controlled by a Wittmann Tempro D controller. Injection moulding parameters are given in Table 3 and were defined to achieve a high replication fidelity. The injection temperature was set to the recommended upper limit of the material supplier. The mould temperature was set to a high value to delay the formation of the frozen layer during injection. The volumetric injection rate was set to a high value, to increase shear rates and

thus reduce the melt viscosity during injection. The implemented holding pressure was set to a value just below the occurrence of flash, while also ensuring that there were no demoulding problems due to internal stress within the part.

Table 3: Injection moulding process parameters for the two thermoplastic materials.

| | PP | PC |
|---|---|---|
| **Injection temperature [°C]** | 240 | 315 |
| **Volumetric injection rate [cm³/s]** | 149 | 149 |
| **Holding pressure [MPa]** | 57.5 | 74.9 |
| **Mould temperature [°C]** | 80 | 115 |

The stationary side of the injection mould was equipped with a temperature sensor (Priamus, 4008B) and a piezoelectric pressure sensor (Priamus, 6001B), which allows for precise process control and online measurement of the apparent viscosity. This viscosity measurement is a built-in module in the Priamus FILLCONTROL and is, as described by [220], based on the following Equation (1):

$$\eta = \frac{\Delta P \cdot \Delta t \cdot H^2}{12 \cdot S^2} \quad (1)$$

where $\eta$ is the apparent viscosity, $\Delta P$ the pressure increase between the signal from the pressure and temperature sensor, $\Delta t$ the time required for the polymer melt to flow from the pressure sensor to the temperature sensor, $H$ the height of the mould cavity, and $S$ the distance between the pressure and temperature sensor. The online apparent viscosity is measured for 10 different volumetric injection rates, ranging from 15 cm³/s to 147 cm³/s.

### 4.3.4 Topography characterization

The geometries of the ablated microneedle cavities were characterized using a Phoenix Nanotom micro-computed tomography (μ-CT) system. The device is equipped with a high-power nanofocus X-ray tube and a diamond-tungsten target was chosen for the high X-ray absorbing metal samples. A high-power mode was used to allow focal spot and voxel sizes in the micrometre range. A set of mould inserts, identical to those used in the injection moulding process, were cut down in cubic samples with an edge length of approximately 3 mm, using a metallographic precision saw. The samples were mounted on a sample holder and fixed on a high-accuracy computer controlled rotation stage. For each scan, 2400 X-ray 2D projection images were obtained from incremental rotation of the scanned samples over 360°. Acquisition parameters were fixed for all samples as follows: voltage = 100 kV, current = 158 μA, voxel size = 3.75 μm, and a 0.1 mm copper and 0.1 mm aluminium filter were used during scanning. Reconstruction of the acquired 2D projections into 3D volumes was performed using GE Phoenix datos|x REC software. Reconstructed XY datasets (slices) were exported from the software in 16-bit tiff format for further analysis and visualization within Fiji ImageJ. Before conducting measurements, the Nanotom instrument was calibrated using a calibration rod (Goekeler Messtechnik, VTX18CE000-022) with an uncertainty of 1.0 μm. For each set of laser parameters, one cubic sample containing nine micro holes was measured. The

average length and diameter of these nine holes along with a 95 % confidence interval, using the Student's t distribution was reported in the plotted results.

The geometries of the replicated thermoplastic microneedles were assessed using a digital microscope (Keyence VH-S30) with a maximum magnification of 200X. The system is connected to a VHX-500F monitor with built-in measuring software. The microscope was calibrated using a stage micrometre (Olympus Tokyo, OBMM 1/100) which has an uncertainty of 0.5 μm. Nine samples were injection moulded and on each sample one microneedle was measured for each set of micro holes. The average of these nine measurements along with a 95 % confidence interval, using the Student's t distribution was reported in the plotted results.

### 4.3.5 Contact angle measurements of polymer melts

A Dataphysics OCA 15 plus, equipped with a Dataphysics TEC 350 temperature control unit was used to measure contact angles of molten thermoplastic materials on the different mould surfaces. The equipment utilizes electric heating elements which make it possible to heat up the measurement chamber from 40 °C to 350 °C. The temperature within the chamber is measured and controlled by a thermocouple close to the polymer melt. Square samples of 15 mm x 15 mm were cut out of the different mould materials and were all grinded and polished to a roughness of Ra < 0.1 μm. The measurement starts by placing a polished mould substrate in the chamber for 8 min in order to heat it up evenly. A thermoplastic granule cut in half is then placed on the mould substrate. In order to minimize the initial surface contact, the granule is placed on the substrate with the spherical side facing down, as described by Bex et al. [221]. The measurement was started when the contact angle of the thermoplastic reached a value of 135 °C, as at this angle the granulates formed a drop-like shape for each thermoplastic. Thereafter, the contact angles are registered every 30 s for a total of 20 min. The measurements were carried out under a nitrogen environment to prevent the oxidative degradation of the polymer melt and the oxidation of the metal substrates. The testing temperature of the chamber was set to the processing temperature of the corresponding thermoplastic. For each thermoplastic material, this procedure is repeated three times. The average of these three measurements, along with the 95 % confidence interval Student's t distribution are plotted versus time.

## 4.4 Results and Discussion

### 4.4.1 Diameter of the microcavities

The effects of the number of layers in regards to the obtained cavity diameters at the surface of the mould inserts were evaluated for the three mould materials as depicted in Figure 26. First of all, we can observe small error-bars, indicating a good repeatability. In fact, the highest relative standard deviation for tool steel, copper alloy, and aluminium corresponds to 3.8 %, 3.7 % and 3.4 %, respectively. This indicates a high repeatability of the laser process, in relation to the ablated base diameter. Secondly, the cavity diameter at the mould surface created with 150 layers are in all cases lower than the programmed diameters. This interesting result can be allocated to negative dynamic effects of the optical beam deflector system. This optical beam deflector system is a key component in laser micro machining platforms that consists of reflective mirrors mounted on highly

precise galvanometer motors [222]. The system realises the computer controlled movements of the laser beam along a predefined machining path. Within these machining paths, there will be regions of acceleration and deceleration at the start and end of each machining vector, which will induce a discrepancy between the programmed and the actual beam movements [223]. State-of-the-art beam deflection systems try to compensate these negative dynamic effects by introducing scanner and laser delays which give more time to the mirror galvanometers to complete their programmed movements and adjust the triggering of the laser-on and laser-off delays, respectively [224]. These delays should be optimised for different processing speeds and different machining geometry paths [225]. It can be assumed that this optimisation was not seamless, which resulted in smaller hole diameters at the surface of the mould, compared to the programmed circles. Thirdly, it can be observed that the cavity diameter at the mould surface increases with higher numbers of layers, for all of the investigated mould materials. As the amount of layers increases, the vertical position the focal spot moves deeper inside the material. Therefore, the Gaussian shaped laser beam will start to intersect with the edge of the already created micro-hole. If the power density in this intersecting region of the Gaussian beam is higher than the ablation threshold, additional material will be removed. Thus, as a result of a higher numbers of layers, the diameter of the micro-hole at the surface of the mould insert will increase. At last, it can be observed that there is a difference in the hole dimensions between the investigated materials. This discrepancy will be further discussed in section 4.4.2.

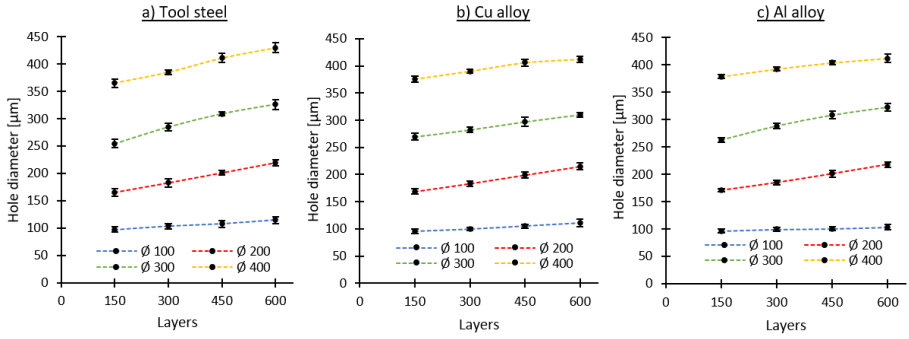


Figure 26: Microcavity diameter at the surface of the mould insert in function of varying number of layers for different programmed diameters for following materials: (a) tool steel, (b) copper alloy, and (c) aluminium alloy. The error bars represent the 95 % confidence interval.

### 4.4.2 Formation of the cone-shaped microcavities

The effects of the laser parameters in regards to the microcavities were investigated for the three different mould materials. Here, the number of layers and the programmed base diameter were both varied in four different levels and the microcavities produced with each of these settings were analysed by the cross sectional views obtained from the µ-CT measurements, as shown in Figure 27. Cone-shaped micro-holes with very low tip radii are observed for all sets of laser parameters and mould materials. The formation of the cone-shape is expected to be a result of two phenomena: (i) a plasma shielding effect and (ii) laser reflectance on a micro-hole with a steep sidewall. This first phenomenon occurs during laser ablation processes with high repetition rates (> 5 kHz) [226]. During such processes, solid material is ablated into vaporised material. This vapour is partially

ejected from the microcavity, yet the other part remains near the surface, held by surface energies. When the laser repetition rate is low (< 5 kHz), the time interval between each pulse is large enough for the vapour to escape the microcavity or to ensure the formation of a recast layer [211]. At higher repetition rates > 5 kHz, the time interval between pulses is reduced to < 200 μs, which causes an interaction between the vaporised material and the incoming pulse, forming a plasma. This plasma absorbs and defocuses the laser beam, creating a protective shield called "plasma shielding effect" [210]. The deeper the ablated micro-hole, the more difficult the vaporised material can escape the hole, which in turn increases the protective shield [212]. The second phenomenon is laser reflectance on a micro-hole with a steep sidewall. When ablating such micro-holes, the steep sidewalls will reflect most of the laser light rather than absorb it. Therefore the ablation efficiency near the edge of the cavity is reduced, causing the diameter to become smaller as the micro-hole is created [227]. In addition, the reflected laser light will partially be redirected to the bottom of the hole, possibly contributing to a deeper and sharper cavity. Thus, due to both phenomena, cone-shaped micro-holes are created using the presented laser strategy.

Although cone-shaped micro-holes are observed for all of the investigated mould materials, the cavity shape and dimensions differ between the materials, yet the same machining strategy and laser parameters were used. This is due to differences in material properties, such as absorptivity, heat capacity, thermal conductivity, and electron–phonon coupling constant [228]. The thermal conductivity has an influence on the re-solidification of the material melt. A low thermal conductivity leads to a high re-solidification time [229]. Hence, the laser pulses will irradiate on a melt surface which reacts like a liquid dielectric [230], [231]. This fluid state requires much higher pulse energy to be ablated, thus the lower thermal conductivity results in a decrease in ablation efficiency. This theory was also confirmed by Cheng et al. [226] who found that the solidification of the melt layer for Al and Cu, both metals with a high thermal conductivity, was very fast, which improved the ablation efficiency. The electron-phonon interaction is another material parameter that influences the ablation rate. This interaction occurs when a laser pulse strikes a metal surface causing electrons in the material to excite through photon absorption. The excited electrons will equilibrate with the surrounding lattice though electron-phonon coupling. The time required for electron-phonon equilibration is proportional to the electron-phonon coupling constant [12]. A high electron-phonon coupling constant results in rapid energy transfer between the electrons and the solid lattice, which in turn leads to a lower electron diffusion depth [13]. Consequently, a high electron-phonon coupling constant causes a large fraction of the laser energy to be retained close to the incident surface, leading to a rapid rise in surface temperature which enhances the ablation efficiency. Researchers determined the electron-phonon coupling constants for 316L stainless steel [232], pure aluminium [233], and pure copper [234]–[236] through pump-probe experiments and the corresponding values are presented in Table 4. Although these materials are not identical to the tool steel, aluminium alloy, and copper alloy used in this study, we assume the coupling constants to be within the same order of magnitude as the corresponding material. Thus, using these values, we have an indication of the thermal conductivity (Table 4) and the electron-phonon coupling constants (Table 2) for our materials, which we will link to the obtained micro-holes through femtosecond laser ablation. The depth of the micro-holes produced in the aluminium alloy are significantly lower compared to the micro-holes made in tool steel and copper. This is due to its low electron-phonon coupling constant relative to the high coupling constant of the tool steel. Besides, the thermal conductivity is lower compared to the copper alloy. The micro-holes for the tool steel and copper

alloy are quite similar, which can be allocated to the high electron-phonon coupling constant and high thermal conductivity respectively. These findings confirm that surface ablation via femtosecond laser irradiation is more favourable on metals with a high electron–phonon coupling constant and a high thermal conductivity.

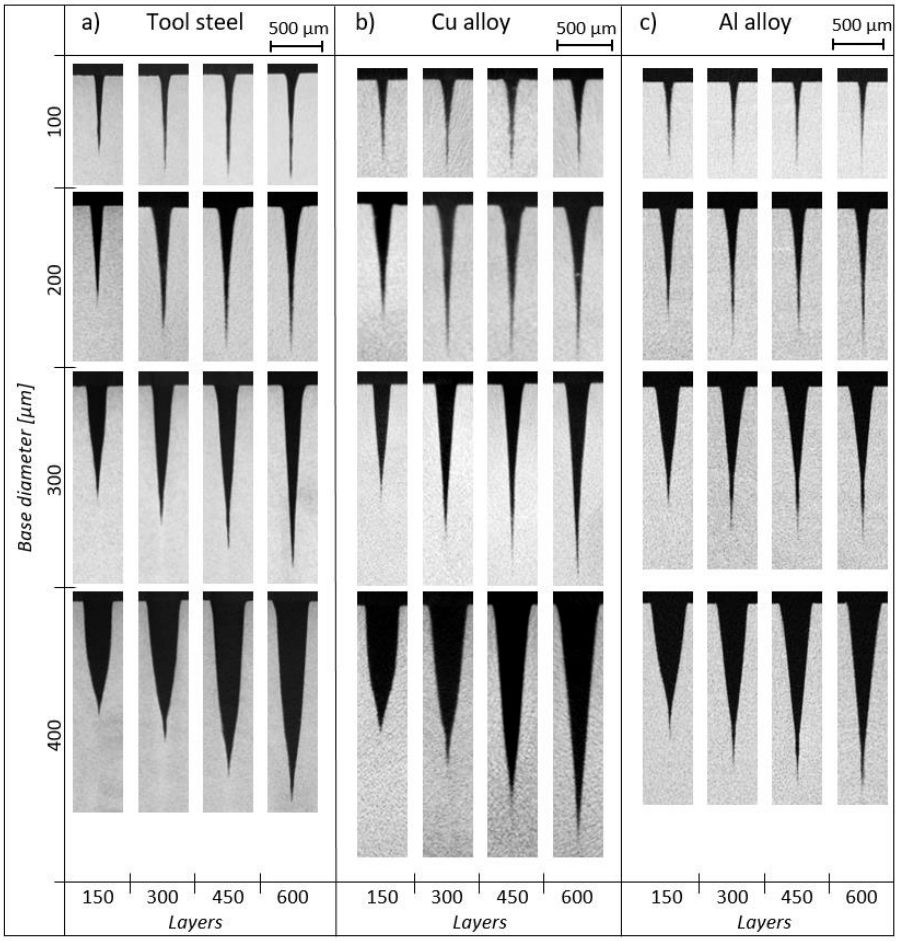


Figure 27: Cross sectional views obtained from the µ-CT measurements of the micro-holes created with the design of laser experiments for following materials: (a) tool steel, (b) copper alloy, and (c) aluminium alloy. A scale bar is included for each of the materials.

Table 4: Electron-phonon coupling constants for stainless steel 316L, aluminium and copper.

| | PP Electron-phonon coupling constant (1017 W m-3 K-1) |
|---|---|
| Stainless steel 316L | 54 [232] |
| Aluminium | 2.45 [233] |
| Copper | 1 [234] ; 0.45 [235], [236] |

### 4.4.3 Depth of the microcavities

The produced microcavities were analysed by measuring the hole depth in the cross sectional views obtained from the μ-CT measurements. The hole depth for the different programmed hole diameters in function of the number of layers is shown in Figure 28.

First of all, all of the error bars are similar. The average confidence interval is approximately 27 μm, indicating a very high repeatability of the ablation process. Consequently, the smaller microcavities have a higher relative error compared to the large cavities. This could be due to measurement errors, as in the needle tip area, the size approaches the measured voxel size of 3.75 μm.

Secondly, for the holes produced with a programmed diameter of Ø400 μm and Ø300 μm it can be seen that with an increase in the number of layers, the depth of the micro holes increases. This can easily be explained by an increase of accumulated fluence, as the number of layers is increased. However, for the holes produced with a programmed diameter of Ø200 μm and Ø100 μm, the increase in depth decreases as the number of layers is increased. In other words, there is a saturation in the depth after a certain number of layers. The smaller the programmed hole diameter, the faster the saturation point is reached. For the holes with a larger diameter, it can be assumed that there will also be a saturation point. However, this saturation was not yet reached within the investigated number of layers. The occurrence of saturation is already known for laser percussion drilling (repeatedly pulsing focused laser energy on one spot) [159], [227]. Within our laser strategy the saturation could be explained as follows: as an ablated hole gets deeper, the diameter of the hole decreases and the walls become steeper, therefore, the reflection and surface area of the wall increase, causing a drop in the absorbed energy density [237]. Consequently, less energy will be absorbed by the bottom of the cavity, creating a saturation depth after a certain number of layers.

Thirdly, when looking at Figure 28, a relation can be observed between the depth of the cavities and the programmed base diameters. As the programmed base diameter increases for a constant number of layers, the microcavities become deeper. As already explained in section 4.4.2, the diameters of the micro holes increase with a higher number of layers. Moreover, we known that the micro holes have conical shapes in which the diameter keeps decreasing throughout the depth of the hole until the diameter becomes very small and forms the tip radius of the hole. When starting with a large base diameter, the amount of layers required to reach this very small tip radius will be larger, compared to a hole with a small base diameter. Thus, deeper holes can be created when starting with a larger base diameter. Moreover, when starting with a small base diameter, the fraction of laser energy that will be reflected near the edge of the hole will be relatively high compared to the total emitted laser energy. Thus, only a part of the laser energy will be utilised for the ablation process, resulting in holes with a lower depth. Holes with a large base diameter will be able to utilise a larger fraction of the emitted laser energy for the ablation process, resulting in a higher accumulated fluence and thus deeper microcavities.

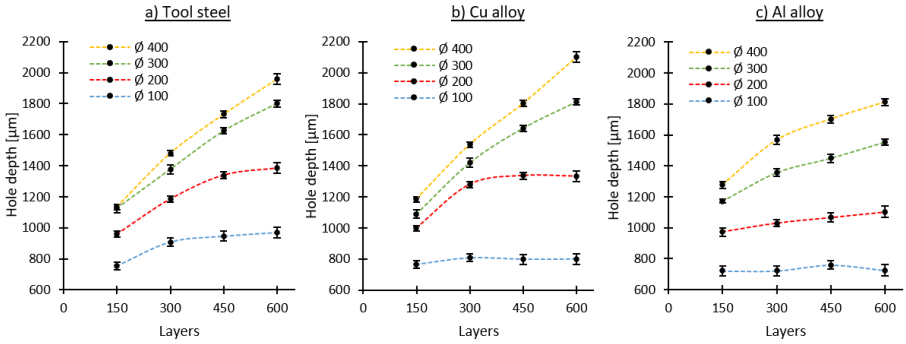


Figure 28: Hole depth in function of the programmed hole diameter for varying number of layers for following materials: (a) tool steel, (b) copper alloy, and (c) aluminium alloy. The error bars represent the 95 % confidence interval.

### 4.4.4 Replication through polymer injection moulding

The mould inserts with laser ablated microneedle cavities are used in the injection moulding process to create polymer microneedles, both in PP and PC. A microscopic image of a PP plate replicated with an aluminium insert is shown in Figure 29 (a), which illustrates the 16 microneedle arrays with different dimensions. Figure 29 (b) shows a representation of a polypropylene microneedle fitted into the corresponding aluminium microneedle cavity created with a diameter of 400 µm and 300 layers. The tip radius of the microneedle corresponds to the hole radius at the depth of the microneedle.

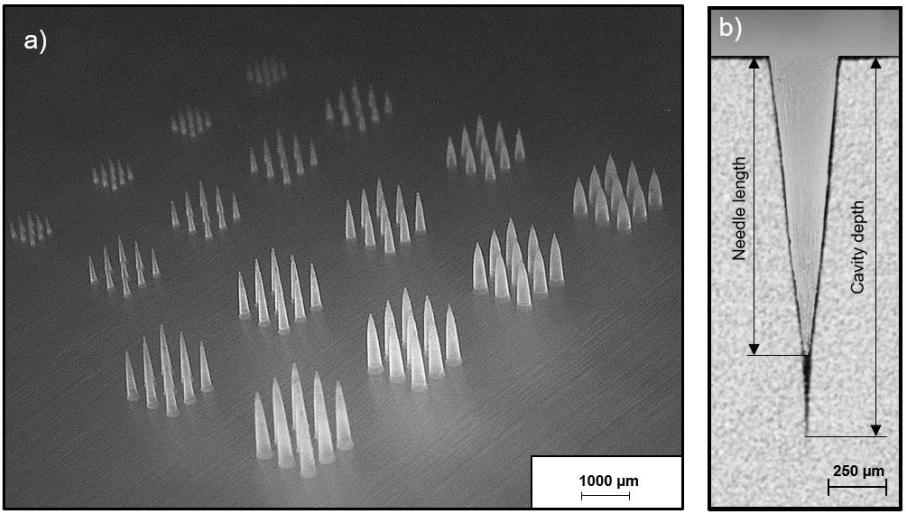


Figure 29: (a) Microscopic image of a polypropylene plate replicated with an aluminium mould insert. (b) Representation of a polypropylene microneedle fitted in the corresponding aluminium microneedle cavity created with a diameter of 400 µm and 300 layers.

During the injection moulding, the polymer melt fills the cavity and is then packed and cooled inside the microneedle mould cavities. This results in a change in specific volume of the polymer melt during a moulding cycle. At the end of the cooling stage, the specific volume has decreased, which corresponds to a volumetric shrinkage of the polymer. The volumetric shrinkage can be determined using the compressibility behaviour of the polymer. This can be modelled by the double domain Tait equations, which specify the specific volume as a function of melt pressure and temperature [217]. The pressure-specific volume-temperature (pvT) plots and corresponding double domain Tait coefficients of the selected polymers are shown in Figure 30. A reasonably accurate estimate of the volumetric shrinkage can be calculated if the polymer, pressure and temperature at the end of the packing stage are known. We assume the pressure at the end of the packing stage to be equal to the holding pressure and the temperature to be equal to the no-flow temperature. First, the specific volume ($v$) is modelled as a function of pressure and temperature as (Equation (2)):

$$v(T,P) = v_0 \cdot \left[1 - 0.0894 \cdot \ln\left(1 + \frac{P}{\beta}\right)\right] + v_T \tag{2}$$

where $v_0$ is the reference specific volume, P the pressure, $\beta$ the compressibility and $v_T$ represents the additional specific volume associated with the transition of semi-crystalline polymers. The ratio of the specific volumes $r_v$ is calculated as a function of the specific volume of the plastic at the end of the packing stage $v(T_{no_flow}, P_{pack})$ and the specific volume of the plastic during end use of the moulded part $v(T_{end_use}, P_{end_use})$, by using Equation (3).

$$r_v = \frac{v(T_{no_flow}, P_{pack})}{v(T_{end_use}, P_{end_use})} \tag{3}$$

Eventually, by assuming the polymer to be isotropic, the linear shrinkage s can be calculated by using Equation (4):

$$s = 1 - \sqrt[3]{r_v} \tag{4}$$

Using the no-flow temperatures corresponding to Table 1, a room temperature of 20 °C, and holding pressures listed in Table 3, a linear shrinkage of 0.43 % and 2.22 % are found for PC and PP, respectively. These values correspond to typical values found in literature for amorphous and semi-crystalline polymers. Thus, both microneedles will undergo a shrinkage, which is approximately 5 times higher for PP compared to PC.

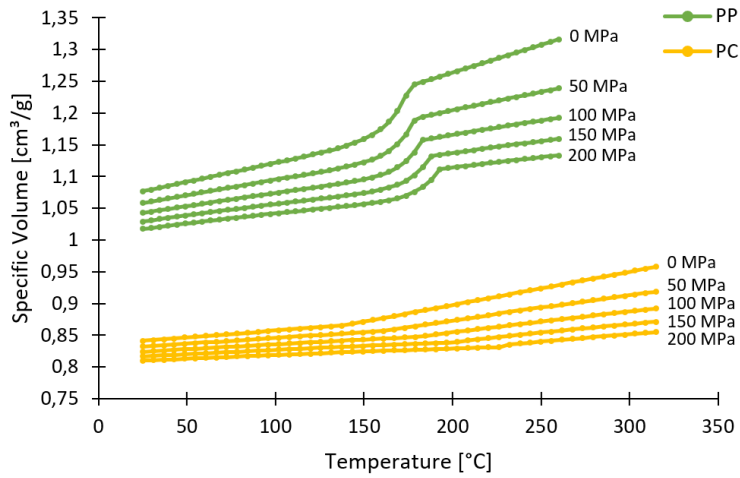


Figure 30: pvT plots of PC and PP, based on the Autodesk Moldflow® 2019 material database.

The replication of the needles is assessed by comparing the height of each needle to the depth of the corresponding microcavity. Thus, the replication of the needles is represented as a filling percentage in height, which also includes shrinkage. The replication of the PC and PP microneedles in height, relative to the aspect ratio of the holes in each of the mould materials is presented in Figure 31. The standard deviation for the replication in height is on average 15 µm for all of the replications. This shows that the injection moulding process has a very high repeatability, in terms of replication. Within each graph, a linear function ($y_{Steel}$, $y_{Cu}$, $y_{Al}$) together with its correlation coefficient (R) is expressed between the replication in height and the aspect ratio of the holes for each of the mould materials. For both thermoplastics, a clear linear relationship between the replication in height and the aspect ratio of the holes can be observed. The higher the aspect ratio of the hole, the lower the replication of the microneedle. This relationship is caused by two phenomena. First, during the initial filling stage the polymer will follow the path of least resistance. Therefore, most of the material will flow in the main flow direction through the macro-scale cavity, leaving the micro features only partially filled, also known as the hesitation effect [238]. These micro features will then only be filled after the rest of the cavity is filled and the pressure rises. Second, with an increase in aspect ratio, the surface area to volume ratio increases, which results in higher heat transfer between the molten polymer and the mould surface [239]. This results in a faster solidification of the polymer. Thus due to the hesitation effect the microcavity is only partially filled during the initial filling stage. In addition, when the macro cavity is filled and the pressure is built up, the polymer is already solidified due to the higher heat transfer. Therefore, microneedle cavities with a high aspect ratio result in a lower replication.

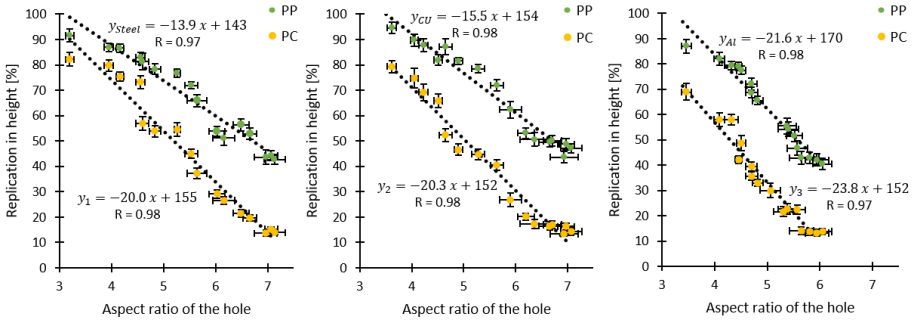


Figure 31: Replication of the PP and PC microneedles in height, relative to the aspect ratio of the holes in (a) tool steel, (b) copper alloy and (c) aluminium alloy. The vertical error bars represent the combined 95 % confidence interval of the hole depth and the replicated microneedle; the horizontal error bars represent the combined 95 % confidence interval of the hole depth and the hole diameter.

### 4.4.5 Difference in replication between the mould materials

In Figure 31 we can distinguish differences in replication between the three mould materials. The replication in height is, as already discussed, related to the aspect ratio of the corresponding micro hole.

The replication of the PP microneedles at a low aspect ratio is similar for the three mould materials. Nonetheless, there is a significant difference in the slope of the linear functions. The slope is the lowest for tool steel, closely followed by the copper alloy, and the highest for the aluminium alloy. For the PC microneedles, it can be observed that the slopes are much steeper compared to PP, meaning the replication decreases faster for an increase in aspect ratio. In addition, the PC microneedles moulded in the aluminium alloy insert have a lower replication at low aspect ratios, compared to tool steel and copper alloy. Similar to PP, the slopes of the linear functions are lower for the tool steel and the copper alloy, and higher for the aluminium alloy. This indicates that the replication of the microneedles with tool steel and copper alloy are comparable, while being much higher compared to the aluminium alloy.

The discrepancy in filling between the three materials is expected to be a result of differences in thermal and wetting properties. Lucchetta et al. [240] investigated the influence of the thermal diffusivity of the mould material on the replication fidelity within injection moulding. It was found that a mould material with low thermal diffusivity could improve the replication of features with high aspect ratios. This effect is related to the ability of the mould material being able to delay the formation of the skin layer during the filling. As a consequence, during the holding phase, the polymer can still be deformed to enhance the filling inside the microcavity. However, as mentioned in section 4.4.2, a mould material with a lower thermal conductivity exhibits a lower ablation efficiency. In our case, the thermal diffusivity of the tool steel is a factor 10 times higher compared to the copper and aluminium alloy, as displayed in Table 2. Based on this fact alone, the tool steel would be expected to result in a better replication fidelity compared to the other two mould materials. However, the difference in thermal properties is not the only factor affecting the replication quality as wetting properties between the molten polymer and the mould surface will also play an important role [241] [242]. A better wettability between the molten thermoplastic and mould material is already known to improve the filling behaviour of micro features and this property can be characterised by contact angle

measurements [187]. The results for the contact angle measurements for both polymer melts on the three different mould materials are given in Figure 32. It is clear that the wetting of PP and PC is best in combination with copper alloy, followed by aluminium alloy and is worst for tool steel. For PP, the difference in wetting is limited around 10° and equilibrium has not yet been reached. Also, for PC, regardless of the mould material, wetting is worse compared to PP. In terms of wetting, this indicates that the replication fidelity of the micro features should be the highest for copper alloy and the lowest for tool steel. However, as already indicated, the difference in replication between the mould materials is expected to depend on both thermal and wetting properties, in which a high thermal diffusivity and a high wetting is desirable. Tool steel has a very low thermal diffusivity, which compensates the lower wettability, while the copper alloy exhibits the highest wettability combined with a higher thermal diffusivity. The aluminium alloy however, also has a high thermal diffusivity, similar to copper combined with a weaker wettability compared to copper. This explains why the replication fidelity of tool steel and copper alloy are similar and why that of aluminium alloy is the lowest.

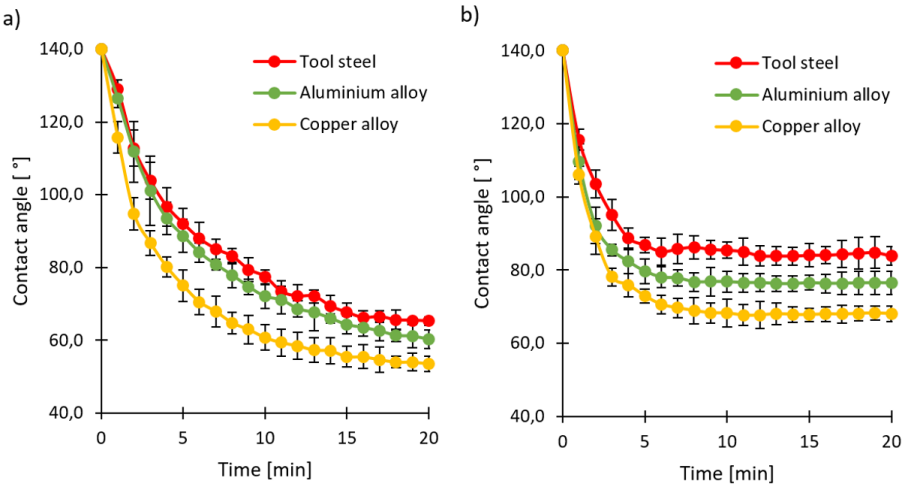


Figure 32: Contact angle of (a) PP and (b) PC, during the spreading on the different mould materials. The error bars represent the 95 % confidence interval.

### 4.4.6 Difference in replication between the thermoplastic

The difference in replication between the two thermoplastics is possibly caused by four factors.

First of all, as already discussed, there is a difference in linear shrinkage for both polymers, corresponding to 0.43 % and 2.22 % for PC and PP, respectively. Thus, the PC microneedles will only exhibit a very low linear shrinkage in the orders of a few micrometres, while the PP will have a linear shrinkage in the orders of a few tens of micrometres.

Secondly, the large surface area to volume ratio of the microneedle cavities, makes interfacial phenomena such as wettability critical. In fact, during the very early contact between the polymer melt and the mould, before the skin formation, the wetting at the interface between the polymer melt and the mould plays an important role in the filling of the micro features. Rytka et al. [241] and Vera et al. [242] observed that a higher work

of adhesion (or spreading coefficient) between the polymer melt and the mould results in a better filling of the micro features. Vera et al. [242] determined a work of adhesion on a steel substrate of 42.8 mJ/m² for PP and 30.0 mJ/m² for PC, which corresponded to a better micro replication of PP compared to PC. Although the PP and PC grades and the steel used in the work of Rytka et al. [241] are not identical to our grades, we expect the interfacial wetting behaviour to be comparable.

The third factor inducing a discrepancy in replication is the different creep deformation behaviour of the two materials. Creep deformation has been reported in literature as an important variable with respect to the replication of small features [243], [244]. During the packing phase, the polymer skin layer has to undergo a deformation in order to further enhance the replication of the features beyond the level reached during the initial filling. This deformation is only possible if the temperature of the skin layer is still higher than the no-flow temperature, which is the temperature when a polymer ceases to flow. The time, t, required for the average temperature of the polymer to reach the no-flow temperature, $T_{nf}$ ,can be estimated using Equation (5), as presented in [245].

$$t = \frac{b^2}{\pi^2 \cdot \alpha} \cdot ln\left[\frac{8}{\pi^2} \cdot \left(\frac{T_i - T_m}{T_{nf} - T_m}\right)\right] \quad (5)$$

with $b$ the thickness of the polymer part, $\alpha$ the thermal diffusivity ,$T_i$ the injection temperature, and $T_m$ the mould temperature. Using this equation and the data from Table 1, on average the times required for PP and PC to reach the no-flow temperature are 8.9 s and 4.8 s, respectively. These values will be much higher than the time required for the skin layer to reach the no-flow temperature. However, we can clearly observe a large difference between both polymers, as the time required for the average temperature of PP sample to reach the no-flow temperature is nearly two times higher than for the PC sample. This will result in a much faster solidification of the PC skin layer compared to PP. In fact, it is possible that at the start of the packing phase, the skin layer of the PC sample is already frozen and is unable to be deformed whereas the PP skin layer is still able to deform.

The fourth parameter inducing the difference in filling between both thermoplastics is the melt viscosity. This viscosity decreases with an increasing shear rate, also known as shear thinning. This effect is caused by the disentanglement of the polymer chains, which align along the direction of shear. Higher shear rates decrease the melt viscosity, which improves the filling of small microcavities. When filling the microneedle cavities, two different orders of shear rates can be distinguished: (i) very high shear rate during the injection phase, which partially fills the microneedle cavities, and (ii) a very low shear rate during the packing phase, which further enhances the filling. The melt viscosity during the injection phase can be determined from Cross-WLF (Cross–Williams–Landel–Ferry) rheology curves extracted from Autodesk Moldflow® and from the actual online apparent viscosity measurements. A comparison between Cross-WLF model viscosities and online apparent viscosity measurements is shown in Figure 33.

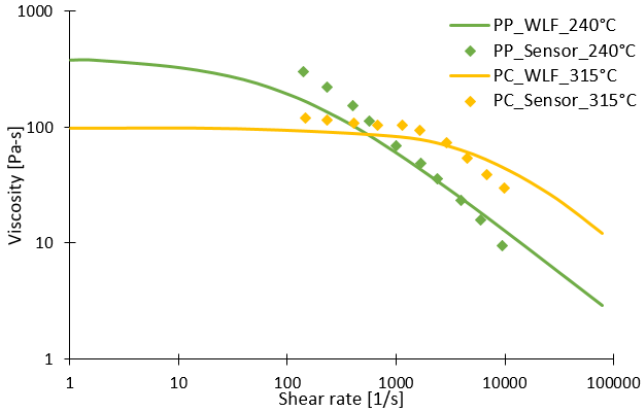


Figure 33: Comparison between Cross-WLF model viscosities and online apparent viscosity measurements for PP and PC.

The online apparent viscosity measurements reveal higher viscosities at low shear rates and lower viscosities at high shear rates compared to the Cross-WLF model, which was also found by [184]. From both the apparent viscosity as the Cross-WLF model viscosity, it can be seen that at very high shear rates, the viscosity of PC is higher than PP. This indicates that the micro features are more easily filled in PP during the initial filling stage at a volumetric injection rate of 149 $cm^3/s$.

### 4.4.7 Surface topography of the replicated microneedles

When analysing the surface topography of the replicated microneedles, micro-grooves were observed along the entire length of the polymer needles for all of the investigated mould materials, as shown in Figure 34 (a). These grooves, being a few micrometres in width and height, are created inside the micro-holes during the laser processing and are replicated during the injection moulding process. The cause of these grooves can be allocated to the applied cross-hatching laser strategy. Because the programmed circular shape is approximated by a grid of parallel lines, the outer contour is not a homogeneous circle. In fact, the contour consists out of micro-ridges along the depth of the needle cavity. Although it is currently unknown whether the micro-grooves have a negative effect on the microneedle functionality, an adapted laser strategy is presented to avoid the formation of the grooves. In this strategy, the linear cross-hatching strategy is changed to a circular-hatching strategy as presented in Figure 34 (b). Here, the laser spot scans a circular region in concentric circles. The process conditions were identical to the cross-hatching strategy, being a steel mould insert, a hatch pitch = 15 µm, a layer pitch = 2 µm a programmed base diameter of 400 µm and the number of layers = 600. It can be observed that the needle has a similar shape and dimension compared to the needle formed with the cross-hatching strategy. However, no micro-grooves along the length of the needle were observed in the circular-hatching strategy. This is due to the fact that the outer contour is now formed by a homogeneous circle, in contrary to the cross-hatching strategy.

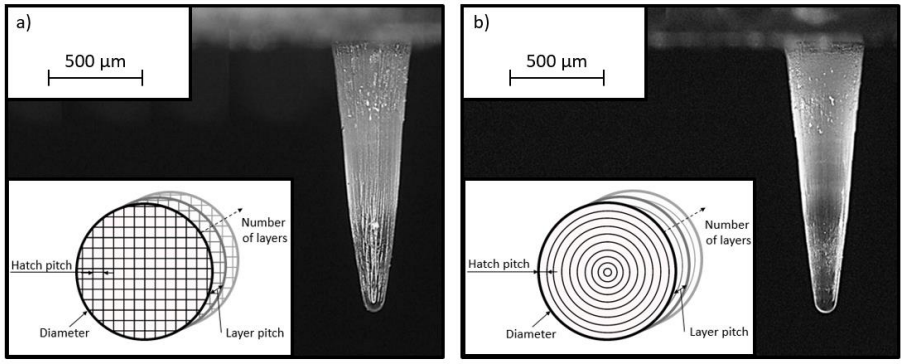


Figure 34: Representation of a replicated PC microneedle (a) with micro grooves along the length of the needle, created with a linear cross-hatching laser strategy; (b) without micro-grooves, created with a circular-hatching strategy.

## 4.5 Conclusion

The present chapter investigated the influence of two laser scanning parameters, being the programmed base diameter and the number of layers, on the geometry of microneedle cavities in tool steel, copper alloy and aluminium alloy. It was found that the depth of the micro-holes increased with a higher number of layers, due to an increase of accumulated fluence. However, there is a saturation in the increase in depth after a certain number of layers, which is reached faster for cavities with a small hole diameter. Furthermore, the replication fidelity of the laser induced cavities in these materials were evaluated for PP and PC using polymer injection moulding. A significant difference was found between the filling of PC and PP, as the replication fidelity for the PP microneedles was in all cases higher compared to the PC needles. Moreover, a linear relationship between the replication in height and the aspect ratio of the holes was found for both thermoplastics. The higher the aspect ratio of the hole, the lower the replication of the microneedle. Furthermore, a difference was identified in filling between the three different mould materials, and this could be explained by differences in thermal and wetting properties.

Thanks to this work, we better understand the effect of the investigated laser scanning parameters on the geometry of the microneedle cavities in tool steel, copper alloy, and aluminium alloy. Furthermore, a deeper insight on the effect of the aspect ratio of microneedle cavities on the replication fidelity is provided, as well as properties of polymer and mould material which affect the replication fidelity during injection moulding.

# Chapter 5 Controlling the flank geometry of injection moulded polymer microneedles made with laser ablated moulds by adapting laser scanning parameters

Evens T., Vanwersch P., Castagne S., Seveno D., Malek O. and Van Bael A. Controlling the flank geometry of injection moulded polymer microneedles made with laser ablated moulds by adapting laser scanning parameters. Conference proceeding in euspen's 21st International Conference & Exhibition, ICE21157, 2021. Some parts of the original publication are left out or modified to avoid redundancy.

## 5.1 Abstract

Microneedle arrays contain minimally invasive devices which facilitate self-administration of drugs in a straightforward and efficient way. In a recent work, we demonstrated a novel methodology to mass produce solid polymer microneedles at a low cost. This production technique utilises a femtosecond laser with a cross-hatching strategy to create cone-shaped micro-holes, which are afterwards replicated using polymer injection moulding. The depth and aspect ratio of the micro-holes can be adapted by changing laser scanning parameters. However, it has not yet been demonstrated how the flank geometry of the needle cavity can be changed. Yet, this flank geometry has a huge impact on both the mechanical strength and the penetration behaviour of the replicated polymer microneedles. In this study, we have modified the flank geometry of laser induced microneedle cavities by adapting laser scanning parameters. This was done by changing the programmed diameter throughout the laser ablation process. Hereby, it was possible to widen the width of a needle near the base to increase its strength and decrease the width near the needle tip of another needle. The laser ablated moulds are replicated through polymer injection moulding, and afterwards the geometry of the resulting microneedles was assessed.

## 5.2 Introduction

Microneedles are micron-sized invasive structures which can be used to deliver vaccines, antibodies or other drugs to the human body through the transdermal route [5], [10], [37], [88]. These microneedles are typically arranged in an array and consist of tens to thousands of microneedles per $cm^2$. Depending on the application, the individual

needle lengths can range from 50 to 2000 μm [3]. The key advantage of microneedles compared to traditional hypodermic needles is their pain-free skin penetration, which is a result of the microneedles not reaching deep enough to stimulate nerve endings [7]. Besides, it is possible to integrate these microneedles on a microfluidic lab-on-a-chip, which facilitates self-administration for patients [12], [133]. This process avoids the need of skilled medical personnel and the risk of cross-contamination [246]. Moreover, due to their small volume, costs related to storage and distribution will be much lower compared to traditional needles. However, manufacturing these microneedles in large volumes at a low cost represents a real challenge [7].

Recently, a novel methodology to mass produce solid polymer microneedles at a low cost was developed [216]. First, cone-shaped microcavities with very sharp tip radii are ablated in metal mould inserts using a femtosecond laser. These mould inserts are then used in an injection moulding process to create polymer cone-shaped microneedles. The injection moulding process enables the use of different polymer materials, yet it is important that proper injection moulding conditions are used to achieve a good replication fidelity. It is already demonstrated that the depth and base diameter of the microneedles can be changed by adapting the laser scanning parameters [247]. However, it is still not known how the flank geometry of the microcavity can be changed, while it is very important for the strength and penetration behaviour of the needles. Sharp needles with small tip radii are needed to effectively pierce the skin at low forces [101], [102]. However, the needle design should also take into account the mechanical performance of the needles, to prevent bending or breaking during needle insertion [42], [72].

In this study, an existing laser scanning strategy is adapted in order to modify the flank geometry of laser induced microneedle cavities. This is done by changing the programmed base diameter throughout the laser ablation process. Three different microneedle designs are created in a tool steel mould insert. The geometry of the microcavities are assessed using micro-computed tomography (μ-CT) and are used in an injection moulding process to create polycarbonate microneedles. Afterwards, the replication fidelity and microneedle geometry are evaluated.

## 5.3 Materials and methods

### 5.3.1 Materials

The thermoplastic material used in this study is polycarbonate (PC, Lexan™ HPX8REU, manufactured by SABIC). The material is a biocompatible amorphous grade, suitable for medical devices and pharmaceutical applications. The melt flow rate is 35 g/10min, which indicates a high flowability.

The selected mould material is a low corrosion tool steel "Stavax" (grade 1.2083 - AISI 420), which is a common mould material within polymer injection moulding. It is often used for its high wear and corrosion resistance, both leading to a long lifetime.

### 5.3.2 Laser machining experiments

A micromachining system (Lasea, Liège, Belgium) with a Satsuma HP femtosecond laser source (Amplitude, Pessac, France) is employed to laser ablate a mould insert with dimensions 70 mm x 60 mm x 4.4 mm. The laser source emits a beam with a pulse duration of 250 fs, a wavelength of 1030 nm and a pulse repetition rate of 500 kHz. The

maximum average power of the laser is 7.85 W, giving a deliverable pulse energy of 15.7 μJ. A galvanometer steers the laser beam within the focal plane, with a spot size of 15.0 μm and an average pulse fluence of 8.88 J/cm². Small dust particles which are formed from ablating the metal surface are extracted by a vacuum collect unit.

A cross-hatching laser scanning strategy, which was recently developed [216], is used in this study for the creation of the microneedle cavities. In this strategy, the laser spot is scanned in a circular region and follows parallel lines in two perpendicular directions. The distance between two consecutive lines is defined as the hatch pitch. Once the laser has scanned one circular grid, the focal point is lowered with a vertical distance, defined as the layer pitch, and the laser scans again the same area. This process is repeated multiple times for a prescribed number of layers.

In this study, we created three different designs, each having a different scanning strategy as illustrated in Figure 35. The first design acts as a reference, as this is created by the conventional laser scanning strategy. Here we scanned a circular region with a constant diameter of 400 μm during a total of 300 layers. In the second design we intend to widen the base of the microneedle by adapting the programmed diameter through the laser ablation process. First, a larger circular region with a diameter of 500 μm was scanned during 10 layers. Afterwards, the size of this feature was decreased to a diameter of 450 μm and was scanned during 25 layers. At last, we decreased the diameter to the reference diameter of 400 μm and this region was scanned for 265 layers. Similar to design 1, the total number of layers corresponds to 300. In the third design we aim to decrease the diameter of the needle throughout its height. In this scanning strategy, the programmed diameter was decreased in four steps of 50 μm, starting from the reference diameter of 400 μm. During each of these steps, the circular feature was scanned for 60 layers, creating again a total of 300 layers. For each of the designs, we created a 2x2 array of microcavities with an interspacing between the cavities of 1 mm. The hatch pitch, layer pitch and scanning speed were constant throughout all of the experiments being 15 μm, 2 μm and 100 mm/s respectively.

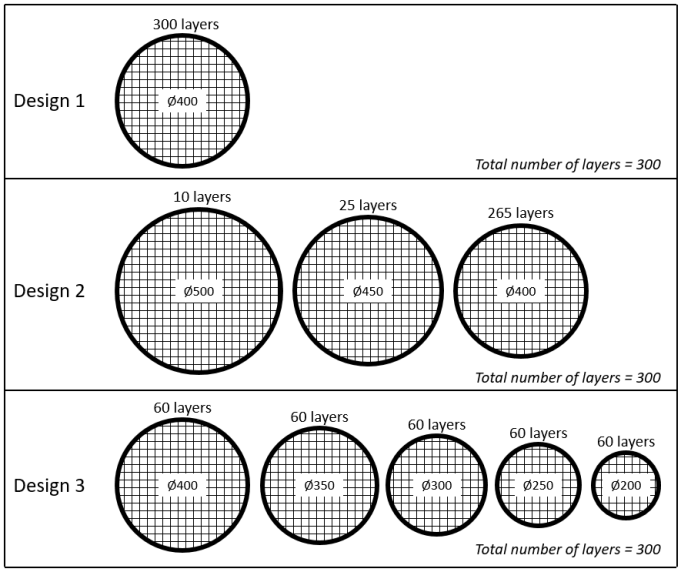


Figure 35: Three different laser scanning designs, each having a different programmed diameter throughout the laser ablation process.

### 5.3.3 Replication through injection moulding

Injection moulding was done on an Engel ES 200/35 HL hydraulic injection moulding machine (Engel, Schwertberg, Austria) with a maximum clamping force of 350 kN and a 25 mm screw with an L/D ratio of 24.8. The mould temperature is controlled by a WITTMANN TEMPRO Controller (Wittmann, Vienna, Austria). The injection moulded part is a 50 mm x 60 mm x 1.5 mm flat plate. Injection moulding parameters are given in Table 5 and were defined to achieve a high replication fidelity. The injection temperature was set to the recommended upper limit of the material supplier. The mould temperature was set to a high value to delay the formation of the frozen layer during injection. The volumetric injection rate was set to a high value, to increase shear rates and thus reduce the melt viscosity during injection. The implemented holding pressure was set to a value just below the occurrence of flash, while also ensuring that there were no demoulding problems due to internal stress within the part. The parts produced in the first 30 cycles were discarded in order to stabilize the process, then the following parts were collected for characterization.

Table 5: Process parameters for injection moulding

| | PC |
|---|---|
| **Injection temperature [°C]** | 315 |
| **Volumetric injection rate [cm³/s]** | 149 |
| **Holding pressure [MPa]** | 74.9 |
| **Mould temperature [°C]** | 115 |

### 5.3.4 Topography characterization

The geometries of the ablated microneedle cavities were characterized using a Phoenix Nanotom μ-CT system. The device is equipped with a high-power nanofocus X-ray tube and a diamond-tungsten target was chosen for the high X-ray absorbing steel samples. A high-power mode was used to allow focal spot and voxel sizes in the micrometre range. The mould insert was cut into cubic samples with an edge length of approximately 3 mm, using a metallographic precision saw. The cubic samples were mounted on a sample holder and fixed on a high-accuracy computer controlled rotation stage. For each scan, 2400 X-ray 2D projection images were obtained from incremental rotation of the scanned samples over 360°. Acquisition parameters were fixed for all samples as follows: voltage = 100 kV, current = 158 μA, voxel size = 3.75 μm, and a 0.1 mm copper and 0.1 mm aluminium filter was used during scanning. Reconstruction of the acquired 2D projections into 3D volumes was performed using GE Phoenix datos|x REC software. Reconstructed datasets (XY-slices) were exported from the software for further analysis and visualization within Fiji ImageJ. For each set of laser parameters, one cubic sample containing four micro-holes were measured. The average length and diameter of the four microcavities, along with the standard deviation was reported in the results.

The geometry of the replicated thermoplastic microneedles were assessed using a Keyence VH-S30 digital microscope (Keyence, Osaka, Japan) with a maximum magnification of 200X. The system is connected to a VHX-500F monitor with built-in measuring software. Ten injection moulded samples were collected and on each sample one microneedle was measured. The average of these ten measurements along with the standard deviation was reported in the results.

## 5.4 Results

### 5.4.1 Laser ablation

The reconstructed μ-CT XY datasets of the laser ablated microneedle designs with corresponding dimensions are shown in Figure 36. First of all, we can clearly observe cone-shaped microcavities with very sharp tip radii for each of the three designs. The formation of this cone-shape is expected to be caused by two laser phenomena, being plasma shielding and laser reflectance on steep sidewalls. Plasma shielding occurs at a laser ablation process with high repetition rates [226]. A part of the vaporized material which is formed during the ablation process will be unable to escape for the microcavity. Therefore, it will interact with the next incoming laser pulse, creating a protective plasma shield [210]. Secondly, the ablation efficiency of the laser is reduced drastically near the edge of the cavity, as most of the laser light is reflected rather than absorbed. This causes the diameter of the microcavity to become smaller as the micro-hole is created [227]. Furthermore, the reflected laser light will partially be redirected to the bottom of the hole, contributing to a deeper and sharper cavity.

When comparing the three different needle designs, we can observe a difference in cavity dimensions. The base diameter of design 2 (500 ± 3 μm) is higher compared to the diameter of reference design 1 (437 ± 2 μm). The diameter of design 2 is only wider near the base of the needle and gradually changes to a comparable shape of design 1. Moreover, it can be seen that the length of both cavities is also the same. Thus, by

increasing the size of the scanned circular feature during the first few layers, the base of the cavity is increased while the rest of the needle shape stays similar to the reference.

In design 3, the diameter is decreased four times throughout the laser scanning process. This results in a microcavity which gradually reduces in diameter throughout the depth, compared to reference design 1. Thus, the needle has a sharper shape compared to design 1. Besides, the cavity base diameter is smaller than reference design 1 and can be explained as followed. During the laser ablation process, the laser focal spot is progressively moved deeper inside the mould material. Therefore, the Gaussian shaped laser beam will start to intersect with the edge of the already created micro-hole, removing additional material. As a result, we can observe that the base diameter of design 1 (437 μm) is larger than the programmed base diameter (400 ± 2 μm). However, for design 3, the scanned diameter is progressively decreased in size, preventing the laser beam to be in contact with the existing micro-hole. Thus, here the size of the base diameter (406 ± 3 μm) is almost identical to the programmed base diameter (400 μm).

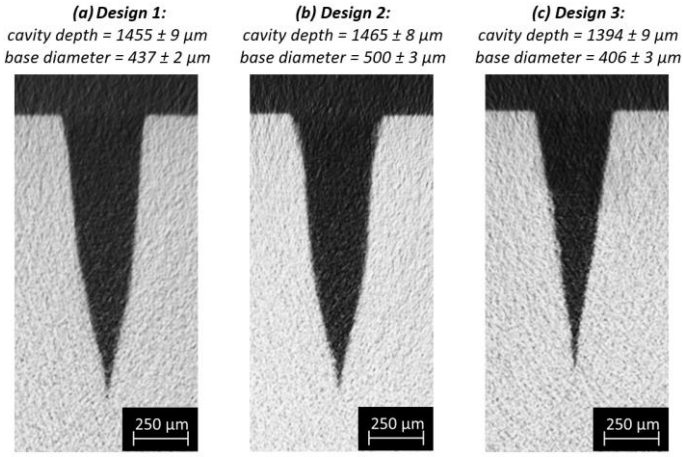


Figure 36: Reconstructed μ-CT XY datasets of the ablated microcavities for: (a) design 1; (b) design 2, and (c) design 3.

### 5.4.2 Injection moulding

The laser ablated mould insert was used in an injection moulding process to replicate the microneedle cavities. The replicated polymer microneedles together with the needle length and replication in height are shown in Figure 37. All of the microneedles show a similar shape as the corresponding microneedle cavity. Yet, the tip of the polymer microneedles are not completely replicated.

Completely filling microcavities is known to be very difficult within polymer injection moulding [134]. When the polymer is injected into the mould, it will follow the path of least resistance. Therefore, most of the material will flow in the main flow direction through the macroscale cavity, leaving the micro-features only partially filled. This behaviour is also known as the hesitation effect [248]. Yet, as soon as the polymer comes in contact with the cold mould surface, a layer of frozen polymer is formed which will prevent the complete filling if the microcavities at the time when the macroscale cavity is filled and the pressure is built up. This behaviour is in our case minimized, by increasing the mould temperature which delays the formation of the frozen polymer layer.

Therefore, a relatively high replication fidelity can be observed for all three designs. The needles replicated for design 1 and design 2 exhibit a very similar replication in height, being 91 % and 92 %, respectively. The lowest replication was observed for design 3, which corresponded to 86 ± 0.9 %.

The reason why the replication of design 3 is lower compared to the other two designs is due to the difference in the shape of the needle cavity. The microcavity of design 3 is much sharper near the needle tip, which increases both the filling resistance of the polymer and the surface area to volume ratio. As a result of the latter, the heat transfer between the molten polymer and the mould surface is higher [239]. This causes a faster solidification of the polymer leading to a faster formation of the frozen layer and in turn a lower replication fidelity.

It is evident that the performance of the three different microneedle designs will be different in terms of mechanical strength and skin penetration behaviour, due to the difference in needle shape. In design 2, a curvature is added to the base of the microneedle. It is expected that this curvature will not affect the insertion behaviour of the needle tip, yet an increase in the penetration force is likely when the whole needle would be completely forced into the skin. Yet, the additional curvature will reduce stress concentrations at the base of the needle and will improve the mechanical performance of the microneedle. The design of needle 3 is expected to reduce the force needed to penetrate the microneedle into the skin, due to the sharper shape of the needle.

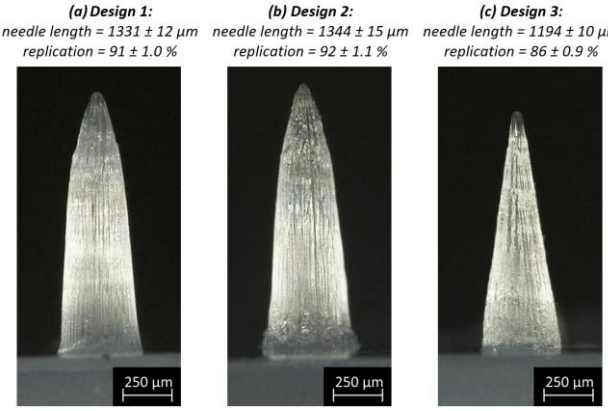


Figure 37: Microscopic images of the polymer microneedles corresponding to: (a) design 1, (b) design 2, and (c) design 3.

## 5.5 Conclusion

In this study, we have shown that it is possible to adapt the flank geometry of laser induced microcavities, by adapting laser scanning parameters. We created three different designs, each having a different scanning strategy. The first design acted as a reference, as it was created by the conventional strategy, which has a constant programmed diameter throughout the scanning process. In the second design we increased the width of the cavity near the surface, by increasing the programmed diameter in the first few layers. In the third design we created a microcavity with a sharp flank geometry compared to the reference design. This was done by decreasing the programmed diameter throughout the number of layers. The ablated microcavities were assessed by µ-CT and were used in an

injection moulding process to create polycarbonate microneedles. A relatively high replication fidelity was observed for all of the three designs, being 91 %, 92 % and 86 %, for design 1, design 2 and design 3, respectively. Design 3 exhibited the lowest replication fidelity, which was caused by its sharper needle geometry. Evidently, the performance of the three different microneedle designs will be different in terms of mechanical strength and skin penetration behaviour, due to the difference in needle shape.

In future work, a model will be developed to simulate the laser ablation process. With the aid of this model, we will further optimise the geometry of the microneedle to improve its mechanical strength and penetration behaviour. This will be done in combination with micromechanical finite element analyses. In addition, micromechanical testing equipment will be developed to quantify this needle strength and penetration behaviour. Furthermore, an in-depth analysis on the replication fidelity during the injection moulding process will be conducted.

# Chapter 6 Predicting the replication fidelity of injection moulded solid polymer microneedles

Evens T., Castagne S., Seveno D. and Van Bael A. Predicting the replication fidelity of injection molded solid polymer microneedles. International Polymer Processing, 37 (3): 237-254, 2022. Some parts of the original publication are left out or modified to avoid redundancy.

## 6.1 Abstract

Microneedles are sharp microscopic features, which can be used for drug or vaccine delivery in a minimally invasive way. Recently, we developed a method to produce polymer microneedles using laser ablated moulds in an injection moulding process. At this moment, extensive injection moulding experiments are needed to investigate the replication fidelity. Accurate predictions of the injection moulding process would eliminate these costly and time expensive experiments. In this study, we evaluated the replication fidelity of solid polymer microneedles using numerical simulations and compared the results to injection moulding experiments. This study was performed for different sizes of microneedles, different thermoplastics (polypropylene and polycarbonate) and different mould materials (tool steel, copper alloy and aluminium alloy). Moreover, different processing conditions and different locations of the microneedles on the macroscopic part were considered. A good correlation with experimental findings was achieved by optimizing the heat transfer coefficient between the polymer and the mould, while using a multiscale mesh with a sufficient number of mesh elements. Optimal heat transfer coefficients between 10,000 W/m²·K to 55,000 W/m²·K were found for the different combinations of polymer and mould materials, which resulted in an accuracy of the simulated microneedle replication fidelity between 94.5 % to 97.0 %.

## 6.2 Introduction

Polymer products with micro surface features are increasingly used in multiple applications and industries such as microfluidics [108], [133], [243], optics [188], [249]–[251], biomimetics [252]–[254], and medical devices [184], [255], [256]. Microneedles are an example of microfeatures found in medical applications, which are often produced in polymers due to their excellent biocompatibility, biodegradability, and low material and production cost. These microneedles are used to pierce the skin, in order to deliver medical solutions or to extract human fluids from a body for sampling applications. Over

the years, various types of microneedles have been developed, most often arranged in an array, having various shapes and lengths ranging from 25 to 2000 μm [5]. Recently we developed a novel mass production method to produce solid [216] and hollow microneedle arrays [257] using polymer injection moulding. Very sharp tipped microneedle cavities can be laser ablated in various mould materials and the cavity geometry can be adapted by changing laser scanning parameters as illustrated in [247].

Currently, extensive injection moulding experiments are needed to investigate the changes in the microneedle replication fidelity that result from variations in (i) the geometry of the macroscopic part, (ii) the shape, size and location of the microfeatures, (iii) the injection moulding processing parameters, (iv) the polymer properties, and (v) the mould material. These costly and time consuming experiments would be drastically reduced if sufficiently accurate injection moulding simulations can be made. Besides reducing the development time, numerical simulations would allow us to gain a better understanding of the underlying filling mechanisms for microfeatures.

Multiple commercially available computer-aided injection moulding simulation tools exist, such as, Moldex3D, Autodesk Moldflow, Sigmasoft, Simpoe-Mold, Cadmould, and Rem3D. These software packages describe the anisothermal, compressible, and viscous flow of molten polymers using Navier–Stokes equations, taking into account the conservation of mass, linear momentum, and energy [183]. Besides the Navier-Stokes equations, additional boundary conditions that describe the polymer flow are added to the system. The double domain Tait equation describes the pressure-specific volume-temperature (pvT) relationship, while the Cross-WLF (Cross–Williams–Landel–Ferry) model defines the velocity-dependent viscosity behaviour [258].

Injection moulding simulations are mostly used to predict the filling, warpage, formation of weld lines, etc. of macroscopic polymer products, yet some researchers have also addressed the filling of microfeatures. Kim & Turng were amongst the earliest to use a two-step macro-micro filling approach for the filling analysis of a part with a micro-surface feature [259]. First, a filling analysis was performed at the macro-scale geometry of the part. Afterwards, a micro-level filling analysis on the micro-size geometry was performed, where the boundary conditions from the macro-level analysis were used as input data. A few years later, Lin & Young constructed a simplified model by assuming that most of the filling takes place during the packing phase [260]. The model showed reasonable correlations with replication trials, yet the assumption that most of the filling takes place during the packing phase is not valid in all cases. Choi & Kim implemented both wall slip and surface tension in a multi-scale flow simulation, using Moldflow Autodesk and Comsol [261]. They observed that a slip model was necessary for channels with a diameter less than 10 μm, and that the capillary effect was only noticeable in the submicron range. Birkar et al. utilized filling simulations with a multiscale mesh to provide insights on the spacing between micro surface features [262]. They demonstrated that the spacing significantly affects the replication fidelity due to variations in the local packing pressure. Very recently, Loaldi et al. presented four case studies in which integrated multi-scale micro injection moulding simulations were employed as a digital process optimization tool [188]. In one of the cases, the replication fidelity of microfeatures on a macroscopic part was predicted with a high accuracy of 91 %.

During an injection moulding cycle, the polymer undergoes a complex thermal process where it is heated to its processing temperature and afterwards injected into the mould cavity where it cools down and solidifies. Throughout this process, the heat transfer between the mould surface and polymer melt, described by the Nusselt number, has a significant influence on the filling and cooling behaviour, which can in turn affect

the component form, surface properties, internal morphology, residual stresses and physical properties [263]. This heat transfer is governed by the thermal contact conductance (TCC) or the heat transfer coefficient (HTC), being the term used in commercial software products. The HTC is affected by the area of the contacting surfaces, the temperature of the polymer and mould, the applied pressure and the surface topography [263]. The HTC at the interface of two surfaces in contact is given by Equation (6) [264]:

$$HTC = \frac{q}{T_h - T_c} \tag{6}$$

where q is the heat flux, $T_h$ is the temperature at the 'hot' interface side and $T_c$ is the temperature at the 'cold' interface side. A number of researchers have studied the heat transfer at polymer/metal interfaces through steady state experiments using an axial flow apparatus as described in [265]. In this apparatus, a polymer sample is placed between two steel surfaces having a temperature gradient of 10 °C. Once a steady state was achieved, the heat flux was determined using thermocouples and the corresponding HTC was calculated. Using such apparatus, a range of varying HTC values was reported, being 250 W/m²·K and 1659 W/m²·K in the work of Marotta & Fletcher [266], 15,000 W/m²·K and 25,000 W/m²·K in the work of Narh & Sridhar [267] and around 7000 W/m²·K in the work of Dawson et al. [268]. However, these values were obtained using solid polymers, low pressures and constant thermal gradients, which is contradictory to the conditions in an injection moulding process.

Throughout the years, various researchers have adapted the default heat transfer coefficient in commercial simulations, in order to improve the correlation between simulations and experiments. For example, Nguyen-Chung et al. investigated the effect of the heat transfer coefficient on the injection pressure and filling degree of a micro spiral, and showed that a good correlation between Moldflow simulations and injection moulding could only be achieved by using a HTC of 15,000 W/m²·K and 25,000 W/m²·K [269]. Tofteberg & Andreassen on the other hand, used a HTC of 30,000 W/m²·K in Moldflow and Ansys, to predict the filling of 2D optical gratings made of cyclic olefin copolymer (COP) with a 3 µm period [270]. Zhang et al. assessed the replication fidelity of micro features on a microfluidic chip, while taking into account the heat transfer coefficient, venting, wall slip and the no-flow temperature [271]. The heat transfer coefficient was varied from 1000 to 50,000 W/m²·K and the best prediction was found at a HTC of 30,000 W/m²·K. Xu et al. proposed a variable heat transfer coefficient within microchannels depending on the change in viscosity when the polymer is cooled down [272]. They found that the variable heat transfer coefficient provided much better results than the conventional constant heat transfer coefficient. Babenko et al. also found that an increased HTC, compared to the default value, improved the accuracy of the simulated replication fidelity of microfeatures and suggested a HTC in the range of 7000 to 8000 W/m²·K for polypropylene and polystyrene [263]. Rytka et al. simulated the polymer melt flow into micro- and nano-features and compared the results to injection moulding trials [273]. They adjusted the transition temperatures in the simulations with experimentally determined no-flow temperatures using melt flow index measurements and varied the heat transfer coefficient. They concluded that the heat transfer coefficient needed to be increased compared to appropriate values for macroscopic injection moulding simulations to correctly represent interfacial polymer/mould effects.

Moreover, to confirm the necessity of a high HTC, they conducted heat transfer simulations using Comsol Multiphysics.

Largely all of the literature dealing with the simulation of microfeatures, investigated only one thermoplastic, one mould material and a fixed set of injection moulding conditions. In this study, we use Moldex3D to simulate the replication fidelity of polymer microneedles on a macroscopic plate and compare the results to injection moulding experiments. We investigate the simulated results for (i) two polymers, being polypropylene and polycarbonate, (ii) different locations of the microneedles on the macroscopic polymer part, (iii) different injection moulding parameters, and (iv) different mould materials being a tool steel, a copper alloy and an aluminium alloy. Moreover, the effect of the mesh size on the replication fidelity is investigated and an optimal heat transfer coefficient is determined for the different combinations of polymer and mould materials.

## 6.3 Materials and Methods

### 6.3.1 Thermoplastic polymers

Two thermoplastic materials were used in this study, a polypropylene (PP, 578N, manufactured by SABIC) and a polycarbonate (PC, Lexan™ HPX8REU, manufactured by SABIC). The polypropylene material is a general purpose semi-crystalline homopolymer, which is easy to process and has a low cost. The polycarbonate material is a biocompatible amorphous grade, suitable for medical devices and pharmaceutical applications. Both materials have a high flowability as indicated by their very high melt flow index and are thus appropriate for filling small microfeatures. Table 6 reports the main characteristics for both thermoplastics.

Table 6: Main properties of the thermoplastics based on material datasheets and the Moldex3D 2020 material database.

| | PP | PC |
|---|---|---|
| **Density [kg/m³]** | 905 | 1190 |
| **Melt flow index [g/10 min]** | 25<br>[230 °C/2.16 kg] | 35<br>[300 °C/1.2 kg] |
| **Elastic Modulus [MPa]** | 2100 | 2300 |
| **No-flow temperature [°C]** | 110 | 167 |

### 6.3.2 Mould insert

A low corrosion tool steel (Stavax, grade 1.2083), a high-strength aluminium zinc alloy (grade 3.4365) and a copper nickel alloy (grade AMPCOLOY 940) mould insert with 16 arrays of microneedle-cavities was manufactured in a previous study [247]. Each array has different microneedle dimensions and contains 9 microneedle cavities in a 3x3 setting. These cavities were created with a femtosecond laser ablation process, using a cross-hatching strategy [216]. The dimensions of the ablated cavities were characterized using micro-computed tomography. The depth of the cavities varies between 720 μm and 2100 μm, with an aspect ratio ranging from 2.8 to 7.1; this geometry is shown in a previous study [247]. The thermal properties of the three mould materials are listed in Table 7.

The stationary side of the injection mould is equipped with a temperature sensor (Priamus, 4008B) and a piezoelectric pressure sensor (Priamus, 6001B), which allow for precise online measurement of the cavity temperature and pressure. Both sensors are located at a distance of 7 mm from the edge of the product, as illustrated in Figure 38.

Table 7: Thermal properties of the different mould materials based on material datasheets.

| | Tool Steel 1.2083 | Aluminium 3.4365 | Copper AMPCOLOY 940 |
|---|---|---|---|
| **Thermal conductivity at 100°C [W/m °C]** | 23.5 | 145 | 226 |
| **Specific heat capacity at 100°C [J/g °C]** | 0.48 | 0.95 | 0.38 |
| **Thermal diffusivity [mm²/s]** | 6.51 | 60.40 | 68.36 |

### 6.3.3 Injection moulding product

The injection moulded part selected for this study is a 50 mm x 60 mm x 1.5 mm flat plate, as shown in Figure 38. The polymer is injected through a hot runner which is located 2.3 mm from the edge of the product, indicated by a white dot. The microneedles are located in a 12 mm x 12 mm area being centred horizontally on the product and are vertically located 10 mm from the edge of the product.

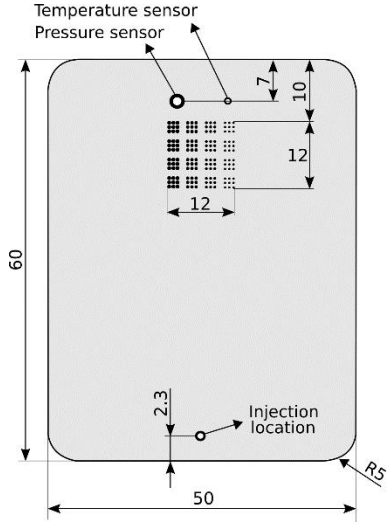


Figure 38: Illustration of the flat plate with all dimensions in mm, the thickness is 1.5 mm.

### 6.3.4 Injection moulding experiments

All injection moulding experiments were conducted on a Engel ES 200/35 HL hydraulic injection moulding machine with a maximum clamping force of 350 kN and a 25 mm horizontal screw. The machine is equipped with a hydraulic accumulator to increase the volumetric injection rate to a maximum of 149 cm³/s. The mould temperature is controlled by a Wittmann Tempro D controller, with a maximum temperature of 180 °C.

The injection moulding parameters used in this study are given in Table 8. These values were determined experimentally to achieve a high replication fidelity. The injection temperature represents the adjustable barrel temperature and was set to the recommended upper limit of the material supplier. The mould temperature was set to a high value to delay the formation of the frozen layer during injection. The volumetric injection rate was set to a high value, to increase shear rates and thus reduce the melt viscosity during injection. The implemented holding pressure was set to a value just below the occurrence of flash, while also ensuring that there were no demoulding problems due to internal stress within the part. For both polymers, the holding pressure time and cooling time were set to 4.5 and 6 seconds, respectively. This ensured that the gate was frozen at the end of the holding phase, and that good solidification of the product was achieved after the cooling phase. The switch-over point, being the position where the filling stage switches to the packing stage, was set to a screw position of 6.4 $cm^3$ for both materials. The total dosing volume was set to 10.8 $cm^3$ and 10.3 $cm^3$ for PC and PP respectively. The parts produced in the first 30 cycles were discarded in order to stabilize the process and the following 30 parts were collected for characterization.

The geometries of the replicated thermoplastic microneedles were assessed using a digital microscope (Keyence VH-S30) with a maximum magnification of 200X. The system is connected to a VHX-500 F monitor with built-in measuring software. The microscope was calibrated using a stage micrometre (Olympus Tokyo, OBMM 1/100). 9 samples were injection moulded and to account for the injection moulding process repeatability, for each sample the first microneedle was measured on each array. Thus, on each injection moulded part, 16 different microneedles were measured. The average of these measurements along with a 95 % confidence interval, using the Student's t distribution was reported in the plotted results.

Table 8: Injection moulding process parameters for the two thermoplastic materials.

| | PC | PP |
|---|---|---|
| **Injection temperature [°C]** | 315 | 240 |
| **Volumetric injection rate [$cm^3$/s]** | 149 | 149 |
| **Holding pressure [MPa]** | 74.9 | 57.5 |
| **Mould temperature [°C]** | 115 | 80 |
| **Holding pressure time [s]** | 4.5 | 4.5 |
| **Cooling time [s]** | 6 | 6 |
| **Switch-over point [$cm^3$]** | 6.4 | 6.4 |
| **Dosing volume [$cm^3$]** | 10.8 | 10.2 |

## 6.4 Injection moulding simulation settings

The commercial software package Moldex3D studio 2020 was used to simulate the injection moulding process. The polymer parts were meshed using Moldex3D designer with a boundary layer mesh to adequately represent the laminar flow of the melt. A three-layer prismatic mesh was generated inwards from the surface mesh and a tetrahedral mesh then filled up the remaining space, to total of 11 layers across the part thickness. Data of the thermoplastic materials such as viscosity, thermal properties and the pressure-specific volume-temperature relation (pvT) were obtained from the embedded Moldex3D software database. During preliminary simulations, it turned out that the cooling sequence, which takes into account the cooling circuit and mould material, did

not affect the replication fidelity of the microfeatures. Thus, to decrease the computational time, only the filling sequence was conducted with a uniform mould temperature.

### 6.4.1 Macroscopic flow

It can be assumed that the macroscopic flow of the polymer is hardly affected by the microscopic surface features. However, the microscopic flow inside the microfeatures will be influenced by the macroscopic flow in terms of filling pressure, temperatures and flow front velocities. Thus, it is essential to compare the simulated macroscopic conditions to the experimental conditions. During injection moulding experiments using the tool steel insert and the in-mould sensors, we measured the cavity temperature and cavity pressure and compared them to the corresponding values obtained with Moldex3D flow simulations. For the simulation, the macroscopic part was meshed in 73000 elements and a "Filling & Packing" analysis was conducted using identical process conditions as the injection moulding experiments combined with the default setting of the heat transfer coefficient.

### 6.4.2 Simulation parameters in Moldex3D

Various simulation settings are important when simulating a macroscopic part with microscopic surface features. First of all, the injection moulding parameters should be identical to the ones used in the injection moulding experiments as they have a significant impact on the filling result. Thus, the holding pressure, melt temperature and mould temperature were set to the same values as in the experiments. The injection speed in Moldex3D was defined as a filling time, which was calculated using the volume of the part and the volumetric injection rate (taking into account the screw acceleration and deceleration). The calculated time corresponded to 0.06 seconds, which is in agreement with the experimental filling time of the injection moulding machine. Another important model parameter, is the heat transfer coefficient between the polymer and the mould. The HTC during the filling stage will be varied throughout the study, while the HTC during the packing and detached phase are set to 2500 $W/m^2 \cdot K$ and 1250 $W/m^2 \cdot K$, i.e. the default values in Autodesk Moldflow. The detached phase represents the time after the packing phase, when the pressure on the mould wall equals zero until the end of the injection cycle. The last parameter that must be adapted from the default value is the criterion for stopping the calculation. This parameter is linked to a function which aims to decrease the computational time. As default, this value is set as 99.95 %, which means that if the product is filled for 99.95%, Moldex3D assumes that the part is completely filled, without a short shot and will end the simulation early to save computational time. In our case, the incomplete filling of the microfeatures is smaller than 0.05 % of the complete volume of the part, thus Moldex3D displays the part as completely filled. To overcome this problem, the criterion for stopping the calculation is changed into 99.9999 %, enabling the simulation of incomplete filled microfeatures. A summary of the adapted simulations parameters in Moldex3D can be found in Figure 39.

| Programme specific parameters | Default | | Adapted | |
|---|---|---|---|---|
| | PP | PC | PP | PC |
| Holding pressure (MPa) | 140 | 160 | 57.5 | 74.9 |
| Melt temperature (°C) | 240 | 305 | 240 | 315 |
| Mould temperature (°C) | 40 | 85 | 80 | 115 |
| Filling time (s) | 0.25 | 0.25 | 0.06 | 0.06 |
| HTC during filling stage (W/m²·K) | Automatically determined | | Variable | |
| HTC packing (W/m²·K) | Automatically determined | | 2500 | |
| HTC detached (W/m²·K) | Automatically determined | | 1250 | |
| Criterion for stopping calculation | 99.95 % | | 99.9999 % | |

Figure 39: Default and adapted simulation parameters in Moldex3D.

### 6.4.3 Mesh convergence study using multi-scale meshing

An important parameter when conducting numerical simulations is the mesh size. Typically a finer mesh results in a more accurate solution, but as a downside requires an increased computation time. Therefore, a mesh convergence study is conducted to define a mesh size, having both a satisfactory solution and a computation time below 2 hours, using an Intel Core i7-9850H Processor. In this study, we varied the total number of mesh elements in the part from 430,000 to 4,900,000 elements in 6 steps. The first step, containing 430,000 elements, consisted out of a uniform mesh, containing roughly the same elements sizes, as illustrated in Figure 40 (a). However, the finite element mesh can also be split in different mesh densities, going from coarse to fine, also known as multi-scale meshing. A fine mesh is necessary within the microfeatures to achieve a precise simulation, while in the macroscopic part a coarse mesh is sufficient. In the transition zone between the coarse and fine elements, the element size needs to be changed gradually. Figure 40 (b) illustrates the multi-scale meshing strategy, corresponding to the 4,900,000 elements.

Using these 6 different sets of finite element meshes, we conducted filling simulations to determine the replication fidelity of the microneedle arrays for the tool steel insert. The height of the simulated microneedles were measured using a built-in measuring tool. For each simulation, the first microneedle on each array was measured, which is the same microneedle as the one measured experimentally. The height of the simulated microneedles were then compared to the average height of the injection moulded needles. The injection moulding parameters used in the simulations were identical to the experiments and the heat transfer coefficient during the filling phase for both thermoplastics were set to values found in literature. For PP the value was set to 10,000 W/m²·K as Nguyen-Chung et al. (2008) found a good correlation between Moldflow simulations and injection moulding with PP for this value. For PC the HTC was set to 30,000 W/m²·K as Rytka et al. (2016a), Xu et al. (2005), and Tofteberg & Andreassen (2010) reported a good correlation for PMMA and COP, both being amorphous materials.

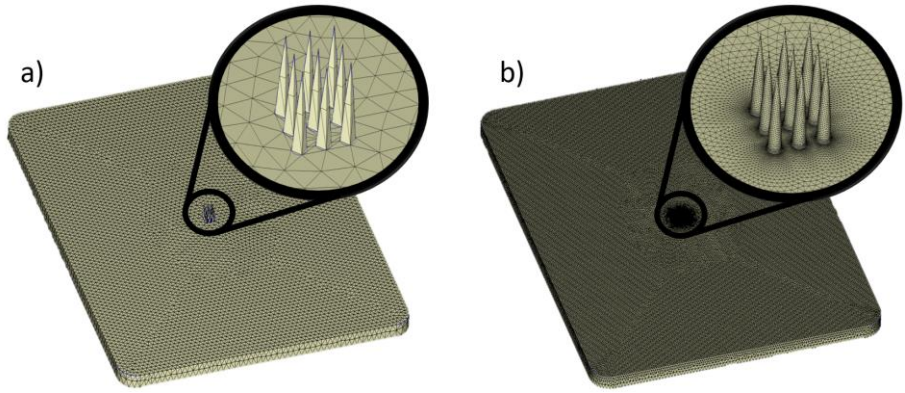


Figure 40: Illustration of (a) a uniform mesh corresponding to the 430,000 elements, and (b) multi-scale meshing corresponding to the 4,900,000 elements.

### 6.4.4 Heat transfer coefficient

As already indicated, the heat transfer coefficient, defining the heat transfer between the polymer melt and the surrounding mould material, is a very important parameter when conducting flow simulations with microscopic surface features. During the initial filling of the polymer melt inside the mould cavity, the temperature gradient between the mould and the melt is maximal, leading to a very high heat transfer between the polymer and the mould. As a result, the outer layer of the polymer cools down very fast, forming a solidified polymer skin layer near the mould surface. This frozen skin layer will act as an insulating barrier, leading to a substantial reduction in the heat transfer between the mould and the remaining molten core [184]. Thus, ideally in an injection moulding process the HTC should not be represented by a constant value, but by a variable in time as indicated by Sridhar et al., Park & Kim and Rytka et al. [273]–[275]. In the current commercially available simulations, it is only possible to specify a variable HTC coefficient in time for midplane or dual domain solvers in Autodesk Moldflow. In all other cases and software packages, it is only possible to set a constant value for the HTC throughout the whole filling simulation. In fact, the default HTC in Autodesk Moldflow 3D analysis is a constant value of 5000 $W/m^2 \cdot K$ for the filling stage. This moderate value of the HTC is a good assumption for macroscopic mould filling, as the melt contact with the mould surface is less important compared the bulk of the polymer. However, when filling microscopic cavities, an increased HTC during the initial contact is essential for the filling behaviour [273]. In Moldex3D, the default HTC is an automatically determined value, based on the selected materials and process conditions. The value of this automatically determined HTC is, however, not visible to the user.

We determined a heat transfer coefficient, having the best correspondence with the experimentally determined replication fidelity, both for PP and PC in combination with the tool steel insert. This was done by varying the HTC from 5000 $W/m^2 \cdot K$ to 40000 $W/m^2 \cdot K$ and calculating the average absolute deviation between the simulated replication fidelity and the experimentally determined replication fidelity. Additionally, for both polymers we also performed a flow simulation using Moldex3D's default automatically determined HTC.

### 6.4.5 Replication fidelity in function of the location of the microfeatures

From literature, it is known that the location of microfeatures on the macroscopic part will affect the replication fidelity. Microfeatures located near the gate will start to fill during the initial injection stage, while microfeatures located near the end of flow path will be filled during the end of the injection stage. This difference in timing causes the polymer melt to have a different temperature, pressure and viscosity during the filling of the microcavities, thus resulting in a different filling behaviour.

We validated the simulated replication fidelity in function of the location of the microfeatures on the macroscopic part by drawing comparisons with the injection moulding experiments. Two identical 3x3 microneedle cavities with an individual depths of 1730 µm were placed at two different locations on the macroscopic part. One array was placed at a distance of 2.3 mm from the injection location, while the other array was placed at 46.5 mm from the injection location, as depicted in Figure 41. 9 samples were injection moulded and to account for the injection moulding process repeatability, the first microneedle was measured for both arrays on each sample. The average of these 9 measurements along with a 95 % confidence interval, using the Student's t distribution was reported in the plotted results. The optimally determined HTC values determined in section 6.5.3 were used for both polymers.

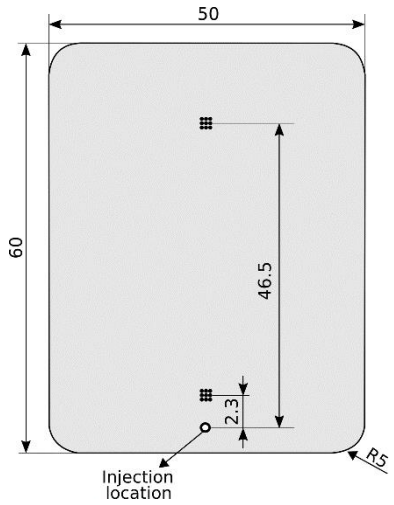


Figure 41: Illustration of the macroscopic part with two identical microneedle cavities, positioned at different distances from the injection location. All represented dimensions are in mm and the part thickness is 1.5 mm.

### 6.4.6 Replication fidelity in function of the injection moulding parameters

The replication fidelity of microfeatures is greatly affected by the selected injection moulding process parameters, in particular the melt temperature, mould temperature, volumetric injection rate and the holding pressure [134]. The mould temperature is known in literature to be the most important parameter when it comes to replicating microfeatures [133], [134], [244]. This parameter determines how fast the frozen skin layer is formed, which hinders the filling of the microfeatures. A higher mould temperature delays the formation of the frozen skin layer and ensures that the polymer

can still be deformed during the packing phase. Thus, a higher mould temperature results in a higher replication fidelity. The replication fidelity is also improved with a higher melt temperature, as it decreases the melt viscosity [276]. Furthermore, a high volumetric injection rate reduces the injection time and prevents premature freezing of the polymer. Besides, high injection velocities promote shear heating, decreasing the melt viscosity locally and therefore improve the replication fidelity [134]. The last parameter is the holding pressure. This parameter primarily compensates the volumetric shrinkage of the polymer and as such, preserves the replicated geometries during the filling stage. Besides, the holding pressure can also further improve the replication fidelity, at least if the initially filled layer can still be deformed. However, this is only possible if the temperature of the skin layer is still higher than the no-flow temperature and the holding pressure is sufficiently high [243], [244].

As the injection moulding parameters are of prime importance for the replication fidelity, we also compared the simulated and experimental replication fidelity for another set of injection moulding parameters. These adapted process conditions were set to a lower value compared to the elevated process conditions defined in section 2.4 and are illustrated in Table 9. 9 samples were injection moulded and to account for the injection moulding process repeatability, for each sample the first microneedle was measured on each array. The average of these 9 measurements along with a 95 % confidence interval, using the Student's t distribution was reported in the plotted results. The optimal HTC values determined in section 6.5.3 were used for both polymers.

Table 9: Adapted injection moulding process parameters for the two thermoplastic materials.

| | PC | PP |
|---|---|---|
| **Injection temperature [°C]** | 300 | 210 |
| **Volumetric injection rate [cm³/s]** | 50 | 50 |
| **Holding pressure [MPa]** | 64.9 | 49.5 |
| **Mould temperature [°C]** | 85 | 40 |

### 6.4.7 Replication fidelity in function of the mould material

The replication fidelity of the microfeatures is also influenced by the selected mould material, as illustrated by Lucchetta et al., Rytka et al., Evens et al., and Vera et al. [240], [241], [247], [277]. Therefore, we also determined the HTC, having the best correspondence with the experimentally determined replication fidelity, for the aluminium alloy and copper alloy in combination with PP and PC, using the same methodology as described in section 6.4.4 for tool steel. The aluminium alloy is typically used for low production series or prototype moulds and the copper alloy is preferred for its very high thermal conductivity which shortens the cooling phase. These mould materials exhibit different thermal properties, thus the previously determined optimal HTC values with the tool steel mould are not relevant anymore.

## 6.5 Results and Discussion

### 6.5.1 Macroscopic flow

Figure 42 and Figure 43 illustrate the comparison between the simulated and experimental mould cavity pressure and temperature as a function of time for polypropylene and polycarbonate, respectively. The experimental curves, obtained using the in-mould sensors, show the average obtained pressure and temperature profile (n = 3) and the shaded area corresponds to the 95 % confidence interval. For polypropylene, the deviation between the simulation and the experimental pressure in MPa and temperature in °C was 10.7 % and 8.7 %, respectively. Similar results are found for polycarbonate, yet for the experimental pressure curve there is still a residual pressure inside the cavity, not predicted by the simulation. This residual pressure could be the result of the low shrinkage of the polycarbonate grade. For polycarbonate, the deviation between the simulation and the experimental pressure in MPa and temperature in °C was 12.6 % and 8.6 %, respectively. Overall, we can conclude that the simulated and experimentally determined mould cavity pressure is in good agreement for PP, while for PC the residual pressure inside the mould cavity was not predicted accurately. For the mould cavity temperature, it can be observed that there is a larger deviation between the experimental and simulated data, compared to the cavity pressure data.

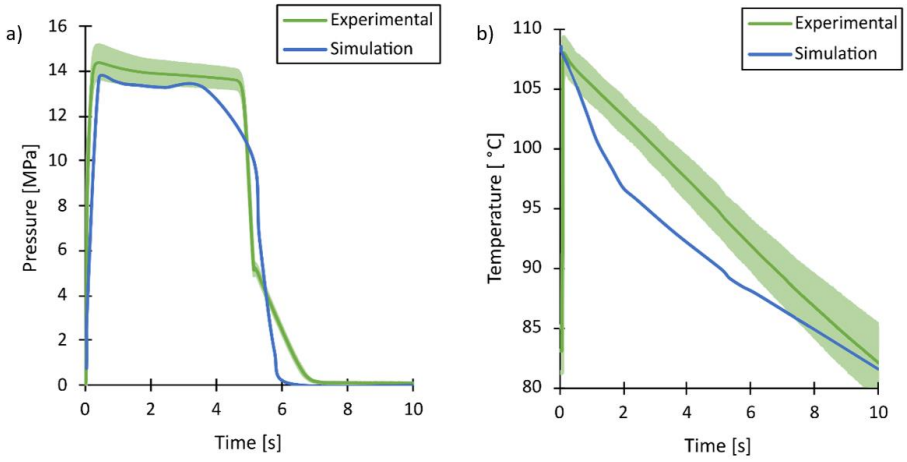


Figure 42: Comparison between the simulated and experimental mould cavity (a) pressure and (b) temperature in function of time for polypropylene. The experimental curve shows the average obtained pressure and temperature profile (n = 3) and the shaded area corresponds to the 95 % confidence interval.

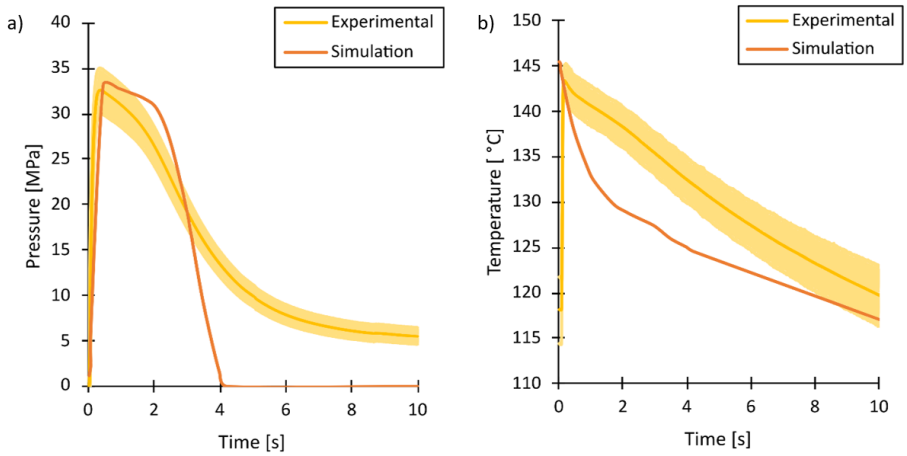


Figure 43: Comparison between the simulated and experimental mould cavity (a) pressure and (b) temperature in function of time for polycarbonate. The experimental curve shows the average obtained pressure and temperature profile (n = 3) and the shaded area corresponds to the 95 % confidence interval.

### 6.5.2 Mesh convergence study

The average absolute deviation between the simulated and experimental replication fidelity of the microneedles in function of the number of mesh elements for PP and PC is shown in Figure 44. It is observed that there is a high average absolute deviation at a low number of mesh elements, indicating a bad correspondence to the injection moulded experiments. However, with an increase of the number of mesh elements, the deviation in the replication fidelity in height between the simulations and experiments drastically decreases from ± 20 % to ± 4 %, for both thermoplastics. In addition, it is clear that the result converges with an increasing number of mesh elements and an accurate result is already found around 2.4 million mesh elements. Thus, in further simulations, the finite element mesh with 2.4 million mesh elements was used, as it results in a satisfactory solution with a computational time lower than 2 hours.

The time needed to predict the simulated replication fidelity of one sample with 16 microneedle arrays for one set of injection moulding parameters and one material combination corresponds to a maximum of 2 hours. In contrast, the time needed to determine the experimental replication fidelity of one sample with 16 microneedles arrays corresponds to approximately 10 hours. Thus, conducting an injection moulding simulation to predict the microneedle replication fidelity is at least 5 times faster compared to the experimental approach.

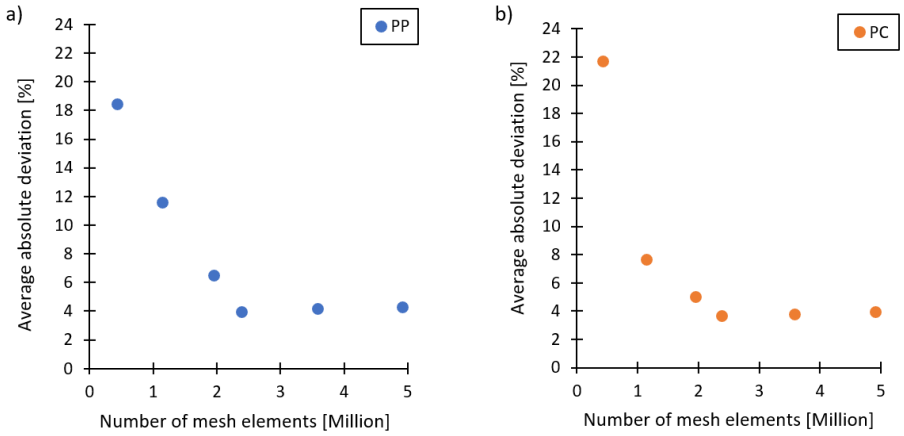


Figure 44: The average absolute deviation between the simulated and experimental replication fidelity of the microneedles in function of the number of mesh elements for (a) polypropylene and (b) polycarbonate.

### 6.5.3 Effect of the heat transfer coefficient

The average absolute deviation between the simulated and experimental replication fidelity of the microneedles in function of the varied HTC for PP and PC is depicted in Figure 45. The red dotted lines correspond to the average absolute deviation when using the automatically determined HTC in Moldex3D. It is observed that the average absolute deviation between the simulated and experimental replication fidelity is clearly affected by the HTC value. At a low HTC, the simulated microneedles are overfilled compared to the experiments, indicated by a large deviation between the simulated and experimental replication fidelity. When the HTC is increased, the filling of the microneedles decreases and a minimum deviation is found. Further increasing the HTC results in a faster solidification of the simulated needles, causing the needles to be underfilled compared to the experiments. Thus, the deviation between the experimental and simulated replication fidelity starts increasing again. For PP the minimum deviation is found at a HTC of 10,000 W/m²·K, while for PC it is obtained at 30,000 W/m²·K. Both values correspond well to optimal HTC values found in literature , being 10,000 W/m²·K for PP [269] and 30,000 W/m²·K for PMMA and COP [272], [273]. The difference in the optimal HTC value between the two thermoplastic polymers is due to the fact that these materials have different thermal properties, such the thermal conductivity, no-flow temperature, and heat capacity which affect the heat transfer between the thermoplastic and the mould material. A surprisingly low average absolute deviation is found between the simulations and experiments at the optimal HTC values of only 4.0 % and 3.7 % for PP and PC, respectively. Thus, the accuracy of the simulated replication fidelity corresponds to 96 % and 96.3 %. Besides, when using the default automatically determined HTC, the deviation between simulation and experiments are still acceptable, being 5.1 % and 7.2 % for PP and PC, respectively.

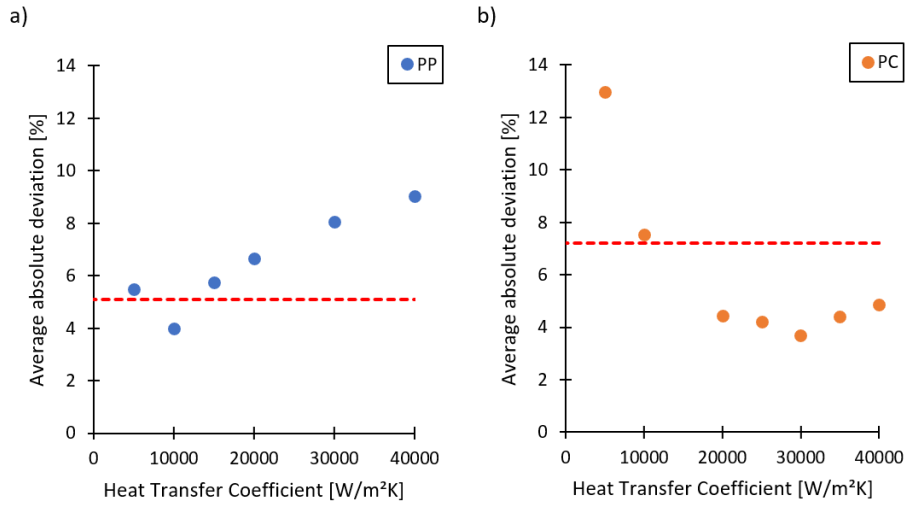


Figure 45: The average absolute deviation between the simulated and experimental replication fidelity of the microneedles in function of the varied HTC for (a) polypropylene and (b) polycarbonate. The red dotted lines correspond to the average absolute deviation when using the automatically determined HTC in Moldex3D.

Figure 46 shows the experimental and simulated replication in height of the 16 different microneedle arrays, in function of the aspect ratio of the microneedle cavity. The optimally determined HTC was used for both polymers, being 10,000 W/m²·K and 30,000 W/m²·K for PP and PC, respectively. A very good correlation between the experimental and simulated replication in height is observed both for PP and PC being 4.0 % and 3.7 %, respectively. Besides, a clear linear relationship between the replication in height and the aspect ratio of the corresponding microneedle cavities is found. This relationship is caused by two phenomena, being an increased hesitation effect with higher aspect ratio microcavities and an increased heat transfer due to the increased surface area to volume ratio, as previously discussed in [247]. Besides, it can be observed that the replication fidelity for the PP grade is higher compared to the PC grade, as the replication in height at an aspect ratio of 7 is approximately 40% for PP and only 15% for PC. This difference in replication is possibly caused by four factors, being linear shrinkage, interfacial wetting behaviour, creep deformation behaviour and melt viscosity as further discussed in [247].

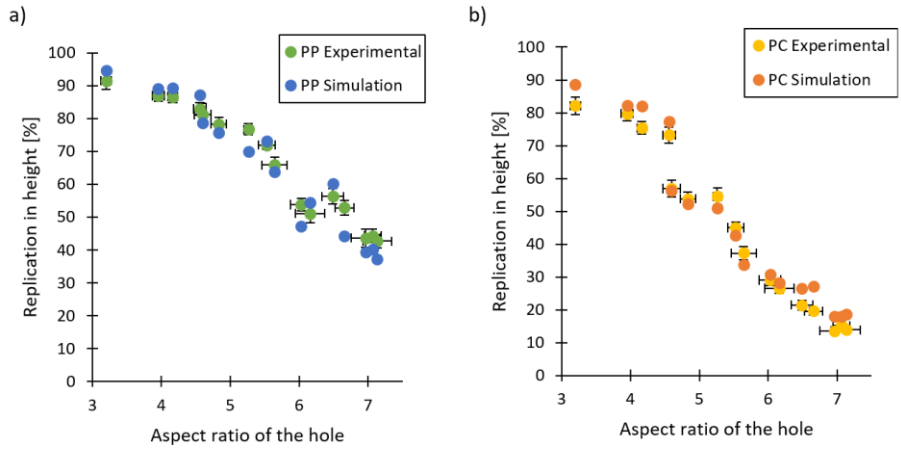


Figure 46: The experimental and simulated replication in height of the 16 different microneedle arrays, in function of the aspect ratio of the micro hole for (a) polypropylene with a HTC of 10,000 W/m²·K and (b) polycarbonate with a HTC of 30,000 W/m²·K. The vertical error bars represent the combined 95 % confidence interval of the hole depth and the replicated microneedle; the horizontal error bars represent the combined 95 % confidence interval of the hole depth and the hole diameter.

### 6.5.4 Replication fidelity in function of the location of the microfeatures

Figure 47 illustrates the replication in height of the microneedles located close to the gate and far from the gate for PP and PC. Again, it can be seen that there is only a small deviation between the simulated replication in height and the corresponding experimentally determined height, for both the array located close to the gate and far from the gate. An average absolute deviation between the simulations and experiments of 5.9 % and 6.5 % was found for PP and PC, respectively. Thus, a good correspondence between the simulated replication fidelity and the experimentally determined replication fidelity is also found for a different location of the microfeatures on the macroscopic part.

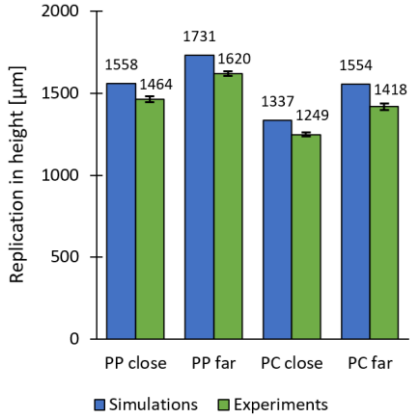


Figure 47: Difference in replication in height between the microneedles close to the gate and far from the gate for polypropylene and polycarbonate. The error bars represent the 95 % confidence interval.

A significant difference in the replication in height is observed between the microneedles located close to the gate and located far from the gate. The difference between the two locations is, as already indicated, a result of a different temperature, pressure and viscosity of the polymer melt during the filling of the two microneedle arrays. In our case, the microneedle array located far from the gate has a higher replication fidelity compared to the array located close to the gate. This result contradicts Lucchetta et al. who found a better replication fidelity for microfeatures closer to the gate [278]. However, the microfeatures investigated in their study are much smaller, being micro grooves with a width of 3 μm and an aspect ratio of 5. In their study, the microfeatures are solely filled during the initial filling stage, as the polymer immediately starts solidifying when coming in contact with the colder mould. Therefore, the area on the product with the highest pressure during the initial injection phase is located close to the gate and results in the best replication fidelity.

To explain the different filling behaviour observed in our case, we generated a XY cross-section of the part, enabling the visualisation of the temperature and pressure gradient throughout the width and thickness of the microneedle as illustrated in Figure 48 (a). The microneedles located close to the gate are almost completely filled during the initial filling stage as shown in Figure 48 (b) and Figure 48 (c). However, the melt rapidly starts cooling down from the moment of the initial contact with the mould. Consequently, at the moment when the cavity is completely filled and the cavity pressure is maximal, the temperature of the melt has already decreased far below the no-flow temperature and thus the microneedle is unable to be further filled. The initial filling of the microneedles located far from the gate is delayed due to increased flow length illustrated in Figure 48 (b) and Figure 48 (c). However, the temperature of the melt during the filling of the microneedles is still very high due to the characteristic fountain flow found for injection moulding. Only shortly after the melt reaches the microneedles far from the gate, the macroscopic part is completely filled and the pressure reaches a maximum, illustrated in Figure 48 (d) and Figure 48 (e). At that moment, the temperature within the needles located far from the gate is still above the no-flow temperature and thus ensures the needles to be further filled.

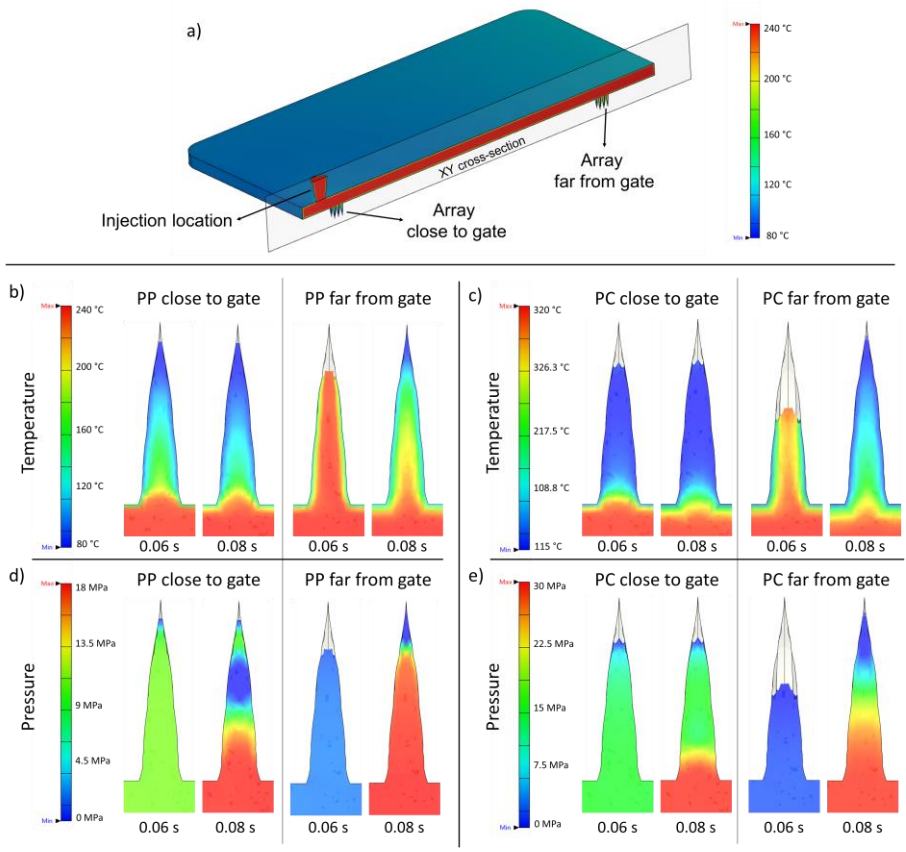


Figure 48: (a) Illustration of the XY cross-section of the PP part; cross-sections with time dependent filling and temperature progress of the microneedles close and far from the gate for (b) PP and (c) PC; cross-sections with time dependent filling and pressure progress of the microneedles close and far from the gate for (d) PP and (e) PC.

### 6.5.5 Replication fidelity in function of the injection moulding parameters

Figure 49 illustrates the experimental and simulated replication in height of the microneedle arrays created with the adapted injection moulding parameters, in function of the aspect ratio of the micro hole, for PP and PC. As expected, the adapted lower injection moulding parameters illustrated in Table 9 resulted as a lower replication fidelity, compared to the replication fidelity created with the elevated injection moulding conditions, illustrated in Table 8. Besides, when comparing the simulated and experimentally determined replication fidelity, it can be perceived that the results are in very good agreement. In fact, the average absolute deviation between the simulated and experimental replication fidelity of the 16 different arrays of 9 microneedles corresponds to 4.3 % and 4.4 % for PP and PC, respectively. Thus, a good correspondence between the simulation and experiments is also found when using different injection moulding parameters.

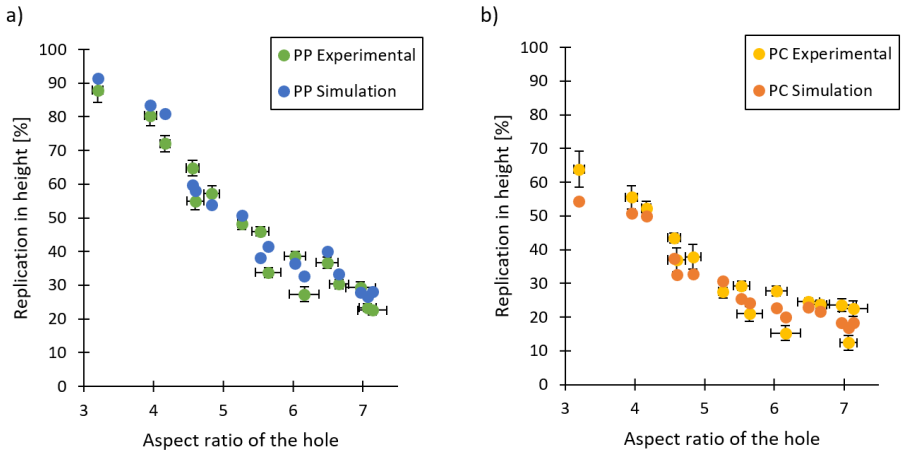


Figure 49: The experimental and simulated replication in height of the 16 different microneedle arrays created with the adapted injection moulding parameters, in function of the aspect ratio of the micro hole, for (a) polypropylene with a HTC of 10,000 W/m²·K and (b) polycarbonate with a HTC of 30,000 W/m²·K. The vertical error bars represent the combined 95 % confidence interval of the hole depth and the replicated microneedle; the horizontal error bars represent the combined 95 % confidence interval of the hole depth and the hole diameter.

### 6.5.6 Replication fidelity in function of the mould material

Figure 50 and Figure 51 depict the average absolute deviation between the simulated and experimental replication fidelity of the microneedles in function of the varied HTC for both polymers, in combination with the aluminium alloy and the copper alloy, respectively. Once again, the same trend is observed that with an increasing HTC, the deviation between the simulation and experiments decreases to a minimum, followed by an increase when the HTC is further increased. For the aluminium alloy, a minimal deviation of 3.0 % is found at a HTC of 25,000 W/m²·K for PP, while for PC a minimal deviation of 5.5 % was observed at a HTC of 55,000 W/m²·K. For the copper alloy, a minimum deviation of 4.7 % is found for PP at 10,000 W/m²·K and for PC a minimum of 3.3 % is found at 35,000 W/m²·K. Thus, also here a high simulation accuracy between 94.5 % to 97.0 % is found by varying the HTC value. For the aluminium and copper alloy, higher absolute average deviations are found when using the automatically HTC by Moldex3D. The highest deviation is observed for PC in combination with aluminium being 16.3 %, which indicates that this automatically determined HTC does not always result in a reliable solution.

Different optimal heat transfer coefficients are found for the three mould materials, as summarised in Table 10. The highest optimal HTC value for both polymers is found for the aluminium alloy insert, while the HTC values for tool steel and copper alloy insert are almost identical. One would assume that the highest thermal diffusivity would correspond to the highest heat transfer coefficient as demonstrated by Lucchetta et al. [240]. However, copper alloy having the highest thermal diffusivity, has a similar HTC value compared to tool steel. Thus, no clear correlation is found between the optimal HTC values and the thermal diffusivity (indicated in Table 7). However, there is a correlation between the HTC values and the experimentally determined replication fidelity for the different mould materials. In our previous study, it was shown that the

replication fidelity of the microneedles with tool steel and copper alloy were comparable, while the replication fidelity with the aluminium alloy was significantly lower [247]. This was explained by the fact that the replication fidelity was not only influenced by the thermal properties of the mould material, but also by the wetting properties between the molten polymer and the mould surface. Tool steel exhibited the best thermal properties, being of a low thermal diffusivity which delayed the formation of the frozen layer, but it was combined with bad wetting properties. Copper alloy on the other hand had the best wetting property, combined with a high thermal diffusivity. The aluminium alloy however, had both bad thermal and wetting properties, which resulted in the lowest replication fidelity. Thus, if different mould materials are used, the heat transfer coefficient should be adapted to compensate both the thermal and the wetting properties.

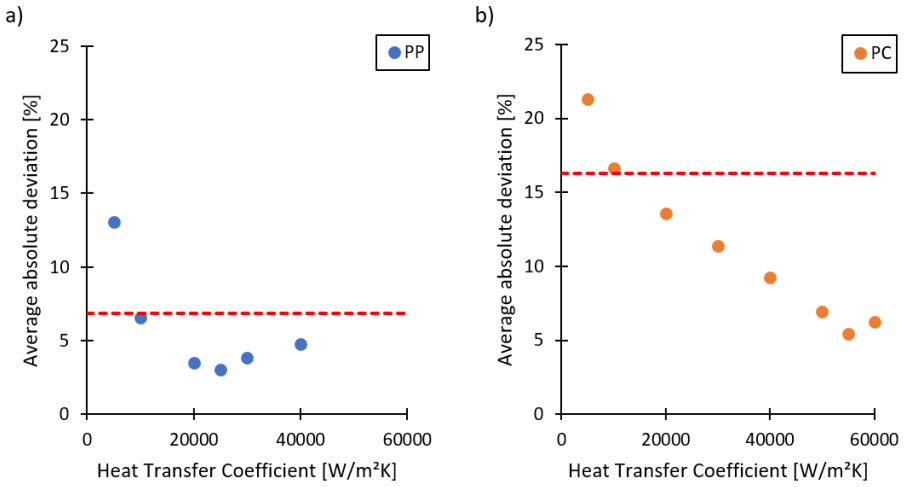


Figure 50: The average absolute deviation between the simulated and experimental replication fidelity of the microneedles created with the aluminium alloy, in function of the varied HTC for (a) polypropylene and (b) polycarbonate. The red dotted lines correspond to the average absolute deviation when using the automatically determined HTC in Moldex3D.

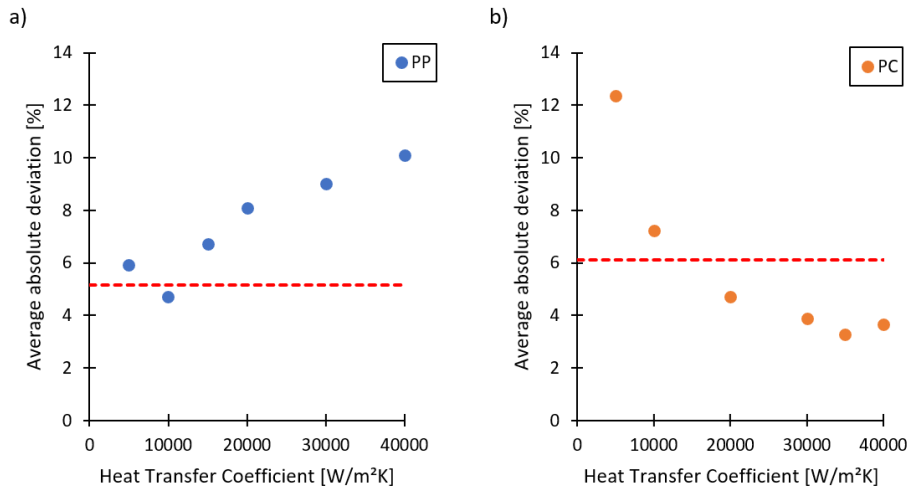


Figure 51: The average absolute deviation between the simulated and experimental replication fidelity of the microneedles created with the copper alloy, in function of the varied HTC for (a) polypropylene and (b) polycarbonate. The red dotted lines correspond to the average absolute deviation when using the automatically determined HTC in Moldex3D.

Table 10: Heat transfer coefficients, corresponding to a minimal average absolute deviation between the simulated and experimentally determined replication fidelity, for the PP and PC in combination with the tool steel, the aluminium alloy and the copper alloy mould insert.

| | PP | PC |
|---|---|---|
| Optimal HTC for tool steel [W/m²·K] | 10,000 | 30,000 |
| Optimal HTC for aluminium alloy [W/m²·K] | 25,000 | 55,000 |
| Optimal HTC for copper alloy [W/m²·K] | 10,000 | 35,000 |

Figure 52 and Figure 53 represent the experimental and simulated replication in height of the different microneedle arrays, in function of the aspect ratio of the microneedle cavity created with the aluminium alloy and copper alloy, respectively. The optimally determined HTC value was used for the different mould materials. As already indicated by the average absolute deviation, a very good correlation is found between the experimentally determined and simulated replication in height for both mould materials and polymers. This indicates that a good correspondence between simulation and experiments for different mould and polymer materials is possible, when using an adequate HTC.

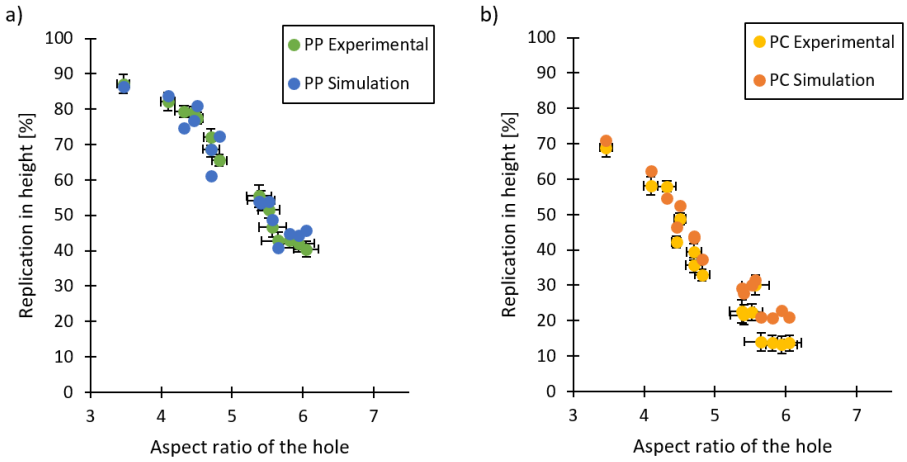


Figure 52: The experimental and simulated replication in height of the 16 different microneedle arrays created in the aluminium alloy, in function of the aspect ratio of the micro hole for (a) polypropylene with a HTC of 25,000 W/m²·K and (b) polycarbonate with a HTC of 55,000 W/m²·K. The vertical error bars represent the combined 95 % confidence interval of the hole depth and the replicated microneedle; the horizontal error bars represent the combined 95 % confidence interval of the hole depth and the hole diameter.

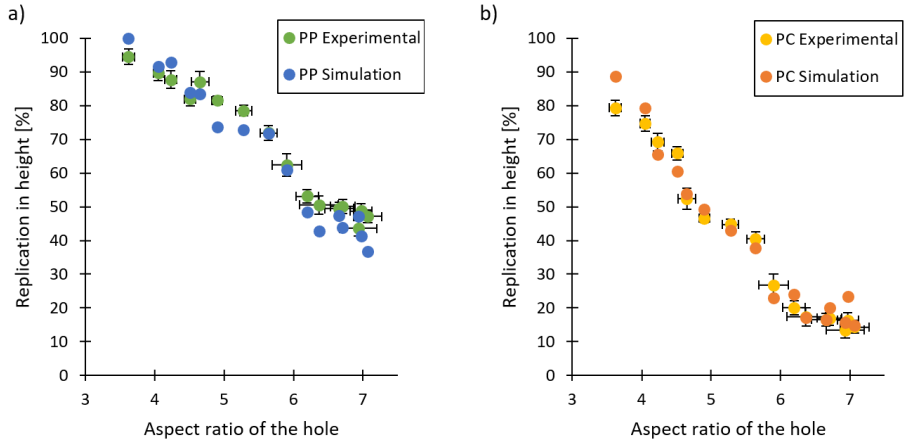


Figure 53: The experimental and simulated replication in height of the 16 different microneedle arrays created in the copper alloy, in function of the aspect ratio of the micro hole for (a) polypropylene with a HTC of 10,000 W/m²·K and (b) polycarbonate with a HTC of 35,000 W/m²·K. The vertical error bars represent the combined 95 % confidence interval of the hole depth and the replicated microneedle; the horizontal error bars represent the combined 95 % confidence interval of the hole depth and the hole diameter.

## 6.6 Conclusion

The present chapter evaluated the simulated replication fidelity of polymer microneedles compared to injection moulding experiments. These simulations could greatly benefit the development of polymer microneedle arrays, as it would be possible to provide quick answers about optimal process parameters and mould materials to achieve a good replication fidelity for different microneedle sizes and geometries without the necessity of carrying out real injection moulding experiments. We validated the simulated replication fidelity for (i) polypropylene and polycarbonate, (ii) different locations of the microneedles on the macroscopic polymer part, (iii) different injection moulding parameters, and (iv) different mould materials being tool steel, copper alloy and aluminium alloy.

To reduce computational time, filling simulations were conducted without including cooling and warping sequences. Macroscale boundary conditions such as the cavity temperature and pressure were validated by comparing in-mould sensor measurements to simulated data-points. An accuracy of the simulated microneedle replication fidelity between 94.5 % to 97.0 % was achieved, when taking into account two key factors. First, the mesh size is an important parameter to achieve accurate simulations. In fact, for macroscopic parts with micro surface features, it is recommended to use multi-scale meshing to achieve a finer mesh within the microfeatures, compared to the other regions of the macroscopic part. We conducted a mesh convergence study, to define a mesh size having both an acceptable solution and a computation time below 2 hours using an Intel Core i7-9850H Processor. It was found that the deviation between the simulations and experiments drastically decreases with an increase in mesh elements. Conducting an injection moulding simulation to predict the microneedle replication fidelity was at least 5 times faster compared to the experimental approach.

Second, the heat transfer coefficient is of prime importance when conducting filling simulations on microscopic features as it determines the formation of the frozen skin layer. We determined an optimal heat transfer coefficients for PP and PC in combination with the three different mould materials, by varying the HTC. Different optimal HTC values between 10,000 $W/m^2 \cdot K$ to 55,000 $W/m^2 \cdot K$ were found for the different mould and polymer combinations due to the differences in thermal and wetting properties. The minimum average deviation at the optimal HTC values was in all cases lower than the automatically determined HTC value by Moldex3D.

A difference in replication in height was observed between the microneedles located close to the gate and located far from the gate. The microneedles located far from the gate had a significantly higher replication fidelity compared to the array located close to the gate. This result was explained by the different temperature and pressure of the polymer melt, during the filling stage between the two different locations. In summary, Moldex3D simulations can be used to accurately predict the filling behaviour of micro surface features on a macroscopic part for different micro-feature sizes and geometries, different injection moulding parameters, different polymers and different feature locations on the macroscopic part, while using an adequate HTC and mesh size.

# Chapter 7 Comparing the replication fidelity of solid microneedles using injection compression moulding and conventional injection moulding

Evens T., Castagne S., Seveno D. and Van Bael A. Comparing the Replication Fidelity of Solid Microneedles Using Injection Compression Moulding and Conventional Injection Moulding. Micromachines, 13 (8): Art.No. 1280, 2022. Some parts of the original publication are left out or modified to avoid redundancy.

## 7.1 Abstract

Polymer surfaces are increasingly being functionalized with micro- and nano- surface features using mass replication methods like injection moulding. An example of these are microneedle arrays, which contain needle-like microscopic structures, which facilitate drug or vaccine delivery in a minimally invasive way. In this study, the replication fidelity of two types of solid polycarbonate microneedles was investigated using injection compression moulding and conventional injection moulding. Using a full factorial design of experiments for the injection moulding process, it was found that the volumetric injection rate had the largest positive effect on the replication fidelity. The mould temperature and holding pressure were also found to have a positive effect, while the effect of the melt temperature was found to be insignificant for the considered temperature range. For the injection compression moulding process, it was found that a larger compression stroke resulted in a better replication fidelity. A comparison between the replication fidelity for the injection moulding and injection compression moulding indicated that the injection compression moulding process resulted in a higher and more uniform replication fidelity. Using finite element flow simulations, a higher and more evenly distributed cavity pressure was observed compared to the conventional injection moulding process.

## 7.2 Introduction

Integrating functional micro- and nano- surface features on polymeric surfaces has become increasingly popular over the last decades, as these products can offer a wide range of potential applications for different markets [279]. An example of this, found in the medical field are microneedle arrays, which are invasive needle-like micro features, used to (i) deliver medical solutions or (ii) to extract fluids from a body for sampling applications. Various types of microneedles have been developed in the recent years,

having various shapes and lengths ranging from 25 to 2500 μm [8]. Over the last years, we have developed a mass production method to produce solid [216] and hollow microneedle arrays [257]. In this method, polymer injection moulding is used to replicate microneedle cavities, which are created using laser ablation. The microneedle cavities can be laser ablated in various mould materials and the cavity geometry can be adapted by changing laser scanning parameters as shown in [247]. Moreover, in a recent work we evaluated the simulated injection moulded replication fidelity using finite element flow simulations and found that the replication fidelity could be predicted with an accuracy between 94.5 % to 97.0 % [280].

Having a low tip radius is essential for the polymer microneedles, as it reduces the penetration force needed to pierce the skin [7]. Although the laser ablated microneedle cavities have already proven to be very sharp, it is still necessary to have a good replication fidelity during the injection moulding process. However, obtaining a high and uniform replication fidelity of micro surface features has proven to be challenging. In order to find injection moulding conditions with an optimal replication fidelity, various researchers have performed Designs of Experiments (DoE) [187], [188], [284]–[288], [193], [244], [276]–[278], [281]–[283]. As a result, it is possible to understand the effect of each injection moulding parameters on the replication fidelity. However, some researchers still observed an inhomogeneous replication fidelity over the product surface, due to an uneven temperature and pressure distributed in the mould cavity [187], [283], [289], [290]. A possible candidate to overcome the inherent limitations of an unevenly distributed cavity pressure in conventional injection moulding, is injection compression moulding.

In injection compression moulding, the melt is injected into a slightly opened cavity, with the two mould halves initially being separated from each other [183]. After the injection phase (i.e. after filling 90-98% of the total product volume), the mould closes and compresses the melt in the cavity. The additional gap between the moulds is defined as the compression stroke, which provides the necessary distance to perform the compressing action. A major advantage of injection compression moulding is the ability to reduce stress in the part, as during the compression phase the closing force is applied on the entire product surface, ensuring a uniform pressure distribution inside the cavity [180], [188], [283]. For this reason, injection compression moulding has been extensively favoured to conventional injection moulding in the production of optical components, as it is proven to reduce birefringence (double refraction) and enhance optical properties [188], [289]. However, the mould compression phase increases the complexity of the production process and the additional compression stroke must be taken into consideration while optimizing the process. Suzuki et al. presented the importance of increasing the compression stroke in order to improve surface replication [291]. Yet on the contrary, Masato et al. [248] observed a negative impact of a large compression gap on the replication homogeneity for micro grooves with a depth of 15 μm and a width of 3 μm. Moreover, a significant interaction between the compression gap and the injection velocity was found, further confirming that the optimization of the compression gap must be taken into account in the overall polymer flow conditions. Injection compression moulding was also successively used to produce microlenses and periodic micro feature arrays by [292] and [293], yet the authors did not investigate the effect of the process parameters on the replication fidelity. Loaldi et al. compared the replication capability of injection moulding and injection compression moulding for a micro structured Fresnel lens. It was shown that the injection compression moulding improved the micro-replication while using a high holding pressure in combination with a lower compression

stroke [188]. A few authors found that the mould temperature had a significant effect on the replication fidelity of micro- and nano- surface texture replicated using injection compression moulding, as high mould temperatures improved the replication fidelity [184], [283], [294].

Although most authors indicate the mould temperature to have a significant positive effect on the replication fidelity, the effect of the other injection moulding parameters is often inconclusive. In fact, some researchers found that the volumetric injection rate, holding pressure and melt temperature had a positive effect on the replication fidelity, while others found these parameters to have a negative or insignificant effect. Moreover, a wide variety of micro surface features have been investigated in literature, yet most of them have a low aspect ratio (< 2) with geometrical dimensions in the range of 10-100 μm. A detailed study on the effect of processing parameters in injection moulding for the replication of large micro surface features with high aspect ratios is currently lacking. The investigated microscopic products in literature are usually small flat plates in the order of a few millimetres, yet the size of the product surface will play an important role in the replication fidelity and replication uniformity. This replication uniformity over the complete product surface is often overlooked or poorly discussed. Although injection compression moulding is often applied to manufacture polymeric products with micro- and nano- surface features, no studies have been found which compare the replication fidelity of large micro features for conventional injection moulding and injection compression moulding, while taking into account the difference in flow behaviour.

In this study, we investigate the replication fidelity of solid polycarbonate microneedles using injection compression moulding and conventional injection moulding. For this, a mould cavity insert for a large 112 mm x 70 mm x 1.7 mm flat polymer plate is created. Two types of microneedle cavities having a depth of 1959 μm and 1125 μm are laser ablated on 15 locations. A DoE will be performed, to define process parameters which correspond to an optimal replication fidelity for the microneedles in the injection moulding process. Furthermore, the compression stroke, which correlates with an optimal replication fidelity of the microneedles will be determined for the injection compression moulding process. Afterwards, a comparison between the replication fidelity of the injection moulding and injection compression moulding process will be made, and the difference in filling behaviour will be discussed using finite element flow simulations.

## 7.3 Materials and Methods

### 7.3.1 Thermoplastic and mould material

The thermoplastic material used in this study is polycarbonate (PC, Lexan™ HPX8REU, manufactured by Sabic, Bergen op Zoom, The Netherlands), as this grade is suitable for medical devices and pharmaceutical applications. The thermoplastic has a high flowability indicated by the melt mass-flow rate of 35 g/10min (300°C/1.2 kg) and a glass transition temperature of 141 °C.

The selected material for the mould insert is a low corrosion tool steel "Stavax" (grade 1.2083 - AISI 420), having a high corrosion and wear resistance.

### 7.3.2 Mould product cavity and laser machining experiments

The mould product cavity is a 112 mm x 70 mm x 1.7 mm flat plate, which is machined within the tool steel mould insert. Moreover, two different arrays of microneedle cavities were machined in the mould product cavity on 15 locations, as illustrated in Figure 54. The machining of the microneedle cavities was done using a femtosecond laser ablation process, as described in a previous work [216]. In this strategy, the laser spot scans a circular region with a specified diameter, and follows parallel lines in two perpendicular directions. The distance between two consecutive lines is defined as the hatch pitch. Once the laser has scanned one circular grid, the focal point is lowered (with a vertical distance defined as the layer pitch) and the laser scans again the same area. This process is repeated multiple times for a prescribed number of layers. The hatch pitch and layer pitch were fixed at 15 μm and 2 μm, respectively. The first type of microneedle cavities will be referred to as "large microneedles" and were created using a base diameter of 400 μm and 600 layers. The second type of cavities will be referred to as "small microneedles" and were created using a base diameter of 300 μm and 150 layers.

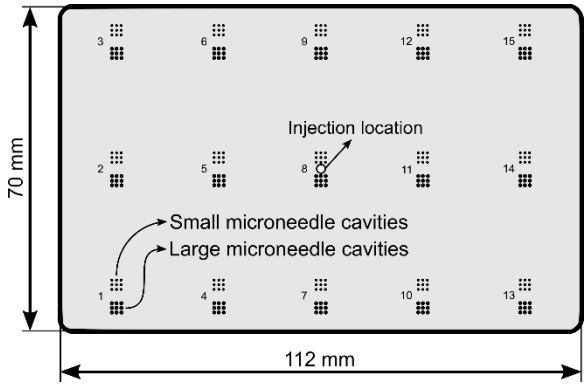


Figure 54: Illustration of the flat plate mould product cavity, including the two different arrays of microneedle cavities located on 15 locations. The polymer is injected through a hot runner, located in the centre of the mould product cavity

### 7.3.3 Experimental injection moulding set-up

The injection moulding machine used for this study is an Engel ES 200/35 HL hydraulic injection moulding machine with a maximum clamping force of 350 kN and a 25 mm horizontal screw with an L/D ratio of 24.8. The machine is equipped with a hydraulic accumulator to increase the volumetric injection rate and the injection speed to 149 $cm^3/s$ and 300 mm/s, respectively. Moreover, the injection moulding machine is also equipped with an injection compression moulding module, which allows the machine to be used for both conventional injection moulding (IM) and injection compression moulding (ICM). The ICM process allows for the polymer melt to be injected in a slightly open mould with a defined compression stroke. Once the injection phase has reached the switch-over point, the machine applies the clamping force and closes the two mould halves. The temperature of the mould is controlled by a Wittmann Tempro D controller. The polymer is injected through a hot runner, located in the centre of the mould product cavity, as illustrated in Figure 54.

The stationary side of the injection mould is equipped with a temperature sensor (Priamus, 4008B, Priamus System Technologies, Schaffhausen, Switzerland) and a piezoelectric pressure sensor (Priamus, 6001B, Priamus System Technologies, Schaffhausen, Switzerland), which are located opposite to array number 7. The sensors allow for precise process control and online measurement of the apparent viscosity. This viscosity measurement is a built-in module in the Priamus FILLCONTROL. The online apparent viscosity is measured for the two volumetric injection rates used in this study, being 50 $cm^3/s$ and 150 $cm^3/s$.

The barrel temperature, volumetric injection rate, holding pressure and mould coolant temperature were varied in the DoE, while the holding pressure time and cooling time were kept constant through all experiments for both IM and ICM at 10 seconds and 20 seconds, respectively. The additional 'compression stroke' parameter within the ICM process was varied from 1 mm to 5 mm in steps of 1 mm, at a compression speed of approximately 50 mm/s. For each experimental run, the first 20 moulded parts were discarded and the following 15 samples were kept for evaluation.

### 7.3.4 Two-level full factorial design

A two-level full factorial design was formulated to identify the combination of injection moulding parameters that have the highest replication fidelity during IM. With a $2^4$ design it is possible to analyse both the main effect as well as the two- and three-factor interactions [295]. Parameters varied in this study are the barrel temperature, volumetric injection rate, holding pressure and mould coolant temperature, as these parameters are widely reported in literature as the most influential for the replication fidelity of micro-features. The levels of the process parameters were identified in preliminary experiments, starting from the manufacturer's recommendations and aiming at obtaining a consistent filling without the occurrence of needle breakage, short shots, sink marks or flash. The different settings for the production of the samples are presented in Table 11. Each setting was repeated 3 times and the injection moulding experiments were conducted in a random order. For each injection moulded sample, the average replicated microneedle length was calculated for both types of microneedles. To account for possible replication differences within the array, the first needle on the first row, the second needle on the second row and the third needle on the third row were measured for all arrays. The length of the replicated microneedles was used as input data in statistical software, being Minitab 17. The significance of each of the resulting terms was tested using a t-test with 0.050 as the significance level. The null hypothesis for this test is that the effect of a specific term is zero. When the P-value for a specific term is smaller than 0.050, we can reject the null hypothesis, concluding that the specific term is significant.

Table 11: Different settings for the process parameters used within the design of experiments.

| DoE run | Barrel temperature [°C] | Mould coolant temperature [°C] | Volumetric injection rate [$cm^3/s$] | Holding pressure [MPa] |
|---|---|---|---|---|
| 1 | 295 | 70 | 50 | 31.5 |
| 2 | 295 | 70 | 50 | 63.0 |
| 3 | 295 | 70 | 150 | 31.5 |
| 4 | 295 | 70 | 150 | 63.0 |
| 5 | 295 | 115 | 50 | 31.5 |

| | | | | |
|---|---|---|---|---|
| 6 | 295 | 115 | 50 | 63.0 |
| 7 | 295 | 115 | 150 | 31.5 |
| 8 | 295 | 115 | 150 | 63.0 |
| 9 | 315 | 70 | 50 | 31.5 |
| 10 | 315 | 70 | 50 | 63.0 |
| 11 | 315 | 70 | 150 | 31.5 |
| 12 | 315 | 70 | 150 | 63.0 |
| 13 | 315 | 115 | 50 | 31.5 |
| 14 | 315 | 115 | 50 | 63.0 |
| 15 | 315 | 115 | 150 | 31.5 |
| 16 | 315 | 115 | 150 | 63.0 |

### 7.3.5 Topography characterisation

The geometries of the ablated microneedle cavities were characterized using a Phoenix Nanotom micro-computed tomography (μ-CT) system. The device is equipped with a high-power nanofocus X-ray tube and a diamond-tungsten target was chosen for the high X-ray absorbing metal samples. For each CT-scan, 2400 X-ray 2D projection images were obtained from incremental rotation of the scanned samples over 360°. Acquisition parameters were fixed for all samples as follows: voltage = 100 kV, current = 158 μA, voxel size = 3.75 μm, and a 0.1 mm copper and 0.1 mm aluminium filter were used during scanning. Reconstructed XY datasets (slices) were exported from the software for further analysis and visualization within Fiji ImageJ. Before conducting measurements, the Nanotom instrument was calibrated using a calibration rod (Goekeler Messtechnik, VTX18CE000-022, Lenningen, Germany) with an uncertainty of 1.0 μm. For both types of microneedles, a 3x3 array of cavities was laser ablated on a tool steel sample (grade 1.2083 - AISI 420), with identical laser scanning parameters to the cavities produced on the mould insert. The average length and diameter of these 9 holes along with a 95 % confidence interval, using the Student's t-distribution was reported in the plotted results.

The geometries of the replicated thermoplastic microneedles were characterized using a digital microscope (model Keyence VH-S30, Keyence, Osaka, Japan) with a maximum magnification of 200X. The system is connected to a VHX-500 F monitor with built-in measuring software. The microscope was calibrated using a stage micrometre (Olympus Tokyo, OBMM 1/100, Tokyo, Japan) having an uncertainty of 0.5 μm.

### 7.3.6 Injection moulding simulations

The commercial software package Moldex3D studio (version 2021, Zhubei, Taiwan) was used to simulate the injection moulding process. In a previous study, the simulated replication fidelity of polymer microneedles using Moldex3D was compared to injection moulding experiments [280]. It was found that the replication fidelity of the microneedles could be predicted with an accuracy between 94.5 % to 97.0 %, using multi-scale meshing and optimizing the Heat Transfer Coefficient (HTC). An ICM module was also tested in the current study to understand the behaviour of the melt flow inside the macroscopic part. Predicting the replication fidelity inside the microneedles, however, was found to be unreliable as mesh elements were often filled inside the microneedle tip, without being in contact with already filled elements. Therefore, the ICM module was only used for simulating the macroscopic flow, while it was not used to predict the microscopic

replication fidelity. All simulations in this study were conducted using an Intel Core i7-9850H Processor with 12 cores and a random access memory (RAM) of 16 GB.

The surface of the polymer part was meshed using a 5-layer prismatic boundary layer mesh. Inwards from this surface mesh, a tetrahedral mesh filled up the remaining space, to obtain a total 11 layers across the part thickness. This amount of layers ensures an adequate representation of the laminar melt flow. Multi-scale meshing was used, in which the mesh is refined within the microfeatures to achieve a precise simulation, while a more coarse mesh is used in the macroscopic part. In our previous study [280], a mesh convergence study was conducted to define a satisfactory mesh size. It was found that the replication fidelity of the microneedles converged around 2.4 million mesh elements, corresponding to a mesh edge length of approximately 100 μm in the large microneedles and 50 μm in the smaller microneedles. Therefore, in this study a mesh edge length of 100 μm was also used in the large microneedles and 50 μm in the small microneedles, resulting in a total number of approximately 3.9 million solid mesh elements.

The injection moulding parameters, being the holding pressure, melt temperature and mould coolant temperature were set to the same values as used in the experiments. The injection speed in Moldex3D was defined as a filling time, which was calculated using the volume of the part and the known volumetric injection rate. The calculated time corresponded to 0.1 seconds, which is in agreement with the experimental filling time of the injection moulding machine. Another important model parameter, is the HTC, which defines the heat transfer between the polymer melt and the surrounding mould material. In our previous study [280], we determined the HTC value, having the best correspondence with the experimentally determined replication fidelity, by manually adjusting it. For PC in combination with a tool steel insert an optimal value of 30,000 $W/m^2 \cdot K$ was found. The HTC during the packing and detached phase were set to the default values used in Autodesk Moldflow, being 2500 $W/m^2 \cdot K$ and 1250 $W/m^2 \cdot K$, respectively. The last parameter that was adapted from the default value is the criterion for stopping the calculation. This parameter is linked to a function which aims to decrease the computational time. As default, this value is set as 99.95 %, which means that if the product is filled for 99.95%, Moldex3D assumes that the part is completely filled, without a short shot and will end the simulation early to save computational time. In our case, the incomplete filling of the microfeatures is smaller than 0.05 % of the complete volume of the part, thus Moldex3D displays the part as completely filled. To overcome this problem, the criterion for stopping the calculation is changed into 99.9999 %, enabling the simulation of incompletely filled microfeatures. A summary of the simulation parameters used in Moldex3D can be found in Table 12.

Table 12: IM simulation parameters.

| | PC |
|---|---|
| **Barrel temperature [°C]** | 315 |
| **Volumetric injection rate [$cm^3/s$]** | 150 |
| **Holding pressure [MPa]** | 63 |
| **Mould coolant temperature [°C]** | 115 |
| **HTC during filling stage [$W/m^2 \cdot K$]** | 30,000 |
| **HTC packing [$W/m^2 \cdot K$]** | 2500 |
| **HTC detached [$W/m^2 \cdot K$]** | 1250 |
| **Criterion for stopping calculation** | 99.9999 % |

## 7.4 Results and Discussion

### 7.4.1 Geometry of the ablated microneedle cavities

Figure 55 represents the XY datasets of the reconstructed μCT analysis for 3 large and 3 small microneedle cavities. The average cavity depth and cavity base diameter along with the standard deviation, for the complete array of 9 microneedles is also displayed for both types of microneedles. A clear difference in dimensions and shape is observed between both type of microneedle cavities, due to the difference in laser scanning parameters used for both types of microneedles. The effect of these laser scanning parameters, being the programmed base diameters and number of layers, on the cavity shape and dimensions are discussed in a previous study [247].

Although both types of microneedle cavities are different in shape and dimensions, it is clear that they both have very sharp tip radii. This is essential for creating sharp polymer microneedles, yet completely filling these needle tips will be nearly impossible in practice. However, the part of the needle tip that cannot be filled, will act as a kind of buffer, in which entrapped air can be collected during the filling process, thus reducing the risk of the so-called "diesel effect". This effect is an undesirable phenomenon causing thermal degradation of the thermoplastic, due to a very high pressure and temperature resulting from highly compressed air.

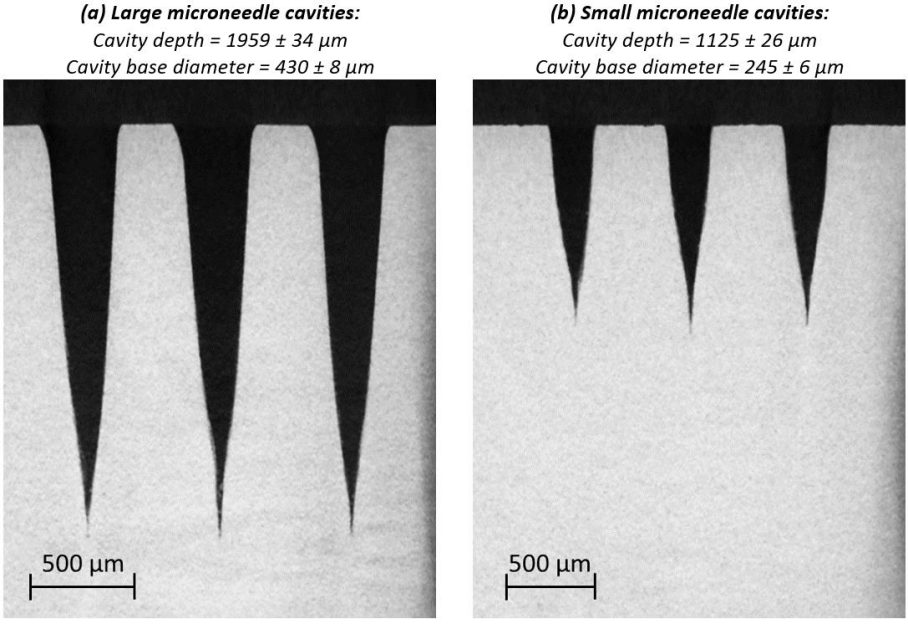


Figure 55: Representation of the XY datasets of the reconstructed μCT analysis for 3 large and 3 small microneedle cavities. The average cavity depth and cavity base diameter along with the standard deviation, for the complete array of 9 microneedles is also displayed for both types of microneedles.

### 7.4.2 DoE to define IM parameters for a high replication fidelity

The influences of the barrel temperature, volumetric injection rate, holding pressure and mould coolant temperature on the replication fidelity of two types of injection moulded microneedles were assessed by a full factorial DoE. During the injection moulding experiments, both microneedle arrays located in the middle of the part (array 8 on Figure 54) broke during demoulding, leaving the microneedles stuck inside the cavities. The reason why these microneedles broke was at first sight unclear and array 8 was therefore excluded from this study. To understand why the needles from array 8 failed, we created a cross section of the microneedle cavities using a metallographic saw and a high precision surface grinder. Figure 56 illustrates the grinded cross section of an empty large microneedle cavity and a large microneedle cavity from array 8 with an entrapped broken microneedle inside. It can be observed that the polymer almost completely filled the microneedle cavity. It is expected that the micro- and nano-surface roughness inside the microneedle cavities, which are induced during the laser ablation process, are therefore also replicated. This replicated roughness causes microscopic undercuts on the microneedle shaft, which result in the needle breakage during demoulding. Hopmann et al. also observed high demoulding forces, which caused micro-structures to break during demoulding [296]. The reason why the replication fidelity is so high for the microneedles from array 8, is due to the cavities being located directly opposite to the gate location. From the injection moulding simulations, it is observed that the polymer is directly injected into the microneedle cavities, causing already a high replication fidelity during the initial filling stage. Moreover, the pressure inside the microneedle cavities is very high during the packing phase, as the cavities are located very close to the gate location.

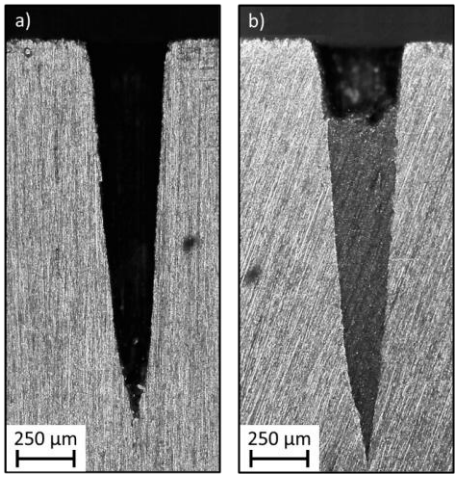


Figure 56: Illustration of a cross section of a microneedle cavity for (a) an empty large microneedle cavity, and (b) a large microneedle cavity from array 8 with an entrapped broken microneedle.

The factorial regression analysis assumes that the observations are normally distributed, randomised, and of equal variance at all response levels. By using the analysis of residuals, these 3 requirements were verified for both types of microneedles [295].

Figure 57 reports the average replication in height for the 16 DoE runs with a repetition of 3 for both the (a) and (b) the small microneedle arrays. No significant difference was noticeable between the 3 repetitions due to the overlapping confidence intervals, thus indicating a good repeatability of the injection moulding process. Clear differences in replication fidelity can be observed between the different DoE runs. This is further illustrated in Figure 58, which depicts one replicated large and small microneedle from array 2 for DoE run 3, 11, 12, and 13.

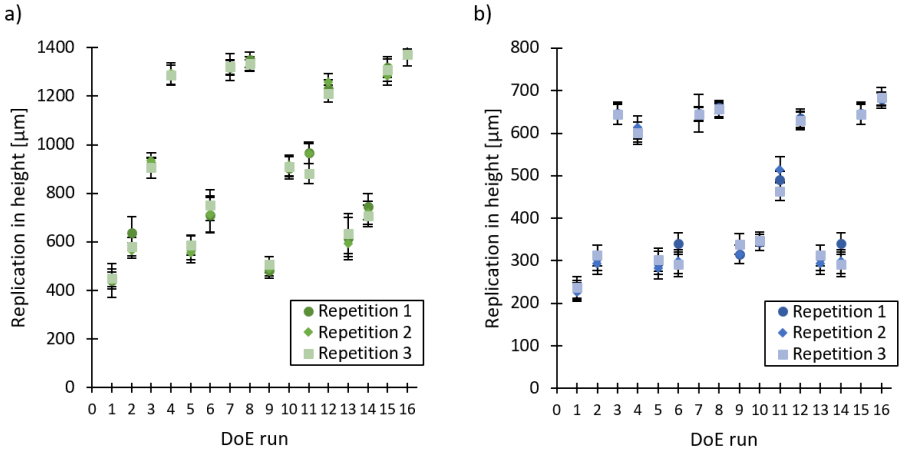


Figure 57: Average replication in height plotted against the 16 DoE runs with a repetition of 3 for (a) the large microneedle arrays and (b) the small microneedle arrays. The error bars represent the 95 % confidence interval.

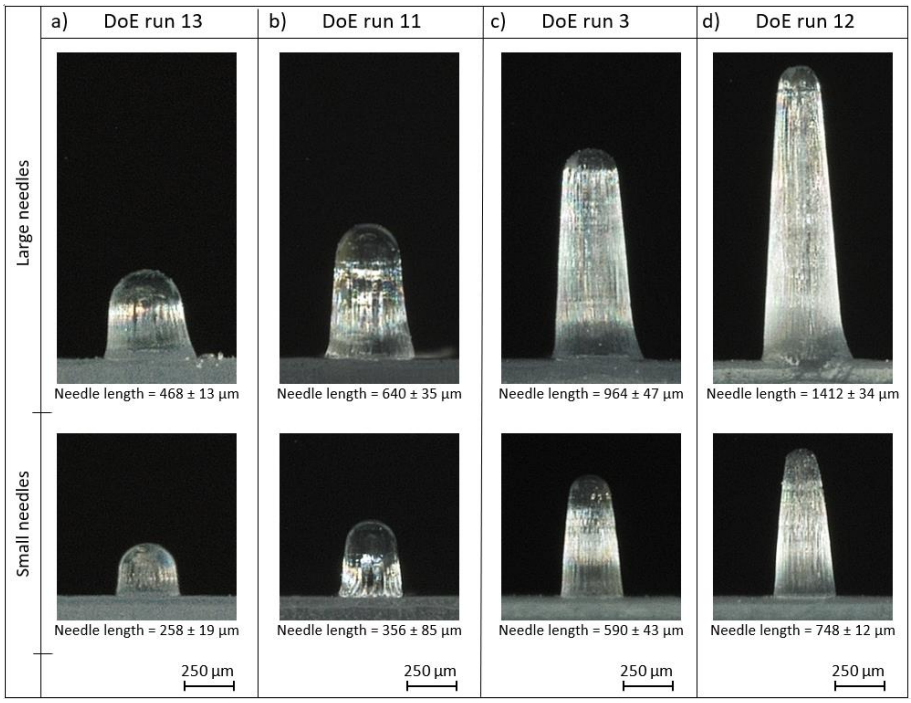


Figure 58: Illustration of one replicated large and small microneedle from array number 2 for (a) DoE run 13 (b) DoE run 11, (c) DoE run 3, and (d) DoE run 12. The average length of the needles are reported together with the standard deviation ($n$ = 9).

The results of the DoE analysis for both the large and small microneedles are depicted in Figure 59. The Pareto charts, main effect plots and two-factor interactions are shown. First, the 4 main effects are discussed for the large microneedles. From the Pareto chart, it can be observed that all main effects have a significant effect on the replication fidelity of the microneedles. The volumetric injection rate has by far the largest positive effect on the replication in height, ranging from approximately 600 to 1200 µm for respectively 50 and 150 cm³/s. This parameter is followed by the holding pressure and the mould coolant temperature, while the melt temperature has the lowest effect on the replication fidelity of the microneedles. Similar results can be found for the small microneedles, yet for these smaller features it can be observed that the melt temperature has no significant effect on the replication fidelity. The volumetric injection rate is once again the key parameter affecting the replication fidelity, ranging from approximately 300 to 650 µm for respectively 50 and 150 cm³/s. The mould and holding pressure have an almost identical positive effect on the replication fidelity.

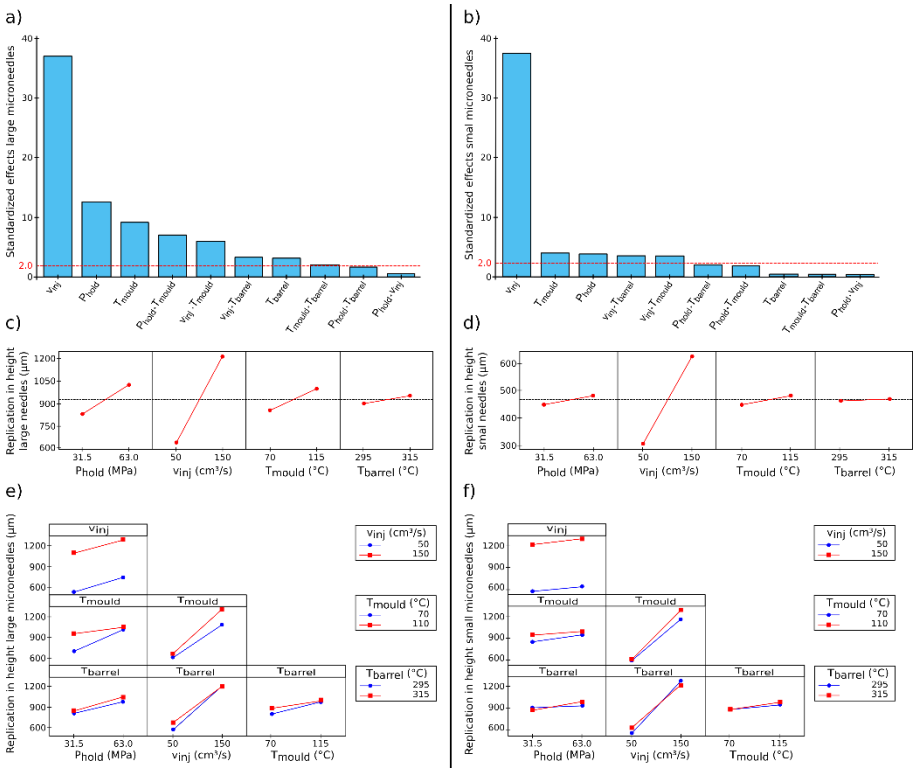


Figure 59: Illustration of the DoE results, with the barrel temperature ($T_{barrel}$), volumetric injection rate ($v_{inj}$), holding pressure ($P_{hold}$), and mould coolant temperature ($T_{mould}$) as the varied parameters. (a) and (b) show the Pareto charts for the large and small microneedles, respectively. The red dashed lines represents the significance limit at a confidence level of at 95%. (c) and (d) show the main effect plot for the replication in height for the large and small microneedles. (e) and (f) show the two-factor interactions for the replication in height for the large and small microneedles respectively.

From the two-factor interaction plots it is clear that for the large needles, the combination of holding pressure and mould temperature had a positive effect on the replication fidelity, while for the small needles this effect was insignificant. A possible explanation for this is that due to the higher mould temperature, the large needles were not completely solidified yet and the higher holding pressure further increased the degree of filling during the packing phase. This effect was not significant for the smaller needles, as these features solidify much faster due to their lower volume and did not deform during the packing phase. The volumetric injection speed in combination with the mould temperature and the volumetric injection speed in combination with the barrel temperature had a significant positive effect on the replication fidelity for both types of microneedles. For both cases, it can be assumed that a high volumetric injection speed in combination with a higher mould or barrel temperature increased the temperature of the polymer melt and decreased the melt viscosity, resulting in a higher replication fidelity.

For both types of microneedles, all main parameters and two-factor interactions were found to have a positive effect on the replication fidelity. This facilitates the setup of the

injection moulding process, as each injection moulding parameters should be set to the highest achievable value without causing injection moulding defects on the products.

#### 7.4.2.1 Volumetric injection rate

The volumetric injection rate has in both types of microneedles the highest positive effect on the replication fidelity. In fact, the volumetric injection rate has two positive effects on the polymer melt that improve the replication fidelity. First, an increase of the volumetric injection rate will promote shear heating, which will locally decrease the melt viscosity. Second, a high volumetric injection rate reduces the injection time, which in turn delays the formation of the frozen skin layer [134], [279]. From literature this parameter is known to have a positive effect on the filling of micro and nano surface features, as described by several researchers [187], [188], [302], [303], [276], [277], [282], [297]–[301]. However, high volumetric injection rates have also been reported to cause polymer degradation due to exceeding the maximum shear stress allowed by the polymer. Moreover, the high generated shear can also cause internal stress in the part, which could lead to damage of the micro-features or a poor surface quality [134], [297].

Figure 60 shows both the Cross-WLF (Cross–Williams–Landel–Ferry) viscosity curves for the investigated PC grade, extracted from Moldex3D and the online apparent viscosity, measured during injection moulding experiments using a barrel temperature of 315 °C. A shear rate of approximately 500 1/s and an apparent viscosity of 106 Pa.s was found for a volumetric injection rate of 50 cm³/s. While for the volumetric injection rate of 150 cm³/s a shear rate of 9900 1/s and an apparent viscosity of 30 Pa.s was found. This significant reduction in viscosity caused by the increase in volumetric injection rate, has for sure have a positive effect on the replication fidelity during the filling stage.

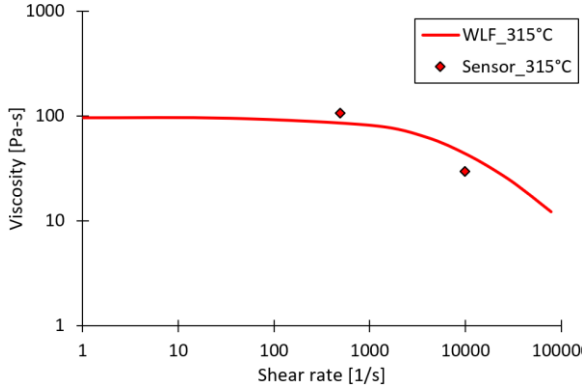


Figure 60: Illustration of the Cross-WLF model viscosity and online apparent viscosity for PC, measured at an injection rate of 50 cm³/s and 150 cm³/s in combination with a barrel temperature of 315 °C.

#### 7.4.2.2 Holding pressure

The second most important parameter influencing the replication fidelity is the holding pressure. In conventional injection moulding, this holding pressure compensates the polymer shrinkage to achieve the desired geometry after demoulding. In the injection moulding of micro and nano surface features, however, the holding pressure plays an

additional important role in the filling of the micro-features. The holding pressure is the key parameter that can force the polymer melt into the micro and nano cavities [260], [279]. No matter how high the melt temperature or how low the melt viscosity, a high pressure is still required to achieve a good replication fidelity. The positive effect of holding pressure on the replication quality of micro-features is also shown in multiple studies [188], [276], [281], [284]–[286], [298].

#### 7.4.2.3 Mould temperature

The mould temperature was found to have a significant positive effect on the replication fidelity of the large and small microneedles. In literature, the mould temperature is generally considered to be the most important parameter when it comes to replicating micro-features [244], [276], [277], [281], [283], [285], [286], [288], [298]. During the filling stage, the filling of the micro-features has to compete with the filling of the rest of the cavity. Yet, most of the material will flow in the main direction of the macroscale cavity as the polymer will follow the path of least resistance, leaving the micro-features only partially filled, also known as the hesitation effect [248]. Further filling the micro-features will only be possible during the packing stage, as during this phase the pressure in the cavity is substantially increased. However, it is impossible to further increase the filling of these micro-features, if they are already solidified at this moment. Therefore, it is essential that the solidification of the skin layer is delayed so the polymer can still be deformed during the packing phase. Some authors even implemented a rapid heat cycling approach, also called variothermal injection moulding to further improve the replication fidelity [184], [187], [278], [284], [287]. Here, the mould temperature is no longer a constant, but it is varied between a high value during the filling stage and a lower value during the cooling stage. The high value during the filling stage is typically taken above the glass transition temperature for amorphous materials and around the melting temperature for semi-crystalline polymers. This way the formation of a frozen layer is delayed, hence leading to a better filling of micro-features. Variothermal injection moulding is more complex and more expensive (due to more expensive moulds and side equipment) than IM, and also cycle times are substantially higher compared to conventional injection moulding. Mainly due to the increase in cycle time, this system was not considered in this study.

In this study, the mould temperature was found to have a significant positive effect on the replication fidelity, yet it is not the parameter with the highest effect. This interesting difference compared to several other studies, is expected to be due to two factors. First of all, there is a difference in size of the investigated micro-features compared to typical micro-features found in literature. In our study, the micro-features are microneedle cavities with a depth of approximately 1 mm and 2 mm, having cavity diameters of approximately 0.25 mm and 0.5 mm for the small and large microneedles, respectively. The investigated microcavities found in literature, however, are typically a few tens of micrometres in depth and width. The small microfeatures found in literature have a much higher surface area to volume ratio, which results in a much higher heat transfer between the molten polymer and the mould surface, which in turn results in a faster solidification of the polymer. Thus, for these smaller microfeatures it is crucial to delay the solidification by increasing the mould temperature. Secondly, some authors used the rapid heat cycling approach to increase the mould temperature, even above the glass transition temperature for amorphous polymers, before the injection phase. By doing so, the replication fidelity was significantly improved compared to conventional

isothermal injection moulding. Therefore, several authors found the mould temperature to be the parameter with the highest effect on the replication fidelity.

#### 7.4.2.4 Melt temperature

The last investigated parameter is the melt temperature. This parameter only had a small impact on the replication fidelity of the large microneedles and was even insignificant for the small microneedles. In literature, this parameter is also only found to have an impact on the replication fidelity of micro-features in a few studies [281], [284], [286]. A high melt temperature will decrease the melt viscosity, which has a positive effect on the replication fidelity of micro-features. A melt temperature above the recommended temperature range of the polymer manufacturer, however, can induce thermal degradation of the polymer inside the barrel and should therefore be avoided.

### 7.4.3 IM using parameters for an optimal replication fidelity

The DoE indicated that increasing all of the investigated parameters, being the barrel temperature, volumetric injection rate, holding pressure and mould temperature had a positive effect on the replication fidelity of the microneedles. Therefore, when aiming for an optimal replication fidelity, each parameter should be set to the highest possible value without causing injection moulding defects. The barrel temperature is set to the highest recommended value provided by the polymer manufacturer, being 315 °C. Increasing the temperature beyond this value could lead to thermal degradation of the polymer. The volumetric injection rate is set to the highest achievable value limited by the injection moulding machine, in this case 150 $cm^3/s$. The holding pressure was varied throughout injection moulding experiments to find the highest possible pressure without causing injection moulding defects. A maximum holding pressure of 63 MPa was found, as flash appeared above this value. The mould coolant temperature was also varied throughout injection moulding experiments. Starting at 115 °C, the mould coolant temperature was increased in steps of 5 °C. At a coolant temperature of 130 °C, which is still below the glass transition temperature of 141 °C, some needles deformed or even broke during the demoulding process. A microscopic image of an undeformed and deformed small microneedle are shown in Figure 61. Even when extending the cooling time to 30 seconds, these defects occurred. Masato et al. also observed breakage of micro features during demoulding at very high mould temperatures [248]. It is expected that similar to the microneedles from array 8, the replication fidelity is very high, which causes the micro- and nano-surface roughness inside the microneedle cavities to be replicated, this time due to the high mould temperatures. Moreover, it should be noted that the tensile strength of the polymer material is lower at higher temperatures. Thus, it is expected that at high mould temperatures, the needle deformation and breakage are the result of higher demoulding forces due to a higher replication fidelity, and a lower tensile strength of the polymeric material. Thus, the optimal replication fidelity is not defined by the best filling of the microcavities but by the best trade-off between filling and demoulding forces. To ensure that no defects occur, the maximum mould coolant temperature is set at 125 °C. A summary of the IM parameters for an optimal replication fidelity are shown in Table 13.

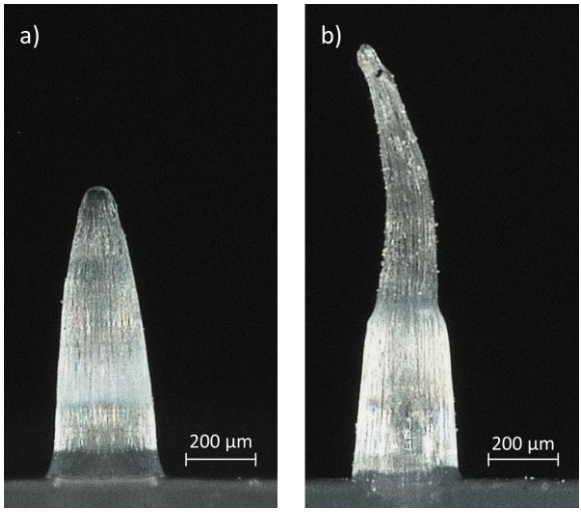


Figure 61: Illustration of a small microneedle which is (a) undeformed during the demoulding process, (b) deformed during the demoulding process.

Table 13: IM parameters for an optimal replication fidelity

| | PC |
|---|---|
| **Barrel temperature [°C]** | 315 |
| **Volumetric injection rate [cm³/s]** | 150 |
| **Holding pressure [MPa]** | 63 |
| **Mould coolant temperature [°C]** | 125 |

Figure 62 shows the experimental and simulated replication in height of the small and large microneedle arrays created with the IM parameters for an optimal replication fidelity. A good correlation between the experimental and simulated replication in height is observed both for the large and small microneedles with a percentual absolute average deviation of 4.4 % and 5.1 %, respectively. The average replication in height together with the standard deviation for the large and small microneedles are 1371 ± 107 µm and 681 ± 41 µm, respectively. This corresponds to an average replication fidelity of 70.0 % for the large microneedles and 60.6 % for the small microneedles.

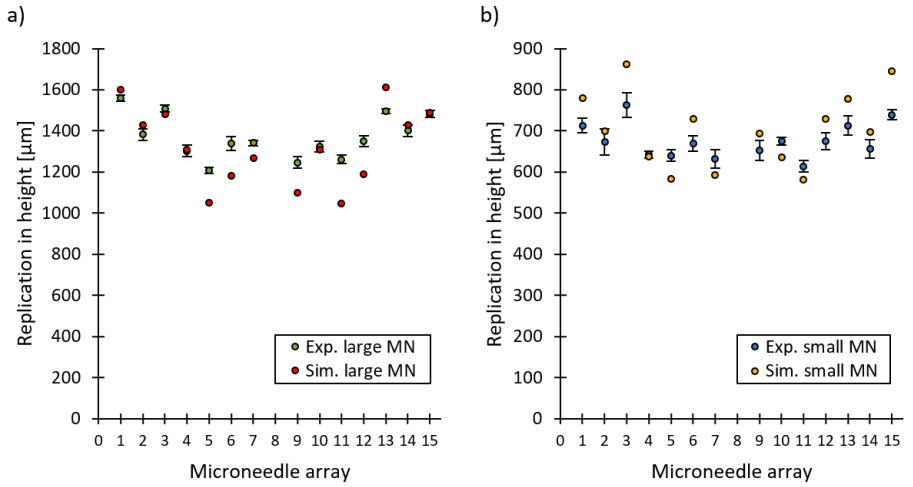


Figure 62: The experimental and simulated replication in height in function of the microneedle arrays, created with the optimal IM parameters for (a) the large microneedle arrays and (b) the small microneedle arrays. The error bars represent the 95 % confidence interval.

Figure 62 clearly shows that there is a deviation in the replication fidelity across the different microneedle arrays. The cause of this deviation can be allocated to the different positions of the microneedles on the macroscopic part, which cause a difference in temperature, pressure and viscosity of the polymer melt during the filling of the microneedle arrays. In fact, when the replication fidelity of the microneedle arrays is displayed as a function of the distance between the corresponding microneedles and the gate location, a clear trend is observed, as shown in Figure 63. A strong linear relationship is found between the replication in height and the location of the microneedles from the gate, indicated by the high values of the linear correlation coefficient (R). This trend is also observed within the injection moulding simulations, as shown in Figure 63 (b), where the experimental and simulated replication fidelity is shown as a function of the distance from the gate. Explaining this trend was recently done within our latest paper, in which the replication fidelity of microneedle close to the gate and far from the gate were compared [280]. Here it was found that the microneedles close to the gate were partially filled during the initial filling phase. Yet, when the macroscopic part was completely filled and the pressure in the cavity increased, the temperature of the melt inside the microneedles had already decreased below the no-flow temperature, thus preventing further filling of the microneedle cavities. The filling of the microneedles located far from the gate, however, is delayed due to the increased flow length. During the filling of these microcavities, the temperature of the melt is still very high due to the characteristic fountain flow present in injection moulding. Only shortly after the melt reaches the microcavities far from the gate, the macroscopic part is completely filled and the pressure reaches a maximum. At that moment, the temperature within the cavities located far from the gate is still above the no-flow temperature and thus ensures complete filling. This behaviour is also present in the current study, as the farther the microfeatures are located from the injection location, the higher the melt temperature is at the moment when the cavity pressure rises. Thus, microneedles located far from the gate have a higher replication fidelity compared to microneedles located close to the gate.

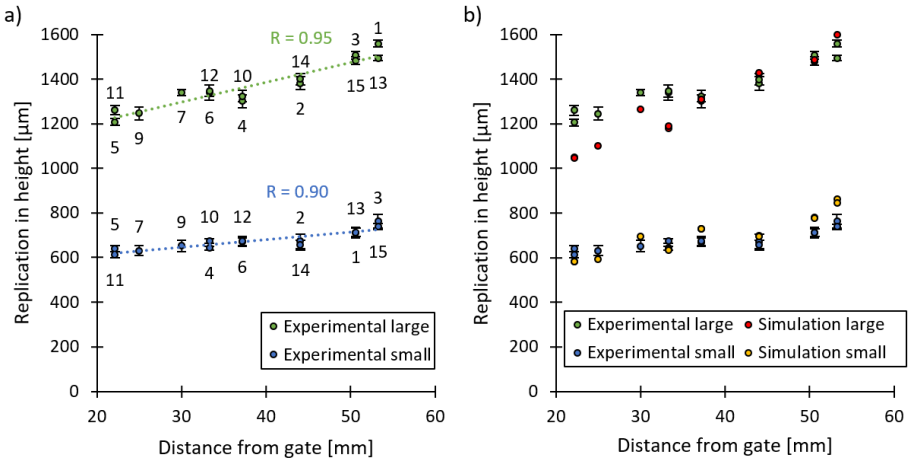


Figure 63: The average replication in height of the microneedle arrays as a function of the distance between the corresponding array and the gate location for (a) the large and small microneedle arrays together with a trendline and the linear correlation coefficient (R); (b) the experimental and simulated replication in height in function of the distance from the gate. The error bars represent the 95 % confidence interval.

### 7.4.4 Injection compression moulding

The defined injection moulding parameters for an optimal replication fidelity of the microneedles were also used during the injection compression moulding experiments. Besides, the additional parameter in the ICM process, being the compression stroke, was varied in 5 steps. Figure 64 illustrates the average replication in height for both the large and small microneedle arrays, in function of the compression stroke. A clear trend can be observed, as the average replication in height increases with an increase in the compression stroke, and stabilizes around 4 mm. This trend can be explained by Figure 65, where for the different compression strokes, the injected melt volume before the mould compression phase is shown inside the mould cavity. The contact area between the injected polymer melt and the mould wall decreases with an increase of the compression stroke. If polymer material is in contact with the mould surface, it will rapidly solidify and form a frozen layer, due to the temperature difference. For the smaller compression strokes, a higher area of polymer will be in contact with the mould, therefore a large area of frozen layer is formed, which will hinder the complete replication of the microneedles during the compression phase. For the larger compression strokes, however, less material is in contact with the mould, therefore the bulk of the polymer melt is still at a high temperature after the initial injection phase. Afterwards, when the mould compression is applied, the bulk of the polymer melt is compressed and distributed over the mould surface, while still having a high temperature. Therefore, the polymer material can still be deformed during the compression phase, which results in a higher replication fidelity of the microneedles.

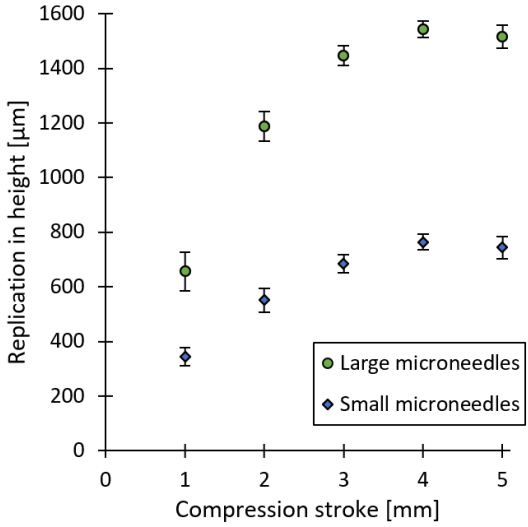


Figure 64: Illustration of the replication in height in function of the compression stroke obtained through ICM, for the large and small microneedles. The error bars represent the 95 % confidence interval.

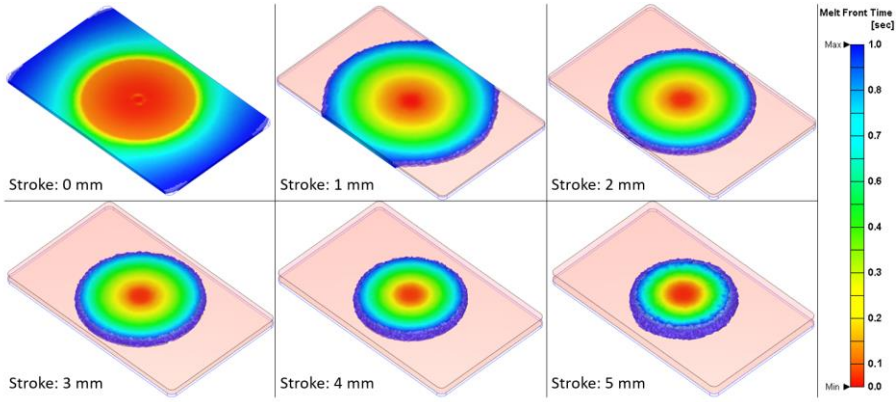


Figure 65: Illustration of the injected melt volume inside the mould cavity, before the mould compression phase, for the different compression strokes. The pink volume represents the compression gap. A compression stroke of 0 mm corresponds to conventional injection moulding.

### 7.4.5 Comparison between IM and ICM

Figure 66 shows the average replication in height of the microneedle arrays as a function of the distance between the corresponding array and the gate location, for injection moulding and injection compression moulding using the process parameters for an optimal replication fidelity. A difference in replication fidelity can be observed between the microneedles produced with IM and ICM. The average replication in height together with the standard deviation, for all large microneedle arrays correspond to 1536

± 81 µm and 1371 ± 117 µm for ICM and IM, respectively. For the small microneedle arrays, an average replication in height together with the standard deviation of 775 ± 38 and 675 ± 46 was found for ICM and IM, respectively. This corresponds to an average replication fidelity for the large microneedle arrays of 79 % for ICM and 70 % for IM. For the small microneedles, a replication fidelity of 68 % and 61 % was found for ICM and IM, respectively. Thus, for both the large and small microneedle arrays, a higher replication fidelity is found for ICM compared to IM. Moreover, a better replication uniformity across the different arrays is achieved for the ICM process, as indicated by the lower standard deviation. A microscopic image of a large and small microneedle from array 1, created with the injection moulding conditions for most optimal replication fidelity, being ICM with a mould stroke of 4 mm, is displayed in Figure 67. The cause of difference in replication fidelity between the two techniques will be discussed in the following section.

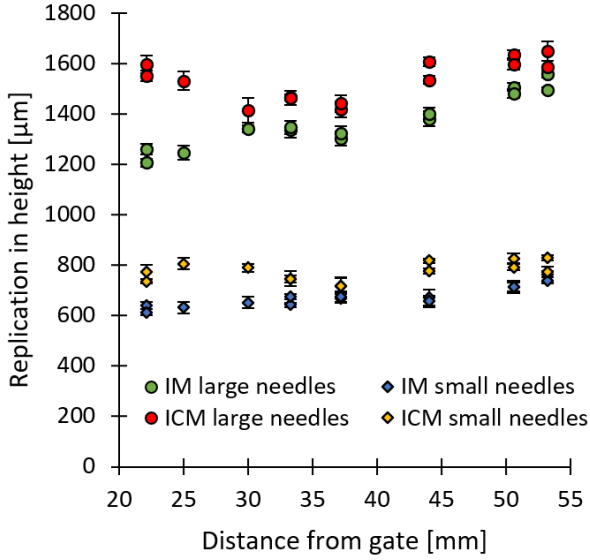


Figure 66: The average replication in height of the microneedle arrays as a function of the distance between the corresponding array and the gate location for injection moulding and injection compression moulding using the process parameters for an optimal replication fidelity.

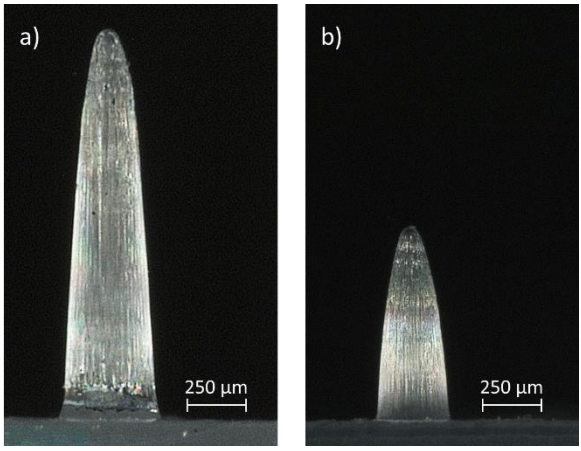


Figure 67: Illustration of a single (a) large and (b) small microneedle from array 1, created with ICM having a mould stroke of 4 mm.

Figure 68 illustrates the simulated melt front time, temperature, and pressure in the macroscopic part and a small microneedle from array 1, for IM and ICM with a stroke of 4 mm, at a filling time of 0.1 and 0.2 seconds. For IM, a filling time of 0.1 seconds corresponds to the switchover position where the filling changes from velocity driven to pressure driven. For ICM, this time corresponds to the compression switch, at which the mould will compress the polymer melt using the clamping force. Hence, a different filling behaviour is observed after 0.1 seconds between both injection moulding techniques. For the IM process, the polymer melt has filled the product cavity for approximately 98% and the microneedles are partially filled due to the pressure inside the mould cavity. For the ICM process, however, the complete product volume is injected into the enlarged mould cavity, creating a bulk of material having only a small contact area with the mould. Moreover, nearly no pressure is present in the cavity, resulting in almost no filling inside the microneedle cavities. At a filling time of 0.15 seconds, the macroscopic product is completely filled in the IM process, due to the additional pressure controlled filling. At that moment, the pressure inside the mould cavity is increased to approximately 35 MPa, yet the partially filled microneedles are already cooled down and solidified, which means that the increased pressure cannot improve the filling any further. Moreover, it should be noted that this pressure is generated at the melt entrance and has to be distributed through the polymer material, resulting in an uneven pressure distribution. In case of the ICM process, the complete melt volume is dispersed in the mould cavity, due to the closing stroke of the mould, at a filling time of 0.2 seconds. Although the complete filling takes more time compared to the IM process, the microneedles have a higher replication fidelity. This is due to the fact that the microneedle cavities were not yet filled at the initial filling stage of 0.1 seconds, and the bulk of material was not in contact with the mould surface, therefore retaining more heat. Moreover, a higher cavity pressure is observed in the ICM process of approximately 50 MPa, which is equivalent to the applied closing force of 350 kN on the product surface. Thus, due to the higher temperature of the melt inside the microneedle cavities, combined with a higher and more evenly distributed pressure inside the cavity, a higher replication fidelity with a better replication uniformity is found for the ICM process.

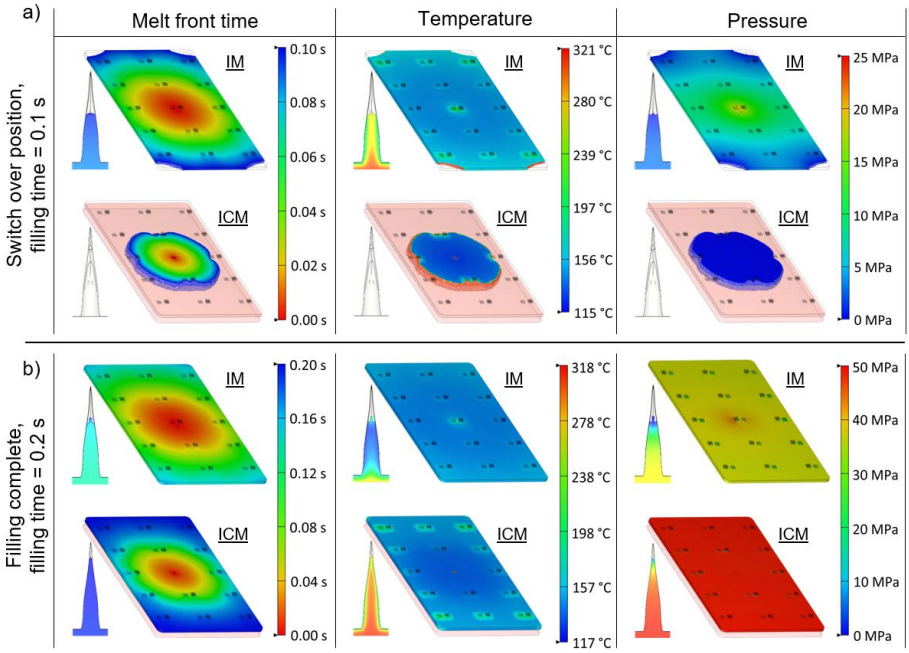


Figure 68: Illustration of the simulated melt front time, temperature, and pressure of the macroscopic part and a small microneedle from array 1 for injection moulding (IM) and injection compression moulding (ICM) with a stroke of 4 mm, at (a) a filling time of 0.1 seconds and; (b) a filling time of 0.2 seconds.

## 7.5 Conclusion

The present chapter investigated the replication fidelity of solid polycarbonate microneedles using injection compression moulding and conventional injection moulding. For this, a mould cavity insert for a flat polymer plate was developed, on which two types of microneedle cavities were laser ablated on 15 locations. The first type of cavities, corresponding to large microneedles, had an average cavity depth of 1959 µm with a cavity base diameter of 430 µm, while the second type of cavity, corresponding the small microneedles, had an average cavity depth of 1125 µm with a cavity base diameter of 246 µm. A two-level full factorial design of experiments was conducted to define injection moulding parameters for an optimal replication fidelity. The investigated parameters were the barrel temperature, volumetric injection rate, holding pressure and mould coolant temperature. For the large microneedles, it was found that all parameters had a significant positive effect on the replication fidelity, with the volumetric injection rate having the largest positive effect. Moreover, all first order interactions, although not all significant, were found to have a positive effect on the replication fidelity. Similar results were found for the small microneedles, yet here the barrel temperature was found to be insignificant. The reason why the volumetric injection rate had the largest positive effect, was first due to the higher shear heating which decreased the melt viscosity and secondly due to a reduction in the injection time, which in turn delayed the formation of the frozen skin layer.

Finite element flow simulations were used to discuss the filling behaviour of the injection moulding process. A good correlation between the experimental and simulated replication fidelity was observed both for the large and small microneedles with a percentual absolute average deviation of 4.4 % and 5.1 %, respectively. Moreover, a deviation in the replication fidelity across the different microneedle arrays was observed and explained using flow simulations. The deviation in replication fidelity between the different microneedle arrays could be allocated to a different temperature, pressure, and viscosity of the melt during the filling of the different needles.

The compression stroke within the injection compression moulding process was varied, and the effect on the replication fidelity was assessed. It was found that a larger compression stroke resulted in a better replication fidelity, with a stagnation after a stroke of 4 mm. Due to the larger compression stroke, less polymer material was in contact with the mould surface during the initial filling stage, which resulted in less heat transfer between the molten polymer and the mould surface.

A comparison between the replication fidelity of the injection moulding and injection compression moulding process was made, using the established parameters for an optimal replication fidelity. It was found that the injection compression moulding process resulted in a higher average replication fidelity together with a better replication uniformity across the different microneedle arrays, compared to the injection moulding process. The average replication in height for the two types of microneedles corresponded to from 79 % and 68 %, respectively. The cause of the difference in replication fidelity between both techniques was allocated to the different flow behaviours, which was discussed using finite element flow simulations. As the polymer was injected into a slightly opened mould for the injection compression moulding process, more heat was retained in the polymer melt, which promoted the filling of the microneedles. Moreover, a higher and more evenly distributed pressure inside the cavity was observed compared to the injection moulding process, due to the evenly distributed closing force on the product.

Thanks to this work, we better understand the effect of the injection moulding parameters on the replication fidelity of the microneedles. Moreover, we now know it is preferential to use injection compression moulding to produce solid polymer microneedles in the future.

Throughout the study we observed some needle deformation and needle breakage, possibly due to a high demoulding force of the microneedles inside the cavities. This excessive demoulding force was caused by the replication of surface roughness on the microneedle shaft, which formed microscopic undercuts. In a future work we will try to micro-polish the microcavities using laser ablation or chemical etching techniques, and to apply physical vapor deposition coatings (PVD-coatings) inside the microneedle cavities, to reduce the surface roughness inside the microcavities.

# Chapter 8 Producing hollow polymer microneedles using ablated moulds in an injection moulding process

Evens T., Van Hileghem L., Dal Dosso F., Lammertyn J., Malek O., Castagne S., Seveno D. and Van Bael A. Producing Hollow Polymer Microneedles Using Laser Ablated Molds in an Injection Molding Process. Journal of Micro and Nano-Manufacturing, 9 (3): Art.No. 030902, 2022. Some parts of the original publication are left out or modified to avoid redundancy.

## 8.1 Abstract

Microneedle arrays contain needle-like microscopic structures which facilitate drug or vaccine delivery in a minimally invasive way. However, producing hollow microneedles is currently limited by expensive, time consuming and complex microfabrication techniques. In this chapter, a novel method to produce hollow polymer microneedles is presented. This method utilizes a femtosecond laser to create hollow microneedle cavities in a mould insert.

This mould insert is used in an injection moulding process, to replicate polymethyl methacrylate microneedles. The combined effect of the mould temperature, volumetric injection rate and melt temperature on the replication fidelity was evaluated. It was found that the combination of high injection moulding parameters facilitated the replication. Furthermore, the functionality of the manufactured hollow microneedles was successfully tested by injecting a controlled flow of coloured water into an agarose matrix. The developed methodology enables the production of low-cost, high-volume microneedle devices, which could be a key asset for large scale vaccination campaigns.

## 8.2 Introduction

Infectious diseases can be tackled both curatively and preventively by the administration of drugs and vaccines, respectively. Although many different administration routes exist, vaccines are most commonly administered by injection [304], [305]. Drugs, on the other hand, are more frequently delivered enterally through the oral route, considering its straightforward dosing and wide acceptance [1], [10]. Nonetheless, as an effect of passing through the gastrointestinal tract, the bioavailability with enteral administration can be critically reduced [6]. Therefore, like for vaccines, many drugs are still delivered parenterally by injection to avoid the gastrointestinal tract. Unfortunately,

hypodermic needles used in the parenteral delivery approach are known to induce discomfort to the patient, carry the risk of infections and require well-trained medical staff [306], [307]. Especially the latter two are known to be problematic in developing countries where about 50% of the needle use is regarded as unsafe [308].

A less invasive parenteral delivery approach is delivery via the skin. This can be done by topically applying formulations or transdermal patches [309]. However, only components with a specific combination of properties can be successfully administered this way, while the large majority of drugs and vaccines are unable to cross the skin's protective barrier, the stratum corneum [310]. Methods to improve absorption rates by surpassing the skin's stratum corneum have been intensively investigated and in 1976, a first concept using microneedles was described in a patent by Alza corporation [1]. Since then, a wide variety of microneedle designs have been developed with needle lengths ranging from 25 to 2500 μm. Usually these designs are developed in arrays which consist of tens or even thousands of individual microneedles [5]. A huge advantage of microneedles is the possibility of pain-free drug delivery and self-administration of drugs and vaccines. An additional advantage for vaccines is the abundance of specialized antigen presenting cells in the skin [1], [3]. Moreover, due to their small volume, costs related to distribution are lower compared to traditional hypodermic needles. These benefits offer a great opportunity for delivery of medicines. Further, it is evident that these systems would worldwide be a significant asset for solving pandemic crises, like the one caused by the COVID-19-virus [126].

In recent work [216], we demonstrated a novel methodology to produce solid polymer microneedles. This method utilizes a femtosecond laser to create cone-shaped microcavities in a mould insert. This insert is subsequently used in an injection moulding process to create solid cone-shaped microneedles with sharp tip radii. The solid needles can be applied for drug or vaccine delivery using two approaches. In the first approach, referred to as 'poke with patch', the microneedles are used to pierce the skin, creating transient aqueous micro-pores through which a formulation can passively diffuse (Figure 69 a). In the second approach, referred to as 'coat and poke', the needles are coated with a drug or vaccine formulation (Figure 69 b). When inserted in the skin, the coating will be dissolved and the medicine will be deposited in the skin. Although these solid microneedles are able to offer significant advantages compared to the conventional hypodermic needles, their application area is limited because they can only deliver small amounts of medicines [39]. A third type of microneedles are dissolving microneedles. These needles consist of a soluble material, such as a biodegradable polymer, in which the drug or vaccine is encapsulated. A specific approach, referred to as 'poke and release' is used for these microneedles, in which the needles are inserted in the skin, where they dissolve and release the drug or vaccine (Figure 69 c). In contrast to solid and dissolving microneedles, hollow microneedles possess a lumen, or internal bore, which enables the transportation of fluids, thus offering a huge potential (Figure 69 d). This strategy, referred to as 'poke and flow', enables the injection of large amount of drugs [34], [311] and vaccines [312] at higher rates.

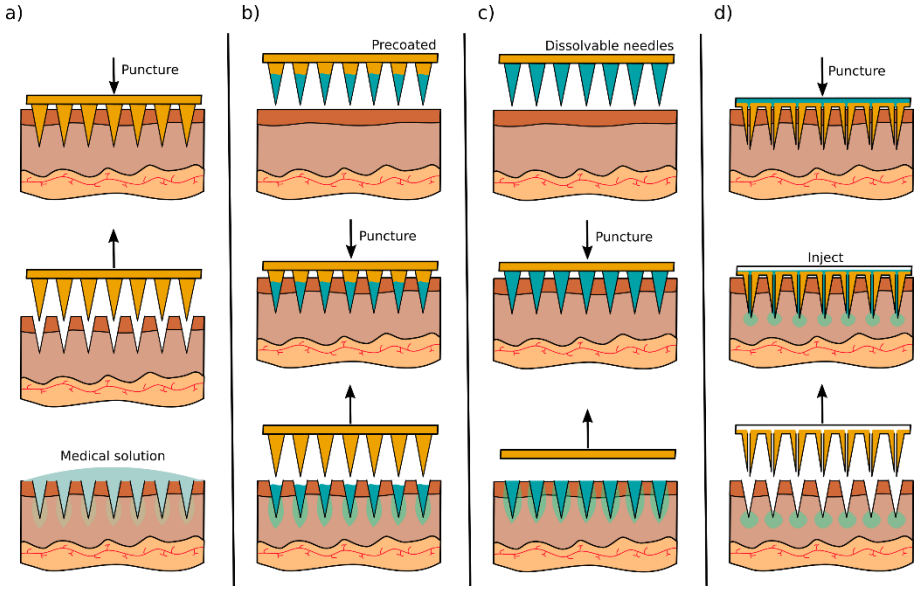


Figure 69: A schematic representation of the different types of microneedles. (a) solid microneedles, (b) coated microneedles, (c) dissolving microneedles, and (d) hollow microneedles for drug and vaccine delivery. Inspired by [7].

Undoubtedly, the most challenging problem for hollow microneedles is their complex production process [108]. In fact, a production process to manufacture hollow polymer microneedle arrays in large volumes and at a low cost is currently not available, as it brings an extra level of microfabrication complexity compared to solid microneedles. Current production methods described in literature are mostly very expensive, time consuming or unable to be used as a mass production process. Deep reactive-ion etching has been used to create off-plane hollow microneedles with a lumen of 75 to 150 μm and a length of 700 to 1000 μm [313]. However, the shapes of the microneedles are cylindrical with a blunt tip, which will be difficult to insert into skin. Wang et al. described a two-step production using photolithography and replica moulding to produce hollow epoxy microneedles [314]. Inductively coupled plasma and anisotropic wet etching methods were also used to fabricate hollow microneedles on a silicon substrate. These needles were integrated with a piezoelectric pump for insulin dosage [34]. Two studies reported a method to produce hollow glass microneedles by pulling fire-polished glass pipettes [63], [311]. The needles were successfully used to deliver insulin to patients with type 1 diabetes in a less painful manner than the conventional hypodermic needles. Stereolithography 3D-printing is another technique suitable to directly create hollow microneedles [37], [95] or to create moulds [208] which can be used in a replication process to create hollow microneedles. Two-Photon-Polymerization is yet another additive manufacturing technique which was used in combination with a femtosecond laser to realize the production of hollow microneedles [96].

The choice of fabrication process depends on the selected material, access to manufacturing technology, and the intended application. As a result, a wide variety of needle designs is available in literature. Yet for all of these designs, the shape of the microneedle tip is important, as sharp microneedles are more effective in penetrating the

skin. Furthermore, the shape of the microneedle tip is essential for the flow resistance, as a blunt-tipped microneedle will compact the skin and will bear a higher risk of clogging [101], [102]. Therefore, microneedles should have a bevelled shape, with the lumen off-cantered or on the side of the microneedle [3].

In this study, a novel method for producing hollow polymer microneedles using laser ablated moulds in an injection moulding process is presented. First, two types of hollow microneedle cavities are created through laser ablation and their shape is assessed using micro-computed tomography (μ-CT). Both types of microneedles are implemented on a mould insert, which is afterwards replicated in an injection moulding process using three different process conditions. The effect of these conditions on the replication process is assessed by a microscopic study of the obtained microneedles. Eventually, the hollow microneedle design with the highest replication fidelity is further validated during single-needle injections. Hereto, the needle is integrated into a microfluidic chip, which is used to inject coloured water into a skin-mimicking agarose matrix.

## 8.3 Materials and Methods

### 8.3.1 Materials

The thermoplastic material used in this study is polymethyl methacrylate (PMMA) due to its excellent biocompatible nature [315]. The selected grade is Plexiglas 8N from Evonik which has a melt volume flow-rate of 3.00 $cm^3$/10 min and a glass transition temperature of 117 °C.

The selected mould material is an aluminium zinc alloy (grade 3.4365), which is regularly used for low production series and prototype moulds, due to its low cost and good machinability.

Agarose powder and water-based microfluidic dyes were acquired from Melford (UK) and Darwin Microfluidics (France), respectively. Pressure-sensitive adhesive (PSA) tape 200MP 7956MPL from 3M (USA) and transparent Polyvinyl Chloride (PVC) sheets of 180 μm thick from Delbo (Belgium) were used for chip fabrication.

### 8.3.2 Representation of the process chain

A micromachining system with a laser source is employed to create hollow microneedle cavities in a mould insert with dimensions 70 mm x 60 mm x 4.6 mm (Figure 70 a). The insert is then placed in the mould (Figure 70 b). Injection moulding is used to replicate the microcavities (Figure 70 c), creating hollow polymer microneedles on top of a solid flat surface (Figure 70 d). As we want to assess the functionality of the microneedles, a fluidic connection between the needles and the polymer plate is needed. In this study, this connection is created by drilling micro-holes though the flat surface, while in future work we aim to design a mould to directly incorporate the fluidic connections during injection moulding.

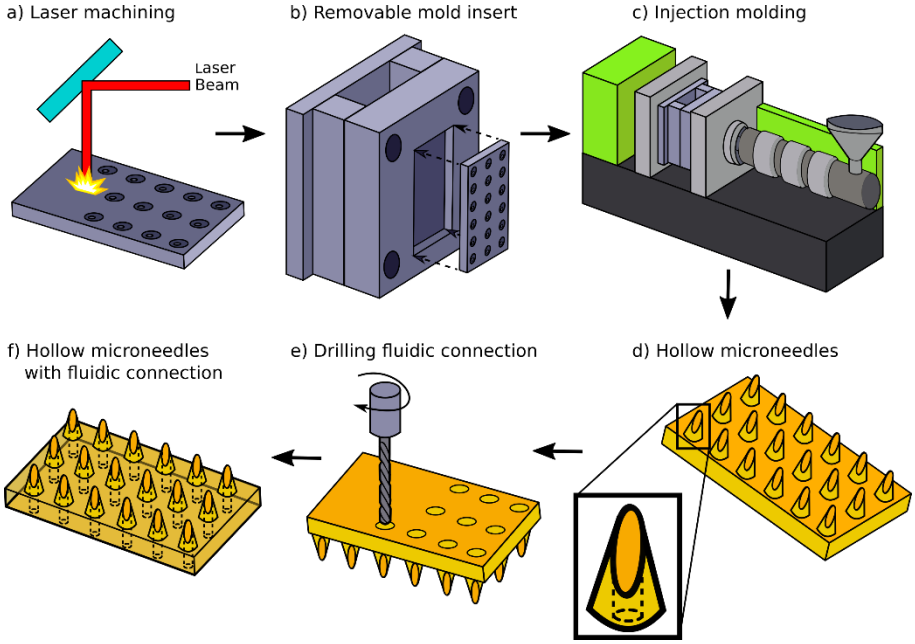


Figure 70: Illustration of the process chain to produce hollow polymer microneedles.

### 8.3.3 Laser machining

A micromachining system (Lasea, Liège, Belgium) with a Satsuma HP femtosecond laser source (Amplitude, San Francisco, USA) is employed to laser ablate a mould insert with dimensions 70 mm x 60 mm x 4.4 mm. The laser source emits a beam with a pulse length of 250 fs, a wavelength of 1030 nm and a pulse repetition rate of 500 kHz. The maximum average power of the laser is 7.85 W, giving a deliverable pulse energy of 15.7 µJ. A galvanometer steers the laser beam within the focal plane, with a spot size of 15.0 µm and a pulse fluence of 8.88 J/cm². Small dust particles which are formed from ablating the metal surface are extracted by a vacuum collect unit. After the laser texturing operation, the mould insert was ultra-sonicated in an ethanol bath for 15 min to remove debris from the micro-holes.

The laser strategy proposed in this work is based on a previous study, in which we developed a method to create cone-shaped micro-holes for the creation of solid microneedles [247]. In this adapted strategy, the laser spot scans a circular region and follows parallel lines in two perpendicular directions, where the distance between two consecutive lines is defined as the hatch pitch. Within the circular region, a scan-free internal area with a specific position is defined to create the lumen of the hollow microneedle. Once the laser has scanned one circular grid, the focal point is lowered with a vertical distance, defined as the layer pitch, and the laser scans again the same area. This process is repeated multiple times for a prescribed number of layers as illustrated in Figure 71. Using the proposed strategy, two arrays of 3 x 3 microcavities were ablated with different positions of the internal scan-free area. In the first array, the edge of the internal scan-free area is tangential to the edge of the scanned area, while in the second design there is a distance of 100 µm between both edges. In both arrays, the interspacing between the microcavities is 1 mm and a 475 µm base diameter was programmed with a

hatch pitch of 15 µm. The diameter of the scan-free area is 100 µm and a total of 450 layers was created with an individual layer pitch of 2 µm.

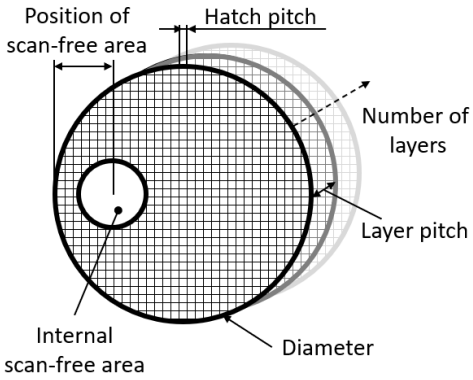


Figure 71: Illustration of the laser strategy with internal scan-free area.

### 8.3.4 Polymer injection moulding

The injection moulded part for this study is a 50 mm x 60 mm x 1.5 mm flat plate. The array of micro needles is approximately 2,5 mm x 2,5 mm in size, positioned at a distance of approximately 45 mm from the injection location.

Injection moulding was done on an Engel ES 200/35 HL hydraulic injection moulding machine (Engel, Schwertberg, Austria) with a maximum clamping force of 350 kN and a 25 mm screw with an L/D ratio of 24.8. The mould temperature is controlled by a WITTMANN TEMPRO Controller (Wittmann, Vienna, Austria). Three sets of injection moulding parameters were defined within the recommended limits of the material supplier as given in Table 14. The first set of parameters is defined as 'low' and corresponds to the lowest recommended conditions. The second set is defined as 'middle' and corresponds to the average between the upper and lower process conditions. The third set is defined as 'high' and correspond to the highest recommended conditions. The holding pressure was kept constant in each set of parameters to completely fill the macroscopic polymer plate without sink marks. In each of the experiments, the parts produced in the first 30 cycles were discarded in order to stabilize the process, then the following parts were collected for characterization.

Table 14: Three sets of injection moulding parameters: 'low', 'middle' and 'high'.

| | Low | Middle | High |
|---|---|---|---|
| **Injection temperature [°C]** | 240 | 250 | 260 |
| **Volumetric injection rate [cm³/s]** | 50 | 100 | 150 |
| **Holding pressure [MPa]** | 80 | 80 | 80 |
| **Mould temperature [°C]** | 70 | 90 | 110 |

### 8.3.5 Micro drilling

The micro drilling tests were carried out on a Computer Numerical Control (CNC) machining centre (Kern Microtechnik, Eschenlohe, Germany) at a spindle speed of 40,000 RPM. A DIXI Polytool 1131 micro drill with a diameter of 100 μm and a length of 700 μm was used. Due to the small length of the micro drill, the thickness of the polymer plate at the location of the microneedles had to be reduced to a thickness of approximately 500 μm. This operation was done using a ProtoTRAK RMX 3500 milling machine (Southwestern Industries, Rancho Dominguez, USA).

### 8.3.6 Topography characterization

The geometries of the ablated microneedle cavities were characterized using a Phoenix Nanotom μ-CT system. The device is equipped with a high-power nanofocus X-ray tube and a diamond-tungsten target was chosen for the high X-ray absorbing aluminium samples. A high-power mode was used to allow focal spot and voxel sizes in the micrometre range. The two arrays of microneedle cavities were cut into cubic samples with an edge length of approximately 3 mm, using a metallographic precision saw. The cubic samples were mounted on a sample holder and fixed on a high-accuracy computer controlled rotation stage. For each scan, 2400 X-ray 2D projection images were obtained from incremental rotation of the scanned samples over 360°. Acquisition parameters were fixed for all samples as follows: voltage = 100 kV, current = 158 μA, voxel size = 3.75 μm, and a 0.1 mm copper filter was used during scanning. Reconstruction of the acquired 2D projections into 3D volumes was performed using GE Phoenix datos|x REC software. Reconstructed datasets (slices) were exported for further analysis and visualization within Fiji ImageJ. Before conducting measurements, the Nanotom instrument was calibrated using a calibration rod (Goekeler Messtechnik, VTX18CE000-022, Lenningen, Germany), having an uncertainty of 1.0 μm. For each set of laser parameters, one cubic sample containing nine micro-holes were measured. The average length and diameter of the nine microcavities, along with the standard deviation was reported in the results.

The geometry of the replicated thermoplastic microneedles were assessed using a Keyence VH-S30 digital microscope (Keyence, Osaka, Japan) with a maximum magnification of 200X. The system was connected to a VHX-500F monitor with built-in measuring software. The microscope was calibrated using a stage micrometre (Olympus Tokyo, OBMM 1/100, Tokyo, Japan) which has an uncertainty of 0.5 μm. Ten injection moulded samples were collected and on each sample one microneedle was measured. The averages of these ten measurements along with the standard deviations are reported in the results.

### 8.3.7 Preparation of a skin-mimicking substrate

An agarose gel with concentration of 2.65% (w/v) was prepared by dissolving the agarose powder in distilled water by heating on a hot plate under constant magnetic stirring until the solution had completely cleared out (±20 minutes). Then, the solution was poured into a petri dish to obtain a gel of about 1 cm thick. The substrates were used for injection experiments at least two hours after solidification and on the same day.

### 8.3.8 Validation of single-needle injections

Channels of 1 mm width were cut from the PSA using a CO2 laser cutter (Speedy 300, Trotec Laser, Plymouth, USA). With this fabrication method, the channel height is defined by the thickness of the PSA tape, in this case being 153 µm. The PVC layers, designed to contain also the connection holes for the microneedle and pump, were cut with a digital craft cutter (Maxx Air 24 in., KNK, USA). After chip assembly (Figure 72) by exerting pressure on the well-aligned and sandwiched layers, the microneedle with its substrate was integrated using a laser cut PSA connector piece, to assure a tight sealing.

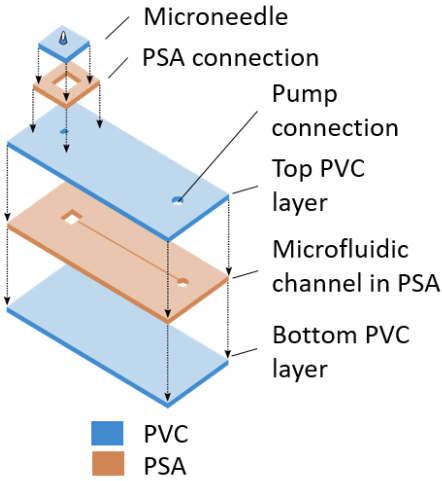


Figure 72: Exploded view of the chip containing a single, straight microfluidic channel. A single microneedle was tightly incorporated into the chip by a PSA connecting piece. At the other end of the channel, a hole serves for connecting a fluidic pump.

To inject distilled water with a 1/100 diluted blue dye into a (biological) matrix, a fluid flow was controlled by the setup as shown in Figure 73. Using a pressure controller (LineUp™ Push/Pull, Fluigent, France) and a flow sensor (S model, Fluigent, France), injections into the agarose matrix were controlled while monitoring the obtained pressures in real-time every second (1 Hz). To guarantee a good insertion of the microneedles into the agarose slab throughout the experiment, a small weight was applied on top of the chip after manually inserting the microneedle. Injection profiles were followed-up by filming the process from the side using a smartphone camera and snapshots of the recorded dispersion profiles after 0, 2, 5, 10 and 15 minutes were collected. The injection was repeated 3 times on 3 different agarose slabs and the average pressure along with one standard deviation are reported in the results.

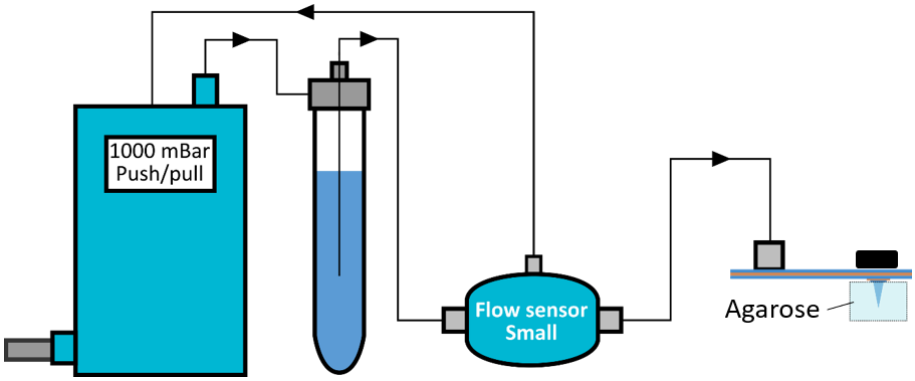


Figure 73: Setup for controlling the injection into agarose. From left to right the pressure controller, a pressurized reservoir containing the to be injected liquid, the flow sensor with feedback to the pressure controller, the microfluidic chip with integrated microneedle and the agarose slab.

## 8.4 Results and Discussion

### 8.4.1 Laser ablation

Two arrays of 3 x 3 microneedle cavities were formed during the laser ablation process, which took approximately 9.5 minutes for each array. Cross sectional views of the produced microcavities for both arrays are depicted in Figure 6. The XY images represent cross sections throughout the depth of the cavity, while the XZ and YZ images represent cross sections throughout the width of the cavity. The distance below each image indicates the position of the cross section. For XY, 0 µm corresponds to the mould surface, while for XZ and YZ 0 µm corresponds to the edge of the microneedle.

In both arrays, we can observe that the internal scan-free area has formed a tapered feature inside the microcavity, which will form the lumen of the hollow microneedle. The position of the tapered feature is different for both arrays due to the difference in position of the internal scan-free area. For array 1, the distance between the edge of the tapered feature and the edge of the micro-hole is only a few micrometres, while for array 2 this distance is approximately 100 µm. Evidently, the laser will also ablate material in the region between the tapered feature and the edge of the micro-hole, therefore inducing a trench between the tapered feature and the edge of the micro-hole. The depth of this trench in array 2 is much deeper compared to the trench in array 1, being 508 ± 11 µm and 110 ± 9 µm, respectively. This discrepancy can be explained by the larger surface area of array 2, which will cause higher accumulated energy in this region compared to array 1.

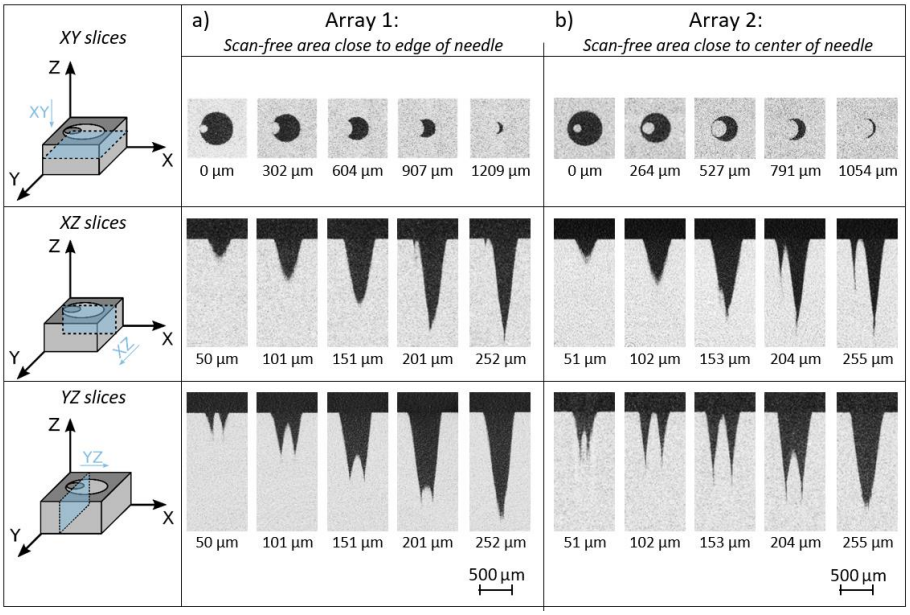


Figure 74: Cross sectional views obtained from the µ-CT measurements of the micro-hole arrays, with the scan-free area: (a) close to the edge of the needle and (b) close to the center of the needle. The distance below each image indicates the position of the cross section. For XY, 0 µm corresponds to the mold surface, while for XZ and YZ 0 µm corresponds to the edge of the microneedle.

Cone-shaped micro-holes with an internal tapered feature can be observed for both arrays. The formation of this conical shape is expected to be the result of two laser phenomena, being laser reflectance on steep sidewalls and possibly a plasma shieling effect. First, steep sidewalls will cause most of the laser light to be reflected rather than absorbed. Therefore, the ablation efficiency near the edge of the cavity is drastically reduced, causing the diameter to become smaller as the micro-hole is created [227]. Moreover, the reflected laser light will partially be redirected to the bottom of the hole, contributing to a deeper and sharper cavity. A possible second phenomenon occurs for laser ablation processes with high repetition rates [226]. Vaporized material that is unable to escape from the microcavity interacts with the next incoming laser pulse, forming a plasma. This plasma will defocus the laser beam, creating a protective shield referred to as "plasma shielding".

The cavity diameters at the mould surface are similar for both arrays, being 504 ± 5 µm for array 1 and 510 ± 3 µm for array 2. However, these dimensions are higher than the programmed base diameter of 475 µm. This difference can be explained as follows. During the laser ablation process, the laser focal spot is progressively moved deeper inside the mould material. Therefore, the Gaussian-shaped laser beam will start to intersect with the edge of the already created micro-hole. If in this intersecting region the power density of the Gaussian beam is higher than the ablation threshold, additional material will be removed. Thus, during the laser ablation process, the microcavities will progressively increase in diameter. Secondly, the depth of the microcavities in array 1 are deeper compared to the cavities in array 2 being 1513 ± 12 µm and 1318 ± 12 µm, respectively. As in array 2, the internal scan-free area is located more

towards the centre of the micro-hole, less energy can be induced in the centre region of the micro-hole, resulting in shallower holes compared to array 1.

We can observe low standard deviations for the cavity depth, cavity diameter at and the depth of the trench. In fact, the highest coefficient of variation for all of the measurements corresponds to approximately 3 %. This indicates a very high repeatability of the laser ablation process.

### 8.4.2 Replication through injection moulding

Figure 75 shows an image of the replicated polymer microneedles of array 1 created with a scan-free internal area close to the edge of the needle (Figure 75 a), and array 2 created with a scan-free area close to the centre of the needle (Figure 75 b). These samples were created with the 'high' injection moulding parameters at a cycle time of approximately 18 seconds. For both arrays, we observe hollow cone-shaped microneedles with a bevel shaped tip, which is similar to conventional hypodermic needles. The trench which was formed between the tapered feature and the edge of the microcavity has now been replicated to form an upstanding ridge which partially encloses the sides of the lumen. This could be beneficial, as the ridge could prevent fluids from leaking between the microneedle and the skin of the patient when the microneedle has not completely penetrated in the skin. In the further stages of this chapter we continue using only array 2, as these needles have the highest potential to form functional microneedles.

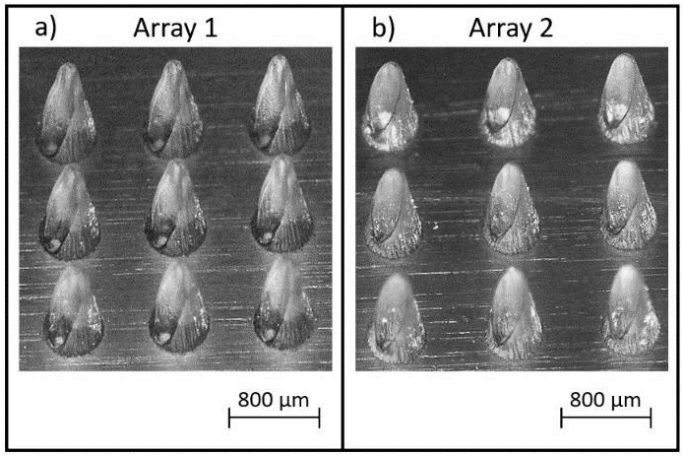


Figure 75: Microscopic image of the replicated polymer microneedle arrays created with a scan-free internal area (a) close to the edge of the needle, and (b) close to the centre of the needle.

The three different sets of injection moulding parameters were used to replicate the microneedle cavities from array 2. Figure 76 shows the microscopic images of the front and side view of the replicated microneedles and Figure 77 shows the measured needle length, ridge height and tip wall thickness of the replicated microneedles in function of the three different sets of injection moulding parameters. In addition, the replication of the microneedle in height was expressed, calculated based on the length of the needle and the depth of the corresponding microcavity. It is to be noted that the volumetric replication fidelity will be much higher than the expressed percentage of the replication

in height. This due to the fact that the volume gradually decreases throughout the height of the cone-shaped needles.

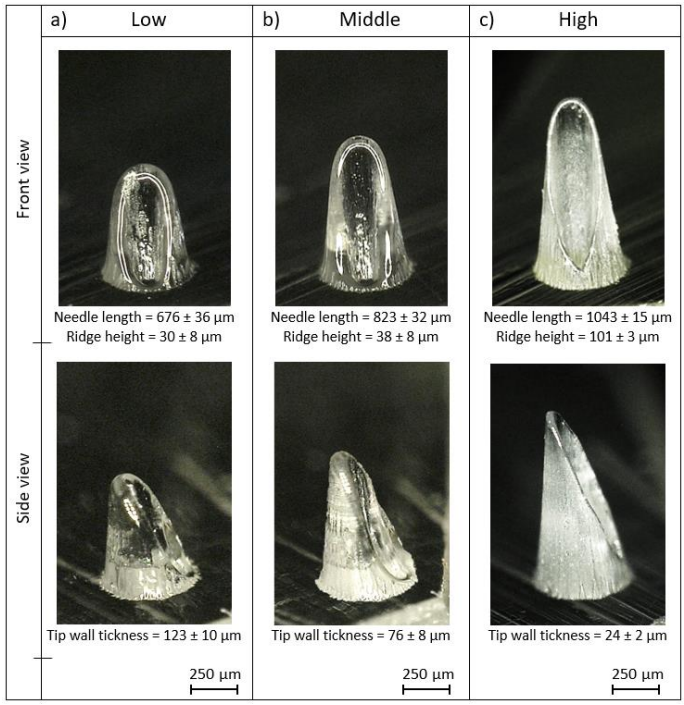


Figure 76: Microscopic image of the front and side view of the replicated polymer microneedles created with: (a) 'low' injection moulding parameters, (b) 'middle' injection moulding parameters and (c) 'high' injection moulding parameters. The average value of the dimensions of the needles are reported together with the standard deviation (n = 10).

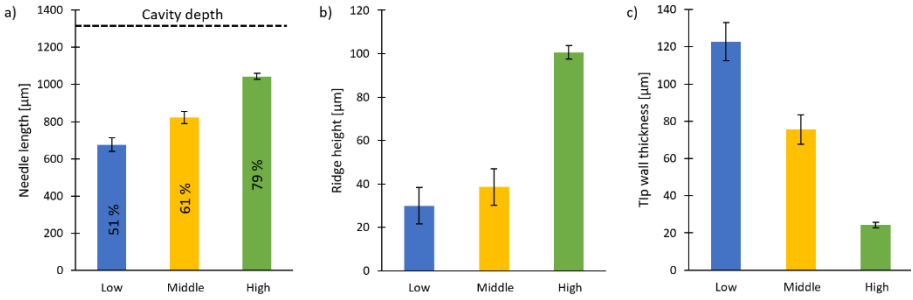


Figure 77: (a) Needle length, (b) ridge height and (c) tip wall thickness of the replicated microneedles from array 2 in function of the three different sets of injection molding parameters, being 'low', 'middle' and 'high'. The percentages in (a) represent the replication in height.

The three parameters that were varied between the different sets of injection moulding parameters are the melt temperature, the volumetric injection rate and the mould temperature. All of these parameters will, to some extent, influence the replication

of the microneedles. The first parameter is the mould temperature, which is in literature known to be the most important parameter when it comes to replicating micro-features [133], [134], [244]. When a macro-scale cavity with micro-features is injection moulded, the filling of the micro-features has to compete with the filling in the rest of the cavity. Since the polymer will follow the path of least resistance, most of the material will flow in the main flow direction through the macro-scale cavity, leaving the micro-features only partially filled, also known as the hesitation effect [238], [248]. These micro-features will then only be filled after the rest of the cavity is filled and the pressure rises. Yet, as soon as the polymer is in contact with the mould, a layer of frozen polymer material (skin layer) will be formed. The rapid solidification of the skin layer hinders the filling of the micro-features and can lead to incomplete filling [256]. By increasing the mould temperature, the formation of the frozen layer can be delayed, leading to the polymer still being able to be deformed during the packing phase, resulting in a better replication of the micro-features [184], [277], [316]. The second parameter is the volumetric injection rate. High volumetric injection rates reduce the injection time and can prevent premature freezing of the polymer. Moreover, a high injection velocity promotes shear heating, which can locally decrease the melt viscosity and can therefore improve the replication [134]. The highest volumetric injection rate used in this study was set to the limit of the injection moulding equipment. The last parameter is the melt temperature. High temperatures of melt ensure lower melt viscosity, lower cavity pressure drop, and the ability of the melt to flow into micro-features [276]. The upper melt temperature is limited, as it should be selected consistent with the polymer properties to avoid thermal degradation.

It can clearly be observed that there is a significant difference in replication fidelity between the three different injection moulding conditions. The low injection moulding parameters resulted in the shortest microneedles having a very low ridge and a large wall thickness of the needle tip. The needles created with the 'middle' parameters are already better compared to the needles obtained with the low injection moulding parameters. Yet, the highest replication fidelity is observed for the 'high' injection moulding parameters. Here, the tallest needles are found combined with a high ridge and low tip wall thickness. Besides, these microneedles have the lowest standard deviation for all of the measurements. This indicates a more stable injection moulding process, which in turn results in a high reproducibility of the produced samples. Furthermore, the microneedles created with the 'high' injection moulding conditions appear to be more opaque compared to the other two sets of microneedles. This opaque appearance is caused by micro- and nano surface roughness, which are replicated using the 'high' process conditions. The replication of the microneedles will also be affected by the volumetric shrinkage of the polymer. This volumetric shrinkage can be determined using the compressibility or pressure-specific volume-temperature (pvT) behaviour of the polymer and can be modelled by the double domain Tait equations [217]. An estimate of the volumetric shrinkage can be calculated by assuming the pressure at the end of the packing stage to be equal to the holding pressure and the temperature to be equal to the no-flow temperature. Consequently, a linear shrinkage of 0.28 % was calculated for the PC material, which corresponds to only a very small portion of the incomplete replication.

Not only the tip of the microneedle is subjected to incomplete replication, but also the ridge of the microneedle will be affected. In fact, the ridge of the microneedle is much more sensitive to incomplete replication as the aspect ratio of this component is much higher. With an increase in aspect ratio, the surface area to volume ratio increases, which corresponds to a higher heat transfer between the molten polymer and the mould surface [239]. This results in a faster solidification of the polymer, causing a higher fraction of

incomplete filling. For the microneedles replicated with the low injection moulding conditions, the filling of in height of the ridge corresponds to only 20 %.

### 8.4.3 Validation on skin-mimicking substrate

To proof that the microneedles are compatible with microfluidic technologies for injecting drug or vaccine substances, single microneedles were integrated into a chip connected to a pressure pump. Performing injections with a single microneedle was preferred over arrays to reduce complexity while studying release profiles and phenomena like leakage. The patch was vertically inserted into a 2.65% (w/v) agarose gel to mimic intradermal injection [317], [318]. As the gel is transparent, the injection profile could be followed-up easily by the blue coloured water.

The frames and graph in Figure 10 show the dispersion profile through the agarose and pressure profile during the injection of 7.5 µL of coloured water at a flow rate of 0.5 µL/min, respectively. Pressure data were corrected for the pressure required to maintain the flow through the setup, including the chip with microneedle, without insertion into the skin model. The results clearly depict that after a few minutes a constant pressure is reached and maintained, indicating a constant flow from the microneedle into the matrix. The injected liquid could be observed by the naked eye after approximately one minute, after which a uniform release profile consistently evolved. This proves the feasibility of the microneedles to inject liquids when integrated in a microfluidic platform.

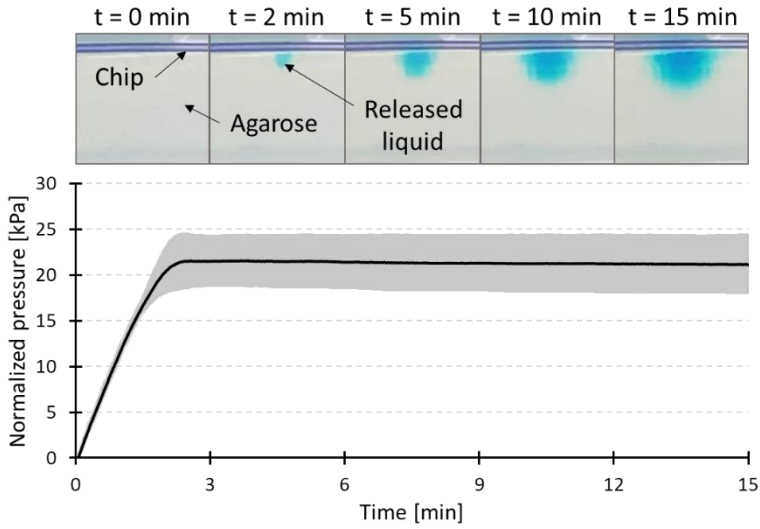


Figure 78: Injection profiles accompanied with the pressure obtained during injection through a single microneedle into skin-mimicking agarose at 0.5 µL/min. The black curve shows the average obtained pressure profile (n = 3) and the grey shaded area shows one standard deviation.

## 8.5 Conclusion

In this study, a novel method to produce hollow polymer microneedles was successfully demonstrated. We were able to create hollow microneedle cavities in an aluminium mould insert by laser ablation. The position of the lumen inside the microneedle was changed by adapting the laser scanning strategy. Polymer injection moulding was used to replicate the hollow microneedles using three sets of moulding conditions. The replication fidelity for each of these conditions was evaluated through microscopic measurements. It was found that the combination of a high mould temperature, volumetric injection rate and melt temperature facilitated the replication. At last, the functionality of the manufactured hollow microneedles was evaluated during single-needle injections. We effectively injected coloured water into an agarose matrix using a pressure pump. The developed methodology has a huge potential, as it acts as a mass production technique for low-cost, high-volume microneedle devices. Moreover, it is possible to change the design of the microneedle by adjusting the laser scanning parameters, which allows for further improvements.

In the nearby future, we will attempt to directly incorporate the fluidic connections between the needles and the polymer plate during the injection moulding process, by adapting the mould design. Besides, we will further improve the microneedle design in terms of functionality for different conditions and applications.

# Chapter 9 Valorisation plan

## 9.1 Introduction

In this PhD, a method to produce solid and hollow microneedles using injection moulding has been developed. These microneedles could first of all be marketed as standalone microneedles on top of solid polymer surface which could be used in the "poke with patch" and "coat and poke" strategy explained in section 2.2.3. A second option is to integrate the microneedles in a specific polymer product. A promising example is the integration of hollow microneedles in a complete microfluidic lab-on-a-chip, which enables the precise control and manipulation of fluids. In fact, medical substances could, for example, be mixed and transported towards the microneedles to achieve the controlled delivery of a specific volume of the substance. Moreover, the microneedles could also be used to extract fluids from the body, which can directly be used for sensing or diagnostic applications without the need for trained medical personnel. This chapter provides a valorisation plan concerning the injection moulding of solid and hollow polymer microneedles using the developed methods.

## 9.2 Existing patents

An important aspect to any company interested in valorising the research results is the freedom to operate. Therefore, an extensive search for existing patents related to the manufacture of microneedles was carried out. An overview of existing patents related to microneedle manufacturing is listed in Table 15. To the best of our knowledge, there are currently no patents that prevent the valorisation of the obtained research results.

Table 15: List of existing patents related to microneedle manufacturing.

| Patent number | Title of the patent | Date | Description |
|---|---|---|---|
| US3964482 | Drug delivery device | 22/06/1976 | First drug delivery device compromised of microneedles for penetrating the stratum corneum skin layer. |
| US5658515 | Polymer micromold and fabrication process | 19/08/1997 | Fabrication of a mould for the development of a microneedle by using precision machining, electroplating and etching |
| US6551849 | Method for fabricating arrays of micro-needles | 22/04/2003 | Method of manufacturing silicon hollow and solid microneedles using etching techniques. |

| | | | |
|---|---|---|---|
| US20030135161 | Microneedle devices and methods of manufacture | 17/07/2003 | Company 3M – Manufacturing a device with protruding microneedles from a substrate, with a cover placed over the substrate surface |
| US6749792 | Micro-needles and methods of manufacture and use thereof | 15/06/2004 | Method for fabricating microneedles using injection moulding, where the needle cavities are fabricated with electrical machining discharge |
| US6899838 | Method of forming a mold and molding a micro-device | 31/05/2005 | A method of forming a master for replication of microneedles, using an etching technique. |
| US6924087 | Polymer microneedles | 02/08/2005 | Method using a radiation sensitive polymer material to produce hollow and solid MN arrays for drug delivery. |
| US7658728 | Microneedle array, patch, and applicator for transdermal drug delivery | 10/01/2006 | Company AdminMed - The microneedle array device includes a substantially planar substrate having an array of steel microneedles. |
| US7497980 | Microneedles and microneedle fabrication | 03/03/2009 | Method for manufacturing a mould for making microneedles, by cutting a block of material in at least two different directions. |
| US20100312191 | Microneedle devices and methods of manufacture and use thereof | 09/12/2010 | Method of manufacturing hollow and porous microneedles using etching and electroplating techniques. |
| US7918814 | Method for drug delivery to ocular tissue using microneedle | 05/04/2011 | A method to manufacturing single solid microneedles using an infrared laser to cut microneedles from a stainless steel sheet. |

## 9.3 Target group and positioning

The main target group for our developed methods are injection moulding companies. These companies can either be an original equipment manufacturer (OEM) or a contract moulding company. In Europe, the plastics industry which includes plastic producers, plastic processing, plastic recyclers, and plastic machinery producers is the 8$^{th}$ most value adding sector, standing at a similar level to the pharmaceutical and electrical equipment industry [319]. It accounts for an employment of 1.5 million people divided over 52,000 companies. In total, a turnover of 330 billion euro is generated yearly. The vast majority of companies in the plastics sector in Europe are SMEs as the average number of employees per company is around 29 people [319]. The global injection moulding market size was estimated at USD 261.8 billion in 2021 and is anticipated to expand at a compounded annual growth rate of 4.8% from 2022 to 2030. The injection moulding market witnessed a rise due to the COVID-19 pandemic, as capacities needed to be increased to meet the growing demand for medical equipment [320]. Belgium is the

biggest plastics processer and producer in the world on a per capita basis and processes more than 2 Mt of plastics on a yearly basis [321]. In Flanders there are about 70 injection moulding companies, most of which are SMEs without their own R&D centre [322]. Therefore, most injection moulding companies in Flanders rely on research organisations for the development of innovative products or techniques, which they can further valorise in the future.

A second industrial sector that can benefit from the valorisation of the obtained results is the micro machining market, as this sector is responsible for machining the microcavities within the moulds. The sector was valued at USD 2.51 billion in 2019 and is excepted to expand at a compound annual growth rate of 7.3% from 2020 to 2027. The growth is driven by the increasing adoption of these systems for the fabrication of micro-components in industries such as healthcare [323]. In these fields, Flanders can count on prominent actors like Sirris, Flanders Make and many mould making companies (e.g. Tool Manufacturer Winters, Comate, Melotte), possibly interested in valorising the research results.

A third and fourth sector that can capitalise on the valorisation of the research results is the global in vitro diagnostics market and the vaccine market. The global in vitro diagnostics market is projected to grow from USD 71.4 billion in 2022 to USD 107.4 billion in 2029. The global intradermal in vitro diagnostics (delivery into the dermis skin layer), which can be targeted by microneedle systems, is sized at USD 16.3 billion in 2019 [324]. Some of the most prominent players in the global in vitro diagnostics market are Roche Diagnostics, Abbott, Siemens Healthineers, Danaher Corporation and Thermo Fisher Scientific [325]. Yet, it is expected that small to mid-sized Flanders based companies such as Biocartis, Novosanis and apDia could also benefit from the obtained research results. The vaccine market on the other hand, was valued at over USD 38 billion in 2021 and is expected to reach USD 72 billion by 2031. The key players in the global vaccines market include Serum Institute, Pfizer, Johnson & Johnson, AstraZeneca, Sanofi Aventis and the Belgium Janssen Pharmaceutica [326].

## 9.4 Position in the market

In 2018, over 2 billion vaccines were annually produced and administered worldwide using a classic syringe together with a hypodermic needle [327]. However, due to the Covid-19 pandemic, an additional 12.6 billion vaccine shots were administered between 2020 and 2022 [328]. Still, more than 1.1 million people die annually from vaccine preventable diseases as of today [329]. Most of these deaths occur in developing countries, due to the scarce diffusion of health centres, a lack of trained medical personnel, and due to needle phobia. Most microneedle systems that are currently developed, target the vaccine industry, as they can overcome current drawbacks in traditional vaccine delivery systems. First, microneedles are not long enough to pierce the nerve system. Therefore you can deliver vaccines in a pain-free way, hereby overcoming needle phobia. Second, self-administration could be possible by integrating the microneedles in a small disposable patch, eliminating the need for trained medical personnel.

Throughout the past decade, there has been a significant increase in industrial activity in the field of microneedle systems, especially in terms of the delivery of medical substances, such as vaccines. Currently, a select number of companies are developing microneedle systems, including AdminMed, 3M, Becton Dickinson Technologies, Sanofi

Pasteur, Zosano Pharma, Nanopass Technologies, Debiotech, and Idevax. Yet, it should be noted that no microneedle device is currently commercially available on the market for drug delivery. Micronjet™ from the Nanopass and Soluvia™ from Becton and Dickson Technologies are already available, yet they are not actually microneedle systems but rather very short conventional needles that can be used for intradermal injections using a classic syringe.

AdminMed is actively developing an innovative range of microneedle-based drug delivery devices. First they developed the AdminPatch™, which are SS316L stainless steel microneedle arrays made of SS316L stainless steel manufactured through a number of precision stamping and bending processes. Their second system, AdminPen™, is a pen-injector device which consists out of a moulded plastic part which is attached to the back surface of the AdminPatch™ microneedle array. The system can be attached to a standard commercially available syringe and is designed for vaccine delivery [330].

3M developed the Microstructured Transdermal System™, which can include both solid and hollow microneedles. The solid microneedles can be coated with water-soluble, polar, and ionic molecules, such as lidocaine, which can be delivered to the skin. The hollow microneedles can be used to deliver formulations up to 2 ml with various viscosities [10].

Becton Dickinson Technologies developed Soluvia™, which is a pre-fillable microinjection system which contains a 1.5 mm long 30G needle, having a capacity of 0.2 to 15 ml. Preclinical studies on the system have shown that it can successfully be used for intradermal delivery of an influenza vaccine with a similar effectiveness as a conventional intramuscular delivery [331].

Sanofi Pasteur developed the first intradermal micro-injection system, called Intanza™, for the delivery of influenza vaccines. The system uses the Soluvia™ injector developed by Becton Dickinson technologies and contains a 1.5 mm long hypodermic needle attached to a syringe injector [12]. Clinical studies indicated that Intanza enabled several benefits, yet in 2018 the product was withdrawn from use in the European Union at the request of the marketing authorization holder [332].

Zosano Pharma developed a transdermal microneedle system for the treatment of migraine, called Qtrypta™. The system consists of solid microneedles which are coated with zolmitriptan. The company reported that 2 hours after patients were treated with Qtrypta™, they were completely relieved from pain or felt relieved from the most bothersome symptoms. However, in 2020 the Food and Drug Administration (FDA) rejected Qtrypta™ as it did not meet the requirement of the FDA. Yet, the company is currently addressing the identified deficiencies and plans to resubmit the application [333].

Nanopass Technologies developed the MicronJet™, which is composed of four hollow silicon needles with a length of 500 μm attached to a plastic device which can be connected to a conventional syringe. The system was successfully used to administer the influenza vaccine and equivalent immunogenicity was demonstrating using only 20% of the vaccine dose used in the conventional delivery strategy [42]. In 2010, NanoPass was the first company to received FDA clearance for a delivery system using needles with a length below 1 mm with its MicronJet™ [334].

Debiotech is an injector system containing a single or multiple hollow silicon microneedles called DebioJect ™. The length of the microneedles can range from 350 to 900 μm and the system can be used to deliver up to 500 μl in 5 seconds [335].

Idevax is a Belgium company which was very recently founded in 2020. The company developed a platform with a preconfigured commercial 32G or 27G needle, called VAX-

ID™, which can be used for intradermal drug delivery with a penetration depth of 0.85 and 1.2mm, respectively [336].

It is clear that several pharmaceutical companies and research laboratories are involved in the development of microneedle based products. As such, a broad range of microneedle systems, with our without an application device have been fabricated in a variety of materials, using different manufacturing methods. To the best of our knowledge, none of these companies is involved in the development of a completely injection moulded polymer microneedle device. Moreover, there is also no information on the development of a microfluidic lab-on-a-chip with integrated hollow microneedles. As such, it can be concluded that a position in the market could be established with the developed methodology.

## 9.5 Economical evaluation

This section economically evaluates the developed methodology to produce polymer microneedles by means of injection moulding using laser ablated moulds. As already explained in previous sections, the microneedles can be integrated in various existing products, such as a lab-on-a-chip microfluidic systems. The additional manufacturing cost required to achieve this integration will vary depending on the desired application or product. Therefore, in this economical evaluation, a 25 x 25 x 1.5 mm³ flat plate with an array of 25 microneedles as illustrated in Figure 79. The thermoplastic material considered in this study is the polycarbonate Lexan™ HPX8REU grade, manufactured by SABIC, as this biocompatible material is suitable for medical devices and pharmaceutical applications.

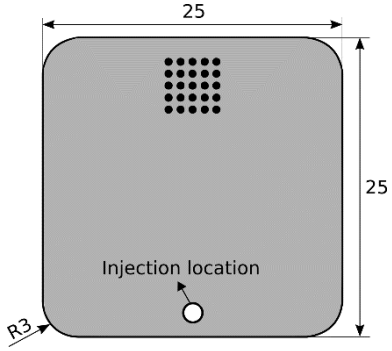


Figure 79: Illustration of the flat plate used in the economic evaluation. All represented dimensions are in mm and the part thickness is 1.5 mm.

### 9.5.1 Derivation of the product cost

The cost of an injection moulded product can be divided into the material cost, the mould cost and the production cost. The material cost per product can be calculated using Equation (7).

$$Material\ cost = m \cdot C_t \tag{7}$$

In this equation, $m$ is the mass of the polymer product and $C_t$ is the cost of the polymer material.

An injection mould consists out of a mould housing and mould cavities. A single cavity mould can produce 1 part during each injection moulding cycle, while a multi cavity mould is able to product multiple parts during each cycle. Producing multiple identical mould cavities will increase the manufacturing cost. However, this increase is not just a linear multiplication of the manufacturing cost for one cavity. Moreover, a multi cavity mould will also increase the size and complexity of the mould housing, resulting in an increased cost. The mould cost is typically divided over the total number of products produced. The higher the series size, the lower the mould cost per product. The mould cost is therefore defined by Equation (8).

$$Mould\ cost = \frac{(C_c + C_a) \cdot (0.5\ N + 1) + C_H \cdot (0.05\ N + 1)}{Z} \tag{8}$$

In this equation $C_c$ is the cost per cavity, $C_a$ is the cost for laser ablating the microneedle cavities, $N$ is the number of cavities, $Z$ is the series size, and $C_H$ is the cost for the mould housing.

The main factors influencing the production cost are the hourly machine cost, hourly labour cost, cycle time, and the number of cavities used. Equation (9) was used to calculate the production cost.

$$Production\ cost = \left( \frac{(C_m + C_l \cdot a) + \frac{C_{IM}}{D \cdot H}}{N} \right) \cdot \frac{t}{3600} \tag{9}$$

In this equation, $C_m$ is the hourly machine cost, $C_l$ is the hourly labour cost, $a$ is the man/machine ratio, $C_{IM}$ is purchase cost of the injection moulding equipment, $D$ is the depreciation period, $H$ is the total production time per year, $N$ is the number of cavities, and $t_c$ is the cycle time. The equation indicates that the production cost decreases with a lower cycle time and higher number of cavities. Moreover, by using a multicavity mould, several products are produced in each cycle, reducing the production cost per product. The hourly machine cost is the sum of the purchase cost, the maintenance cost and the energy cost.

### 9.5.2 Input data

The input data used in the equations for the derivation of the product cost are again segmented into the required data for the material cost, mould cost, and production cost. The material used in this study, is as already indicated, a polycarbonate material. The required amount of material for the considered product was calculated using the volume of the product and the density of the thermoplastic being 0.94 cm³ and 1.19 g/cm³, respectively. An estimated material price was provided by the material supplier. Total material costs are indicated in Table 16.

Table 16: Input data associated with the material cost.

| Description | Symbol | Input data |
|---|---|---|
| Mass of the thermoplastic [g] | $m$ | 1.12 |
| Material price [€/kg] | $C_t$ | 10 |

The input data associated with the mould cost is represented in Table 17. Cost estimation for the purchase of the standard mould parts (e.g. ejector pins and guide pillars) and the production of the mould cavity and mould housing was estimated based on previously purchased moulds that were manufactured by Loomans Technics BVBA. The cost related to machining the laser machining cavities was provided by Sirris, while the number of cavities and series size will be varied throughout the cost calculation.

Table 17: Input data associated with the mould cost.

| | Symbol | Input data |
|---|---|---|
| Mould cavity cost [€] | $C_c$ | 7500 |
| Cost for laser machining microneedle cavities [€] | $C_a$ | 515 |
| Number of cavities | $N$ | variable |
| Mould housing cost [€] | $C_H$ | 4500 |
| Series size | $Z$ | variable |

The input data associated with the production cost is represented in Table 18. The hourly machine cost includes the energy consumption, the cost of the floor space, and maintenance cost. The hourly energy cost is estimated at 5.27 kWh per kg material [337]. The yearly rent was estimated at 30 €/m² and the yearly maintenance cost for an injection moulding machine was estimated at € 3000. This results in an estimated hourly machine cost of € 2.6. In 2021 the hourly labour cost in Belgium was estimated at € 41.6 [338]. The man/machine ratio, which determines how many machines a single person can operate was set to 0.2. The purchase cost for the injection moulding equipment (e.g. the injection moulding machine and tempering unit) was estimated at € 85,000 based on previously purchased equipment. These purchase costs were depreciated over a period of 10 years, which is a typical depreciation period for injection moulding machines. The total production time of the company was estimated at 2000 hours, which corresponds to 250 production days of 8 hours. The cycle time for producing the thermoplastic part was estimated at 8 seconds, based on injection moulding experiments and simulations.

Table 18: Input data associated with the production cost.

| | Symbol | Input data |
|---|---|---|
| Hourly machine cost [€] | $C_m$ | 2.6 |
| Hourly labour cost [€] | $C_l$ | 41.6 |
| Man/machine ratio | $a$ | 0.2 |
| Purchase cost injection moulding equipment [€] | $C_{IM}$ | 85,000 |
| Depreciation period [years] | $D$ | 10 |
| Total production time per year [hours] | $H$ | 2000 |
| Number of cavities | $N$ | variable |
| Cycle time [s] | $t_c$ | 8 |

### 9.5.3 Results of the economic evaluation

The product cost is usually presented in function of the series size, as illustrated in Figure 80. It can be observed that the product cost decreases as the series size increases. This is due to the reason that the mould cost is divided by the total series size. For example, when producing only one product, the price of this one product should cover the complete mould cost. Therefore, injection moulding is usually unsuitable for small series sizes (< 10,000 products), due to the high mould costs.

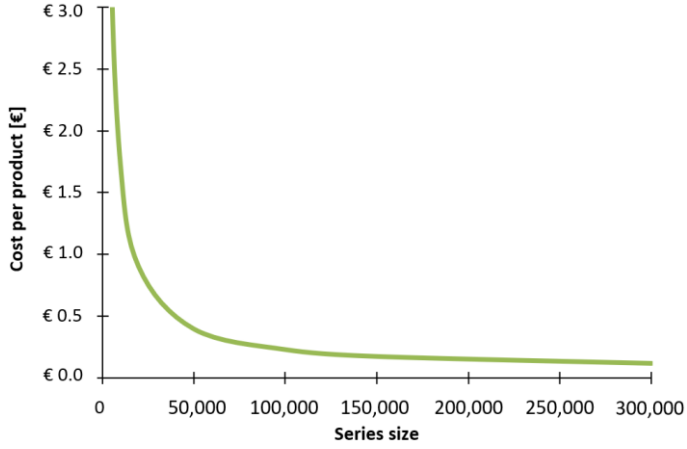


Figure 80: Product cost in function of the series size for injection moulding.

The composition of the product cost for a series size of 50,000 and 300,000 products is depicted in Figure 81. For a series size of 50,000 products, the product cost of € 0.4 is mainly determined by the mould cost, while only a small percentage is covered by the material and production cost. This is, as already explained, due to the high mould cost, which have to be covered by the total series size. For the series size of 300,000 products, the total product cost is decreased to € 0.12, yet might seem that the material cost and production cost have increased. However, this is only a relative value as the material cost is independent of the series size. Thus, the percentual increase in material and production cost can be allocated to the relative mould cost which has nearly been halved.

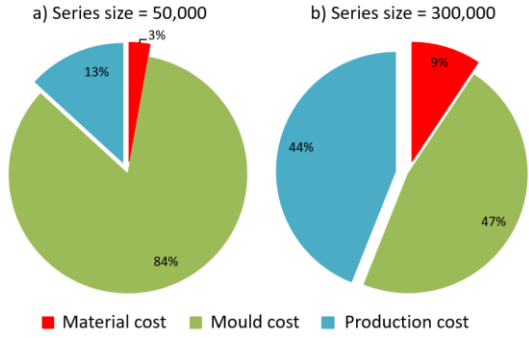


Figure 81: Composition of the product cost for a series size of (a) 50,000 products and (b) 300,000 products.

Figure 82 illustrates the product cost in function of the number of mould cavities for a specific series size of 300,000 products. Moreover, the required production days to manufacture the 300,000 products have also been indicated. From Equation (8), it is clear that the mould cost increases when using multiple mould cavities, since more work is required to manufacture the mould. The production cost on the other hand, decreases with a higher number of cavities, as multiple parts can be manufactured simultaneously. This trend is also observed in the graph, as with a higher number of cavities the mould cost (green) increases, while the production cost (blue) decreases. The material cost, however, is observed as a constant, as it is independent of the number of mould cavities. The total product cost (yellow) first decreases to a minimum value, before increasing again. The amount of production days also decrease as indicated in the figure. The minimal product cost for producing 300,000 products, corresponds to € 0.10 and requires 417 production days. However, for each specific case a trade-off between the production time and product cost should be considered.

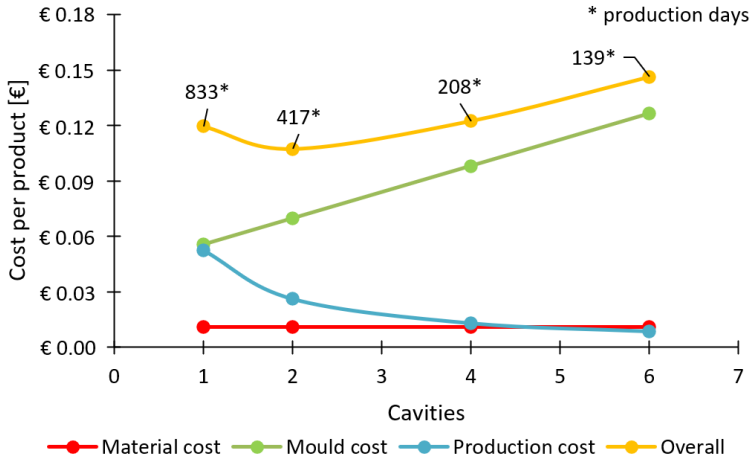


Figure 82: Product cost in function of the number of mould cavities for a series size of 300,000 products.

## 9.6 Intellectual property rights

The obtained research results reported in this thesis are not confidential and are being widely disseminated. During the PhD, this has been done through attendance at international symposia (e.g. Micro manufacturing Colloquia of the The International Institution for Micro Manufacturing), conferences (e.g. Polymer Processing Society), seminars, and through scientific publications in peer review international journals (e.g. Journal of Manufacturing Processes). After the PhD, efforts will be put in dissemination activities to further inform external stakeholders such as injection moulding companies, biotechnology companies, and international health organizations.

## 9.7 Future perspectives

### 9.7.1 Current status

At this stage, an extensive proof-of-concept is available to fabricate solid and hollow polymer microneedles at a high volume and low cost, using laser ablated moulds and polymer injection moulding. In fact, a laser machining strategy was developed which allows for the manufacturing of solid [216] and hollow [257] microneedle cavities with small tip radii in conventional mould materials. Besides, insights on the influence of the laser scanning parameters on the geometry of the ablated microneedle cavities were provided [247], [339]. Moreover, guidelines for injection moulding microneedles with a high replication fidelity together with a low variability between the individual needles are reported [340]. Furthermore, the capabilities of finite element flow simulations were assessed in order to predict the replication fidelity during injection moulding [280]. However, to valorise or commercialise the obtained results in industry, some gaps still need to be bridged.

### 9.7.2 Gaps towards valorisation

Although the developed methodology should be applicable to a wide range of thermoplastic materials, only two types of thermoplastics were validated in this study being PP and PC. Depending on the application in which the microneedles will be used, the desired thermoplastic can differ compared to the investigated materials. Changing the thermoplastic material, could have an effect on the replication fidelity during injection moulding, which in turn can have an effect on the resulting functionality of the needles. Thus, when using a different thermoplastic compared to the material grades used in this work, a feasibility study should be performed.

While investigating the effect of the laser scanning parameters, various shapes and geometries of the needle cavities were obtained. However, depending on the application in which the microneedles will be used, a specific needle shape and/or geometry might be required. Defining the required laser machining parameters to achieve a specific polymer microneedle geometry is an iterative process. The laser machining parameters will affect the geometry of the microneedle cavity, which will in turn affect the replication fidelity during the injection moulding process. However, using the developed knowledge about the effect of the laser machining parameters on the geometry of the microneedle cavity, a targeted set of laser machining experiments could be defined. Furthermore, finite element flow simulations can be used to predict the replication fidelity, in order to facilitate this iterative development process.

Currently, we are able to create hollow microneedles on top of a solid flat polymeric surface. However, in most applications, a fluidic connection is required between the hollow needles and the bottom of the flat surface. At this moment, we created this fluidic connection by drilling micro-holes through the flat surface. Although successful, this methodology requires an additional delicate, time-consuming process step which should be eliminated. An alternative, could be to directly incorporate the fluidic connections during the injection moulding process, by adapting the mould design.

Quality control is an important aspect within most sectors, especially in the medical field. Within the PhD, a lot of emphasis was put on assessing the replication fidelity of the microneedles, as this will directly affect the functionality of the microneedles. However, this quality assessment was exclusively done by measuring the geometry of the

needles during manual microscopic inspection. In an industrial environment where thousands of microneedles will be produced, this manual, time consuming test methodology is not feasible. Instead, an in-line control system which automatically determines the quality of the injection moulded microneedles should be developed.

# Chapter 10 Conclusions and outlook

## 10.1 Introduction

The literature review highlighted that manufacturing microneedles represents a real challenge. A wide range of process technologies has been proposed to manufacture microneedles, yet a production process with high volume outputs at low cost is currently lacking. An approach which fulfils these criteria is polymer injection moulding, as millions of polymer microneedle systems can be produced at a low cost. However, within the current state of the art, methods for applying the negative of the microneedles on the injection mould are limited to expensive and time consuming precision techniques. Moreover, knowledge on injection moulding microneedle arrays with a high replication fidelity together with a low variability between the individual needles is currently limited. Therefore, the development of a production methodology for the fabrication of high volume, low cost microneedle devices using laser ablated moulds and polymer injection moulding was deemed necessary. In this concluding chapter, the developed methodology, proposed characterisation methods, and investigated process insights and optimisations are summarised based on results from the previous chapters. Furthermore, an outlook is provided with recommendations for further research.

## 10.2 Conclusions

### 10.2.1 Developed methodology

The developed process enables the production of solid and hollow polymer microneedles, through replicating microneedle cavities in an injection moulding process. A cross-hatching laser machining strategy using a femtosecond laser was established to produce cone-shaped microcavities with very small tip radii in commercial mould materials. By replicating these microcavities in an injection moulding process, solid polymer microneedles with small tip radii can be manufactured. Moreover, by including a laser scan-free area within the cross-hatching strategy, it is also possible to produce microneedle cavities with an upstanding pillar, which can afterwards be replicated into hollow polymer microneedles. The major advantage of the proposed laser ablation technique is the flexible manufacturing, which enables the development of microneedle cavities with various shapes and dimensions, by adapting laser scanning parameters. The injection moulding process on the other hand, allows the replication of microneedle cavities in numerous polymer grades (e.g. PP and PC), at short cycle times and a low cost, while the whole process has the potential to be fully automated.

### 10.2.2 Laser ablation

Depending on the targeted medical application, the shape and size of the microneedles should be fine-tuned, while the design should allow for the needles to penetrate into the skin or any other biological tissue without breaking or severely bending. It is then important to know how to set the laser scanning parameters to achieve a specific geometry of the microneedle cavities. Therefore, we investigated the influence of two laser scanning parameters, the programmed base diameter and the number of layers, on the geometry of microneedle cavities. This geometry was characterised using μ-CT measurements and experiments were conducted in three commonly used mould materials, being tool steel, copper alloy and aluminium alloy. It was found that for all the mould materials, the depth of the cavities increased with a higher number of layers, before reaching a saturation. A good correlation was found between the programmed base diameter and the actual ablated cavity diameter, yet small deviations could be observed due to dynamic effects of the optical beam deflector system. Differences in shape and dimensions of the microneedle cavities were observed between the three mould materials, which could be allocated to differences in thermal and wetting properties. Besides the diameter and depth of the microneedle cavities, also the flank geometry of the microcavities was investigated, as this has an impact on both the mechanical strength and the penetration behaviour of the replicated polymer microneedles. It was found that the flank geometry could be adjusted by changing the programmed base diameter throughout the laser ablation process. Hereby, it was possible to change both the needle width near the base to increase its strength, or adapt the needle width near its tip to decrease the penetration force.

### 10.2.3 Injection moulding

A key aspect when replicating the manufactured microneedle cavities using injection moulding is the replication fidelity and uniformity, as this directly affects the functionality of the microneedles. Emphasis was put on the replication fidelity and uniformity during this PhD and it was found that various parameters have an effect on it. Following section explains the effects of these parameters.

The first parameter affecting the replication fidelity is the geometry of the microcavities. During injection moulding experiments with different cavity geometries, a clear linear relationships was found between the aspect ratio of the cavities and the replicated thermoplastic microneedles. The higher the aspect ratio of the hole, the lower the replication fidelity of the polymer microneedle. This is caused by both the hesitation effect and the higher heat transfer of larger aspect ratio cavities, due to the increased surface area to volume ratio.

The replication fidelity is also affected by the selected thermoplastic, as higher replication fidelities were found when using PP compared to PC. This is due to three factors. First, the large surface area to volume ratio of the microneedle cavities makes interfacial phenomena such as wettability critical. Contact angle measurements conducted in literature indicated that spreading coefficient, which is preferential for a high replication fidelity, for PP in combination with steel was higher, compared to PC. Second, the time required for PP to reach the no-flow temperature is nearly two times higher than for PC. This will result in a much faster solidification of the PC skin layer, which hinders the filling of the microneedle cavities. Third, the melt viscosity during the filling stage is

higher for PC compared to PP. Evidently, a lower melt viscosity will improve the replication fidelity.

Besides the thermoplastic material, also the mould material has an effect on the replication fidelity. Different replication fidelities were found between tool steel, copper alloy, and aluminium alloy, with the former having the best replication fidelity. The discrepancy in the filling capacity between the three materials was explained by the differences in thermal and wetting properties.

Another factor playing a significant role in the replication fidelity is the selected injection moulding technique (either conventional injection moulding or injection compression moulding) and corresponding processing parameters. Therefore, a full factorial design of experiments was conducted with the investigated parameters being the barrel temperature, volumetric injection rate, holding pressure and mould coolant temperature. It was found that the volumetric injection rate had the largest positive effect on the replication fidelity. The mould temperature and holding pressure were also found to have a positive effect, while the effect of the melt temperature was found to be insignificant for the considered temperature ranges. Besides, when comparing the conventional injection moulding process and the injection compression moulding process, it was found that the injection compression moulding process resulted in a higher average replication fidelity together with a better replication uniformity across the different microneedle arrays. The average replication in height together with the standard deviation corresponded to 1536 ± 81 μm and 1371 ± 117 μm for injection compression moulding and conventional injection moulding process, respectively. The cause of the difference in replication fidelity between both techniques was allocated to the different flow behaviours. As the polymer was injected into a slightly opened mould for the injection compression moulding process, more heat was retained in the polymer melt, which promoted the filling of the microneedles. Moreover, a higher and more evenly distributed pressure inside the cavity was observed compared to the injection moulding process resulting in a better overall replication.

The last parameter found to have an effect on the replication fidelity is the location of the microneedles on top of the macroscopic product. A clear linear relationship was found between the replication in height and the distance of the microneedles from the gate position or the end of flow. A higher replication fidelity is observed for microneedles located far from the gate position, compared to microneedles located near the gate. The cause for this was explained by the difference in temperature, pressure and viscosity of the polymer melt at the different positions on the product.

### 10.2.4 Numerical flow simulations

To prevent extensive, costly, time consuming injection moulding experiments when developing a new polymer microneedle device, it was investigated if numerical flow simulations could be used to accurately predict the replication fidelity. Therefore, we evaluated the replication fidelity of solid polymer microneedles using numerical simulations and compared the results to injection moulding experiments. This evaluation was conducted for (i) PP and PC, (ii) different locations of the microneedles on the macroscopic polymer part, (iii) different injection moulding parameters, and (iv) different mould materials being tool steel, copper alloy and aluminium alloy. A good correlation with experimental findings was achieved by experimentally optimizing the heat transfer coefficient between the polymer and the mould, while using a fine multiscale mesh. Optimal heat transfer coefficients between 10,000 W/m²·K to 55,000 W/m²·K were

found for the investigated combinations of polymer and mould materials, which resulted in an accuracy of the simulated microneedle replication fidelity between 94.5 % to 97.0 %. As such, numerical flow simulations can be used to accurately predict the filling behaviour of micro surface features on a macroscopic part.

### 10.2.5 Valorisation

A valorisation plan is proposed concerning the injection moulding of solid and hollow polymer microneedles using the developed methods. The freedom to operate was investigated by examining existing patents related to microneedle manufacturing. No patents were found that, to our knowledge, could prevent the industrial valorisation. Furthermore, the target group that could benefit from the obtained research results were identified and an estimation on the market size was provided. The position of the developed methodology in the market was investigated, and a summary of existing microneedle systems was presented. Moreover, an economical evaluation of the developed methodology to produce polymer microneedles using injection moulding using laser ablated moulds was conducted. The minimal product cost for producing 300,000 polycarbonate flat plates (25 x 25 x 1.5 $mm^3$) with an array of 25 microneedles was estimated at € 0.1. Finally, existing gaps that need to be addressed before commercialising the obtained results were summarised. This includes an in-line quality control system within the injection moulding machine or an adaptive mould design, which directly incorporates the fluidic connection in hollow microneedles.

## 10.3 Outlook

Besides the gaps towards valorisation identified in section 9.7.2, additional recommendations for future research can be formulated.

Depending on the application in which the microneedles will be used, a certain size and shape of the microneedle is required to achieve a desired functionality. However, achieving an optimal microneedle for a specific application poses two problems. First, in most applications the required optimal microneedle geometry is unknown. Second, manufacturing a specific microneedle geometry is currently a trial-and-error, complex, time consuming, iterative process. This process consists of two manufacturing steps, being laser ablation and injection moulding. There is currently no simulation model available to predict the required laser scanning parameters. As such, extensive laser machining experiments have to be conducted to create various microneedle cavities. Afterwards, the laser ablated microneedle cavities can either be used in numerical flow simulations or in injection moulding experiments, to predict the replication fidelity. Only after this, the final needle geometry with corresponding replication fidelity is known, and can the needle functionality be assessed. Following suggestions are proposed to improve this iterative process:

(1) To directly assess the effect of the needle geometry (i.e. the needle length, inner and outer diameter, and bevel angle) and special configuration of the array (i.e. number of microneedles and inter-needle distance) on the functionality, it is suggested to produce microneedles using additive manufacturing. Two-photon polymerization is a technique that is capable of producing micro features with a very high print resolution down to 100 nm. As such, it is possible to

manufacture a specific needle geometry and afterwards directly assess its functionality.

(2) A simulation model which is capable of predicting the geometry of the laser ablated cavities can drastically reduce extensive laser machining experiments. Therefore, it is suggested to develop a numerical model to predict the shape and size of the laser ablated microneedle cavities based on both analytical and empirical data. This challenge is being tackled in the PhD project of Pol Vanwersch supervised by Prof. Sylvie Castagne and Prof. Albert Van Bael.

(3) Injection moulding simulations have proven that the replication fidelity of solid microneedles can accurately be predicted. However, this was not yet demonstrated for hollow microneedles. Therefore, the accuracy of injection moulding simulations with hollow microneedles should be investigated.

(4) Besides process simulation tools to predict the microneedle manufacturing, also simulations which could be used to assess the needle functionality would improve the development process. It is therefore suggested to develop a numerical simulation methodology to predict the mechanical behaviour of the needles during skin insertion.

Throughout the PhD study some needle deformation and needle breakage were observed, possibly due to a high demoulding force of the microneedles inside the cavities. This excessive demoulding force was caused by the replication of surface roughness on the microneedle shaft, which formed microscopic undercuts. It is suggested to micro-polish the microcavities using laser ablation or chemical etching techniques in future research. Moreover, it should also be investigated if PVD-coatings could reduce the surface roughness inside the microcavities. An additional benefit of these coatings is their very low thermal conductivity, which could act as a thermal barrier [277]. This barrier can delay the formation of the frozen layer, which will improve the replication fidelity. Thus, these coatings could possible lead to both a lower demoulding force and a higher replication fidelity.

As already indicated in the valorisation plan (section 9.1), integrating microneedles within a complete microfluidic lab-on-a-chip offers a huge application potential. However, manufacturing such a chip is, to the best of our knowledge, not yet done. It is therefore suggested to investigate whether it is possible to manufacture a complete microfluidic chip with integrated microneedles. A possible methodology could be to injection mould the two mould haves, where one will contain the microchannels and the other the hollow microneedles. The two halves should then be assembled using reliable bonding techniques such as transparent laser plastic welding.

# Bibliography


[1] R. F. Donnelly, T. R. R. Singh, E. Larrañeta, and M. T. C. McCrudden, *Microneedles for Drug and Vaccine Delivery and Patient Monitoring*. Chichester, UK: John Wiley & Sons, Ltd, 2018.

[2] M. Urdea *et al.*, "Requirements for high impact diagnostics in the developing world.," *Nature*, vol. 444 Suppl, pp. 73–79, 2006, doi: 10.1038/nature05448.

[3] X. (James) Li and Y. Zhou, "Microfluidic devices for biomedical applications," in *Woodhead Publishing Series in Biomaterials*, Cambridge: Woodhead Publishing Limited, 2013, pp. 1–652.

[4] R. F. Donnelly, T. R. R. Singh, and A. D. Woolfson, "Microneedle-based drug delivery systems: Microfabrication, drug delivery, and safety," *Drug Deliv.*, vol. 17, no. 4, pp. 187–207, May 2010, doi: 10.3109/10717541003667798.

[5] H. Juster, B. van der Aar, and H. de Brouwer, "A review on microfabrication of thermoplastic polymer-based microneedle arrays," *Polym. Eng. Sci.*, vol. 59, no. 5, pp. 877–890, 2019, doi: 10.1002/pen.25078.

[6] A. J. Guillot, A. S. Cordeiro, R. F. Donnelly, M. C. Montesinos, T. M. Garrigues, and A. Melero, "Microneedle-based delivery: An overview of current applications and trends," *Pharmaceutics*, vol. 12, no. 6, pp. 1–28, 2020, doi: 10.3390/pharmaceutics12060569.

[7] E. Larrañeta, R. E. M. Lutton, A. D. Woolfson, and R. F. Donnelly, "Microneedle arrays as transdermal and intradermal drug delivery systems: Materials science, manufacture and commercial development," *Mater. Sci. Eng. R Reports*, vol. 104, pp. 1–32, 2016, doi: 10.1016/j.mser.2016.03.001.

[8] R. Nagarkar, M. Singh, H. X. Nguyen, and S. Jonnalagadda, "A review of recent advances in microneedle technology for transdermal drug delivery," *J. Drug Deliv. Sci. Technol.*, vol. 59, no. June, p. 101923, Oct. 2020, doi: 10.1016/j.jddst.2020.101923.

[9] J. W. Lee, M. R. Han, and J. H. Park, "Polymer microneedles for transdermal drug delivery," *J. Drug Target.*, vol. 21, no. 3, pp. 211–223, 2013, doi: 10.3109/1061186X.2012.741136.

[10] A. Tucak *et al.*, "Microneedles: Characteristics, materials, production methods and commercial development," *Micromachines*, vol. 11, no. 11, 2020, doi: 10.3390/mi11110961.

[11] J. G. Hamilton, "Needle phobia: A neglected diagnosis," *J. Fam. Pract.*, vol. 41, no. 2, pp. 169–175, 1995.

[12] S. Indermun *et al.*, "Current advances in the fabrication of microneedles for transdermal delivery," *J. Control. Release*, vol. 185, no. 1, pp. 130–138, Jul. 2014, doi: 10.1016/j.jconrel.2014.04.052.

[13] R. Mahato, "Microneedles in Drug Delivery," in *Emerging Nanotechnologies for Diagnostics, Drug Delivery and Medical Devices*, vol. 59, Elsevier, 2017, pp. 331–353.

[14] A. Laurent *et al.*, "Echographic measurement of skin thickness in adults by high frequency ultrasound to assess the appropriate microneedle length for intradermal delivery of vaccines," *Vaccine*, vol. 25, no. 34, pp. 6423–6430, Aug.

2007, doi: 10.1016/j.vaccine.2007.05.046.

[15] B. E. Polat, D. Blankschtein, and R. Langer, "Low-frequency sonophoresis: application to the transdermal delivery of macromolecules and hydrophilic drugs," *Expert Opin. Drug Deliv.*, vol. 7, no. 12, pp. 1415–1432, Dec. 2010, doi: 10.1517/17425247.2010.538679.

[16] J. A. Bouwstra, G. S. Gooris, J. A. van der Spek, and W. Bras, "Structural Investigations of Human Stratum Corneum by Small-Angle X-Ray Scattering," *J. Invest. Dermatol.*, vol. 97, no. 6, pp. 1005–1012, Dec. 1991, doi: 10.1111/1523-1747.ep12492217.

[17] J. A. Delgado, I. Quesada, L. M. Montaño, and L. Anasagasti, "Safety of UV radiation for autofluorescence diagnosis of skin cancer," *Rev. Mex. Fis.*, vol. 52, no. 1 SUPPL., pp. 78–83, 2006.

[18] H. Suh, J. Shin, and Y.-C. Kim, "Microneedle patches for vaccine delivery," *Clin. Exp. Vaccine Res.*, vol. 3, no. 1, p. 42, 2014, doi: 10.7774/cevr.2014.3.1.42.

[19] K. Ita, "Transdermal delivery of drugs with microneedles: Strategies and outcomes," *J. Drug Deliv. Sci. Technol.*, vol. 29, pp. 16–23, 2015, doi: 10.1016/j.jddst.2015.05.001.

[20] A. T. Ogunjimi, J. Carr, C. Lawson, N. Ferguson, and N. K. Brogden, "Micropore closure time is longer following microneedle application to skin of color," *Sci. Rep.*, vol. 10, no. 1, p. 18963, Dec. 2020, doi: 10.1038/s41598-020-75246-8.

[21] X. Chen *et al.*, "Dry-coated microprojection array patches for targeted delivery of immunotherapeutics to the skin," *J. Control. Release*, vol. 139, no. 3, pp. 212–220, Nov. 2009, doi: 10.1016/j.jconrel.2009.06.029.

[22] H. S. Gill and M. R. Prausnitz, "Coating Formulations for Microneedles," *Pharm. Res.*, vol. 24, no. 7, pp. 1369–1380, Jul. 2007, doi: 10.1007/s11095-007-9286-4.

[23] Y. C. Kim, J. H. Park, and M. R. Prausnitz, "Microneedles for drug and vaccine delivery," *Adv. Drug Deliv. Rev.*, vol. 64, no. 14, pp. 1547–1568, 2012, doi: 10.1016/j.addr.2012.04.005.

[24] R. F. Donnelly *et al.*, "Hydrogel-forming microneedle arrays for enhanced transdermal drug delivery," *Adv. Funct. Mater.*, vol. 22, no. 23, pp. 4879–4890, 2012, doi: 10.1002/adfm.201200864.

[25] M. Gad-el-Hak, and W. Seemann, "MEMS Handbook," *Appl. Mech. Rev.*, vol. 55, no. 6, pp. B109–B109, Nov. 2002, doi: 10.1115/1.1508147.

[26] S. Badilescu and M. Packirisamy, *BioMEMS: Science and engineering perspectives*. Taylor & Francis Group, 2016.

[27] O. Paul, J. Gaspar, and P. Ruther, "Advanced silicon microstructures, sensors, and systems," *IEEJ Trans. Electr. Electron. Eng.*, vol. 2, no. 3, pp. 199–215, May 2007, doi: 10.1002/tee.20155.

[28] A. Das, C. Singha, and A. Bhattacharyya, "Development of silicon microneedle arrays with spontaneously generated micro-cavity ring for transdermal drug delivery," *Microelectron. Eng.*, vol. 210, no. September 2018, pp. 14–18, Apr. 2019, doi: 10.1016/j.mee.2019.03.019.

[29] J. D. Zahn, N. H. Talbot, D. Liepmann, and A. P. Pisano, "Microfabricated polysilicon microneedles for minimally invasive biomedical devices," *Biomed. Microdevices*, vol. 2, no. 4, pp. 295–303, 2000.

[30] R. F. Donnelly *et al.*, "Microneedle Arrays Permit Enhanced Intradermal Delivery of a Preformed Photosensitizer," *Photochem. Photobiol.*, vol. 85, no. 1, pp. 195–204, Jan. 2009, doi: 10.1111/j.1751-1097.2008.00417.x.

[31] N. Wilke, A. Mulcahy, S.-R. Ye, and A. Morrissey, "Process optimization and characterization of silicon microneedles fabricated by wet etch technology," *Microelectronics J.*, vol. 36, no. 7, pp. 650–656, Jul. 2005, doi: 10.1016/j.mejo.2005.04.044.

[32] S. Pradeep Narayanan and S. Raghavan, "Solid silicon microneedles for drug delivery applications," *Int. J. Adv. Manuf. Technol.*, vol. 93, no. 1–4, pp. 407–422, Oct. 2017, doi: 10.1007/s00170-016-9698-6.

[33] L. Wei-Ze *et al.*, "Super-short solid silicon microneedles for transdermal drug delivery applications," *Int. J. Pharm.*, vol. 389, no. 1–2, pp. 122–129, Apr. 2010, doi: 10.1016/j.ijpharm.2010.01.024.

[34] B. Ma *et al.*, "A PZT insulin pump integrated with a silicon microneedle array for transdermal drug delivery," *Microfluid. Nanofluidics*, vol. 2, no. 5, pp. 417–423, 2006, doi: 10.1007/s10404-006-0083-x.

[35] H. Kim, L. S. Theogarajan, and S. Pennathur, "A repeatable and scalable fabrication method for sharp, hollow silicon microneedles," *J. Micromechanics Microengineering*, vol. 28, no. 3, p. 035007, Mar. 2018, doi: 10.1088/1361-6439/aaa6a8.

[36] Y. Li *et al.*, "Fabrication of sharp silicon hollow microneedles by deep-reactive ion etching towards minimally invasive diagnostics," *Microsystems Nanoeng.*, vol. 5, no. 1, p. 41, Dec. 2019, doi: 10.1038/s41378-019-0077-y.

[37] F. Ceyssens, B. P. Chaudhri, C. Van Hoof, and R. Puers, "Fabrication process for tall, sharp, hollow, high aspect ratio polymer microneedles on a platform," *J. Micromechanics Microengineering*, vol. 23, no. 7, 2013, doi: 10.1088/0960-1317/23/7/075023.

[38] S.-J. Paik *et al.*, "In-plane single-crystal-silicon microneedles for minimally invasive microfluid systems," *Sensors Actuators A Phys.*, vol. 114, no. 2–3, pp. 276–284, Sep. 2004, doi: 10.1016/j.sna.2003.12.029.

[39] N. Roxhed, P. Griss, and G. Stemme, "Membrane-sealed hollow microneedles and related administration schemes for transdermal drug delivery," *Biomed. Microdevices*, vol. 10, no. 2, pp. 271–279, Apr. 2008, doi: 10.1007/s10544-007-9133-8.

[40] H. J. G. E. Gardeniers *et al.*, "Silicon micromachined hollow microneedles for transdermal liquid transport," *J. Microelectromechanical Syst.*, vol. 12, no. 6, pp. 855–862, Dec. 2003, doi: 10.1109/JMEMS.2003.820293.

[41] M. G. McGrath, A. Vrdoljak, C. O'Mahony, J. C. Oliveira, A. C. Moore, and A. M. Crean, "Determination of parameters for successful spray coating of silicon microneedle arrays," *Int. J. Pharm.*, vol. 415, no. 1–2, pp. 140–149, Aug. 2011, doi: 10.1016/j.ijpharm.2011.05.064.

[42] E. Larrañeta, R. E. M. Lutton, a D. Woolfson, and R. F. Donnelly, "Microneedle arrays as transdermal and intradermal drug delivery systems: Materials science, manufacture and commercial development," *Mater. Sci. Eng. R Reports*, vol. 104, pp. 1–32, Jun. 2016, doi: 10.1016/j.mser.2016.03.001.

[43] G. Budinski and K. Budinski, *Materiaalkunde.pdf*. Amsterdam: Pearson Benelux B.V., 2009.

[44] F. J. Verbaan *et al.*, "Assembled microneedle arrays enhance the transport of compounds varying over a large range of molecular weight across human dermatomed skin," *J. Control. Release*, vol. 117, no. 2, pp. 238–245, Feb. 2007, doi: 10.1016/j.jconrel.2006.11.009.

[45] F. J. Verbaan *et al.*, "Improved piercing of microneedle arrays in dermatomed

human skin by an impact insertion method," *J. Control. Release*, vol. 128, no. 1, pp. 80–88, May 2008, doi: 10.1016/j.jconrel.2008.02.009.

[46] Z. Ding *et al.*, "Microneedle arrays for the transcutaneous immunization of diphtheria and influenza in BALB/c mice," *J. Control. Release*, vol. 136, no. 1, pp. 71–78, May 2009, doi: 10.1016/j.jconrel.2009.01.025.

[47] D. P. Wermeling *et al.*, "Microneedles permit transdermal delivery of a skin-impermeant medication to humans," *Proc. Natl. Acad. Sci.*, vol. 105, no. 6, pp. 2058–2063, Feb. 2008, doi: 10.1073/pnas.0710355105.

[48] W. Martanto, S. P. Davis, N. R. Holiday, J. Wang, H. S. Gill, and M. R. Prausnitz, "Transdermal Delivery of Insulin Using Microneedles in Vivo," *Pharm. Res.*, vol. 21, no. 6, pp. 947–952, Jun. 2004, doi: 10.1023/B:PHAM.0000029282.44140.2e.

[49] M. Kaur, K. B. Ita, I. E. Popova, S. J. Parikh, and D. A. Bair, "Microneedle-assisted delivery of verapamil hydrochloride and amlodipine besylate," *Eur. J. Pharm. Biopharm.*, vol. 86, no. 2, pp. 284–291, Feb. 2014, doi: 10.1016/j.ejpb.2013.10.007.

[50] T. Omatsu *et al.*, "Metal microneedle fabrication using twisted light with spin," *Opt. Express*, vol. 18, no. 17, p. 17967, Aug. 2010, doi: 10.1364/OE.18.017967.

[51] M. Rajabi *et al.*, "Flexible and stretchable microneedle patches with integrated rigid stainless steel microneedles for transdermal biointerfacing," *PLoS One*, vol. 11, no. 12, pp. 1–13, 2016, doi: 10.1371/journal.pone.0166330.

[52] E. M. Saurer, R. M. Flessner, S. P. Sullivan, M. R. Prausnitz, and D. M. Lynn, "Layer-by-Layer Assembly of DNA- and Protein-Containing Films on Microneedles for Drug Delivery to the Skin," *Biomacromolecules*, vol. 11, no. 11, pp. 3136–3143, Nov. 2010, doi: 10.1021/bm1009443.

[53] H. S. Gill and M. R. Prausnitz, "Coated microneedles for transdermal delivery," *J. Control. Release*, vol. 117, no. 2, pp. 227–237, Feb. 2007, doi: 10.1016/j.jconrel.2006.10.017.

[54] J. Jiang *et al.*, "Coated Microneedles for Drug Delivery to the Eye," *Investig. Opthalmology Vis. Sci.*, vol. 48, no. 9, p. 4038, Sep. 2007, doi: 10.1167/iovs.07-0066.

[55] E. R. Parker, M. P. Rao, K. L. Turner, C. D. Meinhart, and N. C. MacDonald, "Bulk Micromachined Titanium Microneedles," *J. Microelectromechanical Syst.*, vol. 16, no. 2, pp. 289–295, Apr. 2007, doi: 10.1109/JMEMS.2007.892909.

[56] M. Ameri *et al.*, "Human Growth Hormone Delivery with a Microneedle Transdermal System: Preclinical Formulation, Stability, Delivery and PK of Therapeutically Relevant Doses," *Pharmaceutics*, vol. 6, no. 2, pp. 220–234, May 2014, doi: 10.3390/pharmaceutics6020220.

[57] M. Cormier *et al.*, "Transdermal delivery of desmopressin using a coated microneedle array patch system," *J. Control. Release*, vol. 97, no. 3, pp. 503–511, Jul. 2004, doi: 10.1016/j.jconrel.2004.04.003.

[58] M. Verhoeven *et al.*, "Applying ceramic nanoporous microneedle arrays as a transport interface in egg plants and an ex-vivo human skin model," *Microelectron. Eng.*, vol. 98, pp. 659–662, Oct. 2012, doi: 10.1016/j.mee.2012.07.022.

[59] S. Bystrova and R. Luttge, "Micromolding for ceramic microneedle arrays," *Microelectron. Eng.*, vol. 88, no. 8, pp. 1681–1684, Aug. 2011, doi: 10.1016/j.mee.2010.12.067.

[60] A. DORAISWAMY *et al.*, "Two photon induced polymerization of organic–inorganic hybrid biomaterials for microstructured medical devices," *Acta Biomater.*, vol. 2, no. 3, pp. 267–275, May 2006, doi: 10.1016/j.actbio.2006.01.004.

[61] A. Ovsianikov, B. Chichkov, P. Mente, N. A. Monteiro-Riviere, A. Doraiswamy, and R. J. Narayan, "Two Photon Polymerization of Polymer-Ceramic Hybrid Materials for Transdermal Drug Delivery," *Int. J. Appl. Ceram. Technol.*, vol. 4, no. 1, pp. 22–29, Jan. 2007, doi: 10.1111/j.1744-7402.2007.02115.x.

[62] K. H. Haas and H. Wolter, "Synthesis, properties and applications of inorganic-organic copolymers (ORMOCER®s)," *Curr. Opin. Solid State Mater. Sci.*, vol. 4, no. 6, pp. 571–580, 1999, doi: 10.1016/S1359-0286(00)00009-7.

[63] W. Martanto *et al.*, "Microinfusion using hollow microneedles," *Pharm. Res.*, vol. 23, no. 1, pp. 104–113, 2006, doi: 10.1007/s11095-005-8498-8.

[64] J. Gupta, E. I. Felner, and M. R. Prausnitz, "Minimally Invasive Insulin Delivery in Subjects with Type 1 Diabetes Using Hollow Microneedles," *Diabetes Technol. Ther.*, vol. 11, no. 6, pp. 329–337, Jun. 2009, doi: 10.1089/dia.2008.0103.

[65] P. M. Wang, M. Cornwell, J. Hill, and M. R. Prausnitz, "Precise Microinjection into Skin Using Hollow Microneedles," *J. Invest. Dermatol.*, vol. 126, no. 5, pp. 1080–1087, May 2006, doi: 10.1038/sj.jid.5700150.

[66] M. Gülçür *et al.*, "A cost-effective process chain for thermoplastic microneedle manufacture combining laser micro-machining and micro-injection moulding," *CIRP J. Manuf. Sci. Technol.*, vol. 32, pp. 311–321, Jan. 2021, doi: 10.1016/j.cirpj.2021.01.015.

[67] M. Han, D. H. Hyun, H. H. Park, S. S. Lee, C. H. Kim, and C. Kim, "A novel fabrication process for out-of-plane microneedle sheets of biocompatible polymer," *J. Micromechanics Microengineering*, vol. 17, no. 6, pp. 1184–1191, Jun. 2007, doi: 10.1088/0960-1317/17/6/012.

[68] J. OH *et al.*, "Influence of the delivery systems using a microneedle array on the permeation of a hydrophilic molecule, calcein," *Eur. J. Pharm. Biopharm.*, vol. 69, no. 3, pp. 1040–1045, Aug. 2008, doi: 10.1016/j.ejpb.2008.02.009.

[69] S. Sharma, A. Saeed, C. Johnson, N. Gadegaard, and A. E. Cass, "Rapid, low cost prototyping of transdermal devices for personal healthcare monitoring," *Sens. Bio-Sensing Res.*, vol. 13, pp. 104–108, 2017, doi: 10.1016/j.sbsr.2016.10.004.

[70] K. UCHIUMI, T. TAKAYAMA, H. ITO, and A. INOU, "SURFACE REPLICATION OF MOLDED PRODUCTS WITH MICRONEEDLE FEATURES IN INJECTION MOLDING," *Int. J. Mod. Phys. Conf. Ser.*, vol. 06, pp. 166–171, Jan. 2012, doi: 10.1142/S2010194512003121.

[71] L. Xue, G. Zhou, Y. J. Zhang, J. Zhuang, and D. M. Wu, "Micro Injection Molding and Strength Check of Polymer Micro-Needle," *Adv. Mater. Res.*, vol. 690–693, pp. 3136–3140, May 2013, doi: 10.4028/www.scientific.net/AMR.690-693.3136.

[72] C. T. Uppuluri *et al.*, "Microneedle-assisted transdermal delivery of Zolmitriptan: effect of microneedle geometry, in vitro permeation experiments, scaling analyses and numerical simulations," *Drug Dev. Ind. Pharm.*, vol. 43, no. 8, pp. 1292–1303, Aug. 2017, doi: 10.1080/03639045.2017.1313862.

[73] P. Janphuang *et al.*, "Polymer based microneedle patch fabricated using microinjection moulding," *MATEC Web Conf.*, vol. 192, p. 01039, Aug. 2018, doi: 10.1051/matecconf/201819201039.

[74] S. Gao, Z. Qiu, Z. Ma, and Y. Yang, "Development of high efficiency infrared-heating-assisted micro-injection molding for fabricating micro-needle array," *Int. J. Adv. Manuf. Technol.*, vol. 92, no. 1–4, pp. 831–838, Sep. 2017, doi: 10.1007/s00170-017-0169-5.

[75] S. Gao, Z. Qiu, and J. Ouyang, "The Improvement Effect and Mechanism of

Longitudinal Ultrasonic Vibration on the Injection Molding Quality of a Polymeric Micro-Needle Array," *Polymers (Basel).*, vol. 11, no. 1, p. 151, Jan. 2019, doi: 10.3390/polym11010151.

[76] M. Gülçür *et al.*, "Ultrasonic micromoulding: Process characterisation using extensive in-line monitoring for micro-scaled products," *J. Manuf. Process.*, vol. 58, no. August, pp. 289–301, Oct. 2020, doi: 10.1016/j.jmapro.2020.08.033.

[77] Seong-O Choi *et al.*, "An electrically active microneedle array for electroporation of skin for gene delivery," no. June 2014, pp. 1513–1516, 2005, doi: 10.1109/sensor.2005.1497371.

[78] P. C. DeMuth *et al.*, "Polymer multilayer tattooing for enhanced DNA vaccination," *Nat. Mater.*, vol. 12, no. 4, pp. 367–376, Apr. 2013, doi: 10.1038/nmat3550.

[79] Y.-C. Kim, F.-S. Quan, R. W. Compans, S.-M. Kang, and M. R. Prausnitz, "Formulation of Microneedles Coated with Influenza Virus-like Particle Vaccine," *AAPS PharmSciTech*, vol. 11, no. 3, pp. 1193–1201, Sep. 2010, doi: 10.1208/s12249-010-9471-3.

[80] Y. K. Demir, Z. Akan, and O. Kerimoglu, "Characterization of Polymeric Microneedle Arrays for Transdermal Drug Delivery," *PLoS One*, vol. 8, no. 10, p. e77289, Oct. 2013, doi: 10.1371/journal.pone.0077289.

[81] Y. Ito, E. Hagiwara, A. Saeki, N. Sugioka, and K. Takada, "Feasibility of microneedles for percutaneous absorption of insulin," *Eur. J. Pharm. Sci.*, vol. 29, no. 1, pp. 82–88, Sep. 2006, doi: 10.1016/j.ejps.2006.05.011.

[82] L. Y. Chu, S.-O. Choi, and M. R. Prausnitz, "Fabrication of Dissolving Polymer Microneedles for Controlled Drug Encapsulation and Delivery: Bubble and Pedestal Microneedle Designs," *J. Pharm. Sci.*, vol. 99, no. 10, pp. 4228–4238, Oct. 2010, doi: 10.1002/jps.22140.

[83] S. P. Sullivan, N. Murthy, and M. R. Prausnitz, "Minimally Invasive Protein Delivery with Rapidly Dissolving Polymer Microneedles," *Adv. Mater.*, vol. 20, no. 5, pp. 933–938, Mar. 2008, doi: 10.1002/adma.200701205.

[84] R. F. Donnelly *et al.*, "Design, optimization and characterisation of polymeric microneedle arrays prepared by a novel laser-based micromoulding technique," *Pharm. Res.*, vol. 28, no. 1, pp. 41–57, 2011, doi: 10.1007/s11095-010-0169-8.

[85] R. F. Donnelly *et al.*, "Hydrogel-Forming Microneedles Prepared from 'Super Swelling' Polymers Combined with Lyophilised Wafers for Transdermal Drug Delivery," *PLoS One*, vol. 9, no. 10, p. e111547, Oct. 2014, doi: 10.1371/journal.pone.0111547.

[86] W. Yuan, Sixing Yang, Yan Feng, Lijun Zhang, Nixiang Chen, and Tuo Jin, "A scalable fabrication process of polymer microneedles," *Int. J. Nanomedicine*, vol. 7, p. 1415, Mar. 2012, doi: 10.2147/IJN.S28511.

[87] D. Banks, *Microengineering, MEMS, and Interfacing*, vol. 9, no. 6. CRC Press, 2006.

[88] R. F. Donnelly, T. R. R. Singh, D. I. J. Morrow, and A. D. Woolfson, *Microneedle-mediated Transdermal and Intradermal Drug Delivery*. Pondicherry, 2012.

[89] S. Henry, D. V. McAllister, M. G. Allen, and M. R. Prausnitz, "Microfabricated microneedles: A novel appraoch to transdermal drug delivery," *J. Pharm. Sci.*, vol. 87, no. 25, pp. 922–925, 1998, doi: 10.1089/jop.2017.0121.

[90] R. R. Hartman and U. B. Kompella, "Intravitreal, Subretinal, and Suprachoroidal Injections: Evolution of Microneedles for Drug Delivery," *J. Ocul. Pharmacol. Ther.*, vol. 34, no. 1–2, pp. 141–153, Mar. 2018, doi: 10.1089/jop.2017.0121.

[91] W. Martanto, S. P. Davis, N. R. Holiday, J. Wang, H. S. Gill, and M. R. Prausnitz,

"Transdermal Delivery of Insulin Using Microneedles in Vivo," *Pharm. Res.*, vol. 21, no. 6, pp. 947–952, Jun. 2004, doi: 10.1023/B:PHAM.0000029282.44140.2e.

[92] T. Cetinkaya, B. Ozsoy, Y. O. Cakmak, and O. B. Ozdoganlar, "Fabrication of titanium microneelde probes using micromachining," in *World Congress on Micro and Nano Manufacturing*, 2022, pp. 249–252, doi: doi:10.3850/978-981-18-5180-3_RP51-0063.

[93] B. Cai, W. Xia, S. Bredenberg, and H. Engqvist, "Self-setting bioceramic microscopic protrusions for transdermal drug delivery," *J. Mater. Chem. B*, vol. 2, no. 36, pp. 5992–5998, 2014, doi: 10.1039/C4TB00764F.

[94] S. D. Gittard *et al.*, "Pulsed laser deposition of antimicrobial silver coating on Ormocer® microneedles," *Biofabrication*, vol. 1, no. 4, p. 041001, Dec. 2009, doi: 10.1088/1758-5082/1/4/041001.

[95] C. Yeung *et al.*, "A 3D-printed microfluidic-enabled hollow microneedle architecture for transdermal drug delivery," *Biomicrofluidics*, vol. 13, no. 6, 2019, doi: 10.1063/1.5127778.

[96] A. Trautmann, G.-L. Roth, B. Nujiqi, T. Walther, and R. Hellmann, "Towards a versatile point-of-care system combining femtosecond laser generated microfluidic channels and direct laser written microneedle arrays," *Microsystems Nanoeng.*, vol. 5, no. 1, p. 6, Dec. 2019, doi: 10.1038/s41378-019-0046-5.

[97] K. Lee and H. Jung, "Drawing lithography for microneedles: A review of fundamentals and biomedical applications," *Biomaterials*, vol. 33, no. 30, pp. 7309–7326, Oct. 2012, doi: 10.1016/j.biomaterials.2012.06.065.

[98] D. V. McAllister *et al.*, "Microfabricated needles for transdermal delivery of macromolecules and nanoparticles: Fabrication methods and transport studies," *Proc. Natl. Acad. Sci.*, vol. 100, no. 24, pp. 13755–13760, Nov. 2003, doi: 10.1073/pnas.2331316100.

[99] S. Economidou, C. Pissinato Pere, M. Okereke, and D. Douroumis, "Optimisation of Design and Manufacturing Parameters of 3D Printed Solid Microneedles for Improved Strength, Sharpness, and Drug Delivery," *Micromachines*, vol. 12, no. 2, p. 117, Jan. 2021, doi: 10.3390/mi12020117.

[100] P. Makvandi *et al.*, "Engineering Microneedle Patches for Improved Penetration: Analysis, Skin Models and Factors Affecting Needle Insertion," *Nano-Micro Lett.*, vol. 13, no. 1, p. 93, Jan. 2021, doi: 10.1007/s40820-021-00611-9.

[101] D. W. Bodhale, A. Nisar, and N. Afzulpurkar, "Structural and microfluidic analysis of hollow side-open polymeric microneedles for transdermal drug delivery applications," *Microfluid. Nanofluidics*, vol. 8, no. 3, pp. 373–392, 2010, doi: 10.1007/s10404-009-0467-9.

[102] R. Luttge *et al.*, "Integrated lithographic molding for microneedle-based devices," *J. Microelectromechanical Syst.*, vol. 16, no. 4, pp. 872–884, 2007, doi: 10.1109/JMEMS.2007.899339.

[103] R. F. Donnelly *et al.*, "Design, Optimization and Characterisation of Polymeric Microneedle Arrays Prepared by a Novel Laser-Based Micromoulding Technique," *Pharm. Res.*, vol. 28, no. 1, pp. 41–57, Jan. 2011, doi: 10.1007/s11095-010-0169-8.

[104] M. T. C. McCrudden *et al.*, "Design and physicochemical characterisation of novel dissolving polymeric microneedle arrays for transdermal delivery of high dose, low molecular weight drugs," *J. Control. Release*, vol. 180, no. 1, pp. 71–80, Apr. 2014, doi: 10.1016/j.jconrel.2014.02.007.

[105] R. F. Donnelly *et al.*, "Processing difficulties and instability of carbohydrate

microneedle arrays," *Drug Dev. Ind. Pharm.*, vol. 35, no. 10, pp. 1242–1254, Oct. 2009, doi: 10.1080/03639040902882280.

[106] Q. Yan *et al.*, "Finite Element Analysis for Biodegradable Dissolving Microneedle Materials on Skin Puncture and Mechanical Performance Evaluation," *Polymers (Basel).*, vol. 13, no. 18, p. 3043, Sep. 2021, doi: 10.3390/polym13183043.

[107] S. D. Gittard *et al.*, "The effects of geometry on skin penetration and failure of polymer microneedles," *J. Adhes. Sci. Technol.*, vol. 27, no. 3, pp. 227–243, Feb. 2013, doi: 10.1080/01694243.2012.705101.

[108] Z. Faraji Rad *et al.*, "High-fidelity replication of thermoplastic microneedles with open microfluidic channels," *Microsystems Nanoeng.*, vol. 3, no. 1, p. 17034, Dec. 2017, doi: 10.1038/micronano.2017.34.

[109] A. Hou *et al.*, "Rational Design of Rapidly Separating Dissolving Microneedles for Precise Drug Delivery by Balancing the Mechanical Performance and Disintegration Rate," *Adv. Healthc. Mater.*, vol. 8, no. 21, p. 1900898, Nov. 2019, doi: 10.1002/adhm.201900898.

[110] B. Z. Chen, M. Ashfaq, X. P. Zhang, J. N. Zhang, and X. D. Guo, "In vitro and in vivo assessment of polymer microneedles for controlled transdermal drug delivery," *J. Drug Target.*, vol. 26, no. 8, pp. 720–729, Sep. 2018, doi: 10.1080/1061186X.2018.1424859.

[111] S. P. Davis, B. J. Landis, Z. H. Adams, M. G. Allen, and M. R. Prausnitz, "Insertion of microneedles into skin: measurement and prediction of insertion force and needle fracture force," *J. Biomech.*, vol. 37, no. 8, pp. 1155–1163, Aug. 2004, doi: 10.1016/j.jbiomech.2003.12.010.

[112] J.-H. Park, M. G. Allen, and M. R. Prausnitz, "Biodegradable polymer microneedles: Fabrication, mechanics and transdermal drug delivery," *J. Control. Release*, vol. 104, no. 1, pp. 51–66, May 2005, doi: 10.1016/j.jconrel.2005.02.002.

[113] S. A. Machekposhti, M. Soltani, P. Najafizadeh, S. A. Ebrahimi, and P. Chen, "Biocompatible polymer microneedle for topical/dermal delivery of tranexamic acid," *J. Control. Release*, vol. 261, no. March, pp. 87–92, Sep. 2017, doi: 10.1016/j.jconrel.2017.06.016.

[114] J. Stahl, M. Wohlert, and M. Kietzmann, "Microneedle pretreatment enhances the percutaneous permeation of hydrophilic compounds with high melting points," *BMC Pharmacol. Toxicol.*, vol. 13, pp. 1–7, 2012, doi: 10.1186/2050-6511-13-5.

[115] M. J. Garland *et al.*, "Influence of skin model on in vitro performance of drug-loaded soluble microneedle arrays," *Int. J. Pharm.*, vol. 434, no. 1–2, pp. 80–89, Sep. 2012, doi: 10.1016/j.ijpharm.2012.05.069.

[116] N. Roxhed, B. Samel, L. Nordquist, P. Griss, and G. Stemme, "Painless Drug Delivery Through Microneedle-Based Transdermal Patches Featuring Active Infusion," *IEEE Trans. Biomed. Eng.*, vol. 55, no. 3, pp. 1063–1071, Mar. 2008, doi: 10.1109/TBME.2007.906492.

[117] D. G. Koutsonanos *et al.*, "Transdermal Influenza Immunization with Vaccine-Coated Microneedle Arrays," *PLoS One*, vol. 4, no. 3, p. e4773, Mar. 2009, doi: 10.1371/journal.pone.0004773.

[118] S. Kommareddy *et al.*, "Influenza subunit vaccine coated microneedle patches elicit comparable immune responses to intramuscular injection in guinea pigs," *Vaccine*, vol. 31, no. 34, pp. 3435–3441, Jul. 2013, doi: 10.1016/j.vaccine.2013.01.050.

[119] B.-Z. Wang *et al.*, "Microneedle delivery of an M2e-TLR5 ligand fusion protein to skin confers broadly cross-protective influenza immunity," *J. Control. Release*, vol. 178, no. 1, pp. 1–7, Mar. 2014, doi: 10.1016/j.jconrel.2014.01.002.

[120] Q. Zhu *et al.*, "Immunization by vaccine-coated microneedle arrays protects against lethal influenza virus challenge," *Proc. Natl. Acad. Sci.*, vol. 106, no. 19, pp. 7968–7973, May 2009, doi: 10.1073/pnas.0812652106.

[121] R. L. Atmar, S. M. Patel, and W. A. Keitel, "Intanza ® : a new intradermal vaccine for seasonal influenza," *Expert Rev. Vaccines*, vol. 9, no. 12, pp. 1399–1409, Dec. 2010, doi: 10.1586/erv.10.134.

[122] A. P. Raphael, T. W. Prow, M. L. Crichton, X. Chen, G. J. P. Fernando, and M. A. F. Kendall, "Targeted, Needle-Free Vaccinations in Skin using Multilayered, Densely-Packed Dissolving Microprojection Arrays," *Small*, vol. 6, no. 16, pp. 1785–1793, Aug. 2010, doi: 10.1002/smll.201000326.

[123] S. Kommareddy, B. C. Baudner, S. Oh, S. Kwon, M. Singh, and D. T. O'hagan, "Dissolvable Microneedle Patches for the Delivery of Cell-Culture-Derived Influenza Vaccine Antigens," *J. Pharm. Sci.*, vol. 101, no. 3, pp. 1021–1027, Mar. 2012, doi: 10.1002/jps.23019.

[124] C. Edens, M. L. Collins, J. Ayers, P. A. Rota, and M. R. Prausnitz, "Measles vaccination using a microneedle patch," *Vaccine*, vol. 31, no. 34, pp. 3403–3409, Jul. 2013, doi: 10.1016/j.vaccine.2012.09.062.

[125] J. A. Mikszta *et al.*, "Microneedle-based intradermal delivery of the anthrax recombinant protective antigen vaccine," *Infect. Immun.*, vol. 74, no. 12, pp. 6806–6810, 2006, doi: 10.1128/IAI.01210-06.

[126] E. Kim *et al.*, "Microneedle array delivered recombinant coronavirus vaccines: Immunogenicity and rapid translational development," *EBioMedicine*, vol. 55, pp. 1–12, 2020, doi: 10.1016/j.ebiom.2020.102743.

[127] M. M. Badran, J. Kuntsche, and A. Fahr, "Skin penetration enhancement by a microneedle device (Dermaroller®) in vitro: Dependency on needle size and applied formulation," *Eur. J. Pharm. Sci.*, vol. 36, no. 4–5, pp. 511–523, Mar. 2009, doi: 10.1016/j.ejps.2008.12.008.

[128] A. Singh and S. Yadav, "Microneedling: Advances and widening horizons," *Indian Dermatol. Online J.*, vol. 7, no. 4, p. 244, 2016, doi: 10.4103/2229-5178.185468.

[129] M. C. Aust, D. Fernandes, P. Kolokythas, H. M. Kaplan, and P. M. Vogt, "Percutaneous Collagen Induction Therapy: An Alternative Treatment for Scars, Wrinkles, and Skin Laxity," *Plast. Reconstr. Surg.*, vol. 121, no. 4, pp. 1421–1429, Apr. 2008, doi: 10.1097/01.prs.0000304612.72899.02.

[130] T. M. Blicharz *et al.*, "Microneedle-based device for the one-step painless collection of capillary blood samples," *Nat. Biomed. Eng.*, vol. 2, no. 3, pp. 151–157, 2018, doi: 10.1038/s41551-018-0194-1.

[131] P. M. Wang, M. Cornwell, and M. R. Prausnitz, "Minimally Invasive Extraction of Dermal Interstitial Fluid for Glucose Monitoring Using Microneedles," *Diabetes Technol. Ther.*, vol. 7, no. 1, pp. 131–141, Feb. 2005, doi: 10.1089/dia.2005.7.131.

[132] C. G. Li, C. Y. Lee, K. Lee, and H. Jung, "An optimized hollow microneedle for minimally invasive blood extraction," *Biomed. Microdevices*, vol. 15, no. 1, pp. 17–25, Feb. 2013, doi: 10.1007/s10544-012-9683-2.

[133] U. M. Attia, S. Marson, and J. R. Alcock, "Micro-injection moulding of polymer microfluidic devices," *Microfluid. Nanofluidics*, vol. 7, no. 1, pp. 1–28, Jul. 2009,

doi: 10.1007/s10404-009-0421-x.
[134] G. Tosello, *Micro Injection Molding*. München: Carl Hanser Verlag GmbH & Co. KG, 2018.
[135] D. Masato, L. Piccolo, G. Lucchetta, and M. Sorgato, "Texturing Technologies for Plastics Injection Molding: A Review," *Micromachines*, vol. 13, no. 8, p. 1211, Jul. 2022, doi: 10.3390/mi13081211.
[136] T. Pratap and K. Patra, "Micro ball-end milling—an emerging manufacturing technology for micro-feature patterns," *Int. J. Adv. Manuf. Technol.*, vol. 94, no. 5–8, pp. 2821–2845, Feb. 2018, doi: 10.1007/s00170-017-1064-9.
[137] M. A. Câmara, J. C. C. Rubio, A. M. Abrão, and J. P. Davim, "State of the Art on Micromilling of Materials, a Review," *J. Mater. Sci. Technol.*, vol. 28, no. 8, pp. 673–685, Aug. 2012, doi: 10.1016/S1005-0302(12)60115-7.
[138] J. P. Davim and M. J. Jackson, *Nano and Micromachining*, vol. 1999, no. December. London, UK: ISTE, 2009.
[139] P. Parenti, D. Masato, M. Sorgato, G. Lucchetta, and M. Annoni, "Surface footprint in molds micromilling and effect on part demoldability in micro injection molding," *J. Manuf. Process.*, vol. 29, pp. 160–174, Oct. 2017, doi: 10.1016/j.jmapro.2017.05.024.
[140] R. Melentiev and F. Fang, "Recent advances and challenges of abrasive jet machining," *CIRP J. Manuf. Sci. Technol.*, vol. 22, pp. 1–20, Aug. 2018, doi: 10.1016/j.cirpj.2018.06.001.
[141] H. Wensink, *Fabrication of microstructures by Powder Blasting*. 2002.
[142] D. S. Park, T. I. Seo, and M. W. Cho, "Mechanical etching of micro pockets by powder blasting," *Int. J. Adv. Manuf. Technol.*, vol. 25, no. 11–12, pp. 1098–1104, Jun. 2005, doi: 10.1007/s00170-003-1941-2.
[143] E. C. Jameson, "Electrical Discharge Machining," in *Handbook of Manufacturing Engineering and Technology*, USA: Society of Manufacturing Engineers (SME), 2001.
[144] K. . Ho and S. . Newman, "State of the art electrical discharge machining (EDM)," *Int. J. Mach. Tools Manuf.*, vol. 43, no. 13, pp. 1287–1300, Oct. 2003, doi: 10.1016/S0890-6955(03)00162-7.
[145] I. Fassi and F. Modica, *Micro-Electro Discharge Machining: Principles, Recent Advancements and Applications*. MDPI, 2021.
[146] E. Uhlmann, S. Piltz, and U. Doll, "Machining of micro/miniature dies and moulds by electrical discharge machining—Recent development," *J. Mater. Process. Technol.*, vol. 167, no. 2–3, pp. 488–493, Aug. 2005, doi: 10.1016/j.jmatprotec.2005.06.013.
[147] G. Bissacco, J. Valentincic, H. N. Hansen, and B. D. Wiwe, "Towards the effective tool wear control in micro-EDM milling," *Int. J. Adv. Manuf. Technol.*, vol. 47, no. 1–4, pp. 3–9, Mar. 2010, doi: 10.1007/s00170-009-2057-0.
[148] K. P. Rajurkar, D. Zhu, J. A. McGeough, J. Kozak, and A. De Silva, "New Developments in Electro-Chemical Machining," *CIRP Ann.*, vol. 48, no. 2, pp. 567–579, 1999, doi: 10.1016/S0007-8506(07)63235-1.
[149] D. Patel, V. K. Jain, and J. Ramkumar, "Micro texturing on metallic surfaces: State of the art," *Proc. Inst. Mech. Eng. Part B J. Eng. Manuf.*, vol. 232, no. 6, pp. 941–964, May 2018, doi: 10.1177/0954405416661583.
[150] S. Qian, D. Zhu, N. Qu, H. Li, and D. Yan, "Generating micro-dimples array on the hard chrome-coated surface by modified through mask electrochemical micromachining," *Int. J. Adv. Manuf. Technol.*, vol. 47, no. 9–12, pp. 1121–1127, Apr. 2010, doi: 10.1007/s00170-009-2246-x.

[151] A. Spieser and A. Ivanov, "Recent developments and research challenges in electrochemical micromachining (μECM)," *Int. J. Adv. Manuf. Technol.*, vol. 69, no. 1–4, pp. 563–581, Oct. 2013, doi: 10.1007/s00170-013-5024-8.

[152] W. Natsu, T. Ikeda, and M. Kunieda, "Generating complicated surface with electrolyte jet machining," *Precis. Eng.*, vol. 31, no. 1, pp. 33–39, Jan. 2007, doi: 10.1016/j.precisioneng.2006.02.004.

[153] A. Fadaei Tehrani and E. Imanian, "A new etchant for the chemical machining of St304," *J. Mater. Process. Technol.*, vol. 149, no. 1–3, pp. 404–408, Jun. 2004, doi: 10.1016/j.jmatprotec.2004.02.055.

[154] A. A. G. Bruzzone, H. L. Costa, P. M. Lonardo, and D. A. Lucca, "Advances in engineered surfaces for functional performance," *CIRP Ann.*, vol. 57, no. 2, pp. 750–769, 2008, doi: 10.1016/j.cirp.2008.09.003.

[155] R. Rohith, G. Ruthvik, P. Punithkanthraj, K. P. Raju, and T. S. Nanjundeshwaraswamy, "Chemical Machining Process - A Review," *Proc. Eng. Sci.*, vol. 4, no. 1, pp. 33–36, Feb. 2022, doi: 10.24874/PES04.01.005.

[156] M. D. Shirk and P. A. Molian, "A review of ultrashort pulsed laser ablation of materials," *J. Laser Appl.*, vol. 10, no. 1, pp. 18–28, Feb. 1998, doi: 10.2351/1.521827.

[157] V. Villerius, H. Kooiker, J. Post, and Y. T. Pei, "Ultrashort pulsed laser ablation of stainless steels," *Int. J. Mach. Tools Manuf.*, vol. 138, no. November 2018, pp. 27–35, Mar. 2019, doi: 10.1016/j.ijmachtools.2018.11.003.

[158] S. S. Harilal, J. R. Freeman, P. K. Diwakar, and A. Hassanein, "Femtosecond Laser Ablation: Fundamentals and Applications," 2014, pp. 143–166.

[159] V. Nasrollahi, P. Penchev, T. Jwad, S. Dimov, and K. Kim, "Drilling of micron-scale high aspect ratio holes with ultra-short pulsed lasers : Critical effects of focusing lenses and fluence on the resulting holes ' morphology," *Opt. Lasers Eng.*, vol. 110, no. April, pp. 315–322, 2018, doi: 10.1016/j.optlaseng.2018.04.024.

[160] S. Gräf and F. A. Müller, "Polarisation-dependent generation of fs-laser induced periodic surface structures," *Appl. Surf. Sci.*, vol. 331, pp. 150–155, Mar. 2015, doi: 10.1016/j.apsusc.2015.01.056.

[161] K. M. T. Ahmmed, E. J. Y. Ling, P. Servio, and A.-M. Kietzig, "Introducing a new optimization tool for femtosecond laser-induced surface texturing on titanium, stainless steel, aluminum and copper," *Opt. Lasers Eng.*, vol. 66, pp. 258–268, Mar. 2015, doi: 10.1016/j.optlaseng.2014.09.017.

[162] J.-M. Romano *et al.*, "Springtail-Inspired Triangular Laser-Induced Surface Textures on Metals Using MHz Ultrashort Pulses," *J. Micro Nano-Manufacturing*, vol. 7, no. 2, pp. 4–8, Jun. 2019, doi: 10.1115/1.4043417.

[163] J.-M. Romano *et al.*, "Effects of mould wear on hydrophobic polymer surfaces replicated using plasma-treated and laser-textured stainless steel inserts," *Tribol. - Mater. Surfaces Interfaces*, vol. 14, no. 4, pp. 240–252, Oct. 2020, doi: 10.1080/17515831.2020.1785234.

[164] Y. Li and M. Hong, "Parallel Laser Micro/Nano-Processing for Functional Device Fabrication," *Laser Photon. Rev.*, vol. 14, no. 3, p. 1900062, Mar. 2020, doi: 10.1002/lpor.201900062.

[165] A. Gillner, J. Finger, P. Gretzki, M. Niessen, T. Bartels, and M. Reininghaus, "High Power Laser Processing with Ultrafast and Multi-Parallel Beams," *J. Laser Micro/Nanoengineering*, vol. 14, no. 2, pp. 129–137, Sep. 2019, doi: 10.2961/jlmn.2019.02.0003.

[166] J. Taniguchi, "Electron-Beam Machining," 2018, pp. 555–575.
[167] N. Kawasegi, "Ion Beam Machining," 2018, pp. 529–554.
[168] T. Evens, W. Six, J. De Keyzer, F. Desplentere, and A. Van Bael, "Experimental analysis of conformal cooling in SLM produced injection moulds: Effects on process and product quality," in *AIP Conference Proceedings*, 2019, vol. 2055, doi: 10.1063/1.5084861.
[169] J. P. Kruth, L. Froyen, J. Van Vaerenbergh, P. Mercelis, M. Rombouts, and B. Lauwers, "Selective laser melting of iron-based powder," *J. Mater. Process. Technol.*, vol. 149, no. 1–3, pp. 616–622, Jun. 2004, doi: 10.1016/j.jmatprotec.2003.11.051.
[170] S. L. Sing, C. F. Tey, J. H. K. Tan, S. Huang, and W. Y. Yeong, "3D printing of metals in rapid prototyping of biomaterials: Techniques in additive manufacturing," in *Rapid Prototyping of Biomaterials*, Second Edi., Elsevier, 2020, pp. 17–40.
[171] J.-P. Kruth, S. Dadbakhsh, B. Vrancken, K. Kempen, J. Vleugels, and J. Van Humbeeck, *Additive Manufacturing of Metals via Selective Laser Melting Process Aspects and Material Developments*, vol. 116, no. 3. New York: CRC Press, 2016.
[172] Y. Holovenko, M. Antonov, L. Kollo, and I. Hussainova, "Friction studies of metal surfaces with various 3D printed patterns tested in dry sliding conditions," *Proc. Inst. Mech. Eng. Part J J. Eng. Tribol.*, vol. 232, no. 1, pp. 43–53, Jan. 2018, doi: 10.1177/1350650117738920.
[173] H. Kovacı and Y. Seçer, "Improved tribological performance of AISI 316L stainless steel by a combined surface treatment: Surface texturing by selective laser melting and plasma nitriding," *Surf. Coatings Technol.*, vol. 400, no. July, p. 126178, Oct. 2020, doi: 10.1016/j.surfcoat.2020.126178.
[174] C. W. J. Lim and C. H. Wong, "Investigation of effects of printing patterns on geometry and densification of stainless steel 316L through directed energy deposition," *Proc. Int. Conf. Prog. Addit. Manuf.*, vol. 2018-May, pp. 268–273, 2018.
[175] N. Unno and J. Taniguchi, "3D nanofabrication using controlled-acceleration-voltage electron beam lithography with nanoimprinting technology," *Adv. Opt. Technol.*, vol. 8, no. 3–4, pp. 253–266, Jun. 2019, doi: 10.1515/aot-2019-0004.
[176] C. Wang *et al.*, "Plasmonic Structures, Materials and Lenses for Optical Lithography beyond the Diffraction Limit: A Review," *Micromachines*, vol. 7, no. 7, p. 118, Jul. 2016, doi: 10.3390/mi7070118.
[177] I. De Wolf, *LIGA and Its Applications*, vol. 7. Wiley, 2008.
[178] R. Turner *et al.*, "Tapered LIGA HARMs," *J. Micromechanics Microengineering*, vol. 13, no. 3, pp. 367–372, May 2003, doi: 10.1088/0960-1317/13/3/303.
[179] J. Giboz, T. Copponnex, and P. Mélé, "Microinjection molding of thermoplastic polymers: a review," *J. Micromechanics Microengineering*, vol. 17, no. 6, pp. R96–R109, Jun. 2007, doi: 10.1088/0960-1317/17/6/R02.
[180] H. N. Hansen, R. J. Hocken, and G. Tosello, "Replication of micro and nano surface geometries," *CIRP Ann.*, vol. 60, no. 2, pp. 695–714, 2011, doi: 10.1016/j.cirp.2011.05.008.
[181] D. Loaldi, "PhD Thesis: Integration of Micro and Nano Structures on Injection Moulded Devices. Process Chains and Enabling Technologies," Technical University of Denmark (DTU), 2020.
[182] V. Goodship, *Practical guide to injection moulding*, vol. 52, no. 6. Shrewsbury: Rapra Technology Limited, 1997.
[183] M. Kamal, A. Isayev, and S.-J. Liu, *Injection molding technology and fundamentals*, 1st ed. Munich: Carl Hanser Verlag, 2009.

[184] C. Rytka, P. M. Kristiansen, and A. Neyer, "Iso- and variothermal injection compression moulding of polymer micro- and nanostructures for optical and medical applications," *J. Micromechanics Microengineering*, vol. 25, no. 6, p. 065008, Jun. 2015, doi: 10.1088/0960-1317/25/6/065008.

[185] T. Evens, "Master's thesis: Vergelijkende studie tussen conventioneel, variotherm en hybride variotherm spuitgieten," KU Leuven & UHasselt, 2015.

[186] T. A. Osswald, L.-S. Turng, and P. Gramann, "Special Injection Molding Processes," in *Injection Molding Handbook*, 2nd ed., Munich: Hanser, 2008, pp. 375–479.

[187] M. Sorgato, D. Masato, and G. Lucchetta, "Effect of vacuum venting and mold wettability on the replication of micro-structured surfaces," *Microsystem Technologies*, vol. 23, no. 7. pp. 2543–2552, 2017, doi: 10.1007/s00542-016-3038-5.

[188] D. Loaldi, D. Quagliotti, M. Calaon, P. Parenti, M. Annoni, and G. Tosello, "Manufacturing Signatures of Injection Molding and Injection Compression Molding for Micro-Structured Polymer Fresnel Lens Production," *Micromachines*, vol. 9, no. 12, p. 653, Dec. 2018, doi: 10.3390/mi9120653.

[189] S. Ying Choi, N. Zhang, J. P. Toner, G. Dunne, and M. D. Gilchrist, "Vacuum Venting Enhances the Replication of Nano/Microfeatures in Micro-Injection Molding Process," *J. Micro Nano-Manufacturing*, vol. 4, no. 2, p. 021005, Jun. 2016, doi: 10.1115/1.4032891.

[190] H. Yokoi, X. Han, T. Takahashi, and W. K. Kim, "Effects of molding conditions on transcription molding of microscale prism patterns using ultra-high-speed injection molding," *Polym. Eng. Sci.*, vol. 46, no. 9, pp. 1140–1146, Sep. 2006, doi: 10.1002/pen.20519.

[191] N. S. Ong, H. Zhang, and W. H. Woo, "Plastic Injection Molding of High-Aspect Ratio Micro-Rods," *Mater. Manuf. Process.*, vol. 21, no. 8, pp. 824–831, Dec. 2006, doi: 10.1080/03602550600728083.

[192] S.-H. Yoon, P. Padmanabha, N.-G. Cha, J. L. Mead, and C. M. F. Barry, "Evaluation of Vacuum Venting for Micro-injection Molding," *Int. Polym. Process.*, vol. 26, no. 4, pp. 346–353, Sep. 2011, doi: 10.3139/217.2308.

[193] M. Sorgato, M. Babenko, G. Lucchetta, and B. Whiteside, "Investigation of the influence of vacuum venting on mould surface temperature in micro injection moulding," *Int. J. Adv. Manuf. Technol.*, vol. 88, no. 1–4, pp. 547–555, 2017, doi: 10.1007/s00170-016-8789-8.

[194] S. Kang, "Hot Embossing of Microstructured Surfaces and Thermal Nanoimprinting," in *Micro / Nano Replication*, Hoboken: John Wiley & Sons, Inc., 2012, pp. 123–156.

[195] D. Chu, A. Nemoto, and H. Ito, "Biomimetic superhydrophobic polymer surfaces by replication of hierarchical structures fabricated using precision tooling machine and anodized aluminum oxidation," *Microsyst. Technol.*, vol. 21, no. 1, pp. 123–130, Jan. 2015, doi: 10.1007/s00542-014-2152-5.

[196] M. Han *et al.*, "Improvement in antigen-delivery using fabrication of a grooves-embedded microneedle array," *Sensors Actuators B Chem.*, vol. 137, no. 1, pp. 274–280, Mar. 2009, doi: 10.1016/j.snb.2008.11.017.

[197] S. J. Moon, S. S. Lee, H. S. Lee, and T. H. Kwon, "Fabrication of microneedle array using LIGA and hot embossing process," *Microsyst. Technol.*, vol. 11, no. 4–5, pp. 311–318, 2005, doi: 10.1007/s00542-004-0446-8.

[198] P. Muanchan and H. Ito, "Replication of Micro-/Nanostructures," 2018, pp.

607–634.
[199] S. Kang, "UV-Imprinting Process and Imprinted Micro/Nanostructures," in *Micro / Nano Replication*, Hoboken: John Wiley & Sons, Inc., 2012, pp. 157–195.
[200] H. Tan, A. Gilbertson, and S. Choi, "Roller nanoimprint lithography," *J. Vac. Sci. Technol. B Microelectron. Nanom. Struct.*, vol. 16, no. 6, p. 3926, Nov. 1998, doi: 10.1116/1.590438.
[201] H. Yoshikawa, J. Taniguchi, G. Tazaki, and T. Zento, "Fabrication of high-aspect-ratio pattern via high throughput roll-to-roll ultraviolet nanoimprint lithography," *Microelectron. Eng.*, vol. 112, pp. 273–277, 2013, doi: 10.1016/j.mee.2013.03.117.
[202] N. Kodihalli Shivaprakash, J. Zhang, T. Nahum, C. Barry, Q. Truong, and J. Mead, "Roll-to-roll hot embossing of high aspect ratio micro pillars for superhydrophobic applications," *Int. Polym. Process.*, vol. 34, no. 5, pp. 502–512, 2019, doi: 10.3139/217.3815.
[203] D. Yu *et al.*, "Roll-to-Roll Manufacturing of Micropatterned Adhesives by Template Compression," *Materials (Basel).*, vol. 12, no. 1, p. 97, Dec. 2018, doi: 10.3390/ma12010097.
[204] K. Ita, "Transdermal delivery of drugs with microneedles—potential and challenges," *Pharmaceutics*, vol. 7, no. 3, pp. 90–105, 2015, doi: 10.3390/pharmaceutics7030090.
[205] K. J. NAIR, "PhD thesis, Micro-Injection Moulded Microneedles For Drug Delivery," University of Bradford, 2014.
[206] M. J. Kim *et al.*, "Fabrication of Circular Obelisk-Type Multilayer Microneedles Using Micro-Milling and Spray Deposition," *Front. Bioeng. Biotechnol.*, vol. 6, no. May, pp. 1–13, 2018, doi: 10.3389/fbioe.2018.00054.
[207] Jordan David Hamilton, "Master's thesis, Fabrication and Analysis of Injection Molded Plastic Microneedle Arrays," Georgia Institute of Technology, 2010.
[208] K. J. Krieger, N. Bertollo, M. Dangol, J. T. Sheridan, M. M. Lowery, and E. D. O'Cearbhaill, "Simple and customizable method for fabrication of high-aspect ratio microneedle molds using low-cost 3D printing," *Microsystems Nanoeng.*, vol. 5, no. 1, p. 42, Dec. 2019, doi: 10.1038/s41378-019-0088-8.
[209] T. Henson, "Master's thesis, Replicatie van lasergetextureerde micronaalden met behulp van een kunststof spuitgietproces," KU Leuven, 2019.
[210] A. V Bulgakov and N. M. Bulgakova, "Thermal model of pulsed laser ablation under the conditions of formation and heating of a radiation-absorbing plasma," *Quantum Electron.*, vol. 29, no. 5, pp. 433–437, May 1999, doi: 10.1070/QE1999v029n05ABEH001503.
[211] P. Petkov, S. Scholz, and S. Dimov, "Strategies for material removal in laser milling," in *Conference on Multi-Material Micro Manufacture*, 2008, vol. 3, no. 4.
[212] A. P. Markopoulos, P. Koralli, G. Kyriakakis, M. Kompitsas, and D. E. Manolakos, "Molecular dynamics simulation of material removal with the use of laser beam," in *Materials Forming and Machining*, Elsevier, 2016, pp. 117–153.
[213] J. Held *et al.*, "Design of experiment characterization of microneedle fabrication processes based on dry silicon etching," *J. Micromechanics Microengineering*, vol. 20, no. 2, 2010, doi: 10.1088/0960-1317/20/2/025024.
[214] K. L. Yung *et al.*, "Sharp tipped plastic hollow microneedle array by microinjection moulding," *J. Micromechanics Microengineering*, vol. 22, no. 1, 2012, doi: 10.1088/0960-1317/22/1/015016.
[215] J. S. Kochhar, T. C. Quek, W. J. Soon, J. Choi, S. Zou, and L. Kang, "Effect of

microneedle geometry and supporting substrate on microneedle array penetration into skin," *J. Pharm. Sci.*, vol. 102, no. 11, pp. 4100–4108, 2013, doi: 10.1002/jps.23724.

[216] T. Evens, O. Malek, S. Castagne, D. Seveno, and A. Van Bael, "A novel method for producing solid polymer microneedles using laser ablated moulds in an injection moulding process," *Manuf. Lett.*, vol. 24, pp. 29–32, Apr. 2020, doi: 10.1016/j.mfglet.2020.03.009.

[217] D. O. Kazmer, *Injection Mold Design Engineering*. München: Carl Hanser Verlag GmbH & Co. KG, 2007.

[218] K. Prashanth Reddy and B. Panitapu, "High thermal conductivity mould insert materials for cooling time reduction in thermoplastic injection moulds," *Mater. Today Proc.*, vol. 4, no. 2, pp. 519–526, 2017, doi: 10.1016/j.matpr.2017.01.052.

[219] I. Altenberger, H. A. Kuhn, H. R. Müller, M. Mhaede, M. Gholami-Kermanshahi, and L. Wagner, "Material properties of high-strength beryllium-free copper alloys," *Int. J. Mater. Prod. Technol.*, vol. 50, no. 2, pp. 124–146, 2015, doi: 10.1504/IJMPT.2015.067820.

[220] D. Sykutera, P. Czyzewski, A. Koœciuszko, P. Szewczykowski, L. Wajer, and M. Bieliński, "Monitoring of the injection and holding phases by using a modular injection mold," *J. Polym. Eng.*, vol. 38, no. 1, pp. 63–71, 2018, doi: 10.1515/polyeng-2016-0321.

[221] G. J. Bex, D. Seveno, J. De Keyzer, F. Desplentere, and A. Van Bael, "Wetting measurements as a tool to predict the thermoplastic/thermoset rubber compatibility in two-component injection molding," *J. Appl. Polym. Sci.*, vol. 135, no. 13, 2018, doi: 10.1002/app.46046.

[222] A. Engelmayer, "Galvanometer scanning speeds laser processing," *Ind. Laser Solut.*, pp. 9–11, 2005.

[223] P. Penchev, S. Dimov, D. Bhaduri, S. L. Soo, and B. Crickboom, "Generic software tool for counteracting the dynamics effects of optical beam delivery systems," *Proc. Inst. Mech. Eng. Part B J. Eng. Manuf.*, vol. 231, no. 1, pp. 48–64, 2017, doi: 10.1177/0954405414565379.

[224] S. Buls, T. Craeghs, S. Clijsters, K. Kempen, J. Swevers, and J. P. Kruth, "The influence of a dynamically optimized galvano based laser scanner on the total scan time of SLM parts," *24th Int. SFF Symp. - An Addit. Manuf. Conf. SFF 2013*, pp. 260–266, 2013.

[225] T. Mirtchev, R. Weeks, and S. Minko, "Optimizing the feedback control of Galvo scanners for laser manufacturing systems," *Photonics North 2010*, vol. 7750, no. October, p. 77500T, 2010, doi: 10.1117/12.873068.

[226] J. Cheng, W. Perrie, S. P. Edwardson, E. Fearon, G. Dearden, and K. G. Watkins, "Effects of laser operating parameters on metals micromachining with ultrafast lasers," *Appl. Surf. Sci.*, vol. 256, no. 5, pp. 1514–1520, 2009, doi: 10.1016/j.apsusc.2009.09.013.

[227] E. Audouard and E. Mottay, "Engineering model for ultrafast laser microprocessing," in *Journal of Physics D: Applied Physics*, Mar. 2016, vol. 9740, no. 18, p. 974016, doi: 10.1117/12.2206203.

[228] A. Bharatish and S. Soundarapandian, "Influence of Femtosecond Laser Parameters and Environment on Surface Texture Characteristics of Metals and Non-Metals – State of the Art," *Lasers Manuf. Mater. Process.*, vol. 5, no. 2, pp. 143–167, 2018, doi: 10.1007/s40516-018-0059-1.

[229] M. von Allmen and A. Blatter, *Laser-Beam Interactions with Materials*, vol. 2, no. 3–

4. Berlin, Heidelberg: Springer Berlin Heidelberg, 1995.
[230] K. H. Song and X. Xu, "Explosive phase transformation in excimer laser ablation," *Appl. Surf. Sci.*, vol. 127–129, pp. 111–116, 1998, doi: 10.1016/S0169-4332(97)00619-3.
[231] N. N. Nedialkov, P. A. Atanasov, D. Breitling, G. Heusel, and F. Dausinger, "Ablation of metals by ultrashort laser pulses," in *Proceedings of SPIE*, Apr. 2005, vol. 5830, no. 12, pp. 80–84, doi: 10.1117/12.617375.
[232] E. Bévillon, J. P. Colombier, B. Dutta, and R. Stoian, "Ab initio nonequilibrium thermodynamic and transport properties of ultrafast laser irradiated 316l stainless steel," *J. Phys. Chem. C*, vol. 119, no. 21, pp. 11438–11446, 2015, doi: 10.1021/acs.jpcc.5b02085.
[233] J. L. Hostetler, A. N. Smith, D. M. Czajkowsky, and P. M. Norris, "Measurement of the electron-phonon coupling factor dependence on film thickness and grain size in Au, Cr, and Al," *Appl. Opt.*, vol. 38, no. 16, p. 3614, 1999, doi: 10.1364/ao.38.003614.
[234] H. E. Elsayed-Ali, T. B. Norris, M. A. Pessot, and G. A. Mourou, "Time-resolved observation of electron-phonon relaxation in copper," *Phys. Rev. Lett.*, vol. 58, no. 12, pp. 1212–1215, 1987, doi: 10.1103/PhysRevLett.58.1212.
[235] T. Q. Qiu and C. L. Tien, "Short-pulse laser heating on metals," *Int. J. Heat Mass Transf.*, vol. 35, no. 3, pp. 719–726, 1992, doi: 10.1016/0017-9310(92)90131-B.
[236] S. D. Brorson *et al.*, "Femtosecond room-temperature measurement of the electron-phonon coupling constant in metallic superconductors," *Phys. Rev. Lett.*, vol. 64, no. 18, pp. 2172–2175, 1990, doi: 10.1103/PhysRevLett.64.2172.
[237] A. Ruf, P. Berger, F. Dausinger, and H. Hügel, "Analytical investigations on geometrical influences on laser drilling," *J. Phys. D. Appl. Phys.*, vol. 34, no. 18, pp. 2918–2925, Sep. 2001, doi: 10.1088/0022-3727/34/18/327.
[238] D. Yao and B. Kim, "Injection molding high aspect ratio microfeatures," *J. Inject. Molding Technol.*, vol. 6, no. 1, pp. 11–17, 2002.
[239] S. D. J. Hill, K. P. Kämper, U. Dasbach, J. Döpper, W. Erhfeld, and M. Kaupert, "An investigation of computer modelling for micro-injection moulding," *Proc. microsym'95*, vol. 12, pp. 275–283, 1995.
[240] G. Lucchetta, E. Ferraris, G. Tristo, and D. Reynaerts, "Influence of mould thermal properties on the replication of micro parts via injection moulding," *Procedia CIRP*, vol. 2, no. 1, pp. 113–117, 2012, doi: 10.1016/j.procir.2012.05.051.
[241] C. Rytka, N. Opara, N. K. Andersen, P. M. Kristiansen, and A. Neyer, "On The Role of Wetting, Structure Width, and Flow Characteristics in Polymer Replication on Micro- and Nanoscale," *Macromol. Mater. Eng.*, vol. 301, no. 5, pp. 597–609, May 2016, doi: 10.1002/mame.201500350.
[242] J. Vera, E. Contraires, A. C. Brulez, M. Larochette, S. Valette, and S. Benayoun, "Wetting of polymer melts on coated and uncoated steel surfaces," *Appl. Surf. Sci.*, vol. 410, pp. 87–98, 2017, doi: 10.1016/j.apsusc.2017.02.067.
[243] H. Zhang, F. Fang, M. D. Gilchrist, and N. Zhang, "Filling of high aspect ratio micro features of a microfluidic flow cytometer chip using micro injection moulding," *J. Micromechanics Microengineering*, vol. 28, no. 7, p. 075005, Jul. 2018, doi: 10.1088/1361-6439/aab7bf.
[244] F. Baruffi *et al.*, "Correlating nano-scale surface replication accuracy and cavity temperature in micro-injection moulding using in-line process control and high-speed thermal imaging," *J. Manuf. Process.*, vol. 47, no. August, pp. 367–381, Nov. 2019, doi: 10.1016/j.jmapro.2019.08.017.

[245] K. A. Stelson, "Calculating cooling times for polymer injection moulding," *Proc. Inst. Mech. Eng. Part B J. Eng. Manuf.*, vol. 217, no. 5, pp. 709–713, 2003, doi: 10.1243/095440503322011443.

[246] Q. L. Wang, D. D. Zhu, Y. Chen, and X. D. Guo, "A fabrication method of microneedle molds with controlled microstructures," *Mater. Sci. Eng. C*, vol. 65, pp. 135–142, 2016, doi: 10.1016/j.msec.2016.03.097.

[247] T. Evens, O. Malek, S. Castagne, D. Seveno, and A. Van Bael, "Controlling the geometry of laser ablated microneedle cavities in different mould materials and assessing the replication fidelity within polymer injection moulding," *J. Manuf. Process.*, vol. 62, no. July 2020, pp. 535–545, Feb. 2021, doi: 10.1016/j.jmapro.2020.12.035.

[248] D. Masato, M. Sorgato, and G. Lucchetta, "Characterization of the micro injection-compression molding process for the replication of high aspect ratio micro-structured surfaces," *Microsyst. Technol.*, vol. 23, no. 8, pp. 3661–3670, 2017, doi: 10.1007/s00542-016-3149-z.

[249] C. Hopmann *et al.*, "Injection moulding of optical functional micro structures using laser structured, PVD-coated mould inserts," in *AIP Conference Proceedings*, 2015, vol. 1664, p. 110003, doi: 10.1063/1.4918478.

[250] V. Kalima *et al.*, "Transparent thermoplastics: Replication of diffractive optical elements using micro-injection molding," *Opt. Mater. (Amst).*, vol. 30, no. 2, pp. 285–291, Oct. 2007, doi: 10.1016/j.optmat.2006.11.046.

[251] A. B. Christiansen, J. S. Clausen, N. A. Mortensen, and A. Kristensen, "Injection moulding antireflective nanostructures," *Microelectron. Eng.*, vol. 121, pp. 47–50, Jun. 2014, doi: 10.1016/j.mee.2014.03.027.

[252] M. Yamaguchi, S. Sasaki, S. Suzuki, and Y. Nakayama, "Injection-molded plastic plate with hydrophobic surface by nanoperiodic structure applied in uniaxial direction," *J. Adhes. Sci. Technol.*, vol. 29, no. 1, pp. 24–35, Jan. 2015, doi: 10.1080/01694243.2014.973158.

[253] E. Huovinen, J. Hirvi, M. Suvanto, and T. A. Pakkanen, "Micro–Micro Hierarchy Replacing Micro–Nano Hierarchy: A Precisely Controlled Way To Produce Wear-Resistant Superhydrophobic Polymer Surfaces," *Langmuir*, vol. 28, no. 41, pp. 14747–14755, Oct. 2012, doi: 10.1021/la303358h.

[254] J. Iturri *et al.*, "Torrent Frog-Inspired Adhesives: Attachment to Flooded Surfaces," *Adv. Funct. Mater.*, vol. 25, no. 10, pp. 1499–1505, Mar. 2015, doi: 10.1002/adfm.201403751.

[255] C. Padeste *et al.*, "Replication of high aspect ratio pillar array structures in biocompatible polymers for tissue engineering applications," *Microelectron. Eng.*, vol. 88, no. 8, pp. 1836–1839, Aug. 2011, doi: 10.1016/j.mee.2010.11.051.

[256] C. Gornik, "Injection Moulding of Parts with Microstructured Surfaces for Medical Applications," *Macromol. Symp.*, vol. 217, no. 1, pp. 365–374, Oct. 2004, doi: 10.1002/masy.200451332.

[257] T. Evens *et al.*, "Producing Hollow Polymer Microneedles Using Laser Ablated Molds in an Injection Molding Process," *J. Micro Nano-Manufacturing*, vol. 9, no. 3, pp. 1–9, Sep. 2021, doi: 10.1115/1.4051456.

[258] M. L. Williams, R. F. Landel, and J. D. Ferry, "The Temperature Dependence of Relaxation Mechanisms in Amorphous Polymers and Other Glass-forming Liquids," *J. Am. Chem. Soc.*, vol. 77, no. 14, pp. 3701–3707, Jul. 1955, doi: 10.1021/ja01619a008.

[259] S.-W. Kim and L.-S. Turng, "Three-dimensional numerical simulation of

injection molding filling of optical lens and multiscale geometry using finite element method," *Polym. Eng. Sci.*, vol. 46, no. 9, pp. 1263–1274, Sep. 2006, doi: 10.1002/pen.20585.

[260] H.-Y. Lin and W.-B. Young, "Analysis of the filling capability to the microstructures in micro-injection molding," *Appl. Math. Model.*, vol. 33, no. 9, pp. 3746–3755, Sep. 2009, doi: 10.1016/j.apm.2008.12.012.

[261] S. Choi and S. K. Kim, "Multi-scale filling simulation of micro-injection molding process," *J. Mech. Sci. Technol.*, vol. 25, no. 1, pp. 117–124, Jan. 2011, doi: 10.1007/s12206-010-1025-9.

[262] S. Birkar, G. Mendible, J.-G. Park, J. L. Mead, S. P. Johnston, and C. M. F. Barry, "Effect of feature spacing when injection molding parts with microstructured surfaces," *Polym. Eng. Sci.*, vol. 56, no. 12, pp. 1330–1338, Dec. 2016, doi: 10.1002/pen.24164.

[263] M. Babenko, J. Sweeney, P. Petkov, F. Lacan, S. Bigot, and B. Whiteside, "Evaluation of heat transfer at the cavity-polymer interface in microinjection moulding based on experimental and simulation study," *Appl. Therm. Eng.*, vol. 130, pp. 865–876, Feb. 2018, doi: 10.1016/j.applthermaleng.2017.11.022.

[264] C. V. Madhusudana, *Thermal Contact Conductance*. New York, NY: Springer New York, 1996.

[265] K. A. Narh and L. Sridhar, "U.S. Pat. 6142662," 2000.

[266] E. E. Marotta and L. S. Fletcher, "Thermal contact conductance of polymeric materials," *33rd Aerosp. Sci. Meet. Exhib.*, vol. 10, no. 2, 1995, doi: 10.2514/6.1995-421.

[267] K. A. Narh and L. Sridhar, "Measurement and modeling of thermal contact resistance at a plastic metal interface," *ANTEC Conf. Proc.*, vol. 2, pp. 2273–2277, 1997.

[268] A. Dawson, M. Rides, C. R. G. Allen, and J. M. Urquhart, "Polymer-mould interface heat transfer coefficient measurements for polymer processing," *Polym. Test.*, vol. 27, no. 5, pp. 555–565, 2008, doi: 10.1016/j.polymertesting.2008.02.007.

[269] T. Nguyen-Chung, G. Jüttner, T. Pham, G. Mennig, and M. Gehde, "The importance of precise boundary conditions for the simulation of micro-injection molding," *J. Plast. Technol.*, vol. 4, no. 6, 2008.

[270] T. R. Tofteberg and E. Andreassen, "Multiscale Simulation of Injection Molding of Parts with Low Aspect Ratio Microfeatures," *Int. Polym. Process.*, vol. 25, no. 1, pp. 63–74, Mar. 2010, doi: 10.3139/217.2318.

[271] H. Zhang, F. Fang, M. D. Gilchrist, and N. Zhang, "Precision replication of micro features using micro injection moulding: Process simulation and validation," *Mater. Des.*, vol. 177, p. 107829, Sep. 2019, doi: 10.1016/j.matdes.2019.107829.

[272] G. Xu, L. Yu, L. J. Lee, and K. W. Koelling, "Experimental and numerical studies of injection molding with microfeatures," *Polym. Eng. Sci.*, vol. 45, no. 6, pp. 866–875, Jun. 2005, doi: 10.1002/pen.20341.

[273] C. Rytka, J. Lungershausen, P. M. Kristiansen, and A. Neyer, "3D filling simulation of micro- and nanostructures in comparison to iso- and variothermal injection moulding trials," *J. Micromechanics Microengineering*, vol. 26, no. 6, p. 065018, Jun. 2016, doi: 10.1088/0960-1317/26/6/065018.

[274] L. Sridhar, B. M. Sedlak, and K. A. Narh, "Parametric Study of Heat Transfer in Injection Molding—Effect of Thermal Contact Resistance," *J. Manuf. Sci. Eng.*,

vol. 122, no. 4, pp. 698–705, Nov. 2000, doi: 10.1115/1.1287348.

[275] S. K. Kim, "Effects of Mold Heat Transfer Coefficient on Numerical Simulation of Injection Molding Effects of mold heat transfer coefficient on numerical simulation of injection molding," no. March 2019, 2020, doi: 10.3795/KSME-B.2019.43.3.201.

[276] M. Packianather, C. Griffiths, and W. Kadir, "Micro Injection Moulding Process Parameter Tuning," *Procedia CIRP*, vol. 33, pp. 400–405, 2015, doi: 10.1016/j.procir.2015.06.093.

[277] J. Vera *et al.*, "Factors influencing microinjection molding replication quality," *J. Micromechanics Microengineering*, vol. 28, no. 1, p. 015004, Jan. 2018, doi: 10.1088/1361-6439/aa9a4e.

[278] G. Lucchetta, M. Sorgato, S. Carmignato, and E. Savio, "Investigating the technological limits of micro-injection molding in replicating high aspect ratio micro-structured surfaces," *CIRP Ann.*, vol. 63, no. 1, pp. 521–524, 2014, doi: 10.1016/j.cirp.2014.03.049.

[279] K. Maghsoudi, R. Jafari, G. Momen, and M. Farzaneh, "Micro-nanostructured polymer surfaces using injection molding: A review," *Mater. Today Commun.*, vol. 13, no. September, pp. 126–143, 2017, doi: 10.1016/j.mtcomm.2017.09.013.

[280] T. Evens, S. Castagne, D. Seveno, and A. Van Bael, "Predicting the replication fidelity of injection molded solid polymer microneedles," *Int. Polym. Process.*, vol. 37, no. 3, pp. 237–254, Jul. 2022, doi: 10.1515/ipp-2021-4207.

[281] N. Zhang, J. S. Chu, C. J. Byrne, D. J. Browne, and M. D. Gilchrist, "Replication of micro/nano-scale features by micro injection molding with a bulk metallic glass mold insert," *J. Micromechanics Microengineering*, vol. 22, no. 6, p. 065019, Jun. 2012, doi: 10.1088/0960-1317/22/6/065019.

[282] F. Baruffi, M. Calaon, and G. Tosello, "Effects of micro-injection moulding process parameters on accuracy and precision of thermoplastic elastomer micro rings," *Precis. Eng.*, vol. 51, no. April 2017, pp. 353–361, 2018, doi: 10.1016/j.precisioneng.2017.09.006.

[283] M. Calaon, G. Tosello, J. Garnaes, and H. N. Hansen, "Injection and injection-compression moulding replication capability for the production of polymer lab-on-a-chip with nano structures," *J. Micromechanics Microengineering*, vol. 27, no. 10, 2017, doi: 10.1088/1361-6439/aa853f.

[284] N. Zhang, H. Zhang, C. Stallard, F. Fang, and M. D. Gilchrist, "Replication integrity of micro features using variotherm and vacuum assisted microinjection moulding," *CIRP J. Manuf. Sci. Technol.*, vol. 23, pp. 20–38, 2018, doi: 10.1016/j.cirpj.2018.10.002.

[285] U. A. Theilade and H. N. Hansen, "Surface microstructure replication in injection molding," *Int. J. Adv. Manuf. Technol.*, vol. 33, no. 1–2, pp. 157–166, 2007, doi: 10.1007/s00170-006-0732-y.

[286] K. Mnkknen *et al.*, "Replication of sub-micron features using amorphous thermoplastics," *Polym. Eng. Sci.*, vol. 42, no. 7, pp. 1600–1608, 2002, doi: 10.1002/pen.11055.

[287] D. Masato, M. Sorgato, and G. Lucchetta, "Analysis of the influence of part thickness on the replication of micro-structured surfaces by injection molding," *Materials and Design*, vol. 95. 2016, doi: 10.1016/j.matdes.2016.01.115.

[288] G. Tosello, A. Gava, H. N. Hansen, and G. Lucchetta, "Study of process parameters effect on the filling phase of micro-injection moulding using weld lines as flow markers," *Int. J. Adv. Manuf. Technol.*, vol. 47, no. 1–4, pp. 81–97,

2010, doi: 10.1007/s00170-009-2100-1.
[289] C. Rytka, "Replication of Functional Polymeric Micro- and Nanostructures," *PhD thesis TU Dortmond*, pp. 1–145, 2016.
[290] D. Loaldi *et al.*, "Experimental Validation of Injection Molding Simulations of 3D Microparts and Microstructured Components Using Virtual Design of Experiments and Multi-Scale Modeling," *Micromachines*, vol. 11, no. 6, p. 614, Jun. 2020, doi: 10.3390/mi11060614.
[291] H. Suzuki, T. Takayama, and H. Ito, "Replication Behavior for Micro Surface Features With High Aspect Ratio and Structure Development in Injection Compression Molding," *Int. J. Mod. Phys. Conf. Ser.*, vol. 06, no. 563, pp. 563–569, 2012, doi: 10.1142/s2010194512003789.
[292] M. Roeder, M. Drexler, T. Rothermel, T. Meissner, T. Guenther, and A. Zimmermann, "Injection compression molded microlens arrays for hyperspectral imaging," *Micromachines*, vol. 9, no. 7, pp. 1–14, 2018, doi: 10.3390/mi9070355.
[293] K. Metwally, T. Barriere, and C. Khan-Malek, "Replication of micrometric and sub-micrometric structured surfaces using micro-injection and micro-injection compression moulding," *Int. J. Adv. Manuf. Technol.*, vol. 83, no. 5–8, pp. 779–789, 2016, doi: 10.1007/s00170-015-7602-4.
[294] K. Nagato, T. Hamaguchi, and M. Nakao, "Injection compression molding of high-aspect-ratio nanostructures," *J. Vac. Sci. Technol. B, Nanotechnol. Microelectron. Mater. Process. Meas. Phenom.*, vol. 29, no. 6, p. 06FG10, Nov. 2011, doi: 10.1116/1.3662405.
[295] D. Montgomery, G. Runger, and N. Hubele, *Engineering Statistics*. New York: John Wiley and Sons Inc., 2012.
[296] C. Hopmann, K. Bobzin, T. Brögelmann, M. Orth, N. Kruppe, and M. Naderi, "Replication of micro-structured injection molds using physical vapor deposition coating and dynamic laser mold tempering," *J. Polym. Eng.*, vol. 38, no. 3, pp. 315–322, 2018, doi: 10.1515/polyeng-2017-0131.
[297] B. Sha, S. Dimov, C. Griffiths, and M. S. Packianather, "Investigation of micro-injection moulding: Factors affecting the replication quality," *J. Mater. Process. Technol.*, vol. 183, no. 2–3, pp. 284–296, 2007, doi: 10.1016/j.jmatprotec.2006.10.019.
[298] A.-C. Liou and R.-H. Chen, "Injection molding of polymer micro- and sub-micron structures with high-aspect ratios," *Int. J. Adv. Manuf. Technol.*, vol. 28, no. 11–12, pp. 1097–1103, May 2006, doi: 10.1007/s00170-004-2455-2.
[299] S. H. Park, W. I. Lee, S. N. Moon, Y. E. Yoo, and Y. H. Cho, "Injection molding micro patterns with high aspect ratio using a polymeric flexible stamper," *Express Polym. Lett.*, vol. 5, no. 11, pp. 950–958, 2011, doi: 10.3144/expresspolymlett.2011.93.
[300] S. H. Kim, J. H. Jeong, and J. R. Youn, "Nanopattern insert molding," *Nanotechnology*, vol. 21, no. 20, 2010, doi: 10.1088/0957-4484/21/20/205302.
[301] M. S. Despa, K. W. Kelly, and J. R. Collier, "Injection molding of polymeric LIGA HARMs," *Microsyst. Technol.*, vol. 6, no. 2, pp. 60–66, 1999, doi: 10.1007/s005420050176.
[302] J. Zhao, R. H. Mayes, G. Chen, P. S. Chan, and Z. J. Xiong, "Polymer micromould design and micromoulding process," *Plast. Rubber Compos.*, vol. 32, no. 6, pp. 240–247, 2003, doi: 10.1179/146580103225002614.
[303] L. Yu, C. G. Koh, L. J. Lee, K. W. Koelling, and M. J. Madou, "Experimental

investigation and numerical simulation of injection molding with micro-features," *Polym. Eng. Sci.*, vol. 42, no. 5, pp. 871–888, May 2002, doi: 10.1002/pen.10998.

[304] N. R. Hegde, S. V. Kaveri, and J. Bayry, "Recent advances in the administration of vaccines for infectious diseases: Microneedles as painless delivery devices for mass vaccination," *Drug Discov. Today*, vol. 16, no. 23–24, pp. 1061–1068, 2011, doi: 10.1016/j.drudis.2011.07.004.

[305] J. N. Zuckerman, "The importance of injecting vaccines into muscle," *Br. Med. J.*, vol. 321, no. 7271, pp. 1237–1238, 2000, doi: 10.1136/bmj.321.7271.1237.

[306] K. Mooney, J. C. McElnay, and R. F. Donnelly, "Children's views on microneedle use as an alternative to blood sampling for patient monitoring," *Int. J. Pharm. Pract.*, vol. 22, no. 5, pp. 335–344, 2014, doi: 10.1111/ijpp.12081.

[307] S. Cross and M. Roberts, "Physical Enhancement of Transdermal Drug Application: Is Delivery Technology Keeping up with Pharmaceutical Development?," *Curr. Drug Deliv.*, vol. 1, no. 1, pp. 81–92, 2005, doi: 10.2174/1567201043480045.

[308] L. Simonsen, A. Kane, J. Lloyd, M. Zaffran, and M. Kane, "Unsafe injections in the developing world and transmission of bloodborne pathogens: A review," *Bull. World Health Organ.*, vol. 77, no. 10, pp. 789–800, 1999.

[309] K. Cheung and D. B. Das, "Microneedles for drug delivery: trends and progress," *Drug Deliv.*, vol. 23, no. 7, pp. 2338–2354, Sep. 2016, doi: 10.3109/10717544.2014.986309.

[310] K. S. Paudel, M. Milewski, C. L. Swadley, N. K. Brogden, P. Ghosh, and A. L. Stinchcomb, "Challenges and opportunities in dermal/transdermal delivery," *Ther. Deliv.*, vol. 1, no. 1, pp. 109–131, 2010, doi: 10.4155/tde.10.16.

[311] J. Gupta, E. I. Felner, and M. R. Prausnitz, "Erratum: Minimally invasive insulin delivery in subjects with type 1 diabetes using hollow microneedles (Diabetes Technology and Therapeutics (2009) 11:6 (329-337))," *Diabetes Technol. Ther.*, vol. 11, no. 7, p. 471, 2009, doi: 10.1089/dia.2009.0729.

[312] M. S. Giri Nandagopal, R. Antony, S. Rangabhashiyam, N. Sreekumar, and N. Selvaraju, "Overview of microneedle system: A third generation transdermal drug delivery approach," *Microsyst. Technol.*, vol. 20, no. 7, pp. 1249–1272, 2014, doi: 10.1007/s00542-014-2233-5.

[313] Y. Liu, P. F. Eng, O. J. Guy, K. Roberts, H. Ashraf, and N. Knight, "Advanced deep reactive-ion etching technology for hollow microneedles for transdermal blood sampling and drug delivery," *IET Nanobiotechnology*, vol. 7, no. 2, pp. 59–62, 2013, doi: 10.1049/iet-nbt.2012.0018.

[314] Po-Chun Wang, B. A. Wester, S. Rajaraman, Seung-Joon Paik, Seong-Hyok Kim, and M. G. Allen, "Hollow polymer microneedle array fabricated by photolithography process combined with micromolding technique," in *2009 Annual International Conference of the IEEE Engineering in Medicine and Biology Society*, Sep. 2009, no. September, pp. 7026–7029, doi: 10.1109/IEMBS.2009.5333317.

[315] R. Q. Frazer, R. T. Byron, P. B. Osborne, and K. P. West, "PMMA: An essential material in medicine and dentistry," *J. Long. Term. Eff. Med. Implants*, vol. 15, no. 6, pp. 629–639, 2005, doi: 10.1615/JLongTermEffMedImplants.v15.i6.60.

[316] M. Sorgato and G. Lucchetta, "The evaluation of vacuum venting and variotherm process for improving the replication by injection molding of high aspect ratio micro features for biomedical application," in *AIP Conference Proceedings*, 2015, vol. 1664, no. January 2015, p. 110008, doi: 10.1063/1.4918483.

[317] D. Zhang, D. B. Das, and C. D. Rielly, "Microneedle Assisted Micro-Particle Delivery from Gene Guns: Experiments using skin-mimicking agarose gel," *J. Pharm. Sci.*, vol. 103, no. 2, pp. 613–627, 2014, doi: 10.1002/jps.23835.

[318] F. Dal Dosso, T. Kokalj, J. Belotserkovsky, D. Spasic, and J. Lammertyn, "Self-powered infusion microfluidic pump for ex vivo drug delivery," *Biomed. Microdevices*, vol. 20, no. 2, pp. 1–11, 2018, doi: 10.1007/s10544-018-0289-1.

[319] Plastics Europe, "Plastics Europe Association of Plastics Manufacturers Plastics—The Facts 2021 An analysis of European Plastics Production, Demand and Waste Data," 2021. [Online]. Available: https://plasticseurope.org/knowledge-hub/plastics-the-facts-2021/.

[320] Grand View Research, "Injection Molding Market Size, Share & Trends Analysis Report," 2022. [Online]. Available: www.grandviewresearch.com/industry-analysis/injection-molding-market-report.

[321] Federplast, "Belgium, a powerhouse of the plastics and rubber industry," 2011. [Online]. Available: https://www.yumpu.com/en/document/view/20778718/belgium-a-powerhouse-of-the-plastics-and-rubber-federplastbe.

[322] Knack, "Trends top - Marktanalyse." [Online]. Available: https://trendstop.knack.be/nl/sector/inj/spuitgieten-en-extrusie-van-kunststoffen.aspx.

[323] Grand View Research, "Micromachining Market Size, Share & Trends Analysis Report," 2020. [Online]. Available: https://www.grandviewresearch.com/industry-analysis/micromachining-market.

[324] Fortune Business Insights, "In vitro Diagnostics (IVD) Market Size, Share & Covid-19 impact analysis," 2022. [Online]. Available: https://www.fortunebusinessinsights.com/industry-reports/in-vitro-diagnostics-ivd-market-101443.

[325] Markets and Markets, "In vitro Diagnostics Market by Product and Service," p. 426, 2022, [Online]. Available: https://www.marketsandmarkets.com/Market-Reports/ivd-in-vitro-diagnostics-market-703.html.

[326] Allied Market Research, "Vaccines Market by Technology Type," p. 379, 2022, [Online]. Available: https://www.alliedmarketresearch.com/vaccines-market.

[327] Vaccines Europe, "The EU Vaccine Industry In Figures," 2019. [Online]. Available: https://www.vaccineseurope.eu/wp-content/uploads/2020/02/VE_Factsheet.pdf.

[328] Bloomberg, "More Than 12.6 Billion Shots Given: Covid-19 Tracker," 2022. [Online]. Available: https://www.bloomberg.com/graphics/covid-vaccine-tracker-global-distribution/.

[329] D. Dorling and B. Hennig, "Making visible global injustice in health: mapping the causes of 57 million deaths," in *Medsin Global Health Conference*, 2010.

[330] V. Yuzhakov, "The AdminPen Microneedle Device for Painless & Convenient Drug Delivery," *Drug Deliv. Technol.*, vol. 10, no. 4, pp. 32–36, 2010.

[331] J. B. Alarcon, A. W. Hartley, N. G. Harvey, and J. A. Mikszta, "Preclinical Evaluation of Microneedle Technology for Intradermal Delivery of Influenza Vaccines," *Clin. Vaccine Immunol.*, vol. 14, no. 4, pp. 375–381, Apr. 2007, doi: 10.1128/CVI.00387-06.

[332] European Medicines Agency, "Intanza." https://www.ema.europa.eu/en/medicines/human/EPAR/intanza (accessed

Sep. 13, 2022).
[333] Zosano Pharma, "Zosano Pharma Receives Complete Response Letter from FDA for Qtrypta™," 2020. https://ir.zosanopharma.com/news-releases/news-release-details/zosano-pharma-receives-complete-response-letter-fda-qtryptatm (accessed Sep. 13, 2022).
[334] Nanopass Technologies, "NanoPass's MicronJet microneedle technology." https://www.nanopass.com/ (accessed Sep. 13, 2022).
[335] Debiotech, "DebioJect, micro-needles intradermal injections." https://www.debiotech.com/debioject/ (accessed Sep. 13, 2022).
[336] Idevax, "Improving the accuracy of intradermal drug delivery." https://idevax.com/ (accessed Sep. 22, 2022).
[337] P. Matarrese, A. Fontana, M. Sorlini, L. Diviani, I. Specht, and A. Maggi, "Estimating energy consumption of injection moulding for environmental-driven mould design," *J. Clean. Prod.*, vol. 168, pp. 1505–1512, 2017, doi: https://doi.org/10.1016/j.jclepro.2017.07.144.
[338] Eurostat, "Hourly labour costs," 2022. https://ec.europa.eu/eurostat/statistics-explained/index.php?title=Hourly_labour_costs#Hourly_labour_costs_ranged_between_.E2.82.AC7.0_and_.E2.82.AC46.9_in_2021.
[339] T. Evens, P. Vanwersch, S. Castagne, D. Seveno, O. Malek, and A. Van Bael, "Controlling the flank geometry of injection moulded polymer microneedles made with laser ablated moulds by adapting laser scanning parameters," *Proc. 21st Int. Conf. Eur. Soc. Precis. Eng. Nanotechnology, EUSPEN 2021*, no. June, pp. 65–68, 2021.
[340] T. Evens, S. Castagne, D. Seveno, and A. Van Bael, "Comparing the Replication Fidelity of Solid Microneedles Using Injection Compression Moulding and Conventional Injection Moulding," *Micromachines*, vol. 13, no. 8, p. 1280, Aug. 2022, doi: 10.3390/mi13081280.

# List of Publications

**Publications in international journals**

(1) Evens, T., Castagne, S., Seveno, D., Van Bael, A. (2022). Comparing the replication fidelity of solid microneedles using injection compression moulding and conventional injection moulding. Micromachines, 13 (8), Art. 1280. doi: 10.3390/mi13081280

(2) Evens, T., Castagne, S., Seveno, D., Van Bael, A. (2022). Predicting the replication fidelity of injection molded solid polymer microneedles. International Polymer Processing, 37 (3), 237-254. doi: 10.1515/ipp-2021-4207

(3) Evens, T., Van Hileghem, L., Dal Dosso, F., Lammertyn, J., Malek, O., Castagne, S., Seveno, D., Van Bael, A. (2021). Producing Hollow Polymer Microneedles Using Laser Ablated Molds in an Injection Molding Process. Journal of Micro and Nano-Manufacturing, 9 (3), 1-9. doi: 10.1115/1.4051456

(4) Evens, T., Malek, O., Castagne, S., Seveno, D., Van Bael, A. (2021). Controlling the geometry of laser ablated microneedle cavities in different mould materials and assessing the replication fidelity within polymer injection moulding. Journal Of Manufacturing Processes, 62, 535-545. doi: 10.1016/j.jmapro.2020.12.035

(5) Evens, T., Malek, O., Castagne, S., Seveno, D., Van Bael, A. (2020). A novel method for producing solid polymer microneedles using laser ablated moulds in an injection moulding process. Manufacturing Letters, 24, 29-32. doi: 10.1016/j.mfglet.2020.03.009

(6) Evens, T., Bex, G-J., Yigit, M., De Keyzer, J., Van Bael, A. (2019). The Influence of Mechanical Recycling on Properties in Injection Molding of Fiber-Reinforced Polypropylene. International Polymer Processing, 34 (4), 399-407. doi: 10.3139/217.3770

**Conference proceedings**

(1) Vanwersch, P., Evens, T., Van Bael, A., Castagne, S. (2022). Two-dimensional model for femtosecond laser ablation of metals: validation with percussion drilling experiments. In: Proceedings of the 22nd international conference of the european society for precision engineering and nanotechnology, (91-92). Presented at the euspen 22nd international conference, Geneva, Zwitserland.

(2) Evens, T., Vanwersch, P., Castagne, S., Seveno, D., Malek, O., Van Bael, A. (2021). Controlling the flank geometry of injection moulded polymer microneedles made with laser ablated moulds by adapting laser scanning parameters. In: ICE21157. Presented at the euspen's 21st International

Conference & Exhibition, Technical University of Denmark, 07 Jun 2021-10 Jun 2021.

(3) Evens, T., Six, W., De Keyzer, J., Desplentere, F., Van Bael, A. (2019). Experimental analysis of conformal cooling in SLM produced injection moulds: Effects on process and product quality. In: AIP Conference Proceedings, (070017-1-070017-5). Presented at the Polymer Processing Society PPS, Europe/Africa Conference, Dresden, Germany, 26 Jun 2017-29 Jun 2017. doi: 10.1063/1.5084861

(4) Evens, T., De Schryver, C., Buffel, B., Desplentere, F., De Keyzer, J., Van Bael, A. (2018). The influence of rapid heat cycle moulding on weld lines in fibre reinforced injection moulded products. In: PMI 2018 Conference Proceedings, (1-5). Presented at the International Conference On Polymers And Moulds Innovations, Guimarães, Portugal, 19 Sep 2018-21 Sep 2018. ISBN: 978-989-20-8809-9.

(5) De Schryver, C., Evens, T., Latré, S., Buffel, B., De Keyzer, J., Van Bael, A., Desplentere, F. (2018). The influence of the rib thickness on the strength of ribs in injection moulded short fibre reinforced products: experiments versus numerical simulations. In: Polymer Processing Society Conference Proceedings, (1-8). Presented at the Polymer Processing Society Americas Regional Conference, Boston, Massachusetts, USA, 05

(6) De Schryver, C., Evens, T., Buffel, B., De Keyzer, J., Van Bael, A., Desplentere, F. (2018). The importance of process induced material properties in injection moulded SFRP: radius of curvature in L-profiles. In: PMI 2018 Conference Proceedings, (Paper No. P124), (1-6). Presented at the International Conference On Polymers And Moulds Innovations, Guimarães, Portugal, 19 Sep 2018-21 Sep 2018. ISBN: 978-989-20-8809-9.

# Curriculum Vitae

**Personal data**

Tim Evens
° February 16, 1993 in Genk, Belgium

**Education**

2019-2023
PhD student in Engineering Technology
KU Leuven, Department of Materials Engineering, Diepenbeek Campus, Belgium
Thesis: Injection moulding polymer microneedles using laser ablated moulds

2014-2016
Master of Science in Industrial Engineering
KU Leuven, Diepenbeek Campus, Belgium
UHasselt, Diepenbeek, Belgium
Thesis: Comparative study between conventional, variothermal and hybrid variothermal injection moulding
Graduated Magna Cum Laude

2011-2014
Professional Bachelor Electromechanics
Katholieke Hogeschool Limburg, Diepenbeek campus, Belgium
Graduated Cum Laude

2005-2011
Electromechanics
Technisch Instituut Sint-Michiel, Bree, Belgium
Graduated Cum Laude

**Work experience**

2016-2019
KU Leuven, Diepenbeek Campus, Belgium
Project Engineer at the research group Polymer Processing & Engineering
Main activities:
(1) Vlaio Technology Transfer project "Design of a conformal cooled injection mould through additive manufacturing"
(2) Vlaio Technology Transfer project "Optimisation of the injection moulding of fibre reinforced products by means of new technologies"